BIBLIOGRAPHIC INFORMATION

PB93-214625

Report Nos: REPT-4.1-2

Title: Seismic Behavior of Flanged Masonry Shear Walls. Final Report.

Date: Nov 92

Authors: L. He, and M. J. N. Priestley.

Performing Organization: United States-Japan Coordinated Program for Masonry Building Research.**California Univ., San Diego, La Jolla. Dept. of Applied Mechanics and Engineering Sciences.

Sponsoring Organization: *National Science Foundation, Washington, DC.

Grant Nos: NSF-CES-8722864

Supplementary Notes: See also PB89-147987. Prepared in cooperation with California Univ., San Diego, La Jolla. Dept. of Applied Mechanics and Engineering Sciences. Sponsored by National Science Foundation, Washington, DC.

NTIS Field/Group Codes: 89G, 89D, 50C

Price: PC A13/MF A03

Availability: Available from the National Technical Information Service,
Springfield, VA. 22161

Number of Pages: 295p

Keywords: *Dynamic response, *Masonry, *Walls, *Earthquake damage, Ductility, Stiffness, Matrices(Mathematics), Moments, Reinforcement(Structures), Loads(Forces), Mathematical models, Computer programs, Seismic effects, Tables(Data), Earthquake engineering, Mechanical properties, Flexural strength, Dynamic structural analysis, Test facilities, Strains, *Flanged masonry walls.

Abstract: In the research described here, both experimental and theoretical studies were carried out to investigate the seismic behavior of flanged masonry walls. Based on section analysis, dimensionless design charts and tables for flexural strength, ductility and equivalent stiffness of both unconfined and confined T-section masonry walls have been produced. An inelastic structural component model (SCM) for flanged masonry walls was developed to simulate the overall behavior of a single flanged wall or a T-section component in masonry assemblages. Together with the model, unsymmetrical hysteresis loops for flanged masonry walls were proposed to allow non-linear time-history response analyses. Parallel to the analytical work, the experimental studies involved both pseudo-static and dynamic shake table tests of full scale flanged masonry walls. The experiments investigated the effects of various parameters on the performance of flanged masonry walls and their real response under earthquake attacks. The test data also provide verifications of the analytical models.

米日

U.S. - JAPAN COORDINATED PROGRAM
FOR
MASONRY BUILDING RESEARCH

REPORT NO. 4.1-2

PB93-214625

SEISMIC BEHAVIOR OF FLANGED MASONRY SHEAR WALLS

FINAL REPORT

by

LIMIN HE
M. J. NIGEL PRIESTLEY

November 1992

supported by:

NATIONAL SCIENCE FOUNDATION

GRANT NO. CES-8722864

DEPARTMENT OF APPLIED MECHANICS & ENGINEERING SCIENCES
UNIVERSITY OF CALIFORNIA, SAN DIEGO

1868

This report presents the results of a research project which was part of the U.S. Coordinated Program for Masonry Building Research. The program constitutes the United States part of the United States - Japan Coordinated Masonry Research Program conducted under the auspices of the Panel on Wind and Seismic Effects of the U.S.-Japan Natural Resources Development Program (UJNR).

This material is based on work supported by the National Science Foundation under the direction of Program Director, Dr. S.C. Liu.

米
日

U.S. - JAPAN COORDINATED PROGRAM
FOR
MASONRY BUILDING RESEARCH

PB93-214625

REPORT NO. 4.1-2

SEISMIC BEHAVIOR OF FLANGED MASONRY SHEAR WALLS

FINAL REPORT

by

LIMIN HE
M. J. NIGEL PRIESTLEY

November 1992

supported by:

NATIONAL SCIENCE FOUNDATION

GRANT NO. CES-8722864

DEPARTMENT OF APPLIED MECHANICS & ENGINEERING SCIENCES
UNIVERSITY OF CALIFORNIA, SAN DIEGO

1868

1b

2 of 6 Complete Record

NTIS No: PB89-147987/HDM

Title: Seismic Behavior of Flanged Masonry Shear Walls

Author(s): Limin, H. ; Priestley, M. J. N.

Performing Organization: California Univ., San Diego, La Jolla. Dept. of Applied Mechanics and Engineering Sciences.

Report No: NSF/ENG-88007

Sponsoring Organization: National Science Foundation, Washington, DC. Directorate for Engineering.

Contract No: NSF-CES87-22864

Notes: U.S.-Japan Coordinated Program for Masonry Building Research. Sponsored by National Science Foundation, Washington, DC. Directorate for Engineering.

Date: May 88 Pages: 134p NTIS Price Code: PC A07/MF A01

Language: English Country: United States

Abstract: The report summarizes the results of a research project representing preliminary studies into the flexural strength, ductility, and seismic response of T-Section Masonry Walls. The project consisted of two sections: (1) analytical studies resulting in the development of dimensionless design charts for flexural strength, stiffness and ductility capacity of unconfined and confined T-section walls loaded in the two opposite directions parallel to the web; and (2) shake table testing of a full-size wide-flange T-section wall under sinusoidal and simulated earthquake acceleration input focusing on the expected asymmetric response, and the shear lag in the flange. Results confirmed the importance of the directionality of strength and stiffness characteristics.

Descriptors: *Earthquakes; *Dynamic response; *Walls; Masonry; Dynamic structural analysis; Flexural strength; Ductility; Stiffness; Mechanical properties; Loads(Forces); Graphs(Charts)

Identifiers: NTISNSFENG

NTIS Subject Codes: 89D (Building Industry Technology--Structural analyses); 89G (Building Industry Technology--Construction Materials, Components, and Equipment); 46E (Physics--Structural Mechanics); 71D (Materials Sciences--Ceramics, Refractories, and Glass)

TABLE OF CONTENTS

ABSTRACT

This report summarizes the results of a research on seismic behavior of flanged masonry walls which is listed under Task 4.1 among the specific tasks under the U.S.-Japan Technical Coordinated Committee on Masonry Research(TCCMAR).

Flanged masonry walls have special problems associated with their material and T-section geometry, especially the strong unsymmetrical response in the two opposite directions parallel to the web under earthquake attacks. The contribution of reinforcement in the flange towards the flexural strength in the direction where the flange is in tension will be subjected to shear-lag effects etc.. Although these phenomena have been understood by many designers for some time, they have not previously been systematically investigated and quantified.

In the research described here, both experimental and theoretical studies were carried out to investigate the seismic behavior of flanged masonry walls. Based on section analysis, dimensionless design charts and tables for flexural strength, ductility and equivalent stiffness of both unconfined and confined T-section masonry walls have been produced.

An inelastic structural component model (SCM) for flanged masonry walls was developed to simulate the overall behavior of a single flanged wall or a T-section component in masonry assemblages. Together with the model, unsymmetrical hysteresis loops for flanged masonry walls were proposed to allow non-linear time-history response analyses.

Parallel to the analytical work, the experimental studies involved both pseudo-static and dynamic shake table tests of full scale flanged masonry walls. The experiments investigated the effects of various parameters on the performance of flanged masonry walls and their real response under earthquake attacks. The test data also provide verifications of the analytical models.

The numerical examples of time-history response analyses with the SCM model are presented and the comparison showed very good agreement between the analytical and experimental results. Based on the theoretical and experimental studies, formulas for determining the effective flange width of T-section masonry walls were proposed. Finally, conclusions and some recommendations for further studies are discussed.

LIST OF FIGURES

LIST OF TABLES

ACKNOWLEDGEMENTS

The financial assistance in part by UCSD Academic Senate Grant RM-1179 and in part by the National Science Foundation for this research through Grant No. CES-8722864 (A.J. Eggenberger and H. Lagorio cognizant NSF program directors) is acknowledged. The research described herein formed task 4.1 of the TCCMAR coordinated research program and seismic design of masonry structures.

The conclusions herein are those of the authors alone, and should not be construed to indicate endorsement by the National Science Foundation, the U.S. Government, or TCCMAR.

The research described in this report formed part of the doctoral studies by He, supervised by Priestley.

1. INTRODUCTION

1.1 Characteristics of Flanged Masonry Walls

Masonry, as a structural material, has been used for thousands years and is still very popular in many countries including the United States. Despite this, research about masonry material properties and structural behavior, especially the seismic performance, is less well developed than for other materials, such as steel and reinforced concrete structures. There are certain problems inherent in the prediction of the behavior of masonry structures and the main difficulties are seen to be the following:

(1) Masonry does not contain a single material. It consists of three components, namely masonry units, mortar and grout. Therefore, the property of masonry will depend on the properties of, and interactions between these components.

(2) The properties within masonry structures are neither homogeneous nor isotropic. They depend on the position and direction of the mortar beds and also the reinforcement, when used. Because of masonry tensile cracking, slip between the steel and the surrounding masonry, and the yielding of reinforcement, the behavior of masonry structures is further complicated.

(3) Since masonry structures must be laid-up in-situ, the workmanship may affect the quality and performance of the structures significantly.

The most commonly used construction form for masonry buildings utilizes structural walls. In many practical design situations, the structural requirements for lateral strength in the two principal orthogonal directions of masonry structures will result in intersecting shear walls, creating structural elements of flanged shapes, such as I, T and ⊏ section walls.

For the flanged wall shown in Fig. 1.1, of particular interests is seismic response with the loading direction parallel to the web, because the wall has different flexural strength, stiffness and ductility capacity in the two opposite directions. As idealized in the figure, when the flange is in tension, the flexural strength and post-cracking stiffness are greater than when the flange is in compression, but the ultimate displacement and hence the displacement ductility is greatly reduced. Clearly, the stiffness of such a wall relative to other lateral load resisting elements and the contribution to lateral strength will depend on the direction of seismic attack. Although this directionality effect has been understood by many designers for some time, the effects have not previously been quantified.

There are other problems associated with T-section walls. Flexural strength design will normally be dictated by the weak direction (i.e. with the flange in compression) and web reinforcement for response parallel to the web will be based on providing adequate flexural strength in this direction of loading. Reinforcement in the flange will normally be dictated by strength requirements under seismic response parallel to the flange.

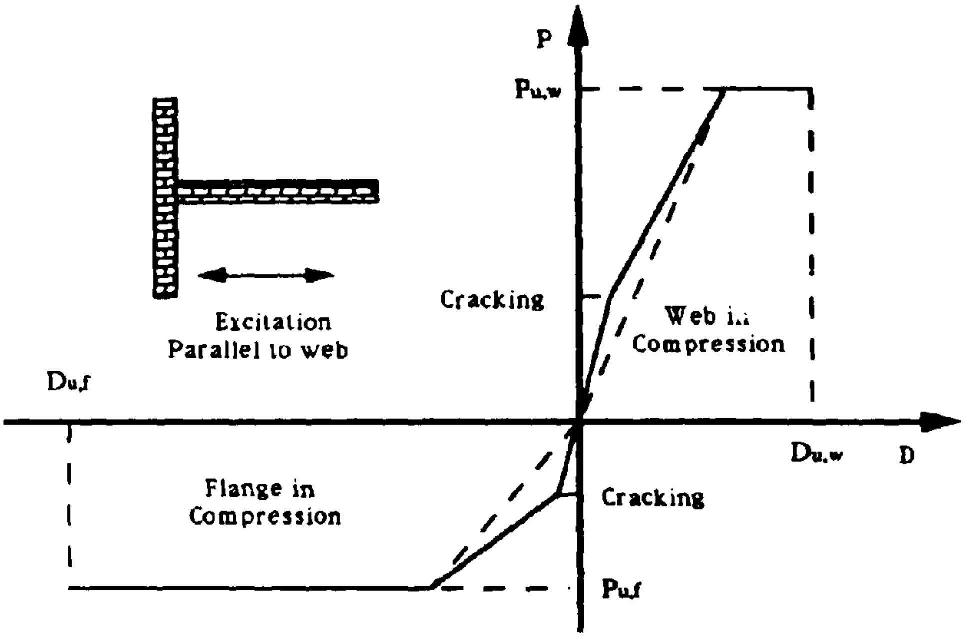

Fig. 1.1 Force-Deflection Characteristics for a T- section Wall Excited Parallel to the Web

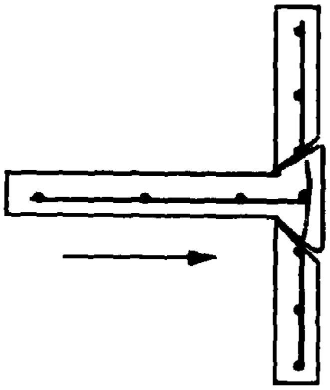

Fig. 1.2 Punching Shear Failure of T-Section Flange Due to Web Sliding on Base

This reinforcement has insignificant influence on the flexural strength parallel to the web with the flange in compression, but contributes greatly to flexural strength in the opposite direction of loading, and may enhance the flexural strength significantly above the level required to satisfy design lateral force levels.

Assuming the structure to be designed for ductile response to earthquakes, it is the actual flexural strength that will be achieved, not the design level. The consequence can be amplification of the response shear force well above the level required to conform to code-level loading. If this situation is not recognized by the designer, and appropriate capacity design[4] measures adopted, shear failure can result.

Shear-lag effects in the flange are poorly understood. The extent to which the flange reinforcement contributes to the flexural strength when the flange is in tension will be influenced by shear-lag. Although the New Zealand Design Code[3] provides some guidance on this matter, its provisions are based on the application of ACI design rules[2] for effective width of T-beam floors, and have not been verified experimentally. Other codes do not appear to have specific recommendations for effective flange width. It seems probably that the extent to which the flange is effective may depend on cracking in the plane of the flange developed by previous inelastic response (if any) perpendicular to the web.

Effectiveness of the connection detail at the intersection between the flange and web is also a matter of concern, and will depend on the block type adopted, amount of transverse reinforcement crossing the intersection, type of connection detail adopted etc.. Again, experimental research is needed to investigate this aspect. Testing of squat flanged reinforced concrete walls by Paulay et al.[5] has indicated that the tendency for such walls to slide on the base in the absence of significant applied axial load can result in punching shear failure, where the sliding web punches through the stationary flange as illustrated in Fig. 1.2. It may be expected that masonry walls with pre-existing planes of weakness imposed by the mortar beds and head joints might be more susceptible to this form of damage than reinforced concrete walls would be. The solution suggested by Paulay et al. of using diagonal reinforcement across the wall base to reduce slip would seem to be impractical for hollow unit masonry construction.

1.2 Review of Relevant Research

In recent years, the behavior of masonry structures, especially relating to their seismic performance has received increased research attention. The basic and important structural form of masonry buildings is rectangular section walls which have been investigated both analytically and experimentally in some detail.

1.2.1 Experimental Studies on Rectangular Section Walls

Experimental studies at the University of Canterbury by Priestley of heavily reinforced squat walls[6] and slender walls[7], subjected to in-plane simulated seismic loading, confirmed that ultimate strength design equations for masonry structural walls are applicable and ductile flexural response can result, provided capacity design procedures are applied, ensuring that the shear strength exceeds the maximum feasible flexural strength.

Tests at the University of California, Berkeley by Mayes et al.[8] on masonry piers investigated the in-plane shear failure mode. In this and the subsequent experiments, they carried out tests of 80 specimens, including double and single piers with height to width ratio from 0.5 to 2. The research variables included the effects of height to width ratio, axial load level, amount of vertical and horizontal reinforcement and type of construction and grouting, on the failure mode and ultimate strength of masonry wall elements.

The above studies indicated that walls failing in a predominantly shear mode exhibited more brittle behavior than those whose inelastic response was dominated by flexural strength, and that the flexural strength of reinforced masonry walls can be accurately evaluated with simple analytical models.

Starting from 1985, a comprehensive program on masonry research in the United States, coordinated with a parallel program in Japan was carried out. The program, funded by the National Science Foundation, has been conducted under the auspices of the UJNR panel on wind and seismic effects and consists of twenty eight specific tasks. Among these, seven projects have dealt with masonry walls, including static and dynamic modelling and experimental studies on in-plane and out-of-plane behavior of one, two and three story walls. A final study of a five story masonry building is currently in the design phase and will be tested in Charles Lee and Powell Structural Laboratory at the University of California, San Diego soon.

Recent studies at the University of Colorado by Shing et al.[10], as part of the TCCMAR program, have been concentrating on defining the strength and ductility of masonry shear-resisting mechanisms, again with squat rectangular section walls. They conducted a experimental program of twenty two 6 foot square masonry wall panels, including sixteen walls with hollow concrete blocks and six with hollow clay bricks. The study interests included the influence of the applied axial load and amount of vertical and horizontal reinforcement on the lateral resistance, failure mechanism, ductility and energy dissipation capacity of masonry shear walls.

The test results of Shing et al. show that the flexural strength increases with the applied axial stress and amount of vertical reinforcement present and the shear strength dominated by diagonal cracking increases with the amount of vertical and horizontal steel, the tensile strength of masonry and the applied axial stresses. However, for the panel dimensions tested, the axial stress had a more significant influence on the flexural strength than on the shear strength, while flexural ductility was substantially reduced at high axial load levels.

Since brittle failure is undesirable for seismic response and also since shear strength is difficult to calculate from first principles, a semi-empirical formula for predicting the shear strength was proposed and calibrated against the experimental results.

In-plane resistance of multi-story masonry walls[15] and the behavior of rectangular masonry walls under out-of-plane loads, especially subjected to earthquake attacks have also been investigated in the TCCMAR Program recently[16,17].

The Japanese side of TCCMAR research program consists of two categories: the Structural Test Program and Material & Construction Program[33]. The Structural Test Program involves tests of masonry wall columns, wall girders, 3-story planar masonry frames and a 5-story reinforced masonry building. Meanwhile, the Material & Construction Program involves tests of masonry units and prisms to set up standard methods of testing and evaluating material properties such as strength and elastic modulus for masonry. Many construction techniques, mainly grout admixture, bonding system, joints and measures to resist frost and salt effects are also investigated under this category. All the researches above have been aimed at developing design and construction guidelines for new reinforced masonry buildings.

The research on masonry walls consists of 5 tasks and 44 specimens have been tested. Teshigawara and Nishi[36,38,40] carried out a group of experiments on diagonal compression test of masonry panels, masonry prism compression and shear wall tests to study the correlation of diagonal cracking and strength between diagonal compression and combined axial load and shear. In another test program, they investigated the seismic capacity of reinforced masonry walls under high axial load. Arivaga and Bara[39] did a similar test of 28 wall panels under diagonal compression. It was concluded from the above tests that diagonal cracking occurred independent of the existence, or amount of horizontal reinforcement, but higher axial force and horizontal reinforcement ratio increased the shear strength of the wall after cracking.

Imai and Miyamoto[35,37] carried out a test program to investigate the effects of openings on seismic behavior of masonry walls. They concluded that with openings, diagonal cracks developed at lower shear level from the corner of the opening to the edge of the wall and the final failure mode could be either bending or shear failure, depending on the relative size of the opening. Shear and flexural strength of masonry walls with openings can be predicted by the same formula as for reinforced concrete walls, but using masonry compression strength instead of concrete compression strength.

The effectiveness of shear enforcement in fully grouted hollow clay masonry walls and effects of lap joint of reinforcement on flexural strength of concrete masonry walls were investigated by Matsumura[36] and Kubota & Murakami[41] respectively. Out-of-plane behavior of masonry wall-slab and wall-subbeam subassemblages was also investigated by Kaminosono et al. [42]

1.2.2 Theoretical Studies

(a) Constitutive Models

Parallel to the experimental studies, many analytical methods of different levels of complexities for predicting the performance of structural masonry walls and assemblages have been developed. In these theoretical studies, a fundamental task has been to determine the relationship between stress and strain for masonry. Based on prism tests, axial compression stress-strain curves of masonry were proposed by Priestley & Elder[18] and Hart et al.[19] which can serve as material constitutive law when analytical methods are used to analyze masonry structures.

Hegemier et al.[20,21] carried out bi-axial tests of full scale concrete masonry panels and proposed stress-strain relationship for both compression and tension, and a failure envelope of the material under bi-axial loading. Based on the above tests, they developed a finite element micro model for reinforced masonry to simulate the pre- and post-fracture behavior of joints or interfaces in assemblages with nonlinear material properties including masonry cracking and effects of reinforcing steel.

Hamid and Drysdale[22] proposed two separated failure criteria for shear failure mode and tension failure mode for brick masonry. The shear failure criterion was based on the assumption that sliding along a single plane of weakness is governed by a linear relationship using the Mohr-Coulomb theory of internal friction. In the meanwhile, for tension failure, the maximum stress theory was adopted. Motta & Damore[23] and Priestley[13] also suggested similar failure envelopes for concrete masonry under bi-axial loading.

(b) Section Characteristics

Priestley carried out analytical studies in dimensionless form to produce design charts predicting the flexural strength[11] and ductility capacity[12] of unconfined masonry walls of rectangular section. He showed that flexural strength was relatively insensitive to the fashion in which the flexural reinforcement was distributed, provided the distribution was symmetrical about the wall centerline. Ductility capacity increased with increasing masonry compression strength, but decreased with increasing axial load level and vertical reinforcement ratio.

(c) Finite Element models (FEM)

Recently, many researchers have been concentrating on developing finite element models for masonry structure analyses at different levels of complexity. Arturo and Abrams[24], in a TCCMAR study, used an elastic finite element model to simulate the dynamic response of two and three storey reinforced masonry buildings subjected to earthquakes. A 3-dimensional element was applied to model perforated flange walls. They examined the influence of different lateral force distributions on normal and shear stresses in the walls and on lateral drifts and compared the computed results with measured values from test results.

Seible et al.[25] developed a nonlinear finite element model for analyzing in-plane reinforced concrete masonry components and subassemblages under seismic loads, as part of the TCCMAR program. The model was based on lower or higher order isoparametric elements in which reinforcement and masonry are treated separately but are overlaid and linked by compatibility requirements. The constitutive law for the fully grouted masonry is orthogonally anisotropic with a smeared crack theory adopted from the Vecchio & Collins model for reinforced concrete[32] . The reinforcement can be treated either in discrete form or as a smeared overlay in horizontal and vertical directions. The model can predict the structural behavior from the initial undamaged conditions to the ultimate collapse, including simulation of cracking, yielding and crushing, and has been used to predict the behavior of single-story walls and flanged wall subassemblages of full-scale reinforced concrete masonry buildings. Analytical results compared favorably with experimental results.

(d) Structural Component Model (SCM)

Although the FEM is versatile and capable of performing structural analyses at different levels, it is time-consuming and expensive due to the fine discrete requirement.

Another analytical method, the structural component model for masonry has been developed by Hart et al.[26] This is a 'macroscopic' approach to simulate the overall behavior of the structure and requires much less computational time than the ordinary FEM. So far, the response of SCM in the form of force-deflection envelope curve for single degree of freedom rectangular walls under monotonic incremental displacement has been completed. Extension of the model to simulate nonlinear behavior of complete structures under cyclic loading is in progress.

1.2.3 Flanged Wall Studies

Although flanged masonry walls are more common in the 'real world' than rectangular section walls, there has been surprisingly little research emphasis to develop an understanding of the performance of such sections under seismic response.

Recent work by Abrams and Paulson[14] at the University of Illinois, Urbana/Champaign involved structural testing of simple complete masonry structures including flanged elements. The scope of the program did not, however, allow a systematic investigation of the characteristics of flanged walls. Apart from this there appear to have been no studies of the behavior of flanged masonry walls. It is of interesting and concern that lack of relevant experimental data on flanged walls extends to reinforced concrete shear walls as well as masonry walls.

Considering the above, a preliminary study on seismic behavior of flanged masonry walls was carried out by Priestley and He[27]. The study was initiated at the University of Canterbury, New Zealand and completed at the University of California, San Diego. This study, which formed the first phase of the more detailed program reported herein consisted of analytical research to extend the dimensionless design charts for flexural strength and ductility of rectangular wall, to flanged walls, and the shake table testing of one wide-flange T-section masonry wall. Both the theoretical analysis and shake table test clearly indicated the unsymmetrical behavior of flanged masonry walls in the two directions parallel to the web, as idealized in Fig. 1.1.

This preliminary study revealed some important aspects of the properties of flanged masonry walls, such as the flexural strength, curvature and displacement ductility capacity, equivalent stiffness and damping, shear-lag in flange, shear stress and deformation in the web etc.. Since the theoretical analysis was limited and only one wall was tested in this project, the more complete study described in this report was undertaken to provide better understanding and quantifying the properties of flanged masonry walls, in a form suitable to the development of a general flanged wall structural component model.

1.3 Overview of Present Research

This report summarizes the results of a research project on flanged masonry walls carried out as part of the US side of research under the auspices of US-Japan Technical Coordinated Committee on Masonry Research (TCCMAR). The research in this project consists of the following aspects:

(1) Theoretical analysis to develop dimensionless design charts and tables for flexural strength, ductility and equivalent stiffness for unconfined and confined T-section masonry walls. The basic assumptions and theoretical formulations are described in Chapter 2. Some selected design charts and a numerical example for demonstrating the use of these charts are also presented in the chapter. The computer program which can be used to produce the above design tables is included in Appendix A for reference.

(2) An inelastic structural component model(SCM) for flanged masonry walls is developed in Chapter 3. The model is formulated in such a way as to simulate the overall behavior of a single flanged wall, or to represent a T-section component in a masonry assemblage by connecting it to the other elements in order to analyze the whole structure. The

basic concepts of the modelling, formulations of the element stiffness matrix in local coordinates and its transformation into global coordinates are summarized. The element formulation includes description of hysteresis loops for flanged masonry walls to allow non-linear time-history response analyses to be carried out.

(3) Experimental studies were also carried out to provide verifications of the analytical models. The work consisted of two phases; pseudo-static tests and dynamic tests.

Chapter 4 provides a general description of the test program, including design and construction of the specimens. The dimensions of the walls, reinforcement arrangement and test results of material properties are also presented in this chapter.

The pseudo-static tests comprised four full scale flanged masonry walls. The influence of variation of vertical reinforcement ratio, the width of flanges, and the use of confined vs. unconfined masonry were investigated. The test set-up, instrumentation and data acquisition system, loading procedure and test results are summarized in Chapter 5.

Chapter 6 introduces the dynamic testing program, which consisted of five full scale flanged masonry walls tested on the shake table, in order to check the differences in the responses under static and dynamic conditions, and to investigate response to simulated earthquake accelerograms. The tests also investigate the influence of loading history and direction as well as vertical reinforcement ratio and confinement on the performance of flanged masonry walls. The test facilities, data acquisition, testing procedures and results of the tests are also described in this chapter.

(4) To compare the theoretical and experimental studies, Chapter 7 compares analytical time-history response predictions using the SCM model developed in Chapter 3 with experimental results obtained in Chapters 5 and 6. Some discussions and conclusions concerning the analytical model are also presented together with the comparisons.

(5) In Chapter 8, both theoretical and experimental methods are applied to investigate shear-lag effects in wall flange. The theoretical studies include elasto-plastic solution and finite element analysis with a 2-dimensional inelastic model for masonry assemblages. The experimental data are adopted from pseudo-static and dynamic tests described in Chapters 5 and 6. Based on the results of above studies, formulas for determining the effective flange width of T-section masonry walls are proposed.

(6) Finally, Chapter 9 summarizes the research project and provides concluding remarks. Some recommendations for further studies are also proposed.

2. FLEXURAL STRENGTH, STIFFNESS AND DUCTILITY OF FLANGED MASONRY WALLS

2.1 Introduction

A typical flanged masonry wall and its idealized load-deflection relationship in the two opposite directions parallel to the web are shown in Fig. 1.1. The flexural strength, stiffness and ductility of the wall depend on the direction of load application. The reason is as follows: with the flange in tension, a high reinforcement tensile force with a large lever arm is mobilized, resulting in a higher flexural strength than when the flange is in compression. However, a consequence of the high tensile force and reduced compression zone width when the flange is in tension is that the distance from the extreme compression fibre to the neutral axis, c, is much greater than when the flange is in compression. This results in increased stiffness of the cracked section and significantly reduced ultimate curvature Φ_u which can be expressed as $\Phi_u = \varepsilon_{cu} / c_u$ where ε_u is the ultimate compression strain of masonry and c_u is the depth of the compression zone.

For the purpose of designing flanged masonry walls, charts and tables of flexural strength, equivalent stiffness and ductility capacity for both unconfined and confined masonry may be produced using the following convenient dimensionless parameters:

$$N = P_e / f'_m \, l_w t \tag{2.1}$$

$$\rho = A_{st} / l_w t \tag{2.2}$$

$$M = m / f'_m \, l_w^2 t \tag{2.3}$$

$$\varphi = \Phi \, l_w \tag{2.4}$$

where N, M, φ and P_e, m, Φ are dimensionless or real axial load, moment and curvature respectively; A_{st} and ρ are flexural reinforcement area and ratio respectively; f'_m is masonry compression strength; l_w and t are web length and thickness respectively.

2.2 Basic Assumptions

The section shape analyzed is shown in Fig. 2.1, together with critical dimensions. Note that if the total flange length $l_f = 0$, the wall section reverts to a rectangular wall of section of l_w by t. The following assumptions are made for the analysis:

(1) Plane sections of the wall remain plane up to the ultimate state.

(2) The discrete reinforcement pattern indicated in Fig. 2.1 (a) can be replaced by an equivalent reinforcement lamina of equal total area as shown in Fig. 2.1 (b).

(3) Shear-lag effects are ignored. Thus all reinforcement in the flange is considered as fully effective (note: this assumption results directly from assumption (1)). Shear-lag effects are considered separately in Chapter 8, enabling the effective flange width to be used in calculation to be considered.

(4) The thickness and local reinforcement ratio of flange and web are equal, i.e. $t_f = t$ and $\rho_f = \rho$. Note that ρ_f is frequently not equal to ρ. However, by adjusting the flange width and using an equivalent width, the effect of different steel ratios in flange and web can be considered. This adjustment is exact when the flange is in tension. When the flange is

in compression, small errors may result because of an incorrectly calculated masonry compression zone depth. The error introduced in strength or stiffness are usually less 1%. Ductility will be affected more significantly, but is almost never a problem when the flange is in compression.

(5) The axial load is uniformly distributed across the T-section. Thus, the vertical line of action of the resultant axial load passes through the geometric center of the gross section.

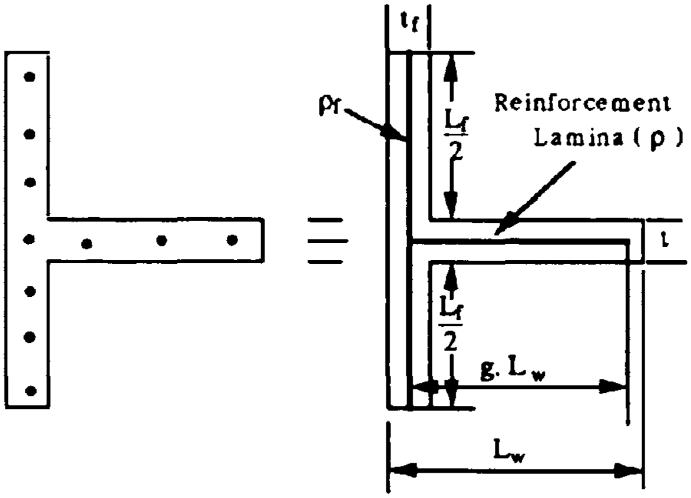

(a) Actual Section (b) Equivalent Section

Fig. 2.1 Cross Section of Flanged Masonry Wall

2.3 Material Properties

The stress-strain relationship of the flexural reinforcement is assumed to be elastic-perfect plastic, ignoring strain hardening effects.

The stress-strain curve for both unconfined and confined masonry, proposed by Priestley and Elder[18] as shown in Fig. 2.2, was employed in the section analyses.

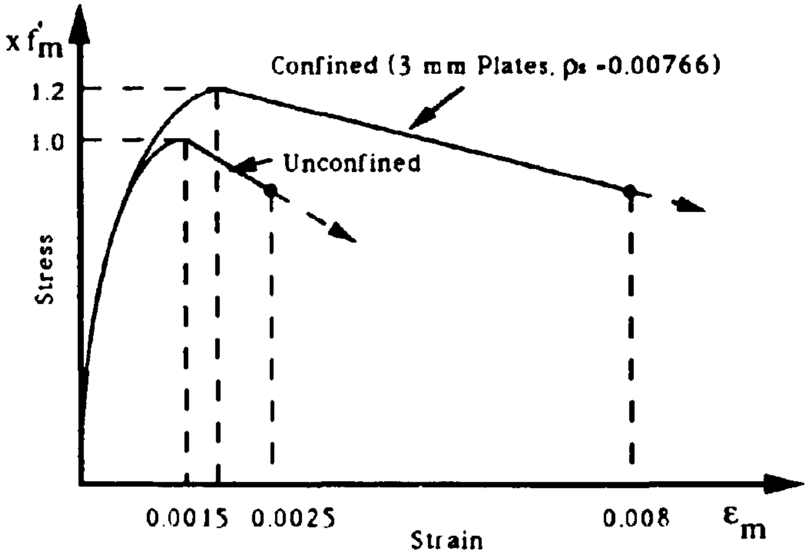

Fig. 2.2 Stress-Strain Curve for Masonry[18]

The curves in Fig. 2.2 can be represented by the following equations:

(a) For Unconfined Masonry:

When $\varepsilon_m \leq 0.0015$, then

$$f_m = 1.067\, f'_m \left[\frac{2\,\varepsilon_m}{0.002} - \left(\frac{\varepsilon_m}{0.002}\right)^2\right] \qquad (2.5a)$$

When $0.0015 \leq \varepsilon_m \leq 0.0025$, then

$$f_m = f'_m\,[1 - Z_m\,(\varepsilon_m - 0.0015\,)] \qquad (2.5b)$$

(b) For Confined Masonry:

When $\varepsilon_m \leq 0.002\,k$, then

$$f_m = 1.067\,k\;f'_m \left[\frac{2\,\varepsilon_m}{0.002\,k} - \left(\frac{\varepsilon_m}{0.002\,k}\right)^2\right] \tag{2.6a}$$

When $0.002\,k \leq \varepsilon_m \leq 0.008$, then

$$f_m = 1.067\,k\,f'_m\left[1 - Z_m\left(\varepsilon_m - 0.002\,k\right)\right] \tag{2.6b}$$

where

$$k = 1 + \rho_s\,f_{yh}\,/\,f'_m \tag{2.7}$$

and

$$Z_m = \frac{0.5}{\dfrac{3 + 0.29\,f'_m}{145\,f'_m - 1000} + \dfrac{3}{4}\,\rho_s\sqrt{\dfrac{h''}{s_h}} - 0.002} \tag{2.8}$$

In Equations (2.5a) through (2.8), the following parameters are used:

f'_m --- compression strength of unconfined masonry

ρ_s --- volumetric ratio of confining steel

f_{yh} --- yield strength of confining steel

h'' --- lateral dimension of the confined core (i.e. block width)

s_h --- spacing of confining steel (i.e. block height)

Tests on masonry prisms confined with 3 mm (0.125 inch) thick stainless or galvanized steel plates within the mortar beds exhibit a changed failure mode from one initiated at mortar beds by vertical splitting to a shear-crushing failure largely within one course[18]. The stress-strain curve for confined prisms has increased strength, higher strain at peak load and a much flatter falling branch. A safe ultimate compression strain for concrete masonry confined in this fashion has been established to be 0.008[18]. It was found that the relationship described by the above equations provided a good agreement with the experimental data.

For masonry which is not confined adequately to change the failure mode, a consistent formula for both unconfined and confined masonry can be used as follows:

When $\varepsilon_m \leq 0.0015\,k$, then

$$f_m = 1.067\,k\,f'_m \left[\frac{2\,\varepsilon_m}{0.002\,k} - \left(\frac{\varepsilon_m}{0.002\,k}\right)^2\right] \tag{2.9a}$$

When $0.0015\,k \leq \varepsilon_m \leq 0.0025 + 0.0275\,(k-1)$, then

$$f_m = k\,f'_m\left[1 - Z_m\left(\varepsilon_m - 0.0015\,k\right)\right] \tag{2.9b}$$

where k and Z_m are given by Equations (2.7) and (2.8).

2.4 Problem Formulation

2.4.1 Moment capacity

<u>Conditions at First Yield of Reinforcement</u>

The distributions of strains and stresses of masonry and reinforcement along the cross section of the flanged masonry wall at first yield are illustrated in the left side of Fig. 2.3. At this stage, the extreme rebar in tension just yields and the extreme fiber of masonry in compression has not reached its ultimate strain. The equilibrium equations for axial forces and moments may be expressed in dimensionless form as follows:

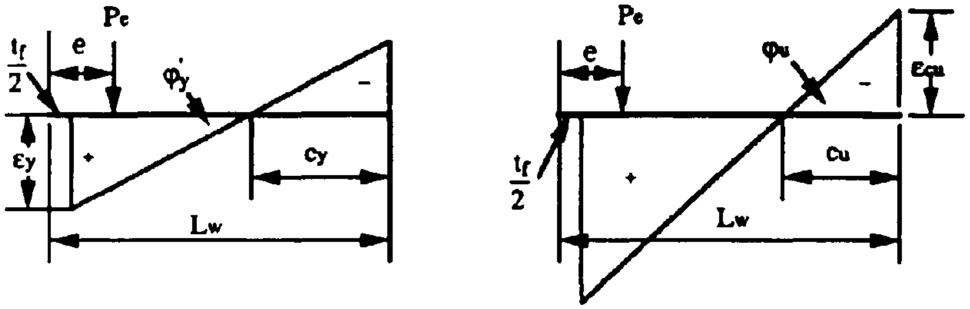

(a) Strain Distribution

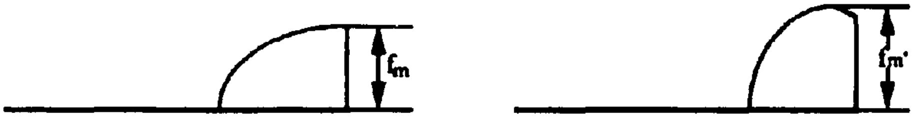

(b) Masonry Stresses

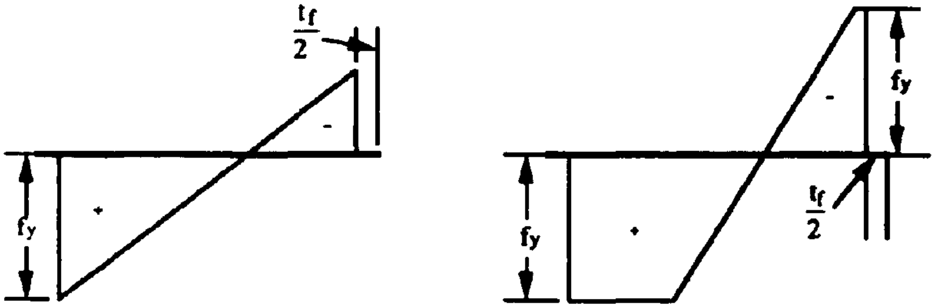

(c) Reinforcement Stresses

At First Yield

At Ultimate State

Fig. 2.3 Distribution of Strain and Stresses

Axial equilibrium:

$$K_A N_A + P K_\rho K_l K_t (1 - R) + 0.5P(1 - c_{yn} - \beta/2)/g - P_c - P_m = 0 \qquad (2.10)$$

Moment equilibrium:

$$K_A N_A[(1 - e_n - c_{yn})(1 - R) + (e_n - c_{yn})R] + P K_\rho K_l K_t (1 - c_{yn} - \beta/2)(1 - R) +$$
$$0.333P(1 - c_{yn} - \beta/2)^2/g + M_c + M_m = M_{yn} \qquad (2.11)$$

Where M_{yn} is the dimensionless external moment at first yield. The first term in the two above equations is axial load or moment of axial load about the neutral axis respectively. The second term is tensile force and moment due to reinforcement in the flange. The third term is tensile force and moment due to distributed reinforcement in the web respectively. P_c, P_m, M_c and M_m are forces and moments contributed by the reinforcement and masonry in compression area respectively. Since the internal forces in cross sections of masonry walls depend on the position of the neutral axis, an iteration approach has to be employed to solve Equation (2.10) for c_{yn}, which will be then substituted into (2.11) to calculate M_{yn}. The detail of expressions of internal forces and moments are presented below and the following dimensionless symbols are used in the expressions.

$c_{yn} = c_y / l_w$

$c_{un} = c_u / l_w$

$e_n = e / l_w$

$k_l = l_f / l_w$

$k_t = t_f / t$

$\beta = t_f / l_w$

$g = 1 - \beta$

$k_\rho = \rho_f / \rho$

$k_A = (l_w t + l_f t_f) / l_w t$

$= 1 + k_l k_t$

$N_A = P_e / f'_m A_g$

$P = \rho f_y / f'_m$

$\varepsilon_y = f_y / E_s$

$f_k = k_l k_t / \beta$

$\varepsilon_1 =$ Strain at maximum compression stress for masonry

$\varepsilon_{cu} =$ Ultimate compression strain for masonry

R is a flag, when the web is in compression, set R=0; if the flange is in compression, set R=1.

Steel Compression Force:

- If $c_{yn} \le 0.5$, then

$$P_c = PK_\rho K_l K_t(c_{yn}-\beta/2)R/(1-c_{yn}-\beta/2) + 0.5P(c_{yn}-\beta/2)^2/[g(1-c_{yn}-\beta/2)] \quad (2.12)$$

$$M_c = PK_\rho K_l K_t(c_{yn}-\beta/2)^2 R/(1-c_{yn}-\beta/2) + 0.333P(c_{yn}-\beta/2)^3/[g(1-c_{yn}-\beta/2)] \quad (2.13)$$

- If $c_{yn} > 0.5$, then

$$P_c = PK_\rho K_l K_t R + 0.5P(1-c_{yn}-\beta/2)/g + P(2c_{yn}-1)/g \quad (2.14)$$

$$M_c = PK_\rho K_l K_t(c_{yn}-\beta/2)R + 0.333P(1-c_{yn}-\beta/2)^2/g + P(c_{yn}-0.5) \quad (2.15)$$

Masonry Compression Force

- If $c_{yn}\varepsilon_y/(1-c_{yn}-\beta/2) \le \varepsilon_1$ and $c_{yn} \ge \beta$, then

$$P_m = \{P1(*)(1+f_k R) - Rf_k P1[*(1-\beta/c_{yn})]\}(1-c_{yn}-\beta/2)/\varepsilon_y \quad (2.16)$$

$$M_m = \{Q1(*)(1+f_k R) - Rf_k Q1[*(1-\beta/c_{yn})]\}(1-c_{yn}-\beta/2)^2/\varepsilon_y^2 \quad (2.17)$$

- If $c_{yn}\varepsilon_y/(1-c_{yn}-\beta/2) \le \varepsilon_1$ and $c_{yn} < \beta$, then

$$P_m = P_1(*)(1+f_k R)(1-c_{yn}-\beta/2)/\varepsilon_y \quad (2.18)$$

$$M_m = Q_1(*)(1+f_k R)(1-c_{yn}-\beta/2)^2/\varepsilon_y^2 \quad (2.19)$$

In equations (2.16) to (2.19), the function P1( ) and Q1( ) represent

$$P1(*) = 533.3 *^2 - 8.89 \times 10^4 *^3/k \tag{2.20}$$

$$Q1(*) = 355.6 *^3 - 6.6 \times 10^4 *^4/k \tag{2.21}$$

where $* = c_{yn} \varepsilon_y / (1 - c_{yn} - \beta/2)$, or is specified in the ( ).

- If $\varepsilon_1 < c_{yn}\varepsilon_y/(1-c_{yn}-\beta/2) \le \varepsilon_{cu}$ and $(c_{yn}-\beta)\varepsilon_y/(1-c_{yn}-\beta/2) \ge \varepsilon_1$, then

$$P_m = (P1(\varepsilon_1) + P2(*)(1 + f_k R) - Rf_k P2(\#)(1-c_{yn}-\beta/2)/\varepsilon_y \tag{2.22}$$

$$M_m = (Q1(\varepsilon_1) + Q2(*)(1 + f_k R) - Rf_k Q2(\#)(1-c_{yn}-\beta/2)^2/\varepsilon_y^2 \tag{2.23}$$

- If $\varepsilon_1 < c_{yn}\varepsilon_y/(1-c_{yn}-\beta/2) \le \varepsilon_{cu}$ and $(c_{yn}-\beta)\varepsilon_y/(1-c_{yn}-\beta/2) < \varepsilon_1$, then

$$P_m = \{[P1(\varepsilon_1)+P2(*)](1+f_{k)}R)-Rf_k P1(\#)\}(1-c_{yn}-\beta/2)/\varepsilon_y \tag{2.24}$$

$$M_m = \{[Q1(\varepsilon_1)+Q2(*)](1+f_{k)}R)-Rf_k Q1(\#)\}(1-c_{yn}-\beta/2)^2/\varepsilon_y{}^2 \tag{2.25}$$

In Equations (2.22) to (2.25)

$$P2(\#) = 1.067k_2((1+\varepsilon_1 Z_m)(\#-\varepsilon_1)-0.5Z_m(\#^2-\varepsilon_1{}^2)) \tag{2.26}$$

$$Q2(\#) = 1.067k_2(0.5(1+\varepsilon_1 Z_m)(\#-\varepsilon_1)-0.333Z_m(\#^3-\varepsilon_1{}^3)) \tag{2.27}$$

where $\# = (c_{yn}-\beta)\varepsilon_y/(1-c_{yn}-\beta/2)$ and $k_2 = 0.9375$ for unconfined masonry ; $k_2 =$ k for confined masonry, and k is defined in Eqn. (2.7). If $c_{yn}\varepsilon_y/(1-c_{yn}-\beta/2) > \varepsilon_{cu}$, then crushing of the extreme compression fiber of masonry occurs before the extreme tension rebar yields and no value for M_{yn} exists.

In the above equations, the functions P1 and P2 will be recognized as integrals of the masonry compression stress block to obtain the total masonry compression force. Q1 and Q2 provide the moment of the total masonry stress block about the neutral axis.

Conditions at Ultimate Compression Strain:

The distribution of strain and stresses of masonry and reinforcement along the cross section is illustrated in the right side of Fig.

2.3. At this stage, the extreme rebar in tension has passed the first yield and the extreme fiber of masonry in compression just reaches its ultimate strain. The equilibrium equations for axial forces and moments expressed in dimensionless form are:

$$K_AN_A+P_t - P_c - P_m = 0 \tag{2.28}$$

$$K_AN_A[(1-e_n-c_{un})(1-R)+(e_n-c_{un})R\} +M_t +M_c +M_m= M_{un} \tag{2.29}$$

Where M_{un} is the dimensionless external moment at the ultimate state. The first term in the two above equations is axial load and moment about the neutral axis respectively. P_t, P_c, P_m, M_t, M_c and M_m are forces and moments contributed by the reinforcement in tension, and the reinforcement and masonry in the compression area respectively. As with the case of first yield, the internal forces in the cross section of masonry walls depend on the position of the neutral axis. Again, an iteration approach has to be employed to solve Equation (2.28) for c_{un}, which is then substituted into (2.29) to calculate M_{un}. Details of expressions of internal forces and moments are presented as follows:

Steel Tension Force:

- If $c_{un}\varepsilon_y/\varepsilon_{cu} \leq (1-c_{un}-\beta/2)$, then

$$P_t = Pk_\rho k_l k_t(1-R)+P[1-c_{un}-\beta/2-c_{un}\varepsilon_y/(2\varepsilon_{cu})]/g \tag{2.30}$$

$$M_t = Pk_\rho k_l k_t(1-c_{un}-\beta/2)(1-R)+0.5P[(1-c_{un}-\beta/2)^2-c_{un}^2\varepsilon_y^2/(3\varepsilon_{cu}^2)]/g \tag{2.31}$$

- If $(1-c_{un}-\beta/2) \leq c_{un}\varepsilon_y/\varepsilon_{cu} \leq (c_{un}-1-\beta/2)$, then

$$P_t = P[c_{un}-\beta/2-c_{un}\varepsilon_y/(2\varepsilon_{cu})]/g-P-Pk_\rho k_l k_t(1-R) \tag{2.32}$$

$$M_t = -P/2[(c_{un}-\beta/2)^2-(c_{un}\varepsilon_y)^2/(3\varepsilon_{cu}^2)]/g+P(c_{un}-1/2)+Pk_\rho k_l k_t(c_{un}-1+\beta/2)(1-R) \tag{2.33}$$

- If $c_{un}\varepsilon_y/\varepsilon_{cu} > (c_{un}-1-\beta/2)$, then

$$P_t = Pk_\rho k_l k_t(1-c_{un}-\beta/2)\varepsilon_{cu}(1-R)/(c_{un}\varepsilon_y) + 0.5P(1-c_{un}-\beta/2)^2\varepsilon_{cu}/(c_{un}\varepsilon_y g) \tag{2.34}$$

$$M_t = Pk_\rho k_l k_t(1-c_{un}-\beta/2)^2\varepsilon_{cu}(1-R)/(c_{un}\varepsilon_y) + 0.333P(1-c_{un}-\beta/2)^3\varepsilon_{cu}/(c_{un}\varepsilon_y g) \tag{2.35}$$

Steel Compression Force:

- If $c_{un}\varepsilon_y/\varepsilon_{cu} \le (c_{un}-\beta/2)$, then

$$P_c = Pk_\rho k_l k_t R + P[c_{un}-\beta/2-c_{un}\varepsilon_y/(2\varepsilon_{cu})]/g \tag{2.36}$$

$$M_c = Pk_\rho k_l k_t R(c_{un}-\beta/2) +0.5P[(c_{un}-\beta/2)^2-c_{un}\varepsilon_y{}^2/(3\varepsilon_{cu}{}^2)]/g \tag{2.37}$$

- If $c_{un} \ge \beta/[2(1+\varepsilon_y/\varepsilon_{cu})]$

$$P_c = Pk_\rho k_l k_t\varepsilon_{cu}(c_{un}-\beta/2)R/(c_{un}\varepsilon_y) + 0.5P\varepsilon_{cu}(c_{un}-\beta/2)^2/(c_{un}\varepsilon_y g) \tag{2.38}$$

$$M_c = Pk_\rho k_l k_t\varepsilon_{cu}(c_{un}-\beta/2)^2R/(c_{un}\varepsilon_y) + 0.333P\varepsilon_{cu}(c_{un}-\beta/2)^3/(c_{un}\varepsilon_y g) \tag{2.39}$$

- Then , for all other cases

$$P_c = -Pk_\rho k_l k_t R- P + P[1-c_{un}-\beta/2-c_{un}\varepsilon_y/(2\varepsilon_{cu})]/g \tag{2.40}$$

$$M_c = Pk_\rho k_l k_t(\beta/2-c_{un})R+ P(1/2-c_{un}) - 0.5\, P[(1-c_{un}-\beta/2)^2-c_{un}{}^2\varepsilon_y{}^2/(3\varepsilon_{cu}{}^2)]/g \tag{2.41}$$

Masonry Compression Force:

For all cases except when $R = 0$ and $c_{un} \ge 1-\beta$

- If $\varepsilon_{cu}(c_{un}-\beta)/c_{un} \ge \varepsilon_1$, then

$$P_m = [P1(\varepsilon_1)+P2(\varepsilon_{cu})(1+f_kR)-Rf_kP2(x)]c_{un}/\varepsilon_{cu} \tag{2.42}$$

$$M_m = [Q1(\varepsilon_1)+Q2(\varepsilon_{cu})(1+f_kR)-Rf_kQ2(x)]c_{un}{}^2/\varepsilon_{cu}{}^2 \tag{2.43}$$

- Else, if $c_{un} \ge \beta$ then

$$P_m = \{[(P1(\varepsilon_1)+P2(\varepsilon_{cu})](1+f_kR)-Rf_kP1(x)\}c_{un}/\varepsilon_{cu} \tag{2.44}$$

$$M_m = \{[(Q1(\varepsilon_1)+Q2(\varepsilon_{cu})](1+f_kR)-Rf_kQ1(x)\}c_{un}{}^2/\varepsilon_{cu}{}^2 \tag{2.45}$$

- Else, for all other cases

$$P_m = [P1(\varepsilon_1)+P2(\varepsilon_{cu})](1+f_kR)c_{un}/\varepsilon_{cu} \tag{2.46}$$

$$M_m = [Q1(\varepsilon_1)+Q2(\varepsilon_{cu})](1+f_kR)c_{un}{}^2/\varepsilon_{cu}{}^2 \tag{2.47}$$

In Equations (2.44) to (2.47), $x = (c_{un}-\beta)\varepsilon_{cu}/c_{un}$. When $R = 0$ and $c_{un} \geq 1-\beta$, then special conditions apply as follows:

- If $(c_{un}-1)/c_{un} \geq \varepsilon_1/\varepsilon_{cu}$, then

$$P_m = [P2(\varepsilon_{cu})+P2(y)f_k-(1+f_k)P2(z)]c_{un}/\varepsilon_{cu} \tag{2.48}$$

$$M_m = [Q2(\varepsilon_{cu})+Q2(y)f_k-(1+f_k)Q2(z)]c_{un}^2/\varepsilon_{cu}^2 \tag{2.49}$$

- Else, if $(c_{un}-1+\beta)/c_{un} \geq \varepsilon_1/\varepsilon_{cu}$ then

$$P_m = \{P2(\varepsilon_{cu})+P2(y)f_k+(1+f_k)[P1(\varepsilon_1)-P1(z)]\}c_{un}/\varepsilon_{cu} \tag{2.50}$$

$$M_m = \{Q2(\varepsilon_{cu})+Q2(y)f_k+(1+f_k)[Q1(\varepsilon_1)-Q1(z)]\}c_{un}^2/\varepsilon_{cu}^2 \tag{2.51}$$

- Else, if $c_{un} \geq 1$ then

$$P_m = [P2(\varepsilon_{cu})+P1(\varepsilon_1)+P1(y)f_k-(1+f_k)P1(z)]c_{un}/\varepsilon_{cu} \tag{2.52}$$

$$M_m = [Q2(\varepsilon_{cu})+Q1(\varepsilon_1)+Q1(y)f_k-(1+f_k)Q1(z)]c_{un}^2/\varepsilon_{cu}^2 \tag{2.53}$$

- Else, for all other cases

$$P_m = [P2(\varepsilon_{cu})+P1(\varepsilon_1)+P1(y)f_k]c_{un}/\varepsilon_{cu} \tag{2.54}$$

$$M_m = [Q2(\varepsilon_{cu})+Q1(\varepsilon_1)+Q1(y)f_k]c_{un}^2/\varepsilon_{cu}^2 \tag{2.55}$$

In Equations (2.48) to (2.55)

$$y = (c_{un}-1+\beta)\varepsilon_{cu}/c_{un} \tag{2.56}$$

$$z = (c_{un}-1)\varepsilon_{cu}/c_{un} \tag{2.57}$$

Solutions of the above equations directly yield dimensionless flexural strength. The other parameters of interests, namely the ductility factor and equivalent stiffness are then calculated in accordance with the following sections.

2.4.2 Curvature ductility

The dimensionless curvature corresponding to the onset of yield strain in the extreme tensile reinforcement is given by

$$\varphi'_{yn} = \varepsilon_y / (1 - c_{yn} - \beta/2) \qquad (2.58)$$

And at the ultimate state by

$$\varphi_{un} = \varepsilon_{cu} / c_{un} \qquad (2.59)$$

In term of an elasto-plastic approach of the moment-curvature relationship, the yield curvature needs to be related to the ultimate moment rather than the reduced moment corresponding to first yield. Extrapolating linearly, as shown in Fig. 2.4, the corrected yield curvature is

$$\varphi_{yn} = \varphi'_{yn} M_{un} / M_{yn} \qquad (2.60)$$

Thus, the curvature ductility factor can be found directly from

$$\eta = \varphi_{un} / \varphi_{yn} \qquad (2.61)$$

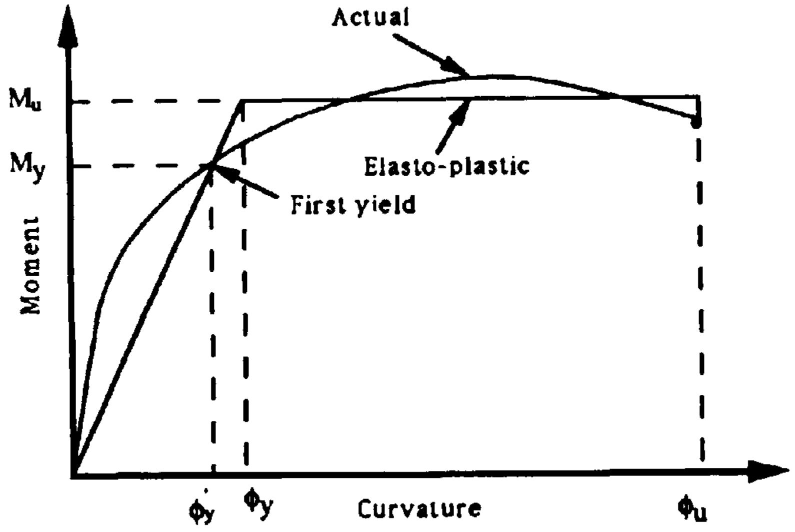

Fig. 2.4 Moment-curvature Relationship

2.4.3 Equivalent Stiffness

For a cantilever member subjected to a concentrated transverse force at the free end, the distribution of moment and curvature along the member after cracking are shown in Fig. 2.5. Assuming that the curvature is linearly distributed along the height at first yield, then the stiffness related to displacements at the top end will be

$$k_f = 3EI_e / h^3 \qquad (2.62)$$

Where I_e is an effective stiffness, taking into account the distribution of curvature up the member. The actual distribution of curvature will be nonlinear, and show local irregularities due to the effects of cracking. It would appear that the assumed straight-line distribution from the computed yield curvature at the member base would overestimate the member flexibility. However, the effects of strain penetration into the base, and tension shift, which increases curvature at the base section to levels higher than predicted based on a simple 'plane-section' analysis have been shown to compensate these effects[28]. A linear curvature distribution as shown in Fig. 2.5, can thus be used to predict equivalent stiffness. Since $m'_y = EI_e \varphi'_y$, therefore

$$I_e = m'_y / E\varphi'_y \qquad (2.63)$$

The stiffness ratio of cracked section to uncracked one is given by

$$\lambda = I_e / I_g \qquad (2.64)$$

Where I_e and I_g are moments of inertia for equivalent and gross sections of the wall respectively, and the later is determined by the dimensions of the wall section.

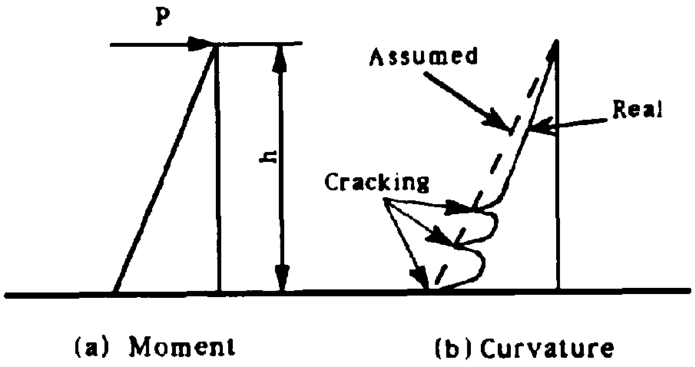

Fig. 2.5 Distribution of Moment and Curvature at First Yield

Note that shear deformation will reduce the effective stiffness, so a shear-adjusted moment of inertia can be expressed as:

$$I_{ev} = I_e / (1+F) \tag{2.65}$$

Where F is the ratio of shear deformation to flexural deformation. An approximate value for F may be based on the uncracked relative stiffness, assuming the shear stiffness is reduced by cracking in proportion to the reduction in flexural stiffness, giving $F = \Delta_s/\Delta_f = K_f/K_s$ where Δ_s, Δ_f, K_s and K_f are displacement or stiffness at the top of cantilever wall due to shear and bending respectively. K_f is given by Eqn. (2.62) and K_s can be calculated as $K_s = GA_e/h$ in which G and A_e are shear modulus and effective shear area of the cross section respectively. Assuming $G = 0.4$ E and A_w/A_e is 1.2 for rectangular section, finally we have

$$F = 9\, I_g / A_w\, h^2 \qquad (2.66)$$

in which A_w is the cross section area of the web. The flange is not considered to contribute to the shear stiffness.

2.5 Design Charts and Tables

Based on the formulas described above, a computer program which can produce the design tables of flexural strength, equivalent stiffness and curvature ductility in dimensionless forms for both unconfined and confined flanged masonry walls was written in FORTRAN 77 and is included in Appendix A for reference.

Table 2.1 Parameters for The Computation

Description	Formulas	Lower Bound	Upper Bound	Increment
Width Ratio	l_f / l_w	0	2.0	0.25
Axial Load Ratio	$N / f'_m A_g$	0	0.4	0.05
Mechanical Reinforcement Ratio	$\rho f_y / f'_m$	0.01	0.2	0.01/ 0.02

The parameters considered in the calculation are summarized in Table 2.1. The reinforcement yield strength considered were f_y = 275 MPa (40 Ksi) and 380 MPa (55 Ksi). A typical masonry compression strength used of f'_m=16 MPa (2.3 Ksi) was adopted for the analyses. As the results are not sensitive to the material strength due to the dimensionless form of the equations, they may be used for a wider range of mechanical properties with only minor errors.

It is also assumed that the flange and web have the same thickness and longitudinal reinforcement ratio in the calculation. For confined masonry, 1/8 inch (3.2 mm) thick mortar bed confining plates of mild steel were used, resulting in a volumetric confining ratio of 0.00785. Two values of g (see Fig. 2.1, 0.95 and 0.80) were selected to produce the design tables, and values for other g may be found with adequate accuracy by interpolating between the above two values.

A selection of the resulting data has been put in graphical form to enable major trends to be emphasized, as shown from Fig. 2.6a to Fig. 2.16, which can be also used for the purpose of design. For all design charts presented, g = 0.95, with the vertical axis was chosen to be dimensionless axial load ratio. Graphs of moment capacity, effective stiffness, and curvature ductility are given for different levels of the mechanical reinforcement ratio. From comparisons, the following trends can be observed:

(a) Moment Capacity:

(1) Strength of reinforcement does not affect the ultimate moment significantly, especially for the direction of loading with flange in compression.

(2) Moment capacity increases generally with increasing axial load level for the direction of loading with flange in compression and the relationship between the above two parameters is very close to linear. But

for wide flange walls in the direction of loading with web in compression above a certain axial load, the moment capacity decreases with increasing axial load due to the failure mode changing from ductile failure (tensile yielding of reinforcement first) to brittle failure (compression crushing of masonry first).

(3) Moment capacity always increases with increasing mechanical reinforcement ratio. In the direction of flange in compression, the relationship is close to linear.

(4) Confining plates on mortar beds do not affect ultimate moment significantly for cases with the flange in compression, or with flange in compression when flange width is small, but increase moment capacity significantly for wider flange walls or when the mechanical reinforcement ratio is high because horizontal confinement improves the ultimate compression strain of masonry and can change the failure mode from brittle to ductile.

(5) Fig. 2.15 shows the influence of flange to web length ratio on moment capacity. It is obvious that in the direction of flange in compression, the increase of flange width has little effects on ultimate moment, but in the opposite direction, moment capacity increases with increasing ratio of flange to web length.

(b) Effective Moment of Inertia:

(1) Effective moment of inertia is more sensitive to the strength of reinforcement than is moment capacity. The wall with lower reinforcement strength has larger effective moment of inertia.

(2) Generally, effective moment of inertia increases with increasing axial load level in both directions. Note that the graphs show discontinuity in the direction of web in compression. The reason is that when the axial load reaches a certain level, the failure mode will change from ductile failure to brittle compression failure. In the case of brittle failure a different definition of 'yield' condition applies, with m_y' and φ_y' in Eqn. (2.63) being substituted by m_u and φ_u. For these cases the stiffness is strongly influenced by inelastic masonry compression stresses.

(3) As with moment capacity, the effective moment of inertia increases with increasing mechanical reinforcement ratio.

(4) Effective moment of inertia is not sensitive to the ratio of flange to web length.

(c) Curvature ductility:

(1) Curvature ductility decreases with increasing axial load level and mechanical reinforcement ratio.

(2) Confining plates improve curvature ductility factor significantly in the direction of web in compression.

(3) With the same axial load and reinforcement ratio, curvature ductility in the direction of flange in compression is much higher than the opposite direction as a result of the great difference in neutral axis depth.

2.6 An Example of Use of Design Charts

To illustrate the use of the design charts and significance of directional characteristics of T-section walls, a specific example is worked in the following:

Problem

Calculate the flexural strength, yield and ultimate displacement and ductility factors for a T-section cantilever masonry wall with the following parameters:

web length: 3.6 m (11.8 ft)

flange length: 3.8 m (12.5 ft)

wall height: 18 m (59 ft)

wall thickness: 190 mm (7.48 in)

masonry compression strength: f = 12 MPa (1740 psi)

flexural reinforcement: D 20, diameter is 20 mm (0.787 in)

f_y = 275 MPa (40 Ksi)

spacing 400 mm (15.7 in)

axial load: 1230 kN (276 Kips)

Solution

$l_f = 3.8 - 0.19 \approx 3.6$ m, $t = 0.19$

$l_f / l_w = 1.0$, $g = (3.6 - 2 \times 0.1) / 3.6 \approx 0.95$

axial load ratio: $p_e / f'_m A_g = 1.230 / (12 \times 2 \times 3.6 \times 0.19) \approx 0.075$

reinforcement ratio: $\rho f_y / f'_m = \pi \times 10^2 \times 275 / (400 \times 190 \times 12) \approx 0.095$

(1) Moment Capacity

With the flange in compression, using Fig. 2.7a, with axial load ratio = 0.075, interpolating between the curves of reinforcement ratio 0.08 and 0.12, we have

$M_{if} = 0.0865\, f'_m\, l_w^2\, t$

$= 2.55$ MNm (22,600 K-in)

With the web in compression, from Fig. 2.7b

$M_{iw} = 0.192\, f'_m\, l_w^2\, t$

$= 5.67$ MNm (50,200 K-in)

(2) Stiffness

With the flange in compression, from Fig. 2.10a

$I_e / I_g = 0.187$

$I_g = 1.73$ m^4

$I_e = 0.324$ m^4 (37.5 ft^4)

With the web in compression, from Fig. 2.10b

$I_e / I_g = 0.308$

$I_e = 0.533$ m^4 (61.6 ft^4)

If the effect of shear is considered,

$F = 9\, I_g / (A_w\, h^2) = 9 \times 1.73 / (3.6 \times 0.19 \times 18^2) = 0.07$

(3) Curvature Ductility

With the flange in compression, from Fig. 2.13a

$\varphi_u / \varphi_y \approx 50$

With the web in compression, from Fig. 2.13b

$\varphi_u / \varphi_y \approx 2.0$

(4) Displacement at Yield (Elasto-plastic Approximation)

Yield displacement can be expressed as:

$$\Delta_y = M_i h^2 / 3 EI$$

Priestley has recommended a value of $E_m = 1000 f'_m$ for deflection calculation to ensure adequately high estimates of stiffness [13]. Thus with flange in compression:

$$\Delta_{yf} = 2.55 \times 18^2 / (3 \times 1000 \times 12 \times 0.324) = 70.8 \text{ mm} (2.79 \text{ in})$$

With web in compression,

$$\Delta_{yw} = 5.67 \times 18^2 / (3 \times 1000 \times 12 \times 0.533) = 95.7 \text{ mm} (3.77 \text{ in})$$

(5) Displacement Ductility

The relationship between displacement ductility and curvature ductility can be expressed[28] as:

$$\mu = 1 + 3 \left(\frac{\varphi_u}{\varphi_y} - 1 \right) \frac{L_p}{h} \left(1 - \frac{L_p}{2h} \right)$$

where μ is displacement ductility factor and L_p is equivalent plastic hinge length. Assuming

$$L_p = 0.5\, l_w = 1.8 \text{ m},$$

then

$$L_p / h = 1.8 / 18 = 0.1$$

With the flange in compression,

$$\mu_f = 1 + 3 \ (50 - 1) \times 0.1 \times (1 - 0.05) = 15.0$$

With the web in compression,

$$\mu_w = 1 + 3 \ (2.0 - 1) \times 0.1 \times (1 - 0.05) = 1.29$$

(6) Ultimate Displacement

Since $\Delta_u = \mu \Delta_y$, then, with the flange in compression,

$\Delta_u = 15.0 \times 70.8 = 1062$ mm (41.8 in)

and with the web in compression,

$\Delta_u = 1.29 \times 95.7 = 123.5$ mm (4.86 in)

The results of the above calculations are summarized in Table 2.2

Table 2.2 Summary of Strength, Stiffness and Ductility for Example Flange Wall

	Flange in compression	web in compression
Flexural strength	2.55 MNm(22,600 Kin)	5.67 MNm(50,200 Kin)
Effective stiffness	0.324 m^4 (37.5 ft^4)	0.533 m^4 (61.6 ft^4)
Curvature ductility	50.0	2.0
Yield displacement	70.8 mm (2.79 in)	95.7 mm (3.77 in)
Displacement ductility	15.0	1.29
Ultimate displacement	1062 mm (41.8 in)	123.5 mm (4.86 in)

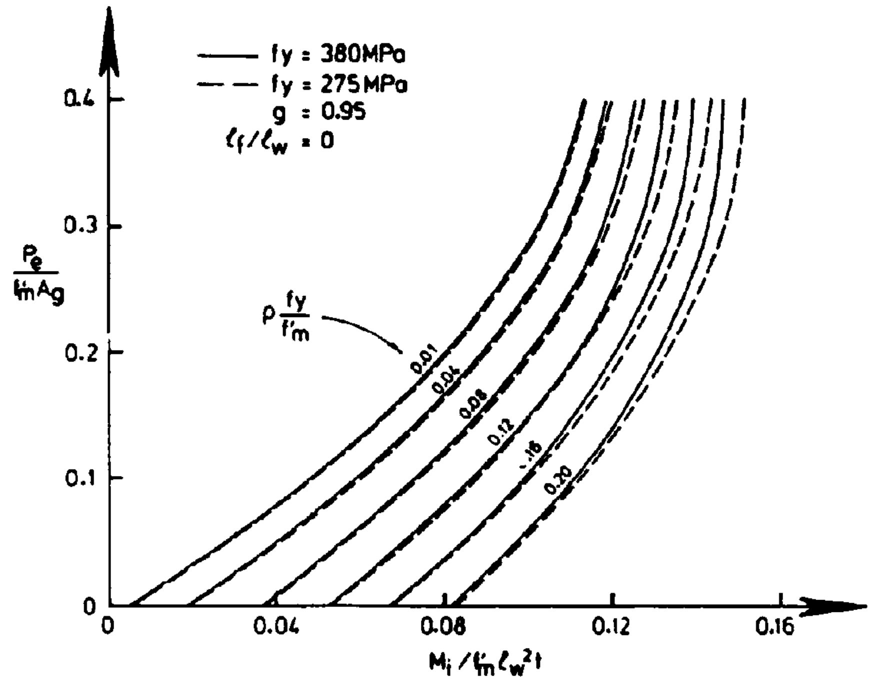

Fig. 2.6a Moment Capacity, $l_f / l_w = 0$ (Rectangular), Unconfined

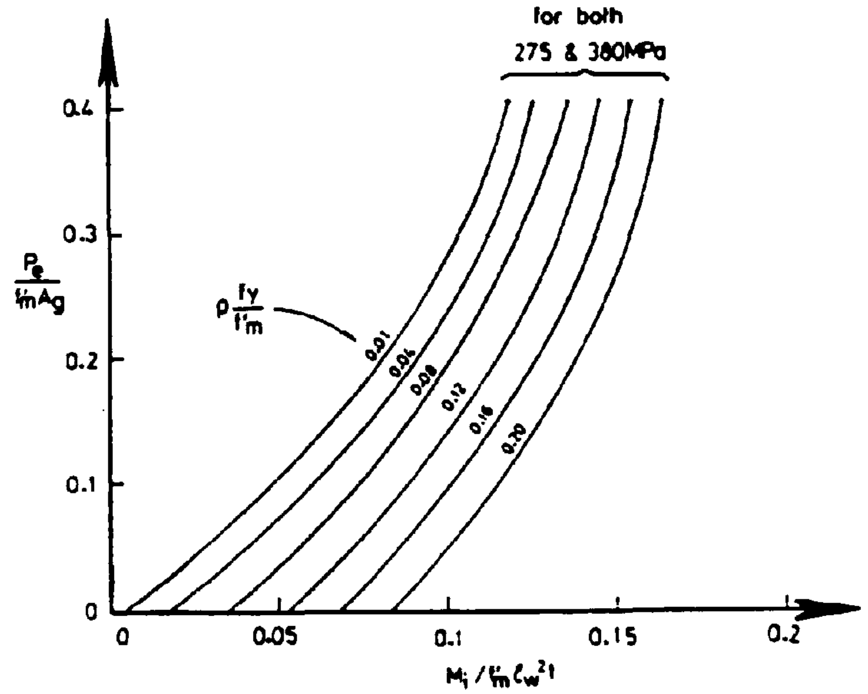

Fig. 2.6b Moment Capacity, $l_f / l_w = 0$ (Rectangular), Confined

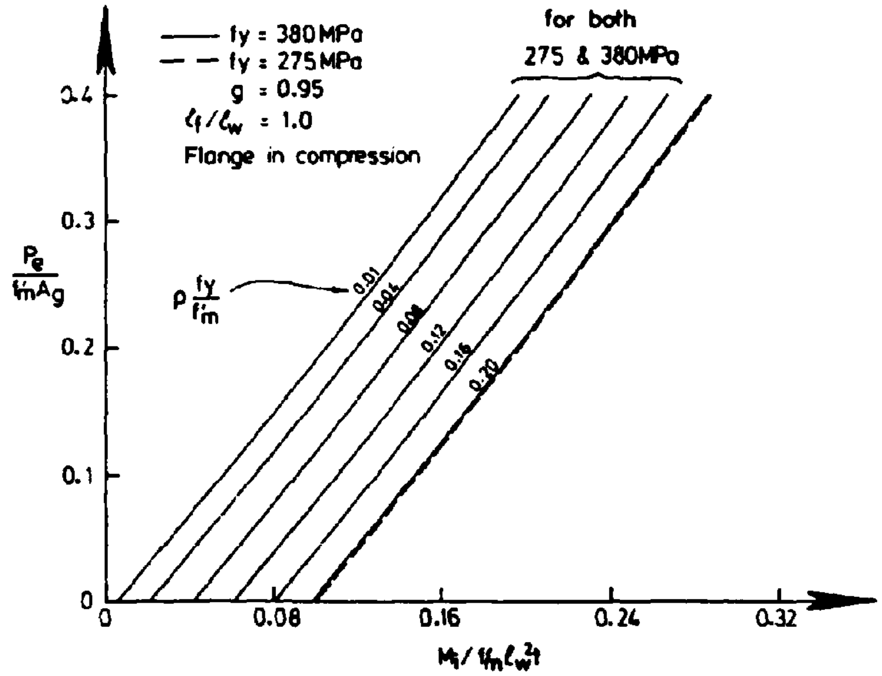

Fig. 2.7a Moment Capacity, $l_f / l_w = 1$, Flange in Compression

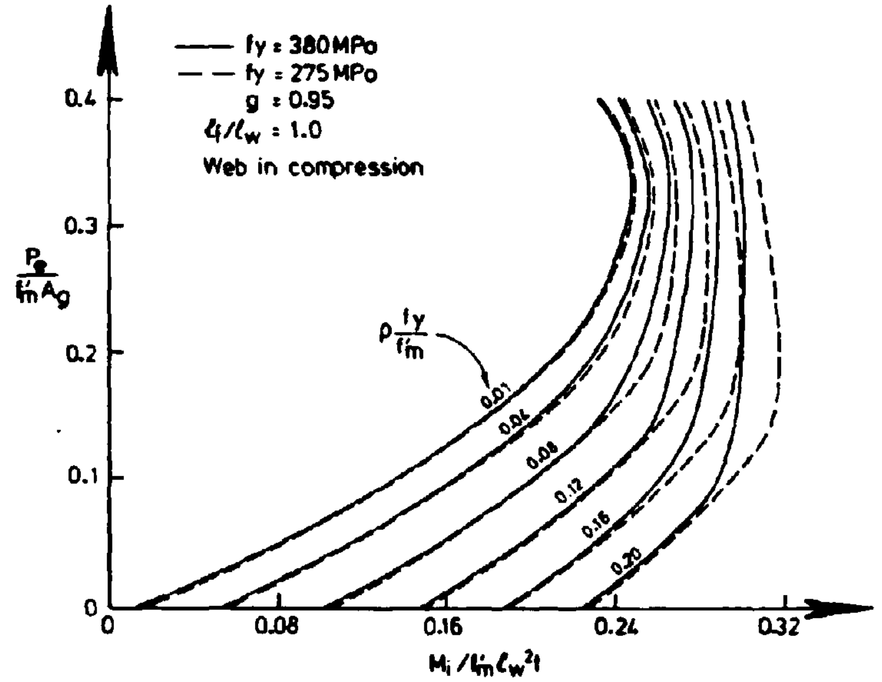

Fig. 2.7b Moment Capacity, $l_f / l_w = 1$, Web in Comp., Unconfined

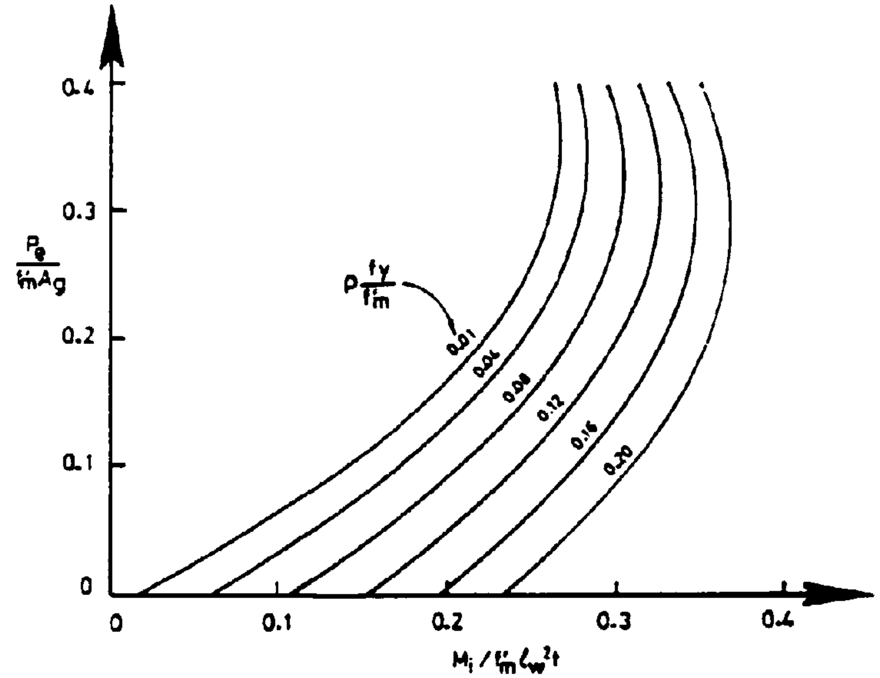

Fig. 2.7c Moment Capacity, l_f / l_w = 1, Web in Comp., Confined

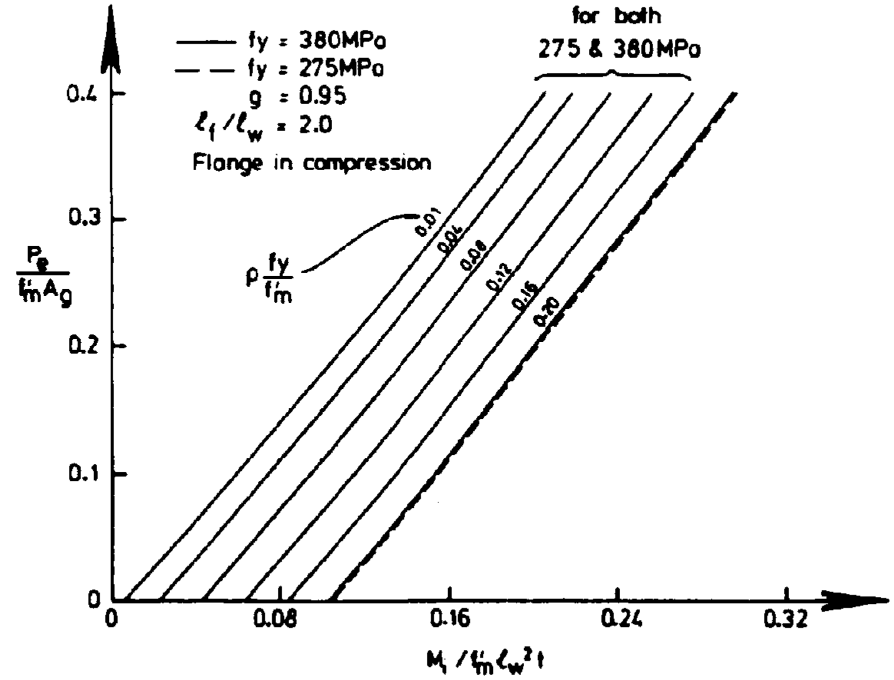

Fig. 2.8a Moment Capacity, l_f / l_w = 2, Flange in Compression

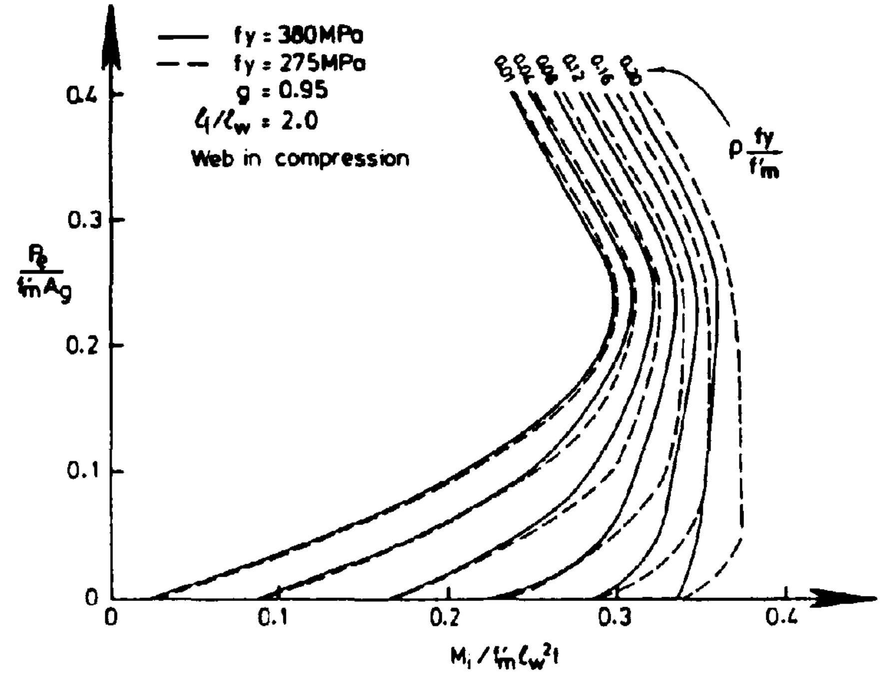

Fig. 2.8b Moment Capacity, l_f / l_w = 2, Web in Comp., Unconfined

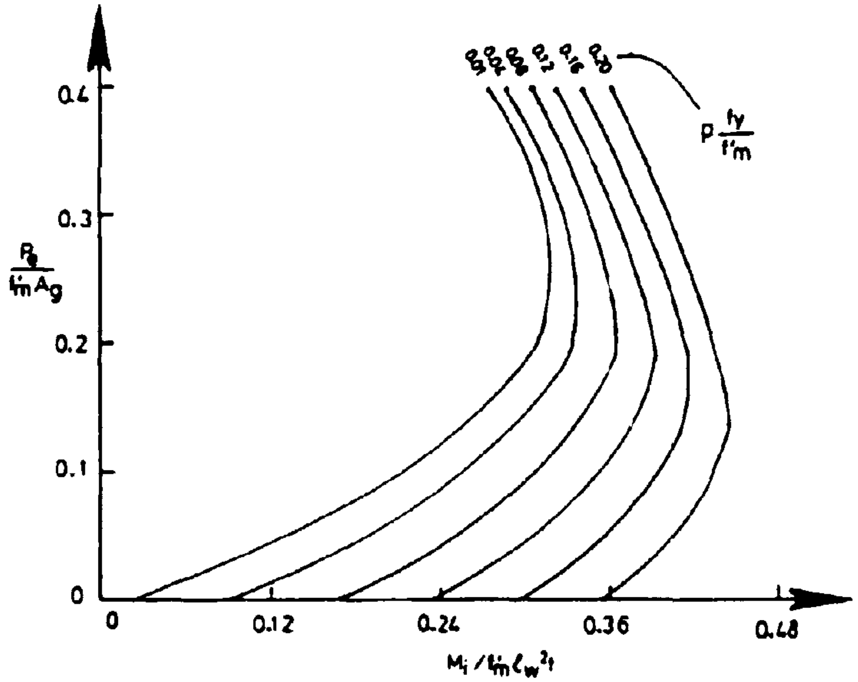

Fig. 2.8c Moment Capacity, l_f / l_w = 2, Web in Comp., Confined

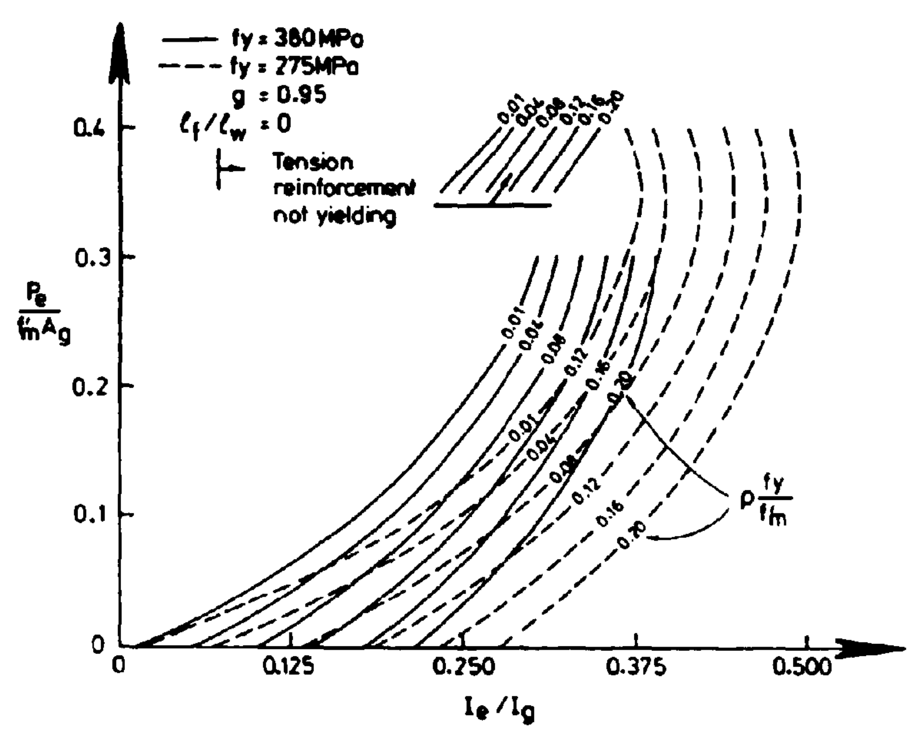

Fig. 2.9a Effective Moment of Inertia, $l_f / l_w = 0$, Unconfined

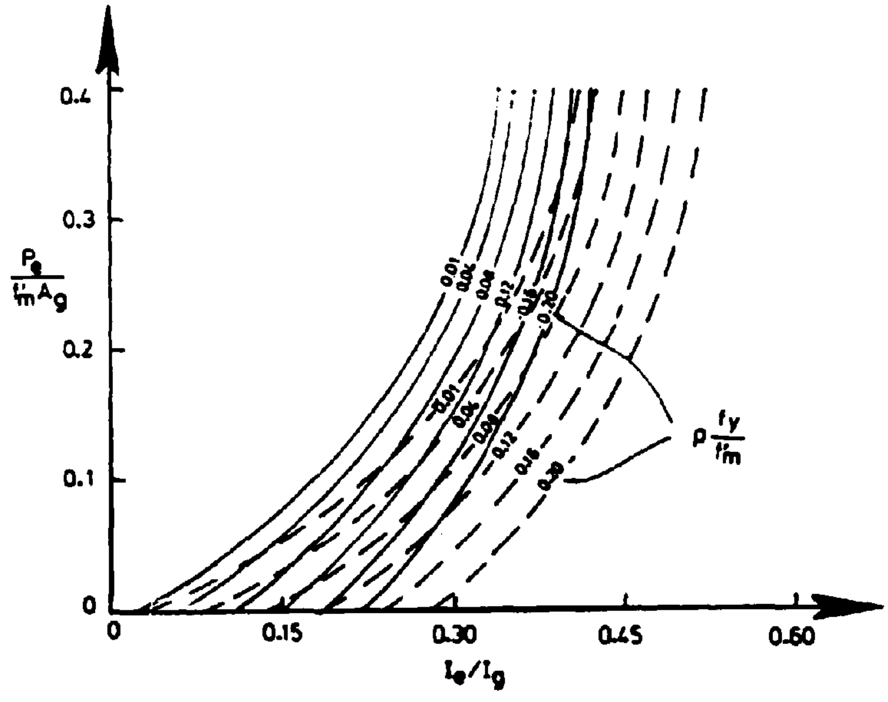

Fig. 2.9b Effective Moment of Inertia, $l_f / l_w = 0$, Confined

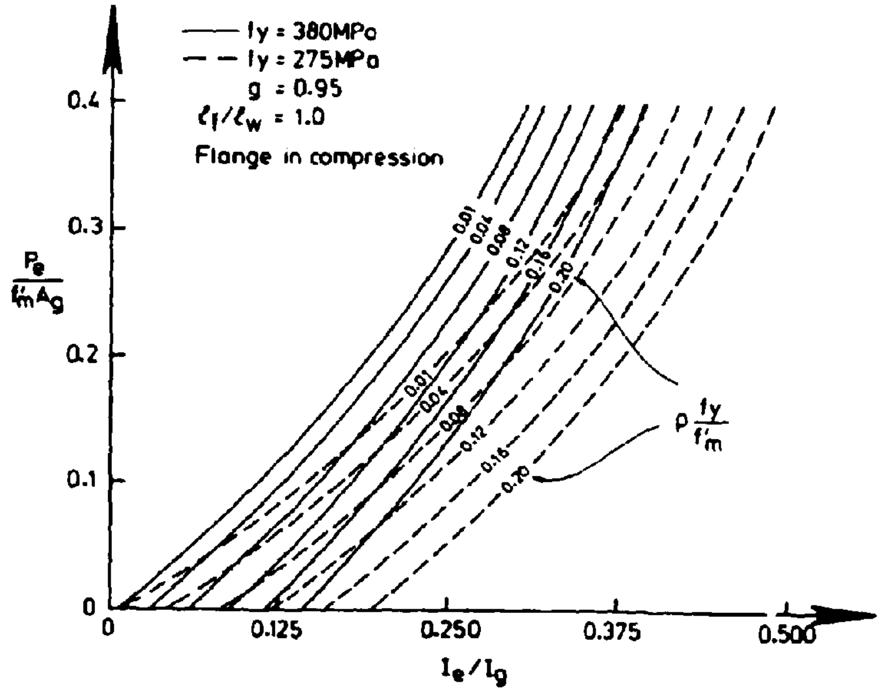

Fig. 2.10a Effective Moment of Inertia, I_f / I_w = 1, Flange in Comp.

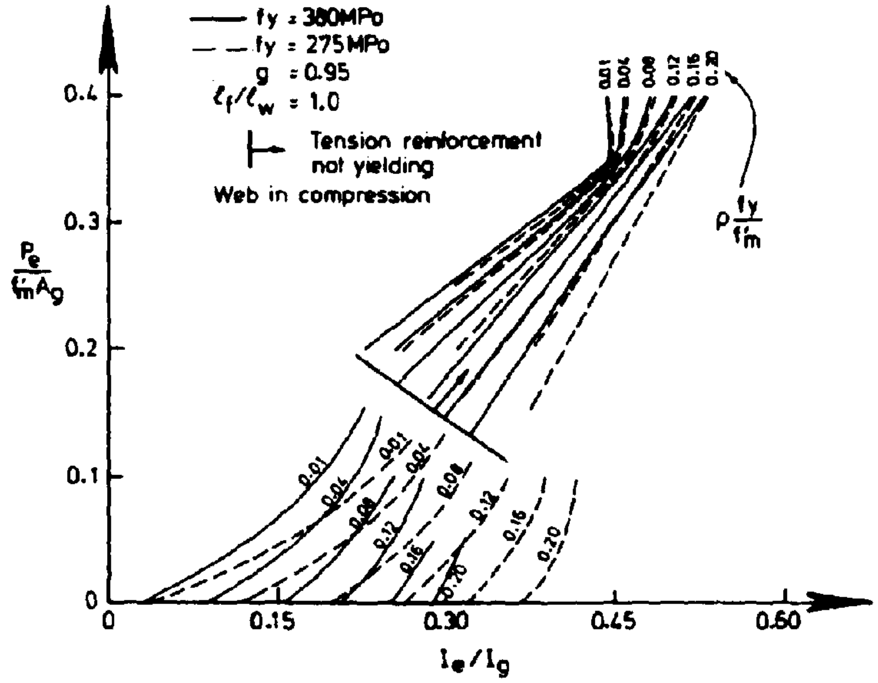

Fig. 2.10b Effective Moment of Inertia, I_f / I_w = 1
Web In Compression, Unconfined

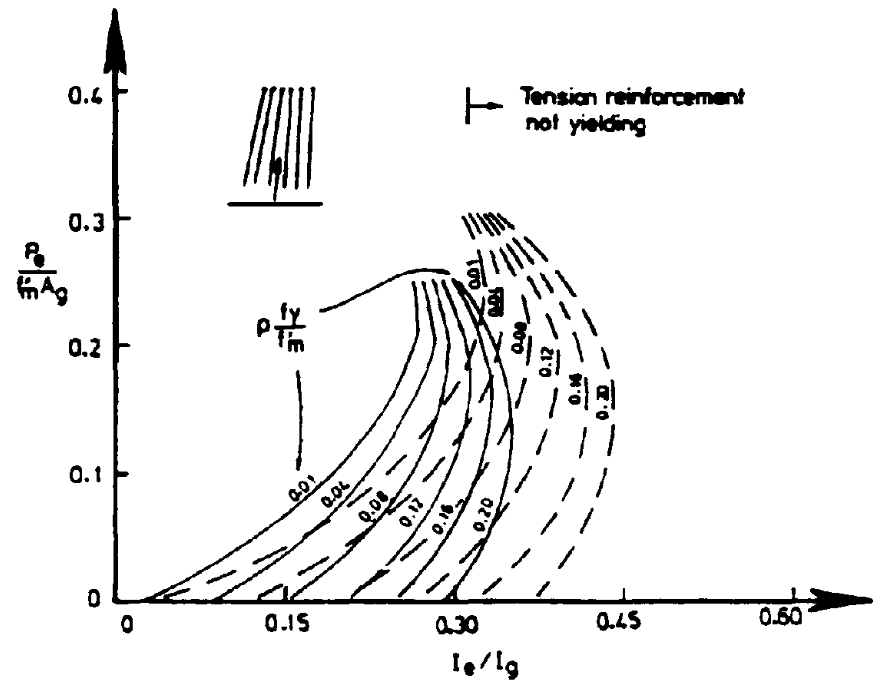

Fig. 2.10c Effective Moment of Inertia, lf / lw = 1
Web In Compression, Confined

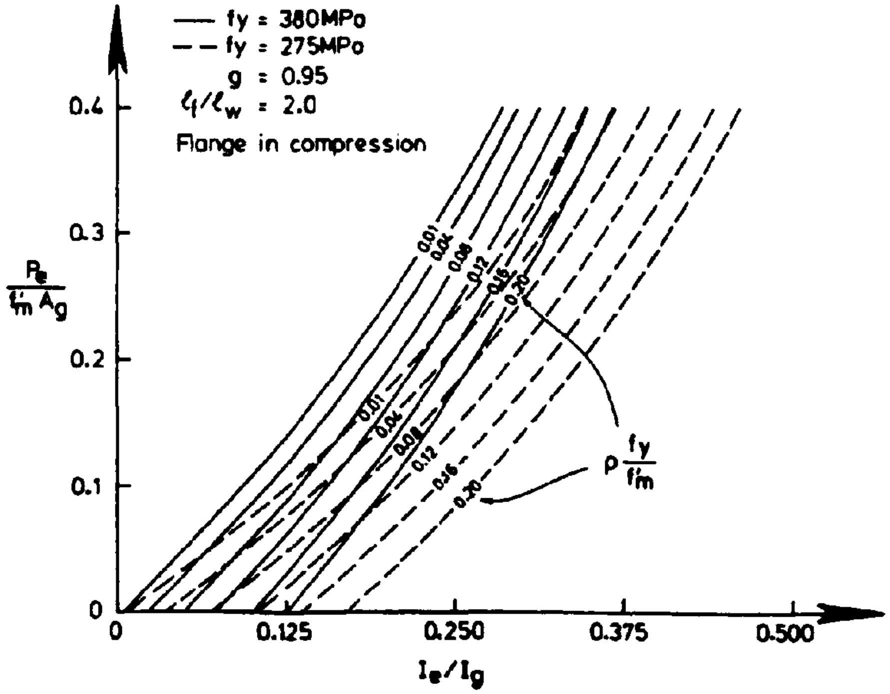

Fig. 2.11a Effective Moment of Inertia, lf / lw = 2, Flange in Comp.

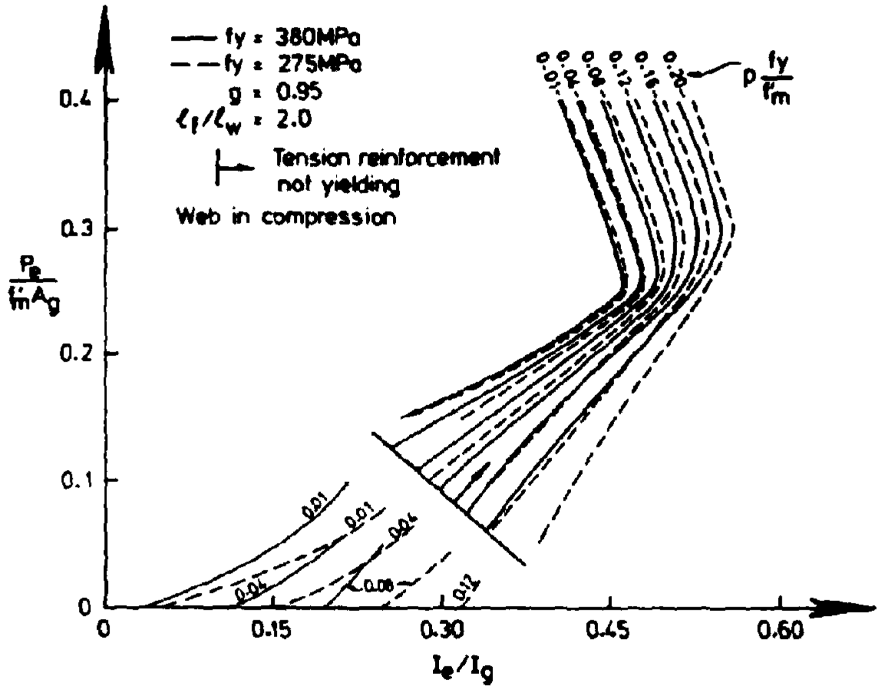

Fig. 2.11b Effective Moment of Inertia, l_f / l_w = 2
Web In Compression, Unconfined

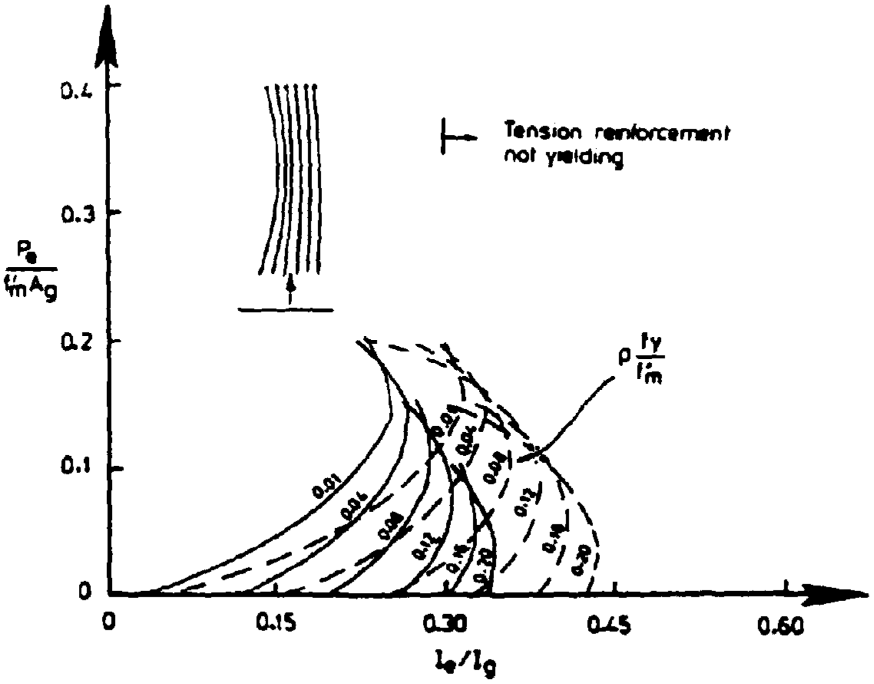

Fig. 2.11c Effective Moment of Inertia, l_f / l_w = 2
Web In Compression, Confined

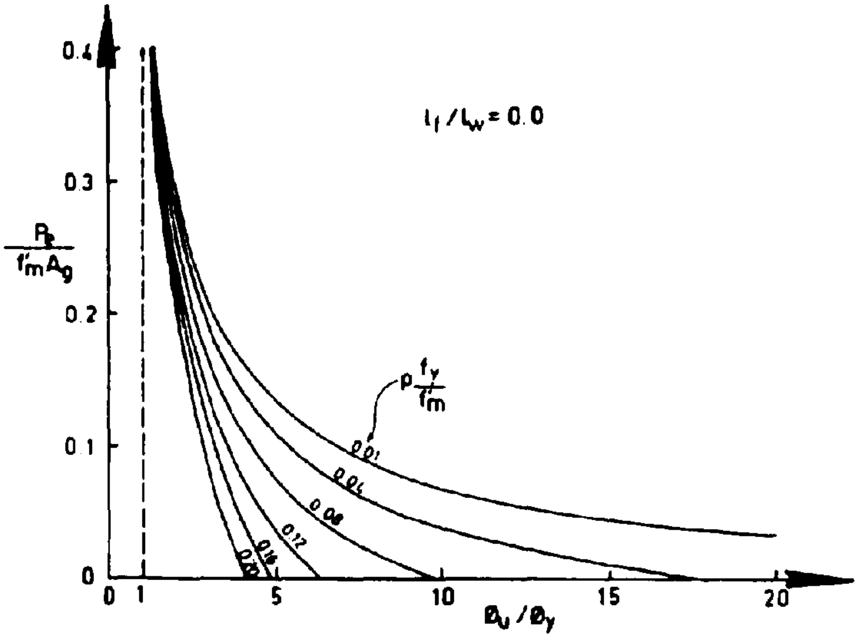

Fig. 2.12a Curvature Ductility, $l_f / l_w = 0$, Unconfined

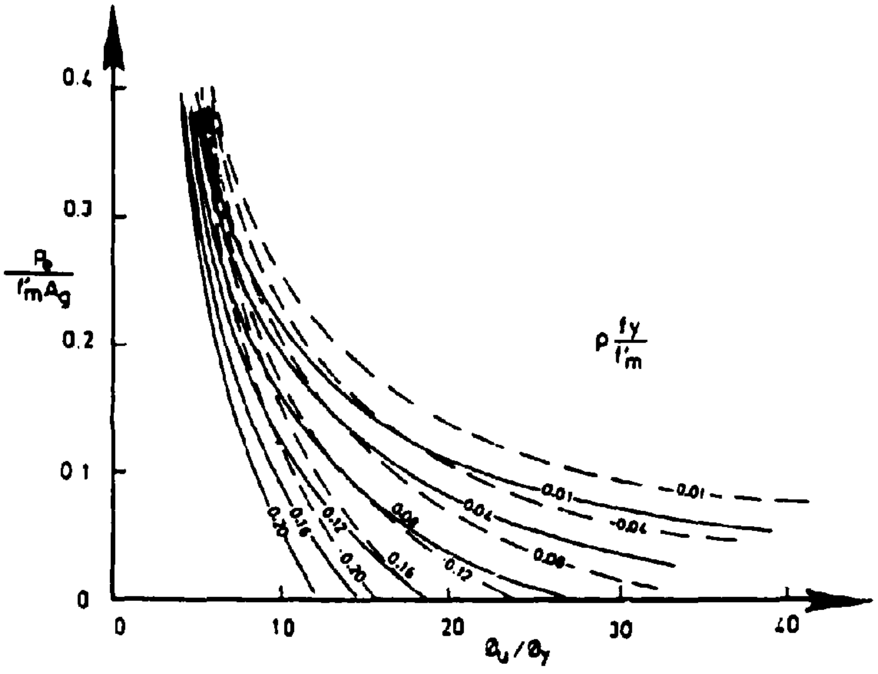

Fig. 2.12b Curvature Ductility, $l_f / l_w = 0$, Confined

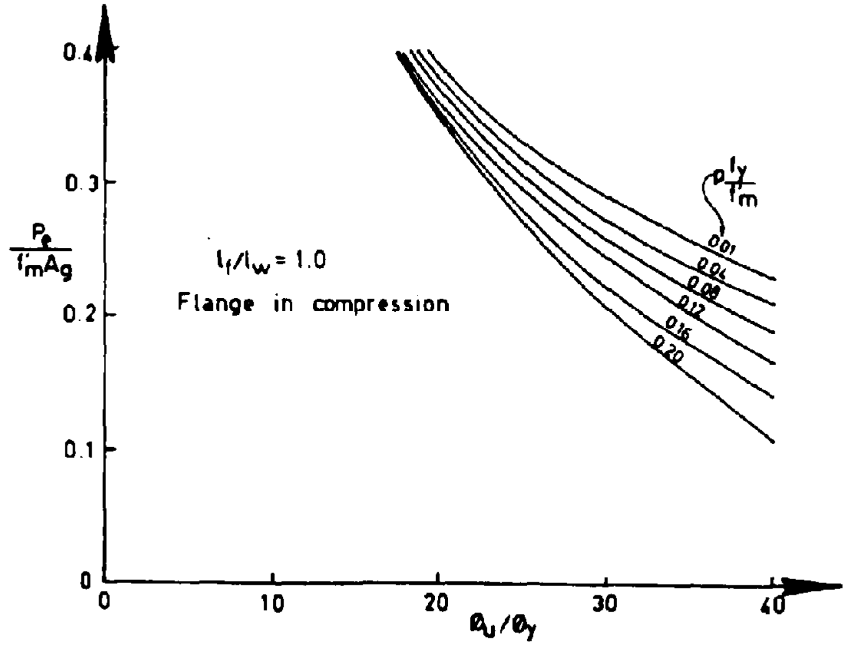

Fig. 2.13a Curvature Ductility, l_f / l_w = 1, Flange in Compression

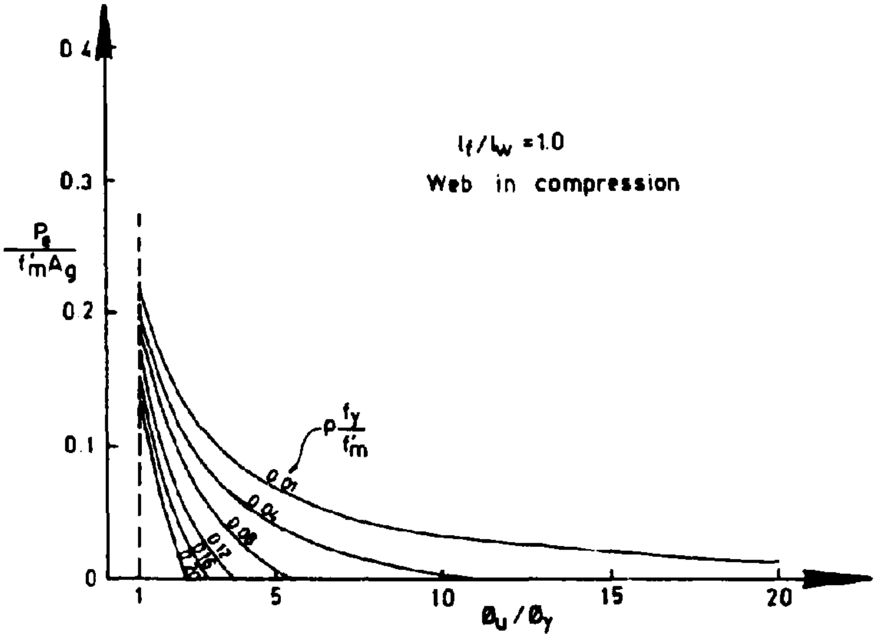

Fig. 2.13b Curvature Ductility, l_f / l_w = 1
Web In Compression, Unconfined

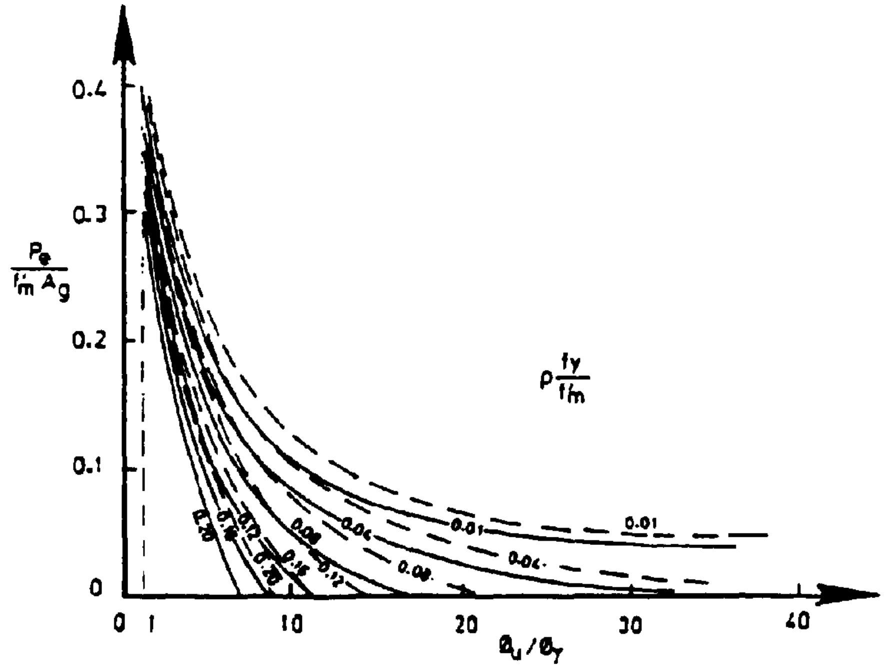

Fig. 2.13c Curvature Ductility, $l_f / l_w = 1$
Web In Compression, Confined

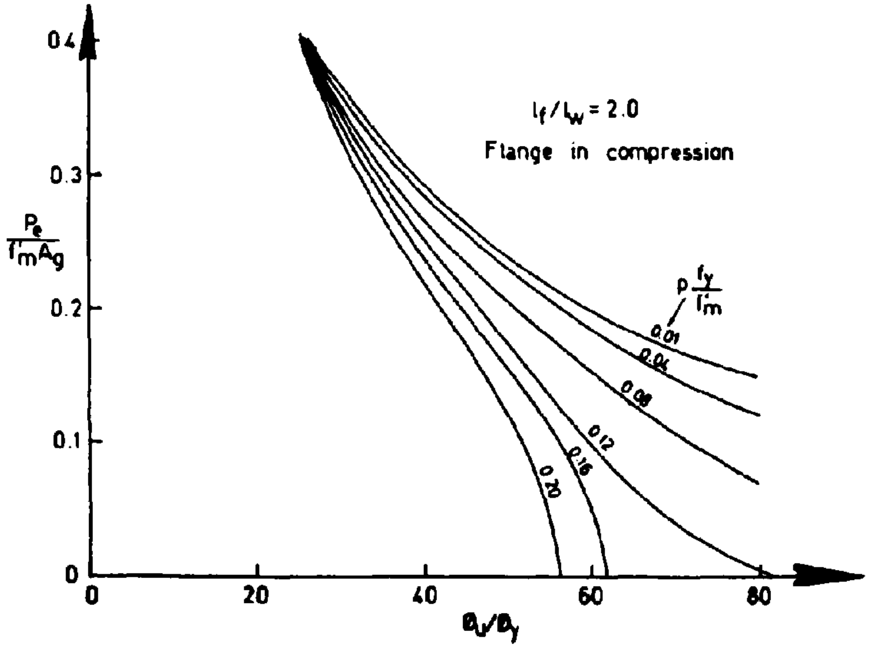

Fig. 2.14a Curvature Ductility, $l_f / l_w = 2$, Flange in Compression

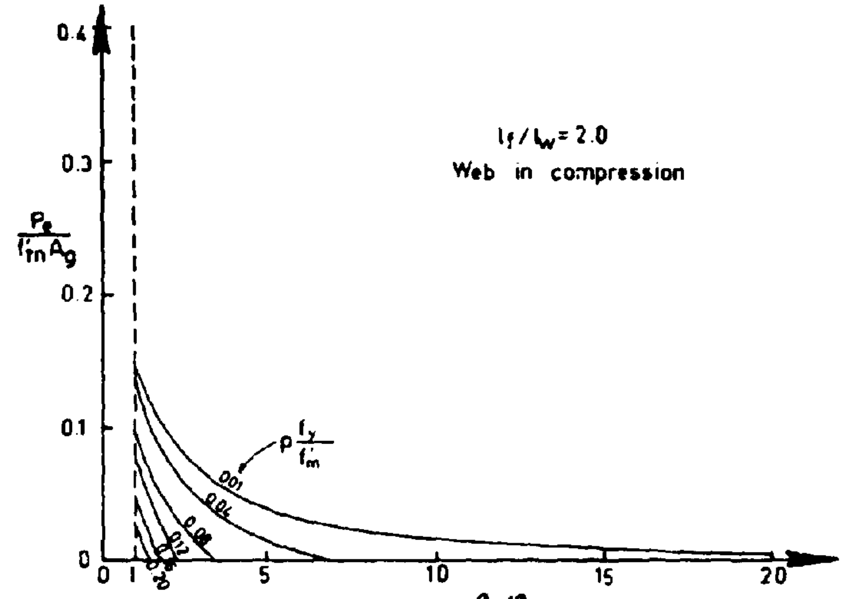

Fig. 2.14b Curvature Ductility, l_f / l_w = 2
Web In Compression Unconfined

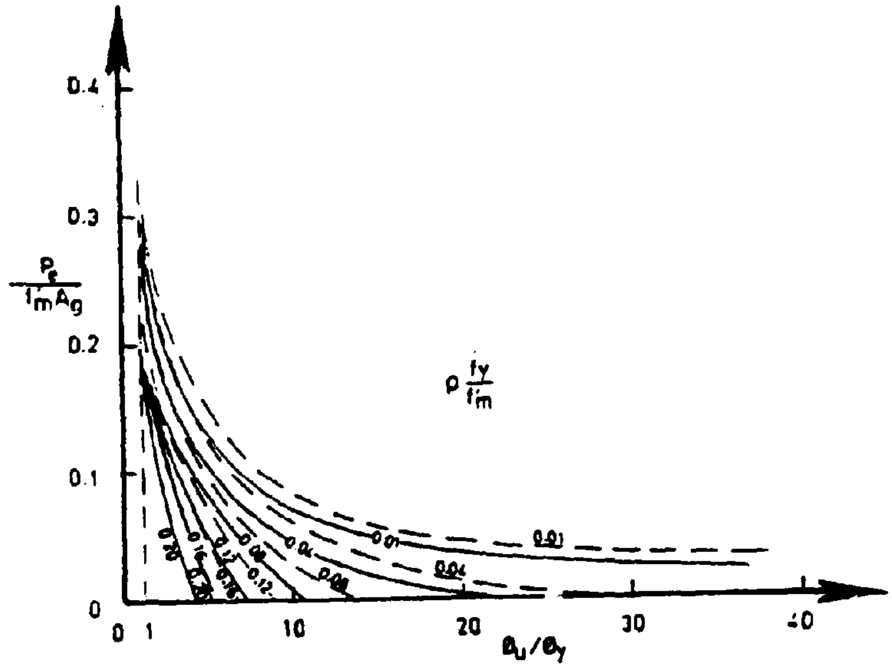

Fig. 2.14c Curvature Ductility, l_f / l_w = 2
Web In Compression, Confined

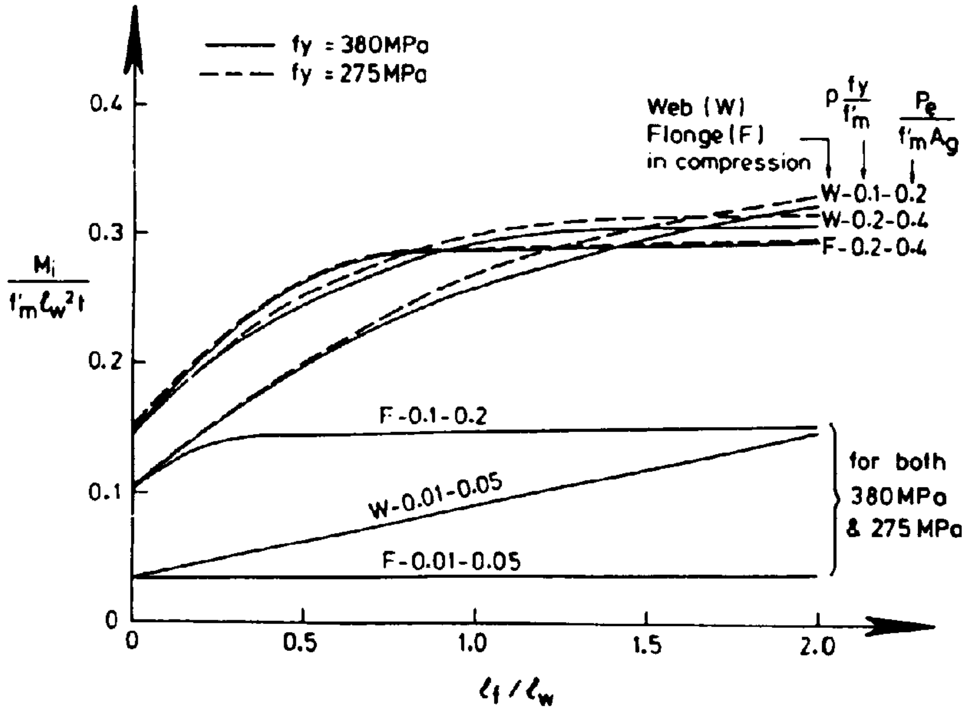

Fig. 2.15 Influence of l_f / l_w on Moment Capacity

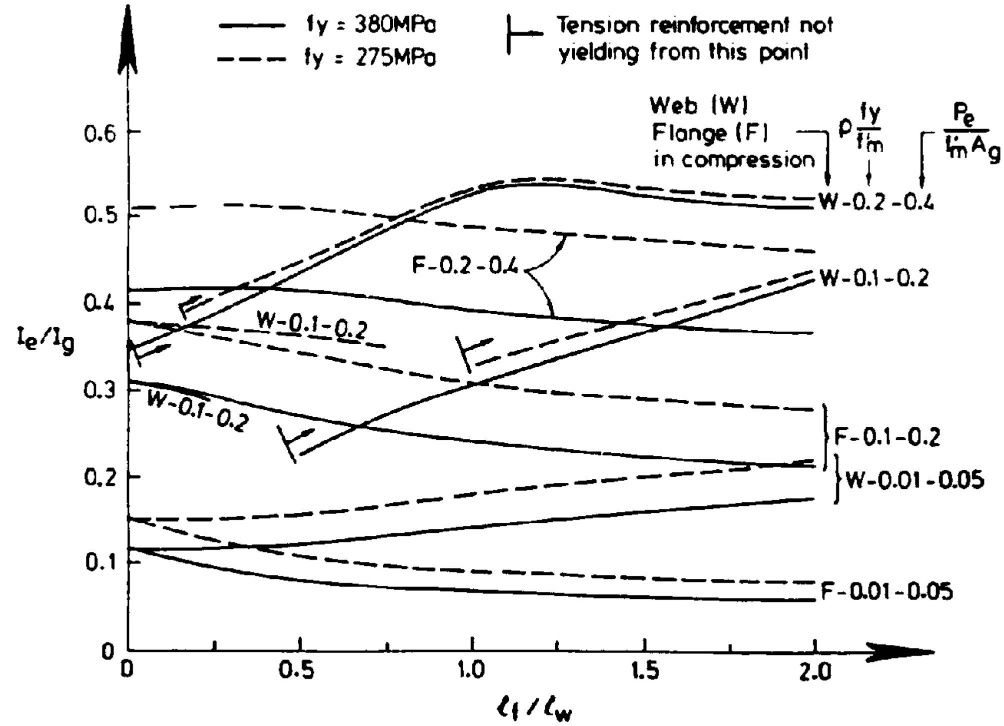

Fig. 2.16 Influence of l_f / l_w on Effective Moment of Inertia

3. AN INELASTIC STRUCTURAL COMPONENT MODEL FOR T-SECTION MASONRY WALLS

3.1 Introduction

Reinforced flanged masonry structural walls are widely used in construction practice. Since they have different properties (stiffness, strength, and ductility) in two opposite directions due to their asymmetric configuration and reinforcement, masonry cracking and steel yielding, when subjected to in-plane loading parallel to the web, a special model is needed to simulate the asymmetric inelastic behavior of these components.

Fig. 3.1 (a) illustrates a typical masonry assemblage with openings. To analyze this structure, there are three main methods which can be employed, each at different levels of sophistication. The ordinary frame model (Fig. 3.1 (b)) uses the simple line element (usually located at the geometric center of the cross section) and rigid connection at the joints. Typically variation of cross section along the member axis is not considered, and the joint regions are either taken as extension of the member , or to be infinitely rigid. As a consequence, applicability to the deep-membered structure of Fig. 3.1 (a) is questionable.

Although the finite element method is versatile and suitable for structural analysis at both elastic and inelastic response levels, it is time-consuming and expensive due to the fine discrete requirement. Fig. 3.1 (c) shows what would be considered to be a very coarse mesh for analyzing this structure.

Between the two methods above, the structural component model(SCM) which divides the structure into its component level (beam, column and joint etc.) may be capable of realistic simulation of deep-membered structures, provided member deformation characteristics are carefully considered. The method would require much less computational effort than the ordinary finite element model, but can expect to be more realistic than the line element approach.

Fig. 3.1 (d) shows the idealization of the masonry assemblage with structural components. The structure is divided as a system of beam members (1), column or wall members (2) , joint members (3) and flanged members (4), connected by corner nodes. Generally, a 4-node plane element has 8 degree of freedom, including three rigid body movements and five basic deformation modes, as illustrated in Fig. 3.2. For the beam and column members of an SCM simulation it is reasonable to assume that strain perpendicular to the principal member axis is zero so that only axial strain, flexural and shear deformation along the longitudinal direction are considered. As a consequence the beam and column elements (including the flanged type 4 element of Fig. 3.1 d) have only 6 degree of freedom, namely 3 rigid body movements and 3 basic deformation modes(modes 1, 2 and 5 in Fig. 3.2). Their stiffness matrices can be derived from the corresponding degenerated plane frame element.

Deformation compatibility of the structure is enforced through the common nodes between the connected components. For interior joint elements, since there are four constraints between displacements of adjacent nodes introduced from connected beam/column elements as

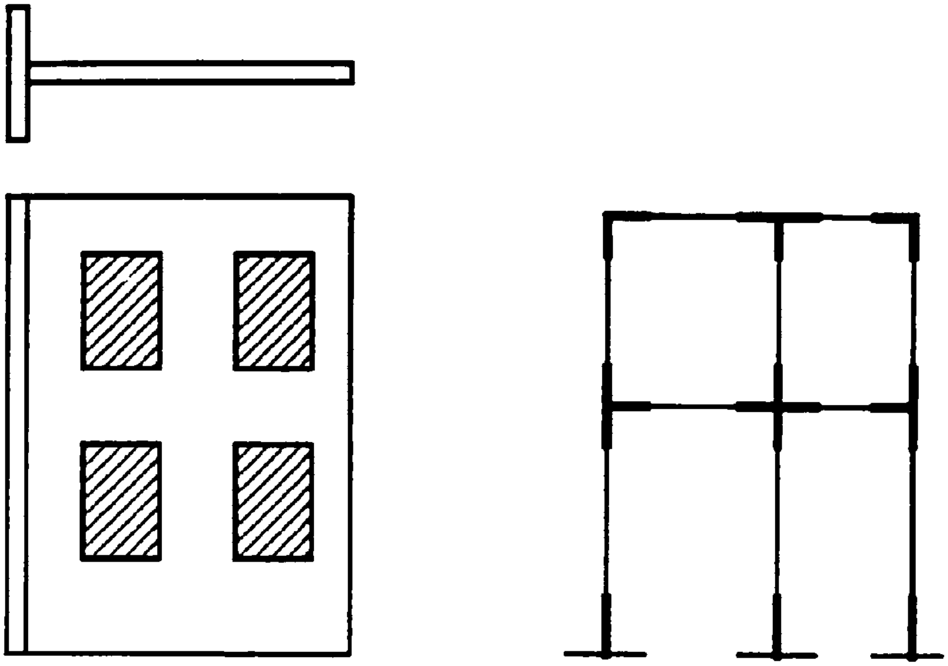

(a) Wall with Openings

(b) Frame Simulation With Rigid End Blocks

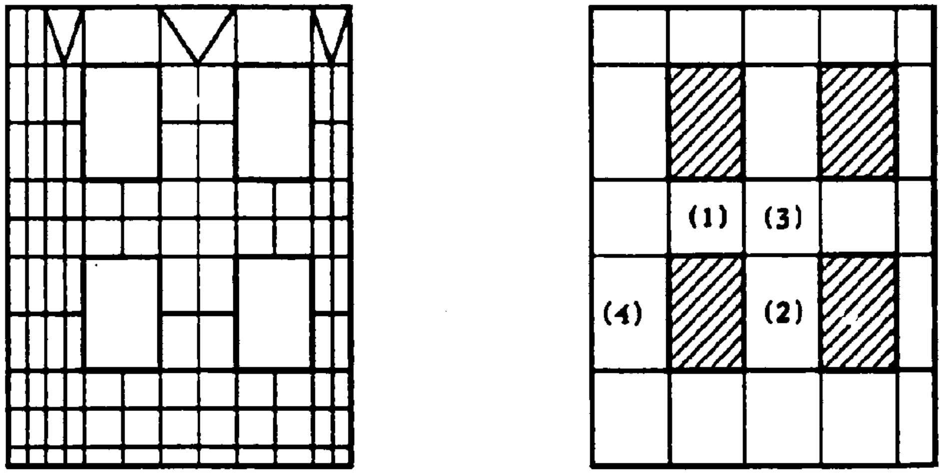

(c) Finite Element Simulation

(d) Structural Component Model Simulation

Fig. 3.1 Masonry Assemblage and its Modelling

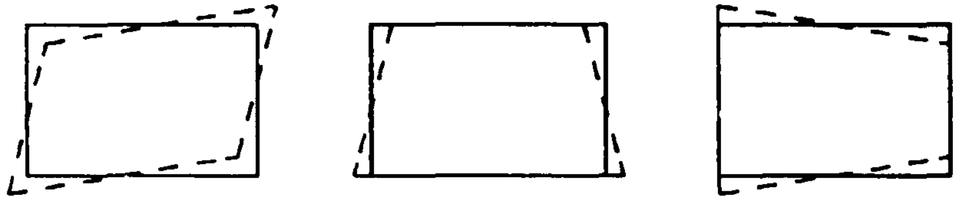

(1) Shear Deformation (2) Axial Flexural (3) Transverse Flexural

(4) Axial Elongation (5) Transverse Elongation

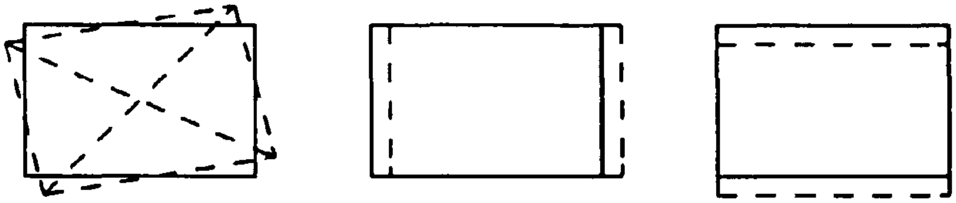

(6) Body Rotation (7) Body Axial Translation (8) Body Transverse Translation

Fig. 3.2 Basic Deformation Modes of 4-node Plane Element

(Element Axis Horizontal)

mentioned above, the effective degree of freedom for this element reduces to 4, including 3 rigid body movements and one basic deformation mode , that of shear deformation.

In this chapter, an inelastic SCM for flanged masonry structural walls is developed. Complete structural analysis using SCM models is beyond the scope of this study and is considered in TCCMAR TASK 2.1(3)[26]. For the flanged member (type 4, Fig.3.1d), the element has the same basic deformation modes as a column/beam component, but a special model is needed in order to simulate its asymmetric characteristics in the two directions parallel to the web.

The model is based on the ordinary shear-flexural element and allows the formation of a flexural hinge with a limited length at each end to simulate the possibility of plastic hinges forming at the top and/or bottom of the SCM. The stiffness matrix is derived through inverting the flexibility matrix of bending and shear deformation. An asymmetric hysteresis loop pattern is also proposed utilizing a tri-linear envelope with modeling of stiffness degradation and pinching effects. The skeleton model for force-deformation is based on the strength, stiffness and ductility calculation developed in the previous chapter. The model can be used to simulate the overall inelastic response of a single flanged masonry wall, or a flanged structural component of a building subjected to earthquake excitation, by connecting it to the other structural members.

3.2 Formulation of the Element Stiffness Matrix

The flanged masonry wall subjected to in-plane loads parallel to the web, as shown in Fig. 3.3 (a), can be modeled as a planar shear-flexural element (Fig. 3.3 (c)). The relationship between node forces and displacements of the element in local coordinates can be expressed as

$$\begin{Bmatrix} p_1 \\ p_2 \\ p_3 \end{Bmatrix} = \begin{bmatrix} k_{11} & k_{12} & 0 \\ k_{21} & k_{22} & 0 \\ 0 & 0 & k_{33} \end{bmatrix} \begin{Bmatrix} v_1 \\ v_2 \\ v_3 \end{Bmatrix} \tag{3.1}$$

or $$\{p\} = [k]\{v\} \tag{3.2}$$

Where $\{p\}$ and $\{v\}$ are node force and displacement vectors respectively and $[k]$ is the element stiffness matrix, as shown in Fig. 3.3 (c).

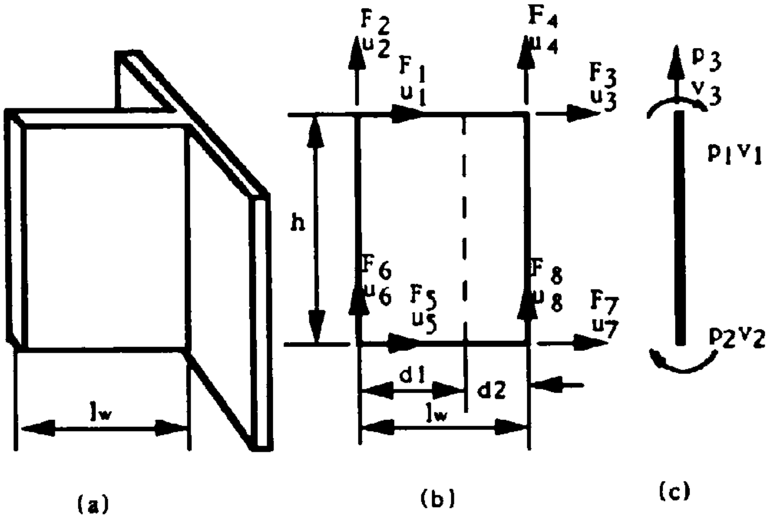

Fig. 3.3 Flanged Wall and Equivalent SCM Simulation

The stiffness matrix [k] depends on the material properties and configuration of the element. Since flanged masonry walls consist of different materials (masonry units, reinforcement, etc.) and the cross sections may crack, yield, or develop plastic hinges at the ends under planar loads, an ordinary stiffness matrix cannot adequately describe its complicated behavior during the different possible loading stages. In this section, the energy principle is employed to obtain the special element stiffness matrix.

3.2.1 Stiffness Matrix in Local Coordinates:

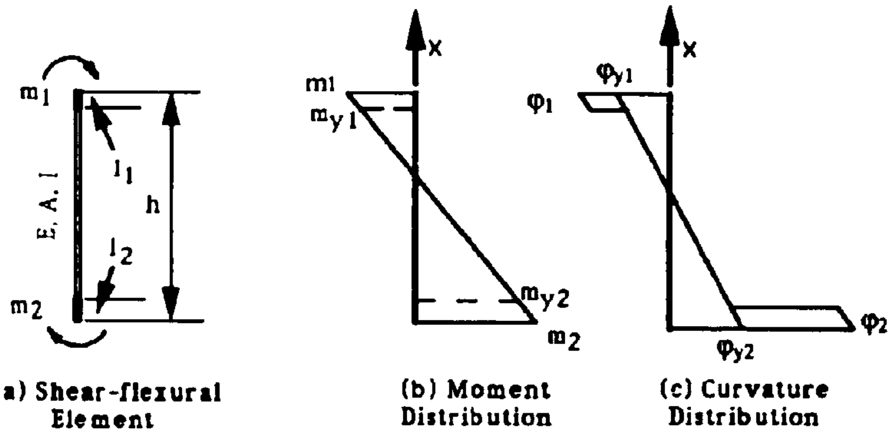

(a) Shear-flexural Element

(b) Moment Distribution

(c) Curvature Distribution

Fig 3.4 SCM Element

Fig. 3.4 (a) shows a column-type element with two plastic hinges, one at each end. The equivalent plastic hinge lengths are l_1 and l_2 respectively which can be determined[28] by

$$l_p = 0.08\,h + 6\,d_b \qquad (3.3)$$

where d_b is the diameter of vertical reinforcement. In the central region of the wall the element remains in the elastic stage and has a constant stiffness(cracked). Note that since behavior at inelastic levels of structural response is of prime concern, the simplification that all sections of the wall between plastic hinges are cracked will induce only small errors. It would, however, be straightforward to add an additional subsection of the element represented uncracked region. The moment is linearly distributed along the element in this case, and the curvature is assumed as shown in Fig. 3.4 (c).

The energy principle will be used to obtain the flexibility matrix of bending and shear deformation, then the stiffness matrix of the element can be derived by inverting the resultant flexibility matrix. The deformation energy of the element in Fig. 3.4 due to bending is

$$U_b = U_e + U_p \tag{3.4}$$

in which U_e and U_p are contributed by elastic and plastic deformations respectively. Since the central region of the element remains in the elastic stage and hence $M(x) = EI\,\Phi(x)$ applies. Further, the curvature in plastic hinge regions can be divided into two parts: elastic and plastic, and hence

$$U_b = \underbrace{\int_0^h \frac{M^2(x)\,dx}{2EI}}_{\text{elastic}} + \underbrace{\overline{m_{l1}}\,(\varphi_1 - \varphi_{y1})\,l_1 + \overline{m_{l2}}\,(\varphi_2 - \varphi_{y2})\,l_2}_{\text{plastic}} \tag{3.5}$$

Where $M(x)$, $\Phi(x)$ are distribution functions of moment and elastic curvature along the element; $\overline{m_{l1}}$ and $\overline{m_{l2}}$ are average moments in top and bottom plastic hinge regions of the element respectively. Using $m_1 \approx \overline{m_{l1}}$

and $m_2 \approx \overline{m_{l2}}$ and the relationship between moment and curvature, the deformation energy can be expressed approximately as

$$U_b = \frac{1}{2EI}\int_0^h \left(m_1 - \frac{m_1 - m_2}{h}x\right)^2 dx + \frac{m_1 (m_1 - m_{y1}) l_1}{EI_1} + \frac{m_2 (m_2 - m_{y2}) l_2}{EI_2} \qquad (3.6)$$

In which EI_1 and EI_2 are equivalent flexural stiffness in the top and bottom regions of the element respectively. Then, the flexibility coefficients of the node rotation due to bending can be derived from the following differential operation

$$[\, f_{ij} \,] = \left.\frac{\partial U}{\partial m_i}\right|_{m_j = 1} \qquad (i, j = 1, 2) \qquad (3.7)$$

Using the approximation of $my_1 \approx m_1$, $my_2 \approx m_2$, again, we have

$$[\, f_b \,] = \begin{bmatrix} f_{11} & f_{12} \\ f_{21} & f_{22} \end{bmatrix}$$

$$= \frac{h}{6EI}\begin{bmatrix} 2 & -1 \\ -1 & 2 \end{bmatrix} + \begin{bmatrix} \frac{l_1}{EI_1} & 0 \\ 0 & \frac{l_2}{EI_2} \end{bmatrix} \qquad (3.8)$$

in which the first part is the normal flexibility matrix due to elastic deformation, and the second one is due to the plastic hinges at the ends.

The flexibility matrix of shear deformation can be easily obtained as

$$[\, f_s \,] = \frac{1}{GA'h}\begin{bmatrix} 1 & 1 \\ 1 & 1 \end{bmatrix} \qquad (3.9)$$

where G and A' are shear modulus and effective shear area respectively. Combining the two matrices above and inverting the resultant flexibility matrix, the stiffness matrix of node rotation can be derived as

$$\{k\}_{2\times 2} = ([f_b] + [f_s])^{-1}$$

$$= \frac{6EI}{h\alpha} \begin{bmatrix} 2+\beta+\gamma_2 & 1-\beta \\ 1-\beta & 2+\beta+\gamma_1 \end{bmatrix} \tag{3.10}$$

in which

$$\alpha = (2+\beta+\gamma_1)(2+\beta+\gamma_2) - (1-\beta)^2$$

$$\beta = 6EI / GA'h^2$$

$$\gamma_1 = 6I\, l_1 / I_1 h$$

$$\gamma_2 = 6I\, l_2 / I_2 h$$

Adding the axial load terms into the above matrix, the stiffness matrix of the element in local coordinates has the final form as

$$[K]_{3x3} = \frac{6EI}{h\alpha} \begin{bmatrix} 2+\beta+\gamma_2 & 1-\beta & 0 \\ 1-\beta & 2+\beta+\gamma_1 & 0 \\ 0 & 0 & \frac{\alpha A}{6I} \end{bmatrix} \tag{3.11}$$

In which A is the area of cross section for axial load.

3.2.2 Stiffness Matrix in Global Coordinates

In global coordinates shown in Fig. 3.3 (b), the flanged wall has 8 degrees of freedom and the relationship between the node forces and displacements is

$$\{F\} = [\,K\,]\ \{u\} \tag{3.12}$$

where

$$\{F\} = [\,F_1, F_2, \text{---}\ F_8\,]^T \tag{3.13}$$

$$\{u\} = [\,u_1, u_2, \text{---}\ u_8\,]^T \tag{3.14}$$

Transformation of node forces from local coordinates {p} to global coordinate forces {F} can be established through the following matrix operation.

$$\{F\} = [T]^T\ \{\,p\,\} \tag{3.15}$$

where

$$[T] = \begin{bmatrix} -\frac{\lambda_2}{h} & \frac{1}{d} & -\frac{\lambda_1}{h} & -\frac{1}{d} & \frac{\lambda_2}{h} & 0 & \frac{\lambda_1}{h} & 0 \\ -\frac{\lambda_2}{h} & 0 & -\frac{\lambda_1}{h} & 0 & \frac{\lambda_2}{h} & \frac{1}{d} & \frac{\lambda}{h} & -\frac{1}{d} \\ 0 & \lambda_2 & 0 & \lambda_1 & 0 & -\lambda_2 & 0 & -\lambda_1 \end{bmatrix} \tag{3.16}$$

is termed the transformation matrix and $\lambda_1 = d_1/l_w$, $\lambda_2 = d_2/l_w$ where l_w, d_1 and d_2 are transverse dimensions, defined in Fig.3.4. Therefore, the element stiffness matrix in global coordinates is

$$[K] = [T]^T [k] [T] \qquad (3.17)$$

Eqn. 3.17 can be used for both static and dynamic analysis of flanged masonry walls or as a T-section member in masonry assemblages. Numerical examples and comparison between the analytical results and experimental results are presented later in Chapter 7 .

3.3 Hysteresis Loops for Flanged Masonry Walls

3.3.1 Moment-Curvature

To match the inelastic structural component element developed above, an asymmetric hysteresis loops for flanged masonry walls is proposed in order to allow time-history response analyses to be carried out.

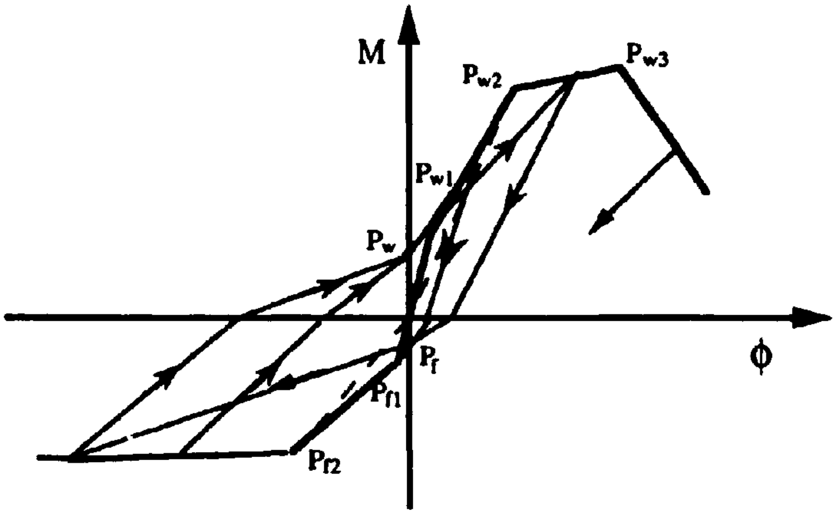

Fig 3.5 Proposed Moment-curvature Hysteresis Loops For Flanged Masonry Walls

Based on the assumption of plane-cross section and the material properties described in Chapter 2, the moment-curvature hysteresis loops for reinforced flanged masonry walls are proposed as shown in Fig. 3.5. The loops have an asymmetric tri-linear envelope in each loading direction and a falling branch when the web is in compression to simulate compression failure of the flexural compression zone at high strain levels. The points on the envelope are defined as

P_{w1} : first cracking, web in compression
P_{w2} : first yield, web in compression
P_{w3} : ultimate state, web in compression
P_{f1} : first cracking, flange in compression
P_{f2} : first yield, flange in compression

The tangent stiffness in each linear segment is

$$k_i = (M_{i+1} - M_i)/(\phi_{i+1} - \phi_i) \tag{3.18}$$

where M_i, ϕ_i are corresponding moment and curvature which can be calculated by cross section analysis or using the design charts or program in Appendices. Fig. 3.5 shows a falling branch to the moment-curvature envelope after crushing occurs at point P_{w3}. With the simplified moment curvature section analysis developed for this study, the slope of the falling branch can not be determined analytically. As a consequence, all analytical prediction using this model extend only to the stage of first crushing. The falling branch characteristics can be modelled by inelastic finite element methods, as reported by Seible et al[25].

Unloading paths have a stiffness degradation factor λ which varies from 0 – no stiffness degradation (unloading parallel to 0 - P_{w2} or 0 - P_{f2}) to 1 – unloading towards the origin, until they reach the x-axis.

Reloading in the opposite direction has a pinching effect, with all the paths directed towards a certain point (p_w or p_f, see discussion in next section) on the moment-axis. After returning to zero deformation, the loading direction will either be towards the maximum previous position or the first cracking point in the opposite direction, whichever is larger.

3.3.2 Shear Deformation

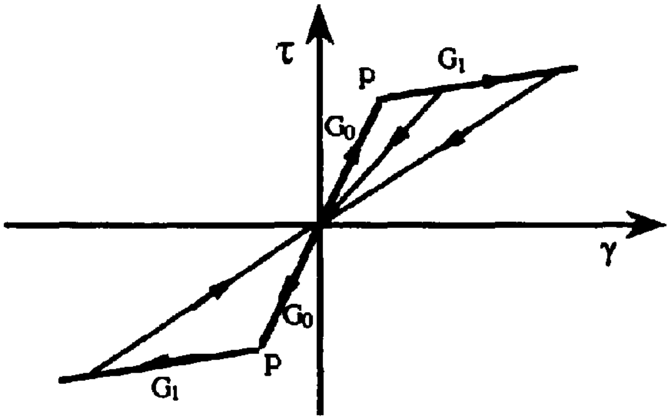

Fig. 3.6 Hysteresis Loops for Shear

Since shear failure is undesirable under seismic response, and is avoided by use of capacity design principles[4], and shear characteristics are expected to be symmetric in the two opposite directions parallel to the web, hysteresis loops for shear deformation are assumed to have a symmetric bi-linear envelope as shown in Fig. 3-6 Point P, on the envelope, represents the onset of shear cracking and all unloading paths are assumed to point to the origin.

The shear stiffness before diagonal cracking is equal to the initial masonry shear modulus as

$$G_0 = G_m = \frac{E_m}{2(1 + \nu)} \tag{3.19}$$

in which ν , G_0 and E_m are Poisson ratio, shear and elastic moduli of masonry respectively. After diagonal cracking, the shear stiffness is assumed to be proportional to the ratio of horizontal reinforcement in the web and its elastic modulus. The equivalent shear modulus thus has the form

$$G_1 = \rho_h \cdot \frac{E_s}{E_m} G_m \tag{3.20}$$

where ρ_h and, E_s are ratio and elastic modulus of horizontal reinforcement in the web respectively.

Theoretically, point P is corresponding to a stress state where the principle tensile stress in the web reaches the tensile strength of masonry. Since the vertical stress varies along the web due to bending, as an average, at the neutral line, the principle tensile stress equals to the shear stress thus the corresponding horizontal load can be determined.

3.3.3 Moment Intercept at Zero Curvature on Reverse Loading

In Fig. 3.5, there are two points P_w and P_f on the moment-axis which the hysteresis loops are directed towards on reloading from an inelastic excursion they allow the pinching effects during the reloading to be simulated. The determination of these two points is discussed briefly as follows:

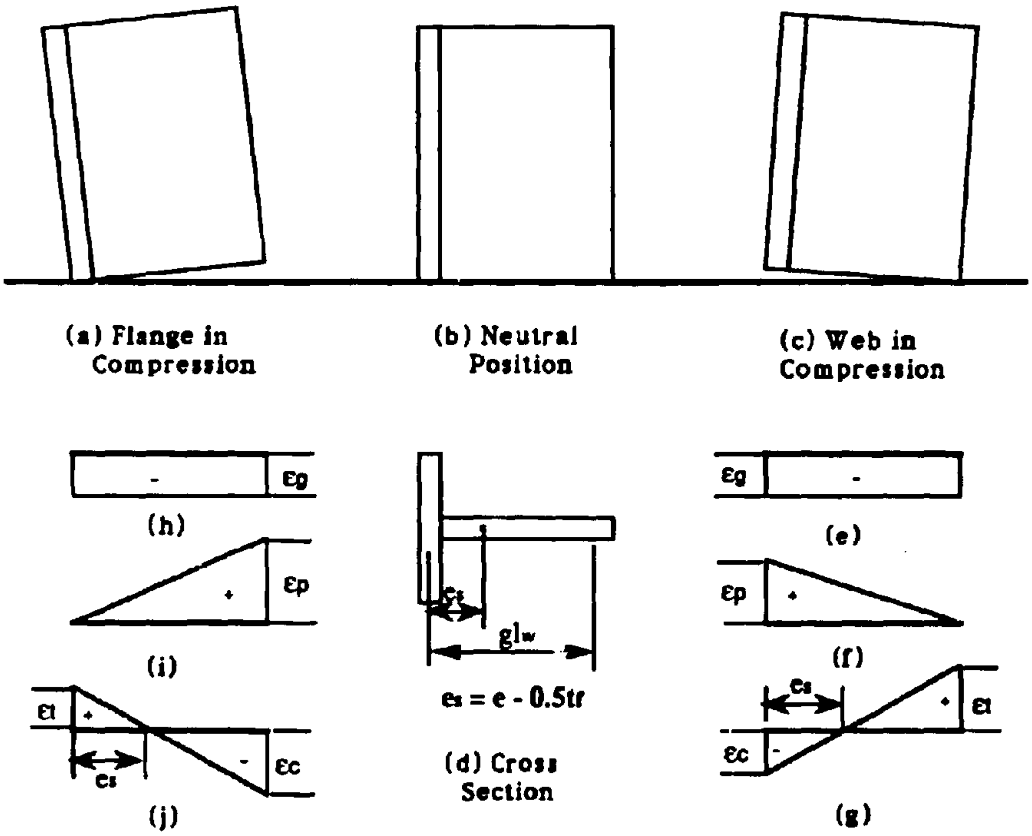
(a) Flange in Compression
(b) Neutral Position
(c) Web in Compression
(d) Cross Section

Fig. 3.7 Strain Distribution on Reloading after an Inelastic Excursion

(a) Reloading From Web In Compression

The positions and strain distributions for the cross-section of a flanged wall at different loading/unloading stages involving previous inelastic response are shown in Fig. 3.7. In the case of the web in compression, at the end of unloading, the moment returns to zero, but there are still residual strains (deformation) at the base cross-section as a consequence of inelastic reinforcement strains in the previous cycle of response as shown in Fig. 3.7 (c). Assuming the position of the resultant vertical loads (center of the cross section) is close to the geometric center of the vertical reinforcement (Fig. 3.7 (d)), the strains due to vertical loads may be considered to be uniformly distributed along all the vertical rebars (Fig. 3.7 (e)). The residual strains due to bending deformation can be assumed to be linearly distributed along the web (Fig. 3.7 (f)). When loading in the reverse direction, the crack will occur (or re-open, if cracked already) before the residual tension strains of vertical rebars in flange are eliminated completely. Since the whole cross section is cracked, the external moment will be carried by the vertical reinforcement only, and the strains due to the applied moment will be linearly distributed along the vertical reinforcement as shown in Fig. 3.7 (g).

When loading to a point where the residual strain is eliminated at the extreme compression bar by the reverse deformation, the crack will be closed and the stiffness of the wall should indicate a sharp increase, as shown in Fig. 3.6. At this stage

$$\varepsilon_p - \varepsilon_g - \varepsilon_c = 0 \tag{3.21}$$

where ε_p, ε_g and ε_c are vertical reinforcement strains in the flange caused by residual deformation, axial load and reverse loading as shown in Fig. 3.7 (f), (e) and (g) respectively. Since the curvature for closing the crack may be written as

$$\varphi_{Pw} = \varepsilon_c / e = (\varepsilon_p - \varepsilon_g) / e \qquad (3.22a)$$

the moment required to generate the above curvature will be

$$M_{Pw} = E_s I_s (\varepsilon_p - \varepsilon_g) / e \qquad (3.22b)$$

where

E_s – Elastic modulus of vertical reinforcement

I_s – Moment of inertia of the cross section based on vertical reinforcement only.

(b) Reloading From Flange In Compression

When the wall is unloaded from the opposite direction , flange in compression, the distributions of the strains along the cross-section are similar to that in the previous case and are shown in Fig. 3.7 (h) to (j). In this case, however, the depth of the compression zone is (gl_w-e) instead of e in the former case. The curvature and moment corresponding for closing the crack at the flexural end can be derived, in similar fashion to the above as

$$\varphi_{Pf} = \varepsilon_c / (gl_w - e) = (\varepsilon_p - \varepsilon_g) / (gl_w - e) \qquad (3.22c)$$

$$M_{Pf} = E_s I_s (\varepsilon_p - \varepsilon_g) / (gl_w - e) \qquad (3.22d)$$

where gl_w is the total length between the extreme vertical rebars along the web and the other parameters are the same as in Eqn. 3.22b.

To simplify the hysteresis loops for both cases, it is reasonable to assume the points are on the moment-axis, i.e., the curvatures are equal to zero or the strains at both extreme sides along the web are equal

$$\varepsilon_p - \varepsilon_c = \varepsilon_t \tag{3.23}$$

Therefore, the curvature due to elastic deformation under reloading is

$$\varphi = (\varepsilon_t + \varepsilon_c)/l = \varepsilon_p/l \tag{3.24a}$$

and the corresponding moment will be

$$M = E_s I_s \varepsilon_p / l \tag{3.24b}$$

Note that in Equations 3.22 and 2.23, the calculated moment will depend on the residual strain ε_p of the extreme rebar. When reloading from flange in compression, ε_p could be much larger than the yield strain, resulting in very high corresponding moment. Actually, under reloading, the extreme rebar at the free end of the web may reach its yield strength long before the residual strain is completely eliminated. Therefore, the corresponding moment will be

$$M = My = \frac{f_y I_s}{(gl_w - c)} \tag{2.25}$$

where f_y is yield strength of the reinforcement and the other parameters are the same as above. The real values for P_w and P_f should be corresponding to the smaller moment between the calculated results from Equations 2.24 and 2.25.

To evaluate the formulas proposed above, wall F1 (for Pseudo-static test) and F5 (for dynamic test) have been calculated with the formulas. In the calculation, fy = 71.2 Ksi (tested result for wall F1), E_s = 30,000 Ksi, P = 80 Kips(axial load) and ε_p was assumed to be 0.5 and 4.0 times of steel yielding strain(0.002) for WIC and FIC respectively. The shear equivalent to the critical moments of both calculated and experimental results are listed in Table 3.1. It is seems that when reloading from web in compression, Equation 3.24 dominates the calculation result, but in the opposite direction, Equation 3.25 will be applicable.

Table 3.1 Critical Shear (Kips)

	Equation 3.24	Equation 3.25	Wall F1 (static)	Wall F5 (dynamic)
Web in compression	3.8	10.9	≤ 4	0
Flange in Compression	30.6	10.9	≤ 11	≤ 15.5

4. EXPERIMENTAL STUDIES - GENERAL DESCRIPTIONS

4.1 Introduction

The single T-section wall tested in preliminary studies[27] had confirmed the predicted behavior in term of stiffness, strength and failure mode. However, as an initial pilot test, there were inevitable problems with experimental technique and the influence of variation of key parameters could not be considered.

In this continuing research (TCCMAR Task 4.1), a comprehensive experimental program was carried out to investigate the seismic behavior of flanged masonry walls. The program consisted of two phases: a pseudo-static phase involving tests of four full scale T-section masonry walls and a dynamic phase, involving tests of five full scale T-section masonry walls on a shake table.

The purpose of the static tests was to investigate the influence of the vertical reinforcement ratio, the flange width, and confinement to the mortar beds at the web toe, on the strength, stiffness and ductility of flanged masonry walls. The test results were also intended to be used to provide a data base for examining and calibrating the theoretical work. Although static testing is very useful and enables detailed observation under controlled conditions during the testing, it does not simulate a dynamic environment necessary to examine the real seismic response of structures.

As the second phase of the experimental studies, the dynamic tests used identical specimens to the walls for static tests, facilitating the investigation of the influence of above parameters under dynamic condition. It also allowed comparison of the structural response between static and dynamic test regimes in order to investigate the reliability of predicting of seismic behavior of flanged masonry walls, using the static analytical and experimental results.

4.2 Design and Construction of the Test Units

4.2.1 Considerations of Test Unit Design

Since identical static and dynamic test units were desired, the size and weight of all test units were limited by the loading capacity and dimensions of the shake table. As a consequence, the effective wall height was chosen to be 12 feet(3.66 m), which may be considered equivalent to two story walls, since lateral forces were applied at the top of the wall in the test, whereas the resultant seismic force in a 2 story wall would be approximately at the mid-height of the second story, as a result of inertial forces at the second floor and the roof levels. Table 4.1 defines wall dimensions, and reinforcement for the two phases of walls. Among the units, wall F1 was considered as the basic wall and the other static walls F2, F3 and F4(confined) were designed to have either different vertical reinforcement ratio, different width of flange or to have confinement plate on mortar beds at web toe in order to investigate the influences of these parameters. Dimensions for wall F1 are shown in Fig. 4.1. As will be seen from Table 4.1 and Fig. 4.1, the dimensions of the basic wall (F1) were such that the ratio of flange to web length was 2.25, and the ratio of wall height to flange length was 1.38. These dimensions were chosen to ensure highly unsymmetrical response characteristics, and to provide a real test of shear-lag effects.

For dynamic tests, units F5, F6 and F7(confined) duplicated walls F1, F2 and F4 respectively (wall F3 was too wide to test on the shake table), in order to compare the results between static and dynamic tests as well as to check the effects of vertical reinforcement ratio and confinement on strength, stiffness and ductility of flanged masonry walls under dynamic conditions. Walls F8 and F9 were identical to wall F5 (also wall F1), but were tested in different ways to investigate the effects of loading history and direction on the response of flanged masonry walls, as will be described in Chapter 6. The only physical difference between the two groups is that the walls for dynamic tests were constructed two masonry courses (sixteen inches) shorter than the static walls in height so that the center of mass for the inertia blocks on the top of the dynamic test units was at the correct position to maintain an equivalent wall height of twelve feet.

In accordance with TCCMAR requirements, all walls were constructed with 6 inch wide (nominal) concrete masonry units and were fully grouted. Three kinds of blocks were used: namely, end closures were either standard open-end units (block type 1) or half open-end units (block type 2) on each side of flange and at the free end of web; all others were open-end bond beam units (block type 3), allowing transverse reinforcement to be placed. The three block styles and their dimensions are shown in Fig. 4.2

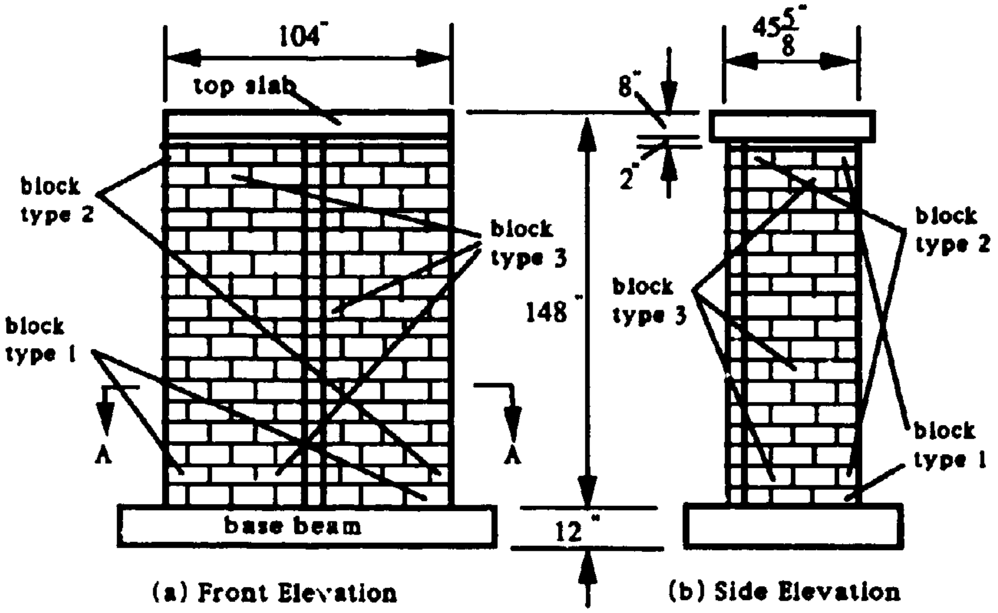

(a) Front Elevation

(b) Side Elevation

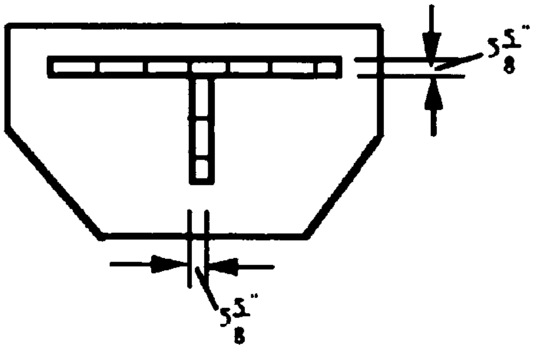

(c) Section Plan A-A

Fig. 4.1 Flanged Masonry Wall F1

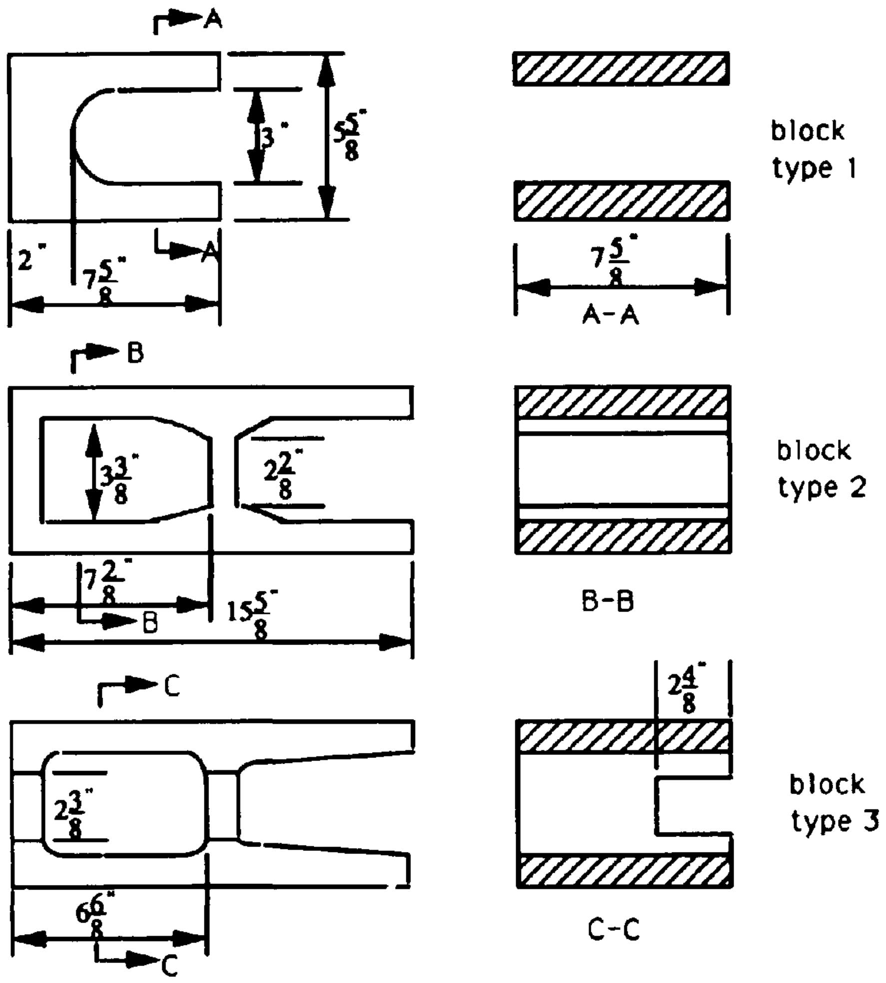

Fig. 4.2 Dimensions of Masonry Units

4.2.2 Reinforcement Arrangement

Vertical reinforcement for wall F1, F4, F5, F7, F8 and F9 consisted of #6 bars (19.05 mm diameter) of grade 60 steel ($f_y = 414$ MPa) at 16 inch (406 mm) nominal centers, resulting in 6 bars in the flange and 4 in the web (including 1 at the web-flange intersection). Over the full cross section, the average vertical reinforcement ratio was 0.00546. Wall F2, F3 and F6 were reinforced vertically with #4 bars (12.75 mm diameter) of grade 60 steel at 16 inch nominal centers, resulting in an average reinforcement ratio of 0.00248.

Table 4.1 Test Matrix for TCCMAR Task 4.1

	Wall	Wall Dimensions H x Lf x Lw*	Axial Load (psi)	Vertical Rebars	No. in web	No. in Flange
Static	F1	12' x 8' 8" x 3'10"	100	#6 @ 16"	4	6
	F2	12' x 8' 8" x 3'10"	100	#4 @ 16"	4	6
	F3	12' x 16' 8" x 3'10"	100	#4 @ 16"	4	12
	F4 *1	12' x 8' 8" x 3'10"	100	#6 @ 16"	4	6
Dynamic	F5	12' x 8' 8" x 3'10"	100	#6 @ 16"	4	6
	F6	12' x 8' 8" x 3'10"	100	#4 @ 16"	4	6
	F7 *1	12' x 8' 8" x 3'10"	100	#6 @ 16"	4	6
	F8 *2	12' x 8' 8" x 3'10"	100	#6 @ 16"	4	6
	F9 *3	12' x 8' 8" x 3'10"	100	#6 @ 16"	4	6

* : H=wall height , Lf=flange length , Lw=web length
*1: confined
*2: Tested with a single severe earthquake input
*3: skewed 45 degree to shake table axis

Vertical reinforcement was continuous from the wall base to mid-height of the wall, where it was lapped with standard laps of 40 bar diameters. Lapping of short starter bars at the wall base was deliberately avoided to alleviate potential bond problems in the plastic hinge region. The vertical bars were bent with 90 degree hooks at both ends into the top concrete slab or the bottom concrete base respectively to assure adequate development length. Detail of the reinforcement arrangement of wall F1 (also F4, F5, F7, F8 and F9) is illustrated in Fig. 4.3. For wall F2 and F6, the only difference is that the diameter of the vertical reinforcement was #4 instead of #6. Wall F3 had twelve vertical rebars in flange rather than six for wall F2 due to its wide flange, as illustrated in Fig. 4.3(d).

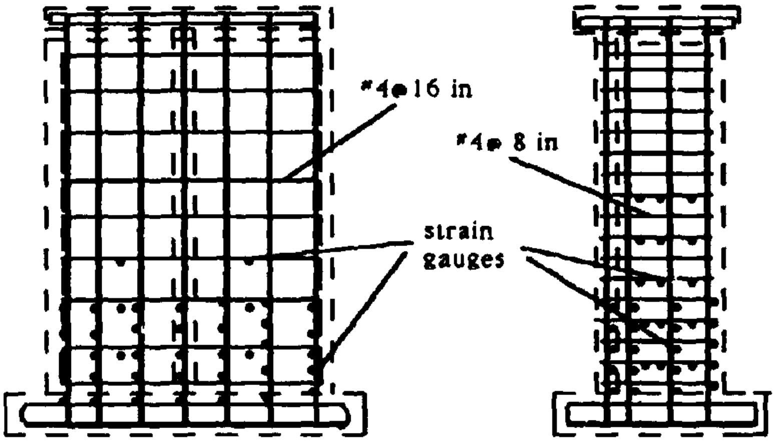

(a) Front Elevation

(b) Side Elevation

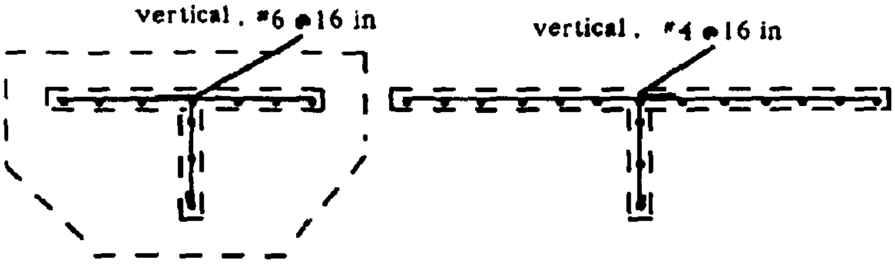

(c) Plan

(d) Cross Section of Wall F3

Fig. 4.3 Reinforcement Arrangement, and Straingauge Locations

Horizontal reinforcement was essentially the same in all 9 walls. In the web, #4 (12.75 mm diameter) grade 60 steel bars were placed at 8 inch (203.2 mm) centers over the full height of the wall. This provided a nominal shear capacity of 81 kips (360 kN) which was greater than the maximum expected force. Web transverse reinforcement was hooked around the vertical rebar at the free end of the web with a 180° hook and bent with a standard horizontal 90 degree hook into the flange at the other end. Because of the small flue dimensions of the 6 inch block units, the hook at free web end had to be rotated 45 degree out of the horizontal plane. In the flange, transverse reinforcement consisted of #4 bars of grade 60 steel at 16 inch vertical center. The bars were bent down into end vertical flues with standard 90 degree hooks.(see Fig. 4.3)

Wall F4 and F7 included 1/8 inch (3.175 mm) thick mortar bed steel confining plates at the free end of the web over the lower 7 mortar beds. The confining plates were 24 inches (609.6 mm) long and cut to the shape of the net block profile, allowing 1/4 inch (6.35 mm) for pointing. The plates were laid into the mortar beds, which was placed in two thin layers, one under and one over the plate. No problems were experienced in laying the plates. Fig. 4.4 shows a mortar bed confining plate being placed during construction.

4.2.3 Foundation Beam, Top Slab and Wall Construction

The walls were constructed on 12 inch (304.8 mm) thick reinforced concrete bases with vertical reinforcement of the wall extended into the bottom of the base and bent 90 degree horizontally to ensure adequate anchorage (see Fig. 4.3). On the base, a pattern of PVC tubes (2 inch

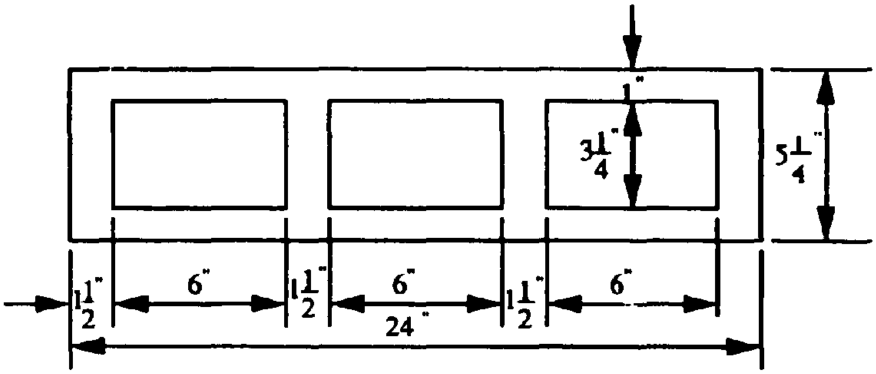

Material: $\frac{1}{8}$" thick A36 steel plate

(a) Dimension of Confining Plate

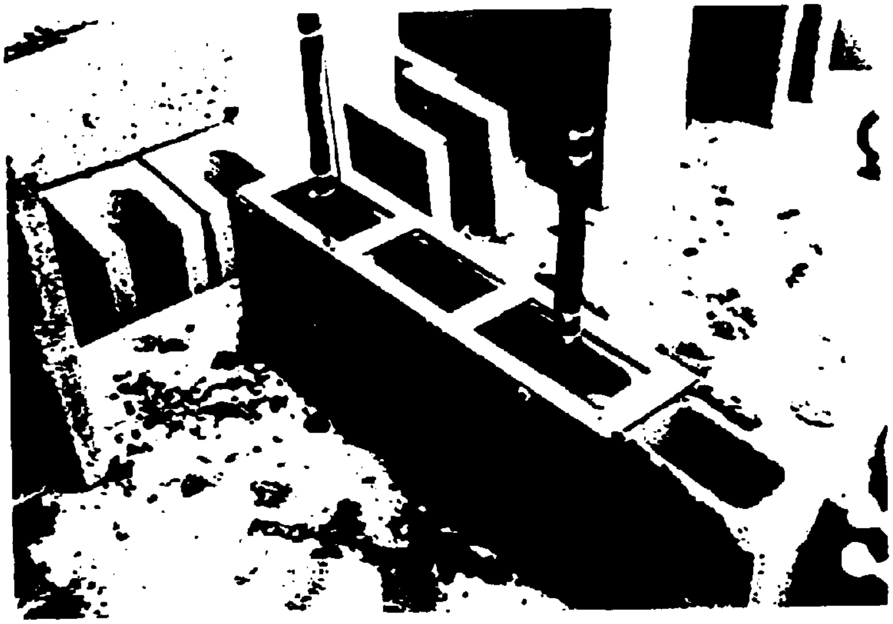

(b) A Confining Plate is Placed During Construction

Fig. 4.4 Confining Plates on Mortar Beds diameter) were cast into the concrete for tieing down the wall onto the strong floor for the pseudo-static test or the shake table for dynamic test. To ensure that there would be no foundation failure, the concrete base beam was a little over reinforced. Both the dimensions and reinforcement arrangement are shown in Fig. 4.5.

On the top of the wall, an 8 inch (203.2 mm) thick reinforced concrete slab was cast to distribute the lateral load. As with the base, the vertical reinforcement of the wall extended into the slab and was bent 90 degree horizontally for adequate anchorage. The dimensions and reenforcement for top concrete slab are presented in Fig. 4.6.

The construction process for each test unit consisted of the following four steps:

(1) Constructing the wood form, placing base reinforcement and casting the concrete foundation beam with the bottom half vertical rebars in position.

(2) Placing horizontal reinforcement and laying blocks up to about half height of the wall, then fully grouting (leaving a length of 40 bar diameter for lap splicing).

(3) Placing horizontal reinforcement and laying the wall to its full height, then placing the top half vertical rebars, tieing to existing bars, and fully grouting.

(4) Constructing the wood form for top slab, placing reinforcement and casting.

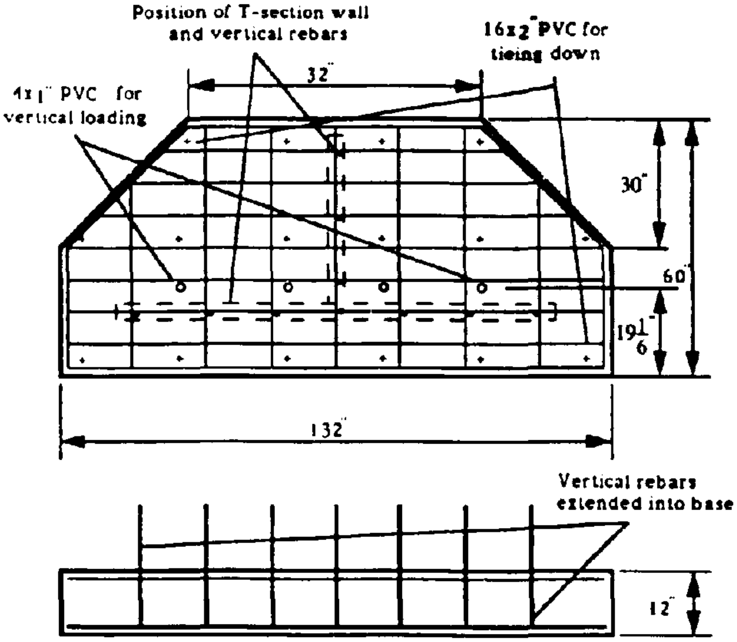

Fig. 4.5 Concrete Foundation Beam

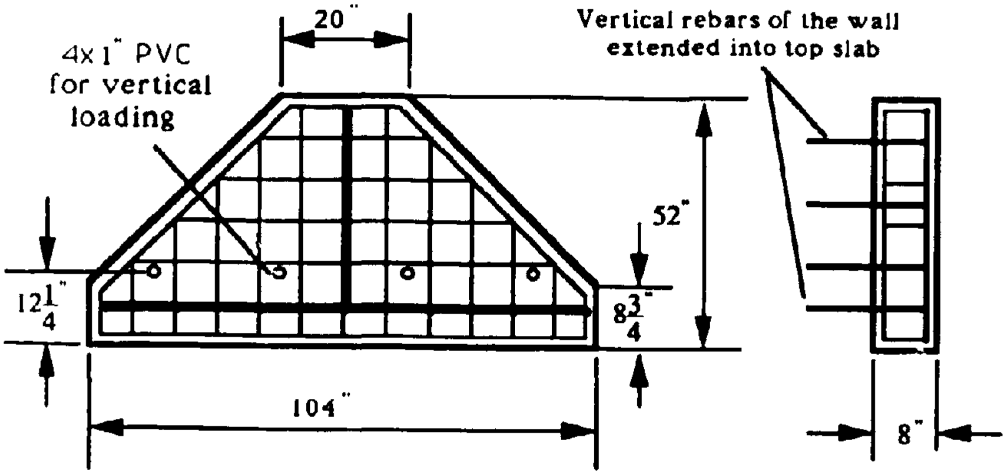

Fig. 4.6 Concrete Top Slab

(a) Concrete Base Completed (b) Bottom Half Wall Completed

(c) Whole Wall Completed (d) Top Concrete Slab Completed

Fig. 4.7 Procedure of Wall Construction

Fig. 4.7 (a) through (d) show photos at each stage of wall construction. The walls were constructed by certified masons to ensure that normal standard of workmanship was achieved. A special mortar mix of cement: lime: sand = 1 : 0.5 : 4.5 by volume, required by TCCMAR was used, and water was added by eye to obtain a mix of satisfactory workability.

The intersection between the web and flange is a natural plane of weakness, subjected to high shear stress and deserves special attention in design and construction. No masonry units penetrated the flange-web interface, but continuity of grout and horizontal reinforcement, and hence monolithic action, was provided by removing the top half of the face shell on the flange block at the interface. When a half unit butted against the flange(the odd courses counted from the base), half depth saw cuts were also made in the end face shell of the block and the top half knocked off to allow continuity of grout and transverse reinforcement.

The walls were fully grouted and compacted with a pencil insertion vibrator. Sika grout aid was added (6 pounds per cubic yard) to compensate for concrete shrinkage. To ensure the bond between grout and concrete base, the concrete base surface was roughened with brush, and a clean-out ports for cleaning the mortar were cut into the block faces at the location of each vertical rebar at the bottom course (see Fig. 4.4 b). These were replaced after cleaning. A similar detail of clean-out ports was provided at the wall mid-height, corresponding to the bottom of the second construction lift.

4.3 Material properties

4.3.1 Strength of Masonry and Its Components

In accordance with the requirement by TCCMAR, the following samples of mortar and grout were taken during the wall construction to determine the material properties.

(1) mortar cubes 2 inch long, using a special bronze mould

(2) mortar cylinders with 4 inch height and 2 inch diameter

(3) grout cylinders with 12 inch height and 6 inch diameter

(4) grout prisms with 6 inch height and 3 inch square cross section, using four masonry units as the mould with absorbant paper placed between the grout and masonry surface to allow proper water absorption by the masonry.

Three-course high stack-bonded prisms were made, using a special jig to ensure precise dimensions[30]. Since the walls were laid up in pairs simultaneously, for example F1 and F2; F3 and F4 etc., one set of materials apply to both walls of the pair. However, since the walls were grouted sequentially and the prisms were laid up approximately half way through the grouting process, it is possible that variation in strength between the critical sections of the walls existed due to variation of grout properties through the mix. In particular, a difference in the amount of water absorbed by blocks from grout could be expected with time as the grout stiffens.

Table 4.2 summarizes the material test results. Also listed in the table is the prism strength predicted by a formula developed from analysis of the mechanics of masonry compression strength[29]. This approach relates the prism strength to the strength of its components by the expression

$$f'_{mp} = 0.6\,\alpha\, f'_{cb} + 0.9\,(1-\alpha)\, f'_{g} \tag{4.1}$$

where f'_{cb} and f'_{g} are compression strength of masonry units and grout respectively, and α is the ratio of net to gross area of the units (in this case, α is 0.62). It will be noted that the predicted strength is about 28% above the measured value f'_{mt} from prism test for walls F3 & F4, and 17% below the test results for both walls F6 & F7 and F8 & F9. It is not clear why such larger discrepancies exist for these walls, but it is possible that insufficient care was taken during construction, capping and testing of prisms for walls F3 & F4, and grout cylinders for walls F6 to F9. Comparison between measured strength and strength interpreted from test results is discussed further in Section 5.3.2.

Table 4.2 Compression Strength of Masonry Prisms and Components(Ksi)

	F1 & F2	F3 & F4	F5	F6 & F7	F8 & F9
f'_{cb}	2.56	2.56	2.56	2.56	2.56
f'_{mo}	3.67	2.82	3.11	1.18	2.69
f'_{g}	5.64	3.94	3.44	2.30	3.11
f'_{mt}	2.60	1.80	2.26	2.10	2.43
f'_{mp}	2.88	2.30	2.13	1.74	2.02

4.3.2 Reinforcement Stress-strain Characteristics

Three samples for each batch of vertical reinforcing steel were taken and tested in a universal testing machine. The mean values of yielding and ultimate tensile strength for each group are listed in Table 4-3. Also straingauges were attached to one steel bar in each group and tensile stress-strain curves were ploted during the testing. The stress-strain curves of vertical #6 and #4 rebars are shown in Fig. 4.8 (a) and (b) respectively.

Table 4.3 Tensile Strength of Reinforcement (Ksi)*

		Yield strength	Ultimate strengh
Vertical rebars	Wall F1& F4 (#6)	71.2	99.7
	Wall F2 & F3 (#4)	75.9	117.2
	Wall F5,7,8 &9 (#6)	68.9	107.4
	Wall F6 (#4)	62.5	97.3
All horizontal rebars		75.9	117.2

*: 1 Ksi = 6.9 MPa

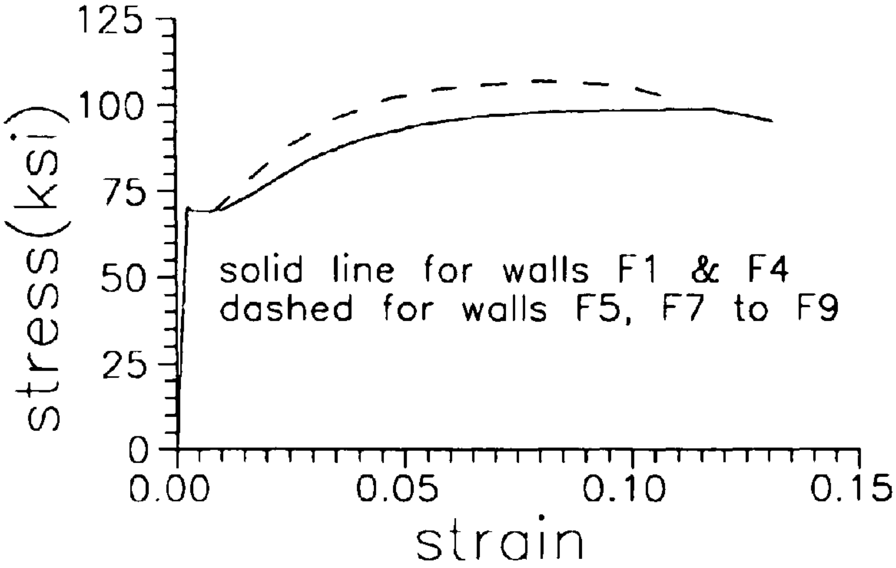

(a) #6 Rebars

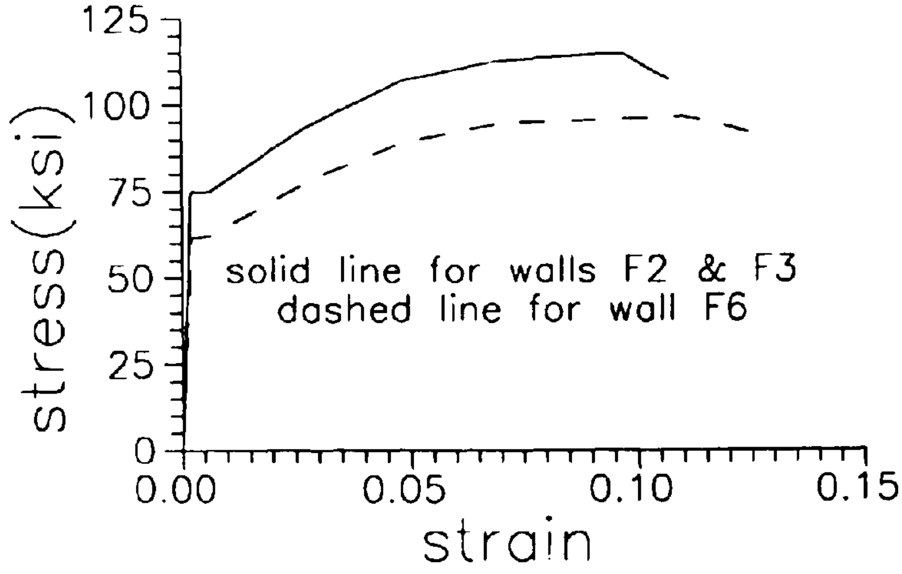

(b) #4 Rebars

Fig. 4.8 Stress-Strain Curve of Vertical Reinforcement

5 PSEUDO-STATIC TESTS

5.1 Test Set Up and Instrumentation

As the first phase of the experimental studies, the pseudo-static tests of four full scale flanged masonry walls were carried out. The walls were tied down onto the strong floor through the holes in concrete base with 1.25 inch DWIDAG bars. A thin layer of hydrostone was cast between the wall base and strong floor and post-tensioning was applied to ensure adequate friction between the base and ground during the testing.

Lateral load was applied by a double-acting 100 kip (450 KN) capacity hydraulic actuator reacting against a strong wall, and supplied with swivel mounts at each end allowing rotation in the vertical plane only (see Fig. 5.1). Vertical load was applied by either 4 (walls F1, F2, F4) or 6 (wall F3) 5/8 inch (16 mm) high strength DWIDAG prestressing bars anchored at the bottom of the concrete base , and stressed against the top slab of the wall, through a stiff coil spring. The flexibility of the springs was specially designed to have a axial compression stiffness of 6 kips/inch (1051 KN/M), which was about one tenth of the axial tensile stiffness of the 5/8" DWIDAG bar. The flexibility of the springs were such that the vertical load provided by the stressed bars would remain essentially constant during lateral displacement, despite the corresponding vertical displacement resulting from the integration of vertical strains. The level of applied axial load was chosen to provide an essentially uniform stress of 100 psi (0.69 MPa) (including wall self weight) at the base of the wall. The vertical load bars were straingauged to enable actual load variations to be monitored during testing. Fig. 5.1 shows the test set up for the pseudo-static testing.

Electric resistance strain gauges were placed on both vertical and horizontal reinforcement within the potential plastic hinge region at location shown in Fig. 4.3. The purpose of this instrumentation was to investigate shear lag effects in vertical reinforcement, and shear forces carried by transverse reinforcement in the web.

Masonry deformation in the lower region of the wall were monitored with linear potentiometers (0.5 inch (12 mm) range) attached to steel studs epoxied into holes drilled into the masonry. The bottom line of gauges measured strains over a 4 inch (102 mm) gauge length, while all other gauge lengths were 8 inches (203 mm). The locations of these gauges are also shown in Fig. 5.1.

Other instrumentation included measurements of gross wall deformations relative to a reference frame, as shown in Fig. 5.1. Gauges 1 (10 inch LVDT), 2 and 3 (4 inch potentiometers) monitored wall horizontal displacements at the line of lateral load application, and at 2/3 and 1/3 of the wall height. Gauges 4 and 5 were 1 inch potentiometers mounted at the mid-length of the web , one on each side , to measure the vertical cracking at the base level and the slip between the web and concrete base. Gauges 6 and 7 (also 1 inch potentiometers) monitored vertical movement of the wall. These data were needed to fully characterize the SCM model, which formed a main part of the theoretical studies in this research project and is discussed in Chapters 3 and 7.

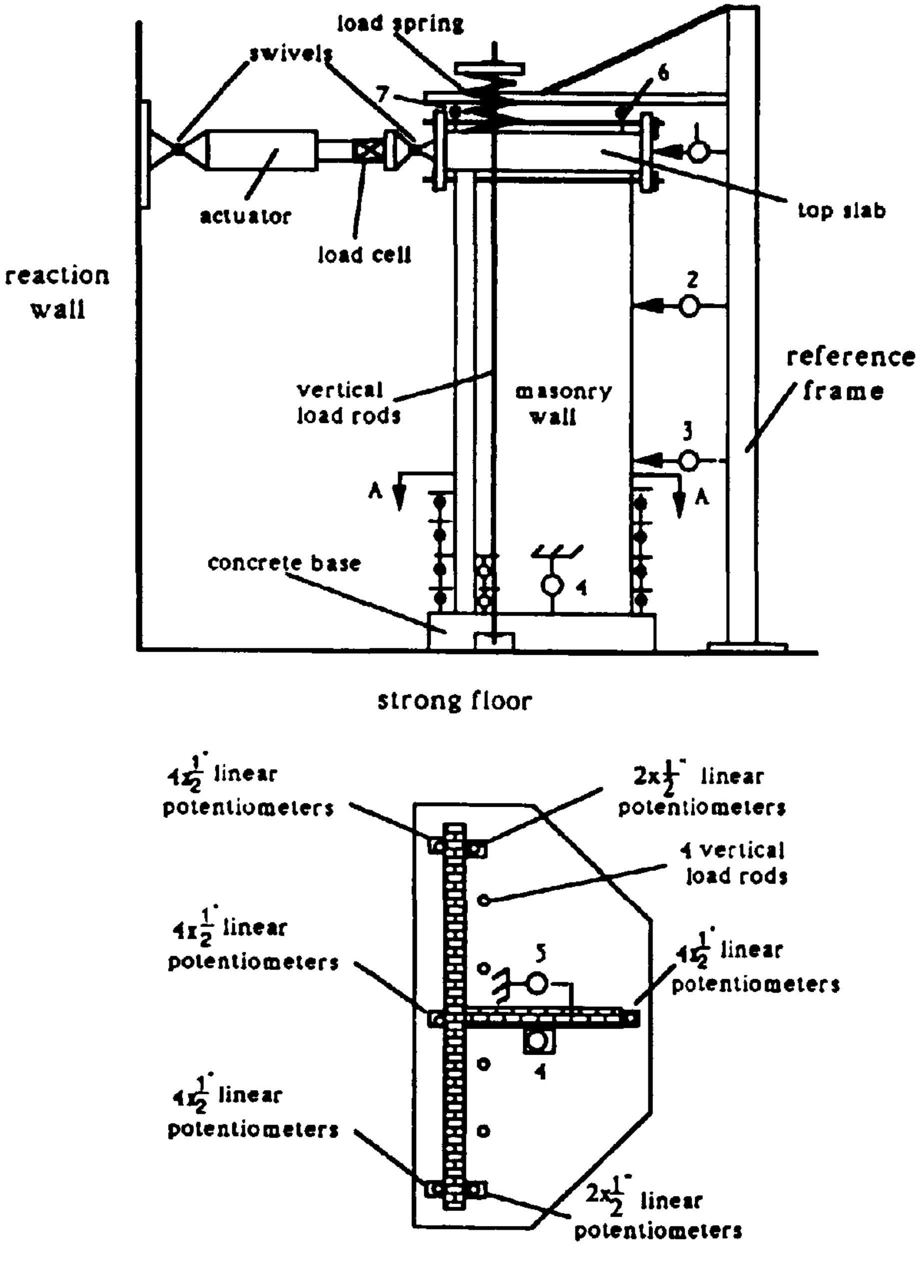

Section Plan A-A

Fig. 5.1 Pseudo-static Test Set Up

At the top of the wall, the load cell and displacement gauge were connected directly to a x-y recorder to plot the load-displacement curve to allow test progress to be monitored, and all the data were recorded and stored by a NEFF DATA ACQUISITION SYSTEM which is capable of reading 512 channels for subsequent processing and analysis. Fig. 5.2 (a) and (b) show wall F1 ready for testing and vertical load springs on the wall top respectively.

5.2 Test Procedure

Lateral loading was carried out under a controlled-displacement test regime, after initial load-controlled cycles at load-levels less than that required to induce yield of vertical reinforcement. The standard TCCMAR test pattern[25] was modified somewhat to recognize the difference in strength, stiffness and expected ductility capacity in the two opposite loading directions.

Fig. 5.3 shows a typical loading procedure for the pseudo-static test. Before yielding, the wall was subjected to two cycles for each load level at 25%, 50% and 75% of the predicted first yield load in each direction. After that, the test was controlled by displacement instead of load. At each test level, the wall was first displaced to the desired displacement level (a defined multiplier of the yield displacement), followed by 2 cycles of lower intensity loading (50% and 25% of yield load respectively), then three complete cycles repeated at the same displacement before increasing displacement to the next level of ductility.

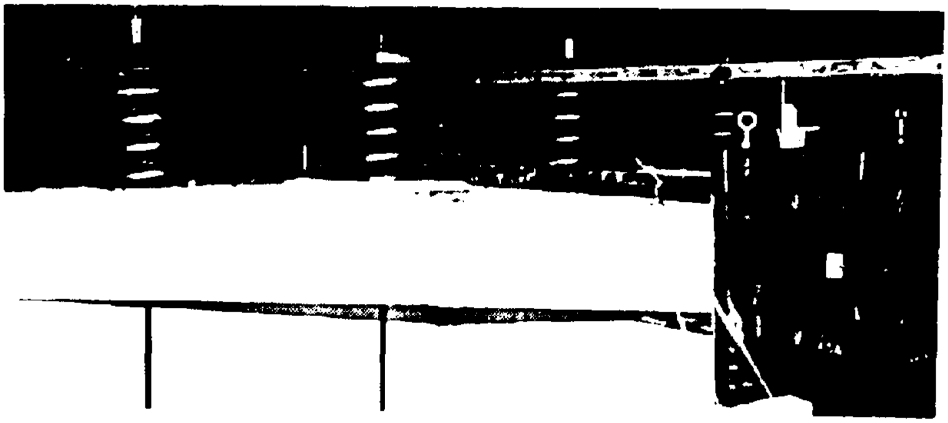

(a) Spring Coils for Vertical Loading

(b) Wall F1 Ready for Testing

Fig. 8.2 Wall F1 Before Testing

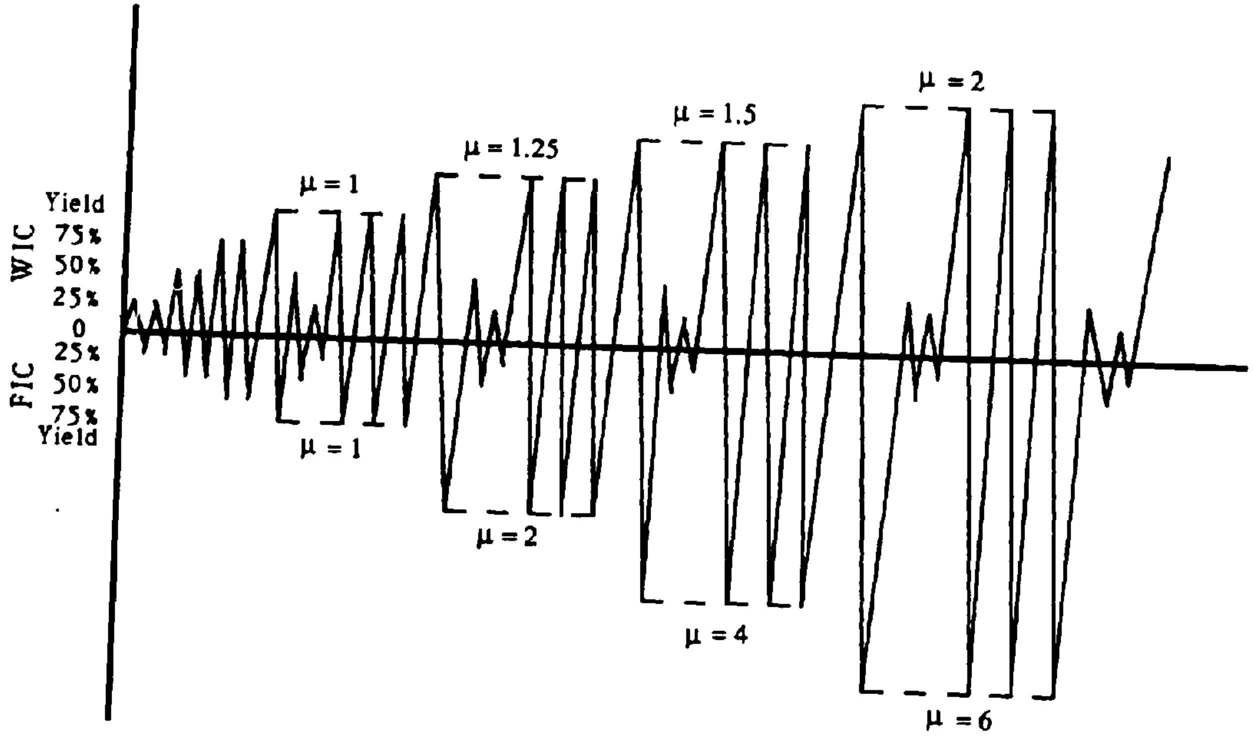

Fig. 5.3 Typical Pattern of Applied Displacement for Pseudo-static Tests

Since the strength and ductility capacity of T-sections are different in the two opposite directions, loading cycles with different ductility factors were assigned for each direction, namely larger (2, 4, 6 etc.) for the flange in compression and smaller steps (1.25, 1.5, 2 etc.) for web in compression until the wall finally failed.

5.3 Observations and Test Results

5.3.1 General Behavior Observed

Before cracking (at very early loading stage), the flanged masonry walls behaved symmetrically in the two opposite directions parallel to the web. Due to the unsymmetrical configuration of the T-section, initial cracking occurred at different loading stages in the two opposite directions, that is , first cracking occurred earlier in the direction of the flange in compression than the web in compression. After cracking, the load-displacement curves softened and as the load increased, more cracks developed at higher sections; diagonal cracking occurred at mid-height of the web due to shear and inclined cracks from web/flange interface up to two ends of the flange also developed due to vertical shear in the flange.

During this stage, the unsymmetrical behavior of the flanged wall became obvious. With the flange in tension, the wall has higher strength, stiffness but less ductility than in the opposite direction when the wall reached its first yielding in the direction of the flange in compression, with the tension rebar yielding at the web toe, the load-displacement curve became very flat, but the wall can still deform stably to much higher ductility level. After yielding occurred in the direction placing the flange in tension, the wall finally failed as the toe of web vertically cracked and face shell spalled off, followed by buckling of vertical reinforcement in the area due to lack of support in the direction perpendicular to the web.

Vertical splitting of the bottom course block at the free end of the web typically originated at displacements of about 0.80-1.00 inch (20-25mm). It was apparent however, that a significant degree of confinement to the bottom block was provided by the foundation pad. This effectively delayed failure until compression strains at the level of mortar course 2 (8 inch above the base) had reached a strain of about 0.003(see Figs. 5.4, 5.5 and 5.6 for unconfined walls). At this stage vertical splitting developed upwards from course 2 and was followed by sudden and catastrophic loss of strength due to collapse of the compression zone. Strength typically dropped to 20-30% of the pre-failure load without significant increase in displacement.

Wall F4, which contained mortar bed confining plates in the lower courses of the web exhibited significantly improved behavior, compared with the other walls, in the form of increased deflection at maximum load, and reduced severity of load degradation following compression zone failure. Since the seven lower courses were all confined with steel plates, it put the failure section down to the bottom course of the wall (see Fig. 5.7), where the curvature reached its maximum value. Wall F4 failed as a consequence of lateral buckling of the web following a loading sequence where the web reinforcement had been subjected to high residual inelastic tensile strains prior to load reversal placing the web in compression. Before the masonry in the web could support compression stress it was necessary for the web reinforcement to yield in compression, to remove the residual tensile strains and close the cracks. During the process there was no effective lateral support to the web vertical reinforcement, which exhibited lateral instability, placing eccentric loads on the web and causing failure.

It is interesting to note that the walls failed in their stronger direction at displacement substantially lower than the reversed direction. For all four walls, the unsymmetrical characteristics of the responses were very similar. However, the ratio of vertical reinforcement, and width of flange, can affect the strength, stiffness and ductility of the wall significantly in both directions. Confining plates in mortar beds of the web toe improves the ductility of the wall in the direction of flange in tension. The influence of above parameters will be discussed in detail in the following sections. The observed details during four wall tests are presented below and following abbreviations are used in the description:

WIC--- direction of loading placing the web in compression
FIC--- direction of loading placing the flange in compression
P_w --- horizontal load with WIC
P_f --- horizontal load with FIC
μ_w ---ductility factor with WIC
μ_f --- ductility factor with FIC

Wall F1 (#6 (19.05 mm) Vertical Reinforcement, Unconfined)

Force-controlled Cycles

Prior to commencing data acquisition, an accidental load of P_f =5.1 Kips (22.7 kN) was applied, causing horizontal cracking in the web at the base, and at the 2nd and 4th mortar beds. These cracks closed when the lateral force was removed.

First cracking with the web in compression occurred at P_w =20 kips(89 kN). At P_w =30 kips(133 kN), vertical cracking at the web/flange interface was noted, and the first indication of shear inclination to flexural cracks occurred. As the lateral force was further increased, under WIC, further inclination of flexural cracks occurred. At P_w =40 kips(178 kN) a flange crack developed at the 4th mortar bed, with considerable associated noise and significant drop in lateral force, as a consequence of the release in strain energy as the flange tension force was released. It was significant to note that the crack did not initiate at the web/flange interface and gradually extend across the width of the flange, but appeared to crack across the full width almost instantaneously. The audible indication of cracking, and the associated irregularity in the force-deformation curve made it possible to accurately assess the instant of cracking, and hence by back calculation, the average flange tension stress at which cracking occurred. At P_w =45 kips(200 kN) more significant flexural shear cracking developed in the web.

In the reversed direction of loading (FIC), the instant of crack formation was less precisely defined, but could still be estimated with reasonable accuracy. At a lateral force of P_f =15 kips(67 kN) web cracks had formed up to the 7th mortar bed, with cracks forming up to the 11th bed at P_f =18 kips(80 kN). The lateral force levels of P_w =45 kips(200 kN) and P_f =18 kips (80 kN) corresponded approximately to theoretical first yield of the extreme tension reinforcing bars. This was confirmed by strain measurements at P_f =18 kips(80 kN) of ε_s=2860 mε, compared with a yield strain of ε_y=2450 mε.

The crack pattern at this stage of testing is shown in Fig. 5.4(a). Note that the shear inclination of the flexural cracks with the web in compression are much steeper (about 55 degree) than with the flange in compression (about 35 degree). Average shear stresses, based on the effective web area of 5.6 X 42.5 = 238 in^2 (153,500 mm^2) were 189 psi (1.30 Mpa) for WIC and 75.6 psi (0.52 Mpa) for FIC respectively. Extrapolation of displacements to the theoretical flexural strength gave the yield displacement as

Δ_{yw} = 0.498 inch

Δ_{yf} = 0.813 inch

Displacement Controlled Testing

On the first displacement controlled cycle, to μ_w = 1.0 and μ_f = 2.0, vertical cracking developed at the toe of web under WIC. The base crack appeared to about 1/8 inch (3 mm) with FIC, and cracks at higher levels were also wide. During subsequent cycles at this level of displacement, no further significant cracking developed, though force and stiffness both degraded . On cycling to μ_w=1.5 and μ_f = 4.0, further flexural cracks developed in the flange at the 6th and 7th mortar beds under WIC loading, with significant increase in inclined shear cracking in the web. Severe cracking in the web toe developed, and the masonry face shell started to spall in this area. The maximum lateral force at this stage was P_w =55 kips, or 92 percent of theoretical strength. Cracks formed under FIC forces opened wide for a height up to the 6th mortar bed.

At μ_w =2.0 and μ_f =6.0, the maximum strength of P_w =63.4 kips was recorded The degradation of the web compression zone continued, with vertical cracking and spalling extending up the bottom 3 courses. On the fourth cycle to this level of displacement, the end vertical reinforcing bar in the web buckled laterally, and the web compression zone crashed, with rapid degradation of strength. Despite this, the wall was capable of sustaining forces in the reverse direction (FIC) with no significant strength degradation. Fig. 5.4 (b) and (c) show the crack pattern and failure mode of wall F1 at the end of testing.

Wall F2 (#4 (12.7 mm) Vertical Reinforcement, Unconfined)

Force-controlled Cycles

Initial displacement reading of 0.033 inch in the direction of WIC was noted before commencing horizontal loading. First flexural cracking at the base of the flange with loading direction of the web in compression occurred at P_w =20 kips. In the reverse direction of loading (FIC), base mortar bed cracked at P_f =5.2 kips, and cracks at the 3rd and 4th mortar beds in the web occurred at P_f =8.7 kips and 10.5 kips respectively. First yield of the extreme tension reinforcing bar at the web toe occurred during first cycle of P_f = 10.5 kips at Δ_{yf} = 0.227 inch. The crack pattern at this stage of testing is shown in Fig. 5.5 (a).

Displacement Controlled Testing

On the first displacement controlled cycle, to μ_w = 1.0 and μ_f = 2.0, the 3rd mortar bed of flange cracked under WIC and first yield occurred during this cycle at P_w =37.3 kips and Δ_{yw}= 0.367 inch. In the reverse direction of loading(FIC), the 5th mortar bed in the web cracked. During subsequent cycles at this level of displacement, no further significant cracking developed, though force and stiffness both degraded. On cycling to μ_w =1.5 and μ_f = 4.0, further flexural cracks developed at the 3rd and 4th mortar beds in the flange at P_w = 46.2 kips under WIC loading. New crack formed at the 7th mortar bed in the web under the loading direction of FIC .

At μ_w =2.0 and μ_f =8.0, vertical cracking at web toe occurred at P_w = 48.6 kips. During cycles of μ_w = 3.0, masonry of bottom 2 courses at web toe crashed at P_w = 50.8 kips and the end vertical reinforcing bar buckled laterally, with rapid degradation of strength. Despite this, the wall was capable of sustaining forces in the reverse direction (FIC) with no significant strength degradation. Fig. 5.5 (b) and (c) show the crack pattern and failure mode of wall F2 after testing.

Wall F3 (#4 Vertical Reinforcement, Wide Flange, Unconfined)

Force-controlled Cycles

First flexural cracking at the flange base with the web in compression occurred at P_w =35 kips. This force was much higher than that for wall F2 due to its wide flange. But in the reverse direction(FIC), the behavior was very similar. First flexural cracking at base mortar bed formed at P_f = 7 kips and the 2nd mortar bed cracked at P_f = 8.7 kips.

Displacement Controlled Testing

On cycling μ_w = 1.0 and μ_f = 1.0, cracking at the 4th mortar bed in the flange formed at P_w = 54.7 kips. vertical cracking developed at the toe of web and four inclined shear cracks were observed in the web at P_w = 59 kips under WIC. No further significant cracking developed in the direction of FIC. On cycling to μ_w =1.5 and μ_f = 3.0, vertical cracking at web toe extended and more shear cracks in the web formed under WIC loading. At P_w = 64.2 kips, inclined cracks in upper part of the flange developed due to shear lag effects and cracks also formed in top concrete slab. In the loading direction of FIC, a few inclined cracks in the web were observed at P_f = 13.6 kips.

At μ_w =2.0 and μ_f =6.0, cracks formed at the 3rd and 6th mortar beds in the flange and more inclined cracks in upper part of the flange developed under WIC. At μ_w =3.0, vertical cracks at web toe were extending quickly after the maximum horizontal load P_w = 70.6 kips was reached and masonry face shell began to spall, then suddenly the bottom three masonry courses crashed and the horizontal load dropped to 19 kips. Despite this, the wall deformed steadily up to μ_f = 12 in the reverse direction (FIC) with no significant strength degradation. Fig. 5.6 (a) shows the crack pattern of the wall at lower load level, and (b) and (c) show its crack pattern and failure mode at the end of testing.

Wall F4 (#6 (19.05 mm) Vertical Reinforcement, Confined)

Force-controlled Cycles

First flexural cracking at the base mortar bed in the flange occurred at P_w =25 kips. 6th mortar bed and center part of the 7th mortar bed cracked at P_w =44.8 kips, and inclined shear cracks in the web also developed at this stage. While the horizontal load was remaining at its peak value, a sudden cracking at 3rd mortar bed happened and the horizontal force dropped obviously.

In the reverse direction, first flexural cracking at base level of the web was observed at P_f = 8.9 kips. The 2nd, 3rd and 5th mortar beds started to crack at P_f = 12 kips and extended obviously when horizontal load reached 15 kips. Inclined shear cracks across the 5th through the 8th masonry courses developed at P_f = 18 kips. During a repeated cycle, the 9th mortar bed in the web also cracked.

Displacement Controlled Testing

On the first displacement controlled cycle, to μ_w = 1.0 and μ_f = 2.0, the 4th and 8th mortar beds in the flange cracked and inclined shear cracks across the 3rd and 4th masonry courses in the web developed at P_w = 49.1 kips. First vertical cracking at the toe of web and shear cracking between the 6th and 9th courses were observed at $P_w = 53.1$ kips under WIC. In the direction of FIC, more inclined cracks across the 4th and 8th masonry courses appeared at $P_f = 20.8$ kips. Flexural cracks at the 8th and 11th mortar beds also formed during this cycle.

On cycling to $\mu_w = 1.5$ and $\mu_f = 4.0$, further flexural cracks developed in the flange at the 7th mortar bed under WIC loading, with significant increase in inclined shear cracking at the mid-height of the web. Severe cracking at the web toe developed, and first vertical cracking along web/flange interface was formed at $P_w = 57.7$ kips. In the reverse direction, cracking at the 12th mortar bed developed and more inclined shear cracks formed in the web at $P_f = 24.4$ kips under FIC.

At $\mu_w = 2.0$ and $\mu_f = 6.0$, 10th mortar bed in the flange cracked at $P_w = 63.7$ kips, this is equivalent to the ultimate strength of wall F1. And although inclined shear cracking and vertical cracking along web/flange interface extended significantly during this cycle, the wall sustained the horizontal load steadily. With increasing horizontal load, flexural cracking at the 12th and 14th mortar beds developed and more shear cracks in the upper part of web and inclined cracking in the flange up to the top concrete slab formed at $P_w = 67.2$ kips. Vertical cracking at web toe began to penetrate into concrete base and masonry face shell started to spall off. In the reverse direction (FIC), extensive shear cracking at mid-hight of the web developed at $P_f = 25.9$ kips. During second repeated cycle, vertical cracking along web/flange interface extended severely.

On cycling to $\mu_w = 3$ and $\mu_f = 8$, in the direction of WIC, more shear cracks in the web developed ($P_w = 68.6$ kips), then the wall suddenly failed due to end reinforcing bar buckling and masonry crash at the web toe, the recorded maximum horizontal force was 70.1 kips. Fig. 5.7 (a) shows the cracking pattern at lower load level, (b) and (c) show the crack pattern and failure mode of wall F4 at the end of testing.

(a) $\mu_\Delta = 0.75$

(b) Immediately before Failure

(c) Toe Crushing, at End of Test

Fig. 5.4 Condition at Different Stages of Testing, Wall F1

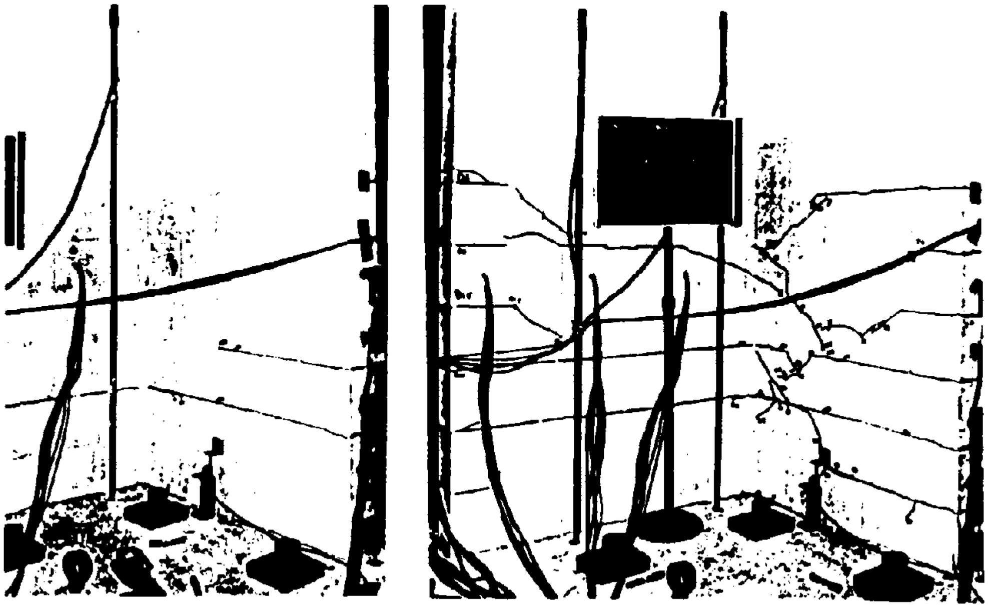

(a) $\mu_\Delta = 0.75$ (b) Immediately before Failure

(c) Toe Crushing, at End of Test

Fig. 5.5 Condition at Different Stages of Testing, Wall F2

(a) $\mu_\Delta = 1$

(b) Immediately before Failure

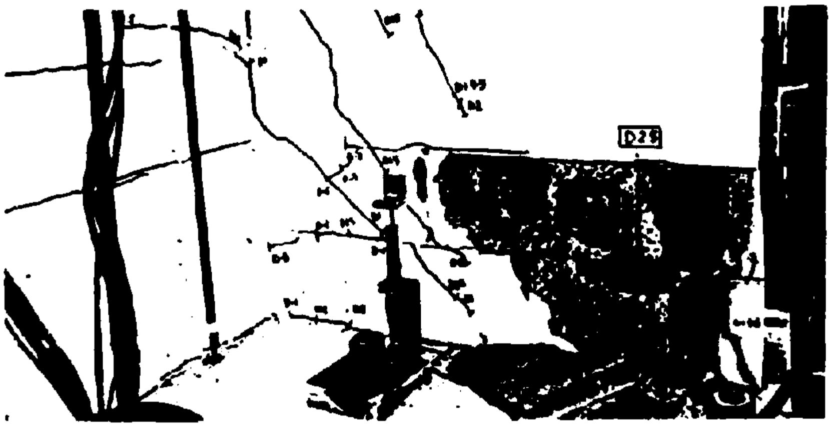

(c) Toe Crushing, at End of Test

Fig. 5.6 Condition at Different Stages of Testing, Wall F3

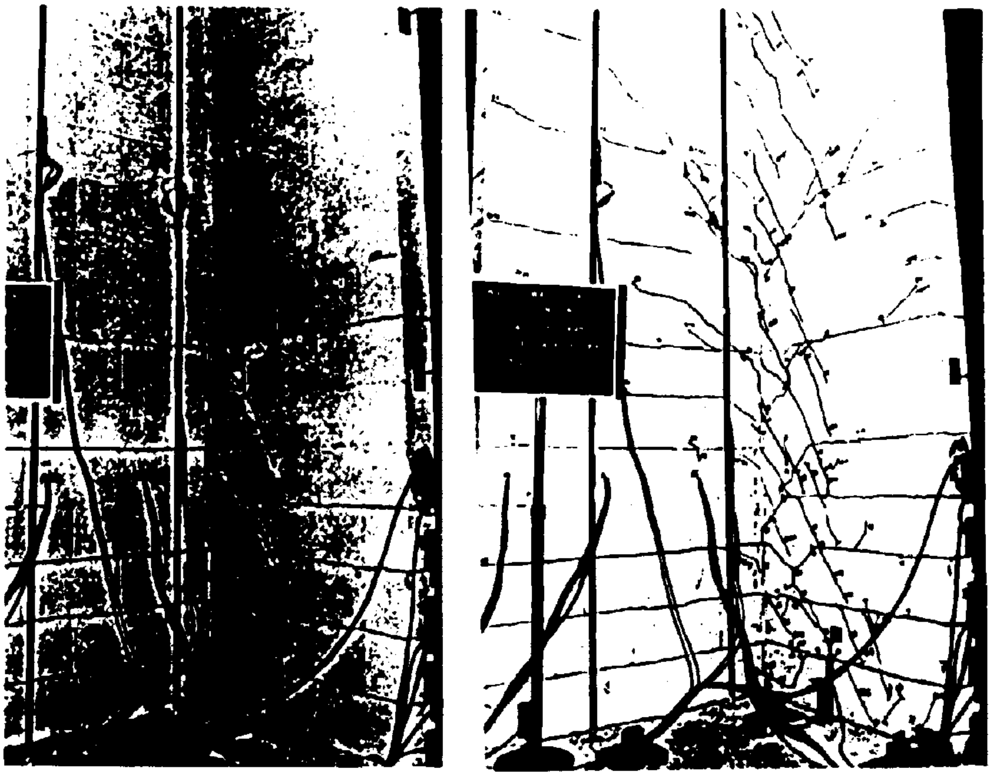

(a) $\mu_\Delta = 1$ (b) Immediately before Failure

(c) Toe Crushing, at End of Test

Fig. 5.7 Condition at Different Stages of Testing, Wall F4

5.3.2 Lateral Load-deflection Response

The test results of lateral load-displacement hysteresis loops for wall Fl to F4 are shown in Figs. 5.8 to 5.11 respectively. All the responses show strong unsymmetrical characteristics in strength, stiffness and ductility in the two opposite directions parallel to the web.

At an earlier phase of the preliminary stages of testing, the strongly asymmetric stiffness characteristics are apparent with the wall being approximately 2.5 times stiffer with the web in compression than with the flange in compression. With the web in compression, the loops are rather thin, particularly on second and subsequent cycles to a given displacement level, indicating poor energy absorption qualities. With the flange in compression, the loops are rather fatter, particularly at the latter stages of testing, when large inelastic strains were developed in the web reinforcement. The very brittle failure mode is apparent in the final stages, where the load-deflection plot drops at a very steep angle. This is a particularly dangerous characteristics for dynamic seismic response. Confined wall F4 exhibited more ductile load-deflection behavior and less steeper falling branch in the direction of the web in compression than unconfined walls.

In the direction of flange in compression, the behavior of all walls was essentially the same, i.e. lower strength and stiffness, but more ductile, even after the walls failed in the opposite direction, they could still sustain deflection without significant degradation of strength and stiffness.

In Figs. 5.8 through 5.11, the lines with * are the predicted load-displacement envelopes for each wall. In the direction of the web in compression, the predicted ultimate strength coincided well with the experimental results, but ultimate displacements which were calculated by the plastic hinge theory which will be discussed later in this chapter were much smaller than the tested results. In the opposite direction, although the tests stopped after the walls failed, it seems that the wall deflection could reach the predicted displacement. Discussion and comparison of experimental results with theoretical analyses will be presented later in this chapter.

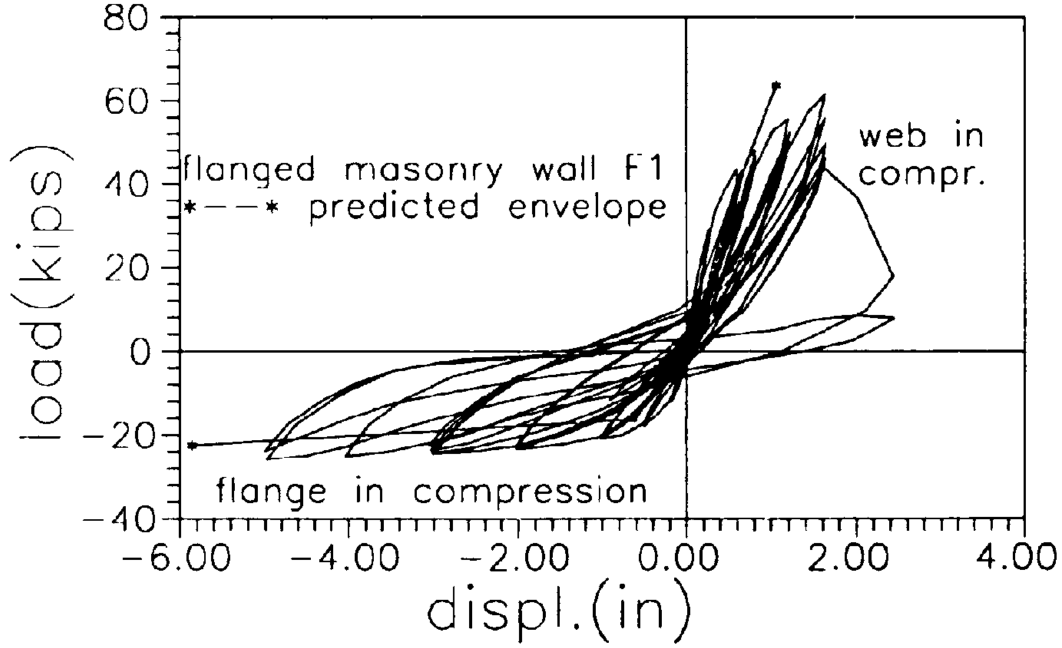

Fig. 5.8 Load-displacement Hysteresis Loops, F1

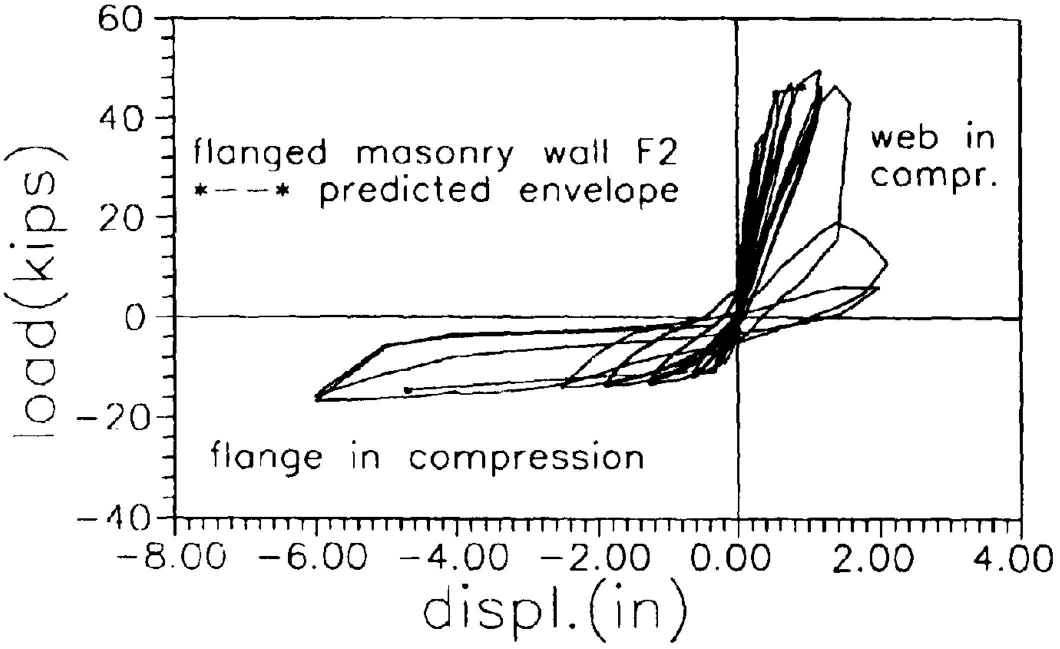

Fig. 5.9 Load-displacement Hysteresis Loops, F2

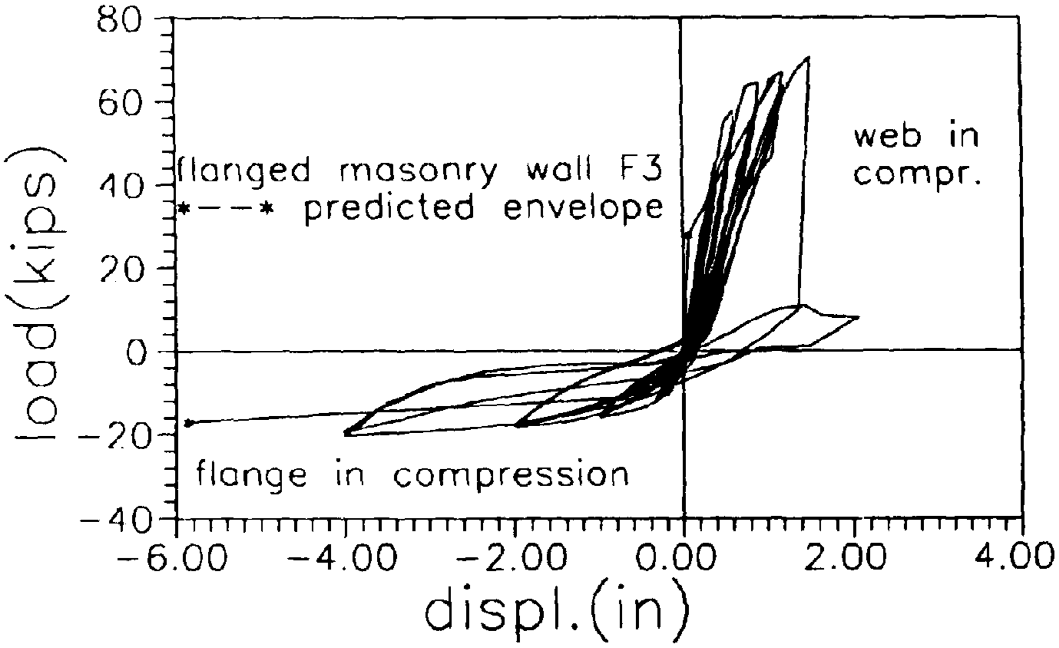

Fig. 5.10 Load-displacement Hysteresis Loops, F3

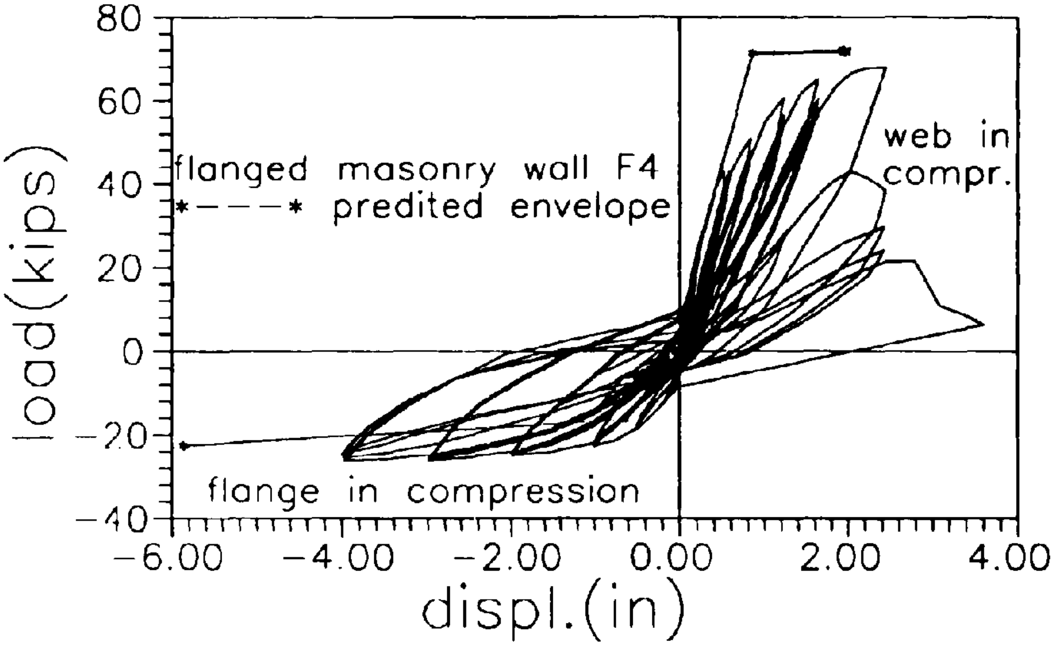

Fig. 5.11 Load-displacement Hysteresis Loops, F4

5.3.3 Flexural Response of Walls

The distribution of vertical strains of reinforcement of wall F1 along the cross section at maximum response in the direction of web in compression are shown in Fig. 5.12 and Fig. 5.13 presents the distribution in the opposite direction after first yielding (the displacement ductility factor μ_f = 2). The measured corresponding vertical deformation of masonry surface by the linear potentiometers are presented in Figs. 5.14 and 5.15. Fig. 5.16 illustrates the vertical strain distribution of wide flange wall F3 at P_w = 64.4 kips, unfortunately lot of the straingauges damaged at ultimate state and can not be presented here. The corresponding vertical deformation of masonry surface is shown in Fig.

5.17. From the above figures, the following tendency in distribution of vertical strains and deformation can be observed:

1. Strain distribution along the height: For wall F1, in the direction of the web in compression, the strains of vertical reinforcement at bottom two courses (16 inch) were almost the same, and all yielded. From the third layer the strains started to decrease gradually. But in the direction of flange in compression, it seemed that all bottom four courses (32 inch) yielded which indicates that the length of plastic hinge zone for flanged walls is also different in the two opposite directions. The vertical strains of wall F3 showed decrease from the bottom along wall height before reached its maximum response.

2. Strain distribution horizontally along the web: The distribution of vertical strain horizontally along the web was close to linear in both directions, but the width of compression zone, therefore the position of neutral axis was quite different due to effects of the flange. In the direction of web in compression, the neutral axis was about 24 inch, a little more than 50% of the web length (Fig. 5.13 (a)). From Fig. 5.15 (a) to (c), the calculated position of neutral axis was 20, 21, 31, and 27 inches respectively, the average was 24.8 inch. In the opposite direction, from Fig. 5.14, the strains of vertical reinforcement at web/flange intersection were close to zero which indicated that the position of neutral axis was coincided with the central line of the flange thickness, i.e. 2.8 inch. The above results can be confirmed by the measured vertical deformation of masonry surface in Figs. 5.14 and 5.15.

3. Strain distribution horizontally along the flange: It is clear from both strain of vertical reinforcement and masonry deformation that at the ultimate state of wall F1, the strains were almost the same along the flange section which implied that shear lag effects could be ignored. But for wide flanged wall F3 before maximum response (Figs. 5.16 and 5.17), the effects of shear-lag was obvious. The strains at flange section decreased from web/flange intersection towards its two ends due to this effect. The shear-lag effects and equivalent flange width will be discussed in Chapter 7.

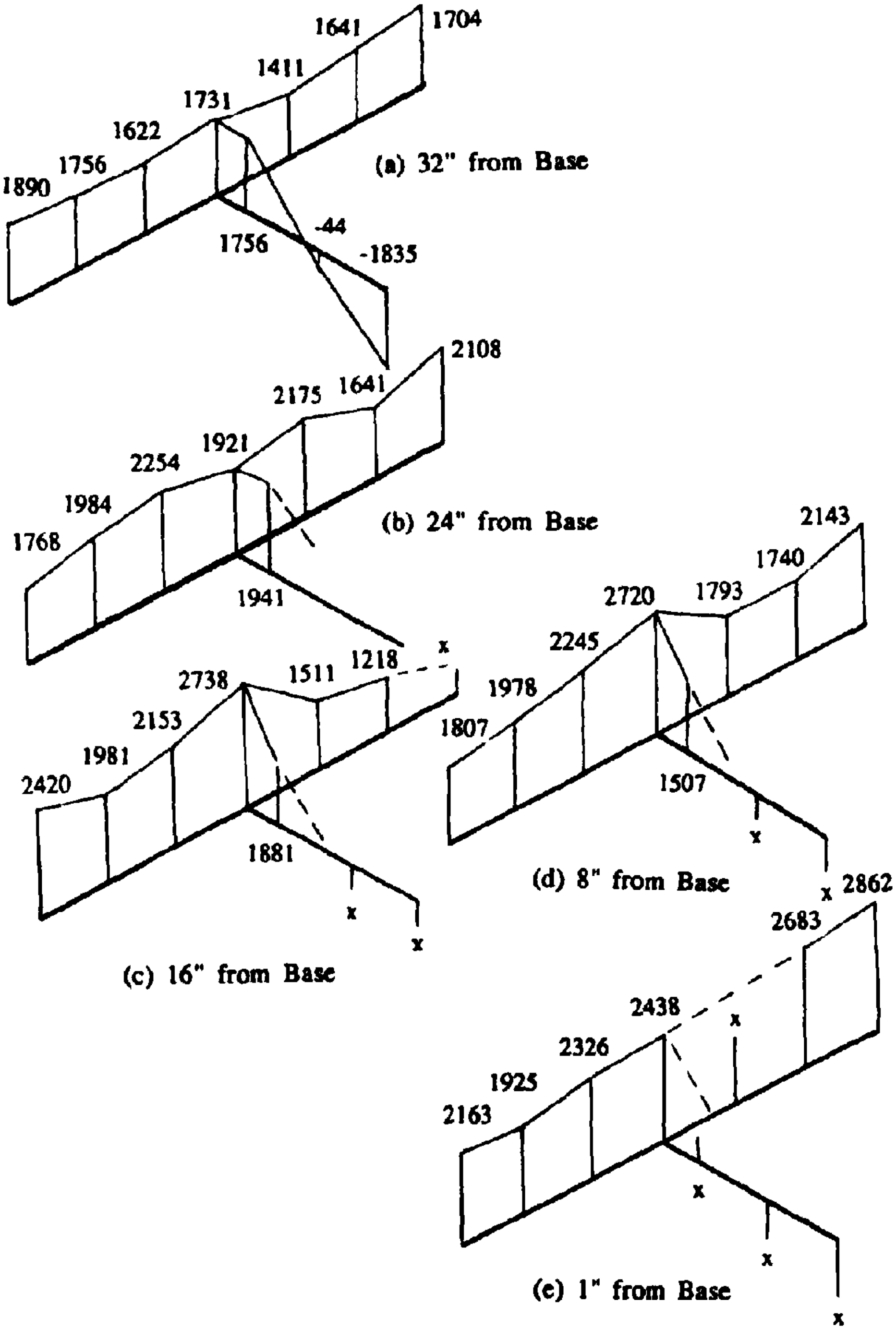

(a) 32" from Base

(b) 24" from Base

(c) 16" from Base

(d) 8" from Base

(e) 1" from Base

Fig. 5.12 Vertical Strain Distribution(mε), F1, WIC, $\Delta=\Delta_{max}$

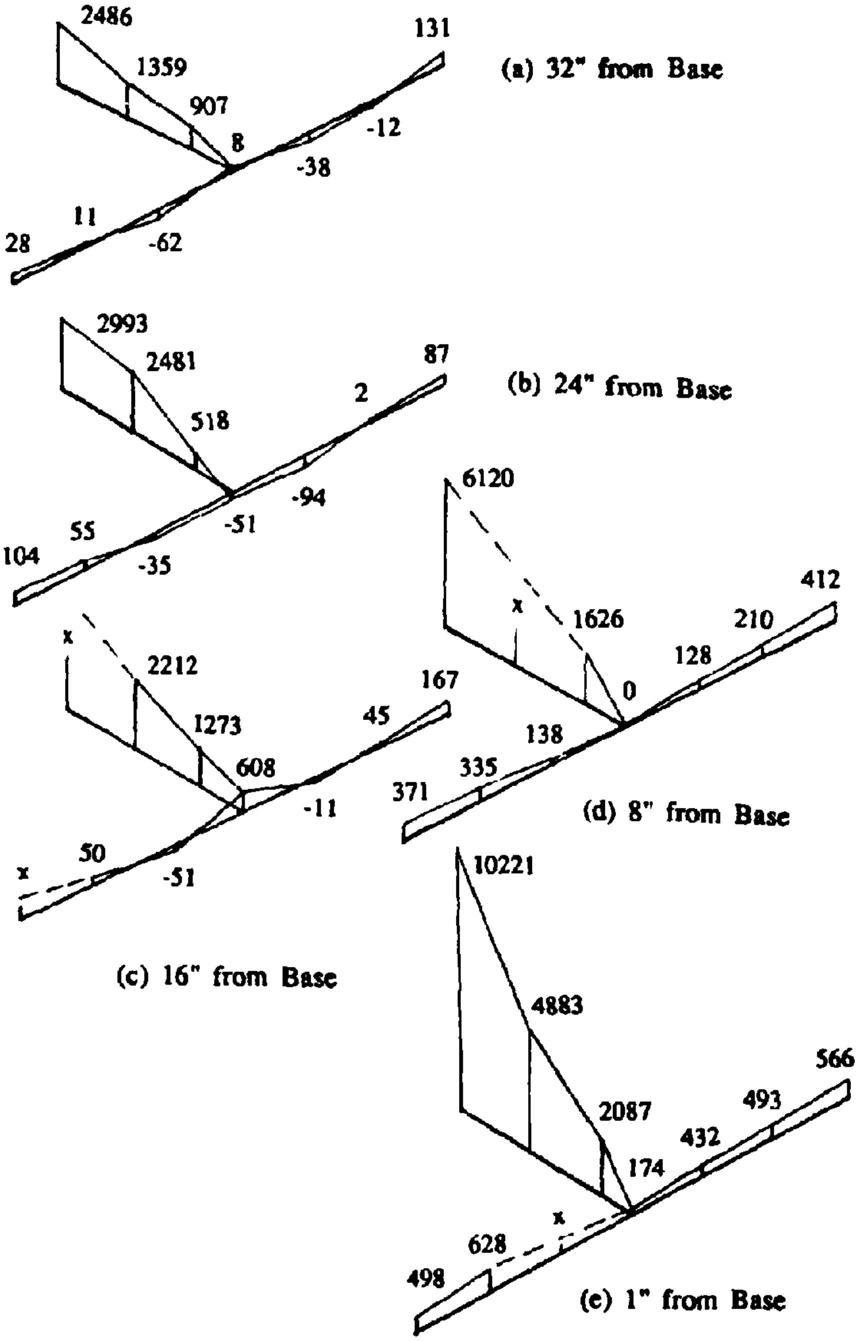

(a) 32" from Base

(b) 24" from Base

(c) 16" from Base

(d) 8" from Base

(e) 1" from Base

Fig. 5.13 Vertical Strain Distribution(mε), F1, FIC, μ =2

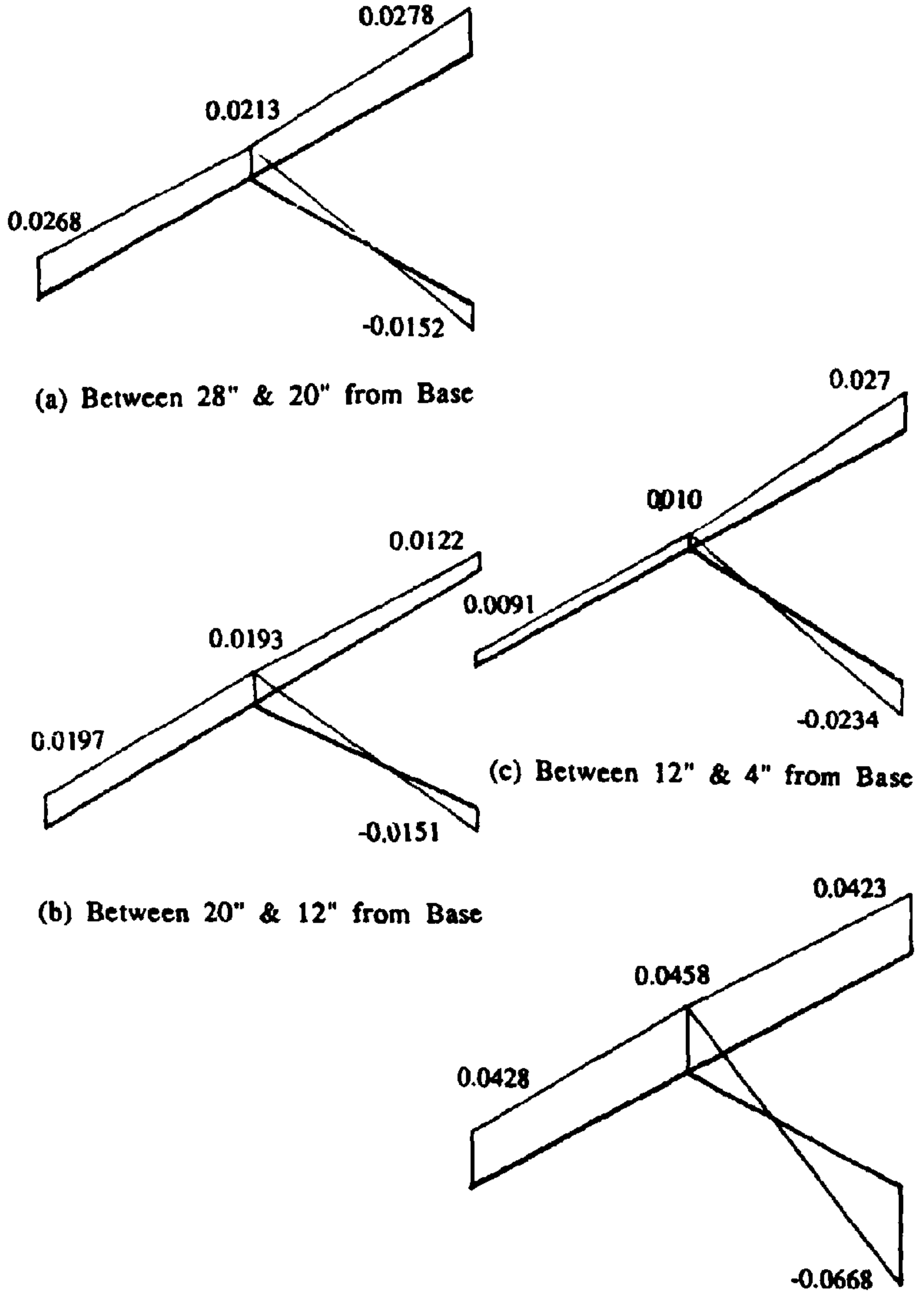

(a) Between 28" & 20" from Base

(b) Between 20" & 12" from Base

(c) Between 12" & 4" from Base

(d) Between 4" & 0" from Base

Fig. 5.14 Vertical Deformation of Masonry(in), F1, WIC, $\Delta=\Delta_{max}$

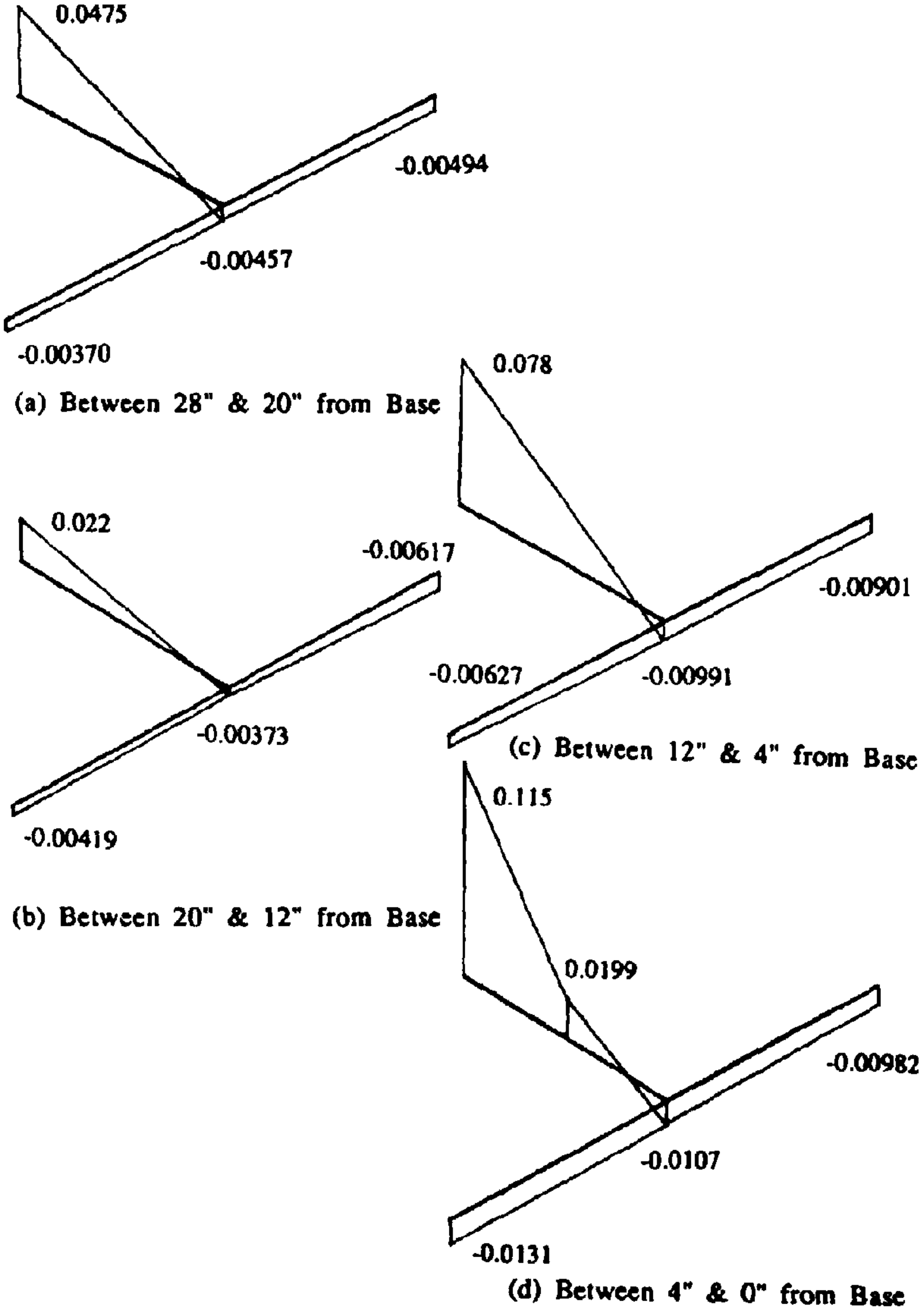

(a) Between 28" & 20" from Base

(b) Between 20" & 12" from Base

(c) Between 12" & 4" from Base

(d) Between 4" & 0" from Base

Fig. 5.15 Vertical Deformation of Masonry(in), F1, FIC, $\mu = 2$

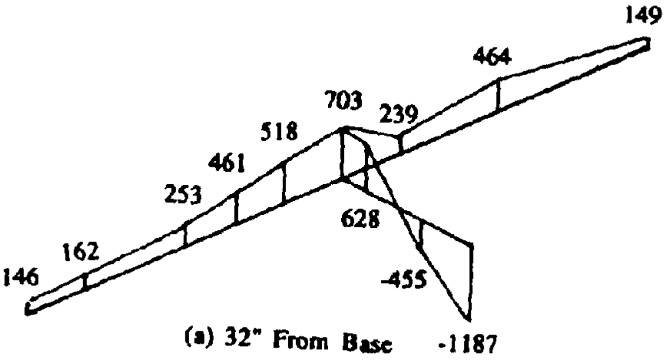

(a) 32" From Base

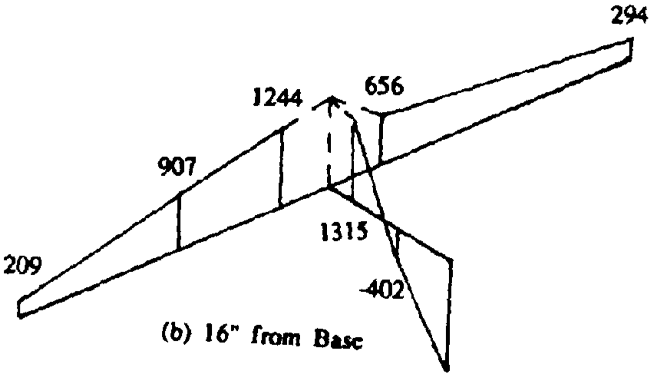

(b) 16" from Base

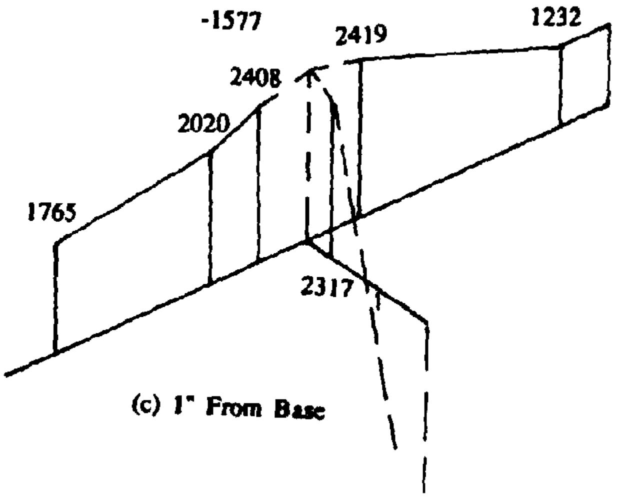

(c) 1" From Base

Fig. 5.16 Vertical Strain Distribution(mε), F3, WIC

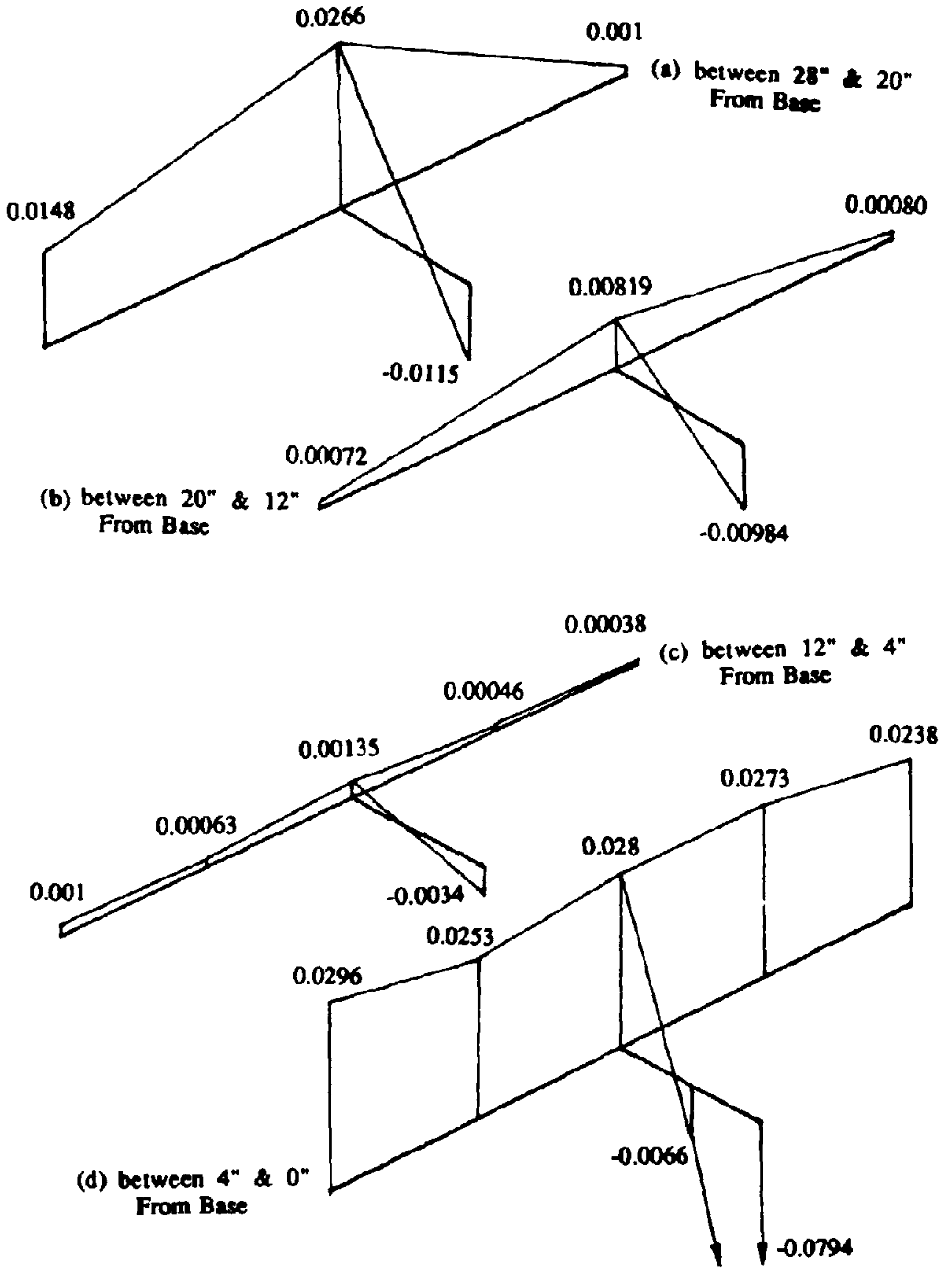

Fig. 5.17 Vertical Deformation of Masonry(in), F3, WIC

5.3.4 Influence of Shear on Response

(a) Strains on Horizontal Reinforcement

The strain distribution of horizontal reinforcement for wall F1 and F2 are show in Figs. 5.18 and 5.19 respectively. For each wall, three load levels, namely before shear cracking, intermediate and ultimate state were selected to show the variation of shear strain distribution at different loading stages. For wall F1, the three load levels were $P_w = 15$ kips, 49 kips and 63.4 kips respectively, and 12 kips, 37.5 kips and 50.8 kips for wall F2 correspondingly. Unfortunately shear strain of horizontal reinforcement for wall F3 and F4 could not be presented here due to excessive damage during construction and testing. From the above figures, the following features of shear strains can be found:

1. Before shear cracking, horizontal reinforcement was not mobilized, which can be proved by very low strains at this loading stage with both walls.

2. It is obvious from comparison between Figs. 5.18 and 5.19 that shear cracking with wall F1 is much more severe than with wall F2 due to its higher loading. This can also be confirmed by comparing the cracking patterns of wall F1 and wall F2 from Figs. 5.4 and 5.5.

3. To estimate the shear capacity of masonry, equation 5.1 was applied as

$$v = v_m + v_s \tag{5.1}$$

where v is the total shear force at the cross section, v_m and v_s are shear carried by masonry and horizontal reinforcement respectively, and

$$v_s = A_s f_y d/s \tag{5.2}$$

in which A_s, f_y and s are area, yield strength and vertical spacing of horizontal reinforcement , d is effective width of the web. The above values in this case are 0.2 in^2, 60 ksi, 8 inch and 38.8 inch respectively. Assuming the angle between shear cracking and horizontal axis to be 55 degree, results in that seven horizontal rebars will be crossed by one shear crack on average. Supposing that the shear crack cross from the 8th mortar bed at web/flange intersection (strain 1920 mε) down to the 2nd mortar bed at free end of the web (strain 346 mε), and estimating the unknowing strains by interpolating the measured strains, will result in the approximate shear carried by the horizontal reinforcement v_s = 42.2 kips. Since the total shear v = 63.4 kips, the shear carried by masonry v_m = 21.2 kips and the corresponding shear stress would be 88.5 psi. Using the same assumptions to wall F2, at the ultimate state, the shear carried by horizontal reinforcement would be 21.5 kips and the shear carried by masonry is given by v_m = 50.8-21.5 = 29.3 kips. In this case, the equivalent shear stress is 122.2 psi.

Since shear in the direction of flange in compression is never a problem, the measurement results and discussion will not be presented.

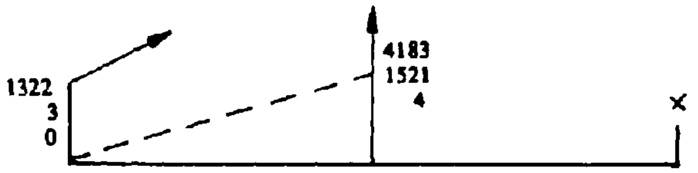

(a) 6'-8" From Base

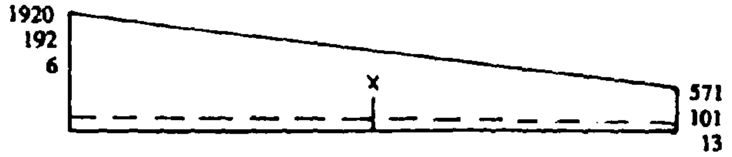

(b) 5'-4" From Base

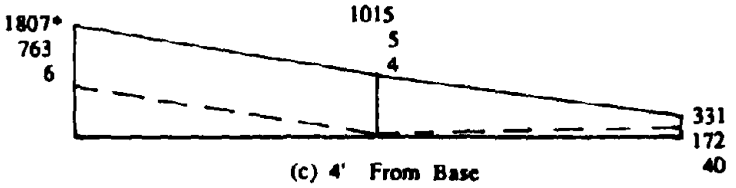

(c) 4' From Base

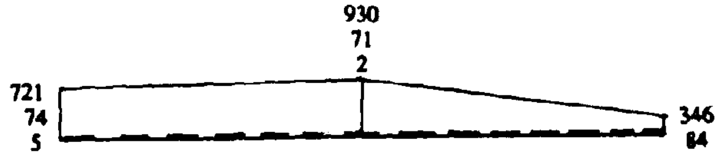

(d) 2'-8" From Base

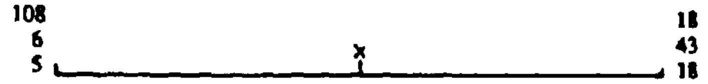

(e) 1'-4" From Base

30" From Free End 20" From Free End 10" From Free End

*: Three strains from top to bottom are corresponding to P_w = 15, 49 and 63.4 Kips respectively.

Fig. 5.18 Shear Strain distribution(mε), F1

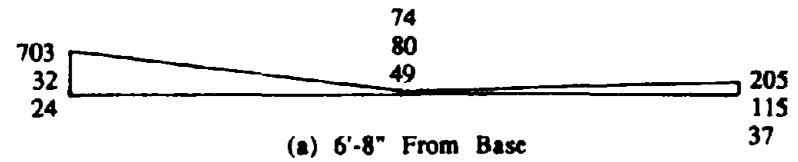

(a) 6'-8" From Base

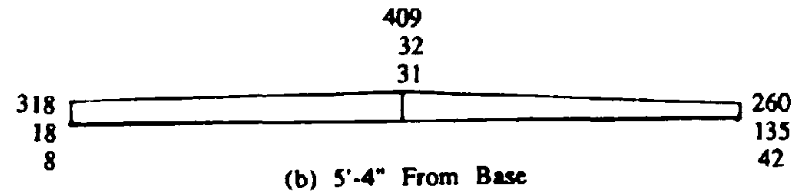

(b) 5'-4" From Base

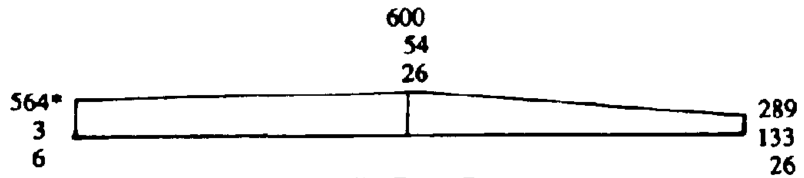

(c) 4' From Base

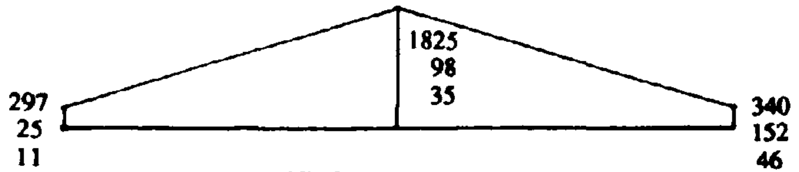

(d) 2'-8" From Base

(e) 1'-4" From Base

30" From Free End 20" From Free End 10" From Free End

*: Three strains from top to bottom are corresponding to P_w = 12, 37.5 and 50.8 Kips respectively.

Fig. 5.19 Shear Strain distribution(mε), F2

(b) Shear Deformation

Figs. 5.21 through 5.24 present the horizontal displacements of four walls at their maximum responses in the direction of web in compression. The four locations of displacement measurement were 12 feet (wall top), 8 feet ,4 feet and zero from the base respectively.

The horizontal displacement due to shear was derived by deducting the displacement caused by flexural deformation from the total displacement measured during testing. The displacement due to flexure was calculated as follows: From the vertical deformation of masonry surface measured with potentiometers at both sides of the web, the average curvature at bottom part of the wall can be derived as

$$\varphi_i = (\Delta_{1i} - \Delta_{2i}) / l\, h_i \qquad (5.3)$$

Assuming a liner curvature distribution from the calculated value at the highest position to the top of the wall, as shown in Fig. 5.20, the displacement at wall top can be estimated using the equation

$$\Delta = \varphi_n (H - \Sigma h_i)^2 / 3 + \Sigma\, \varphi_i h_i (H - \Sigma h_j - 0.5 h_i) \qquad (5.4)$$

where n is the number of total potentiometers at each side, i varies from 1 to n, while j varies from 1 to (i-1), and all other parameters are as shown in Fig. 5.20. The calculated results for four walls are presented in Figs. 5.21 though 5.24, from which it can be seen that the distribution of displacements due to flexural and shear deformation along the wall height is quite different. The displacement due to rotation increased with increase of the height faster than that due to shear deformation, and the combined total displacement is close to linear distribution along the wall height. It is also noted that displacement due to shear is not negligible , it can make up to 30% of the total displacement at the ultimate state for heavy reinforced flanged walls. Based on the gross section properties, the displacement due to shear will be 17% of the total displacement. For wall F2, the shear displacement was relative smaller because of its lower horizontal force resulted from less vertical reinforcement ratio.

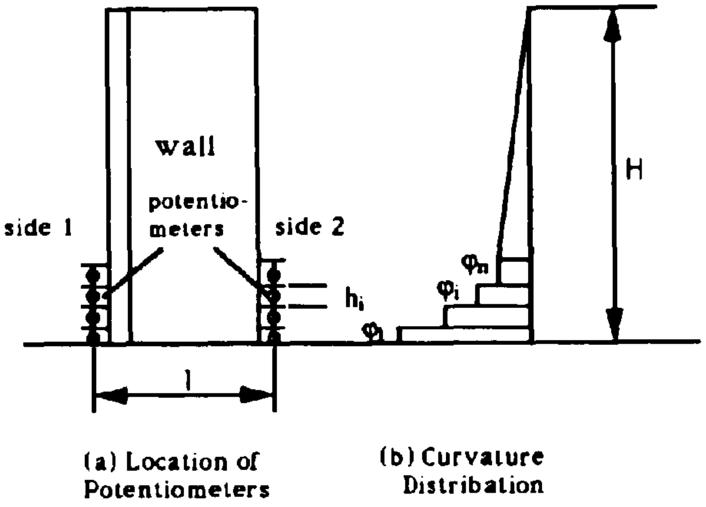

Fig. 5.20 Horizontal Displacement due to Rotation

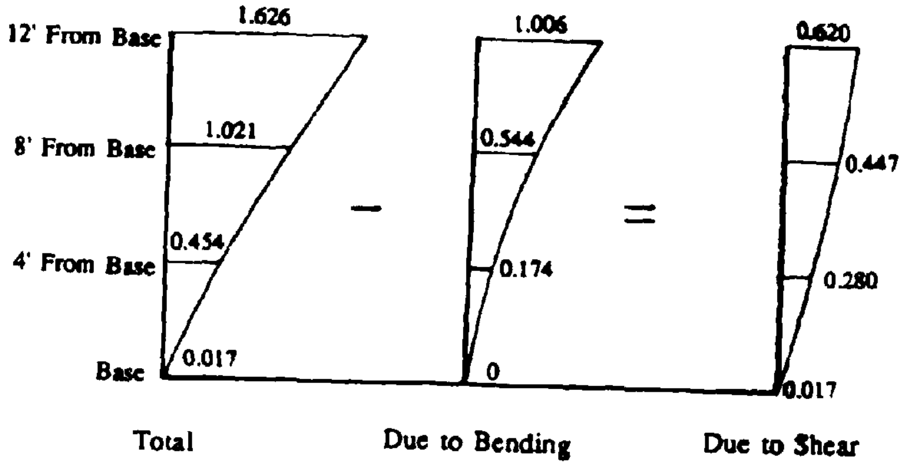

Fig. 5.21 Horizontal Displacement(in), F1

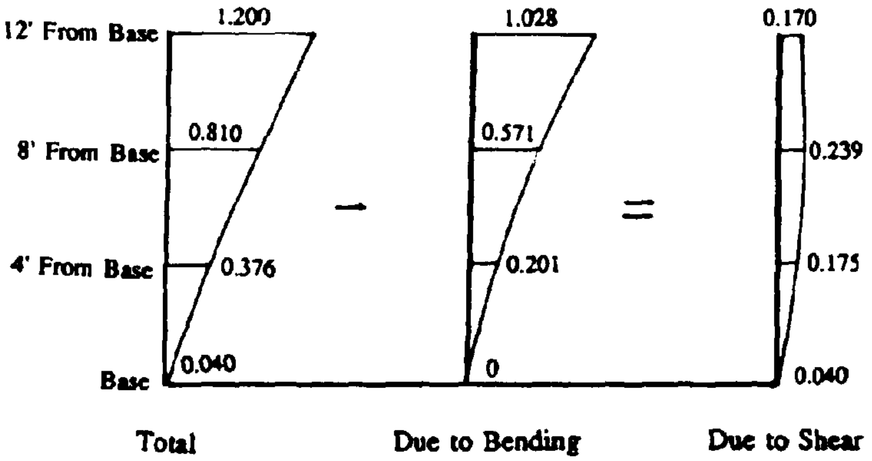

Fig. 5.22 Horizontal Displacement(in), F2

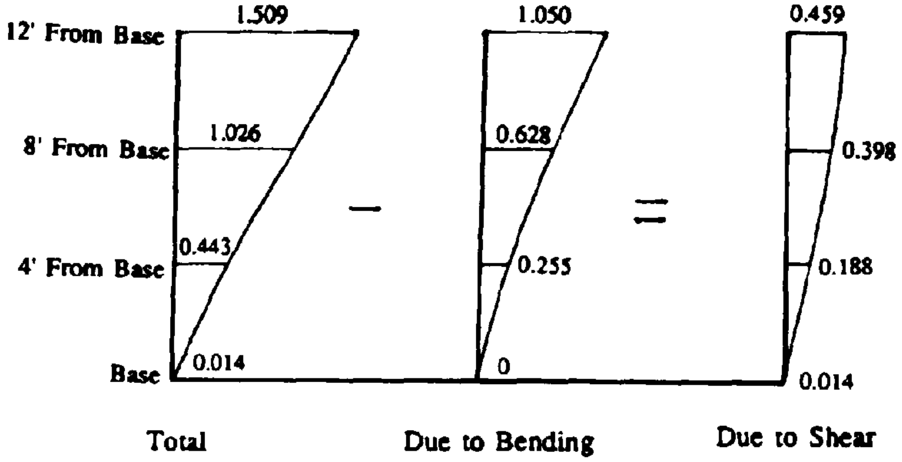

Fig. 5.23 Horizontal Displacement(in), F3

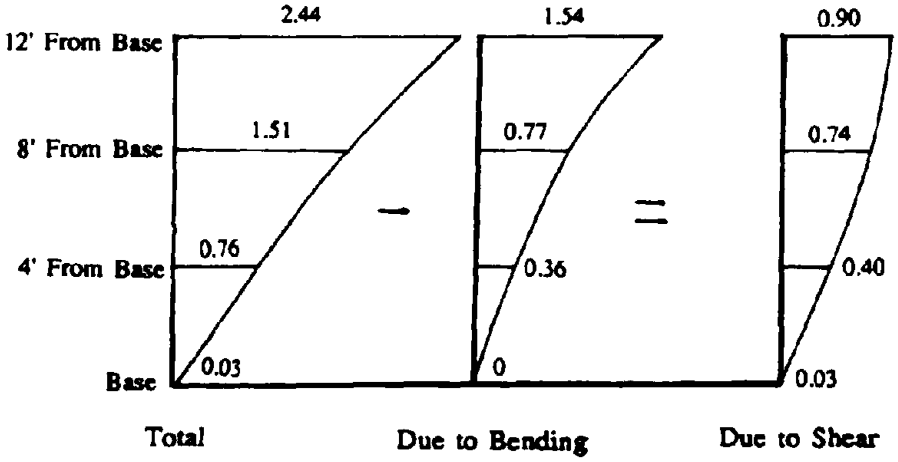

Fig. 5.24 Horizontal Displacement(in), F4

5.3.5 Material Properties Inferred From the Testing Results

Masonry Compression Strength

A estimate of masonry compression strength is possible by section analysis at the wall base at ultimate strength conditions. The linear potentiometers on the line of the web (see Fig. 5.1) allowed the position of the neutral axis, and the reinforcement strains, to be estimated at the wall base. Equilibrium of vertical forces enabled the masonry compression force C_m to be estimated from

$$C_m = \sum_{i=1}^{n} f_{si} A_{si} + P_v \tag{5.5}$$

where f_{si} is the stress (negative for compression) of bar i of area A_{si}, n is the number of vertical reinforcing bars and P_v is the total axial load at the wall base.

Assuming an equivalent rectangular stress block of average stress $0.85\ f'_{mt}$ and extent $a = 0.85\ c$ (c = length of compression zone), the masonry compression strength in the wall is given by

$$f'_{mw} = \frac{C_m}{0.7225\ t.c} \tag{5.6}$$

where t is the wall thickness.

For the direction of loading placing the web in compression, the depth of compression, c, was rather large, particularly for walls F1, F3 and F4. Hence f'_{mt} could be estimated with reasonable accuracy. As Table 5.1 shows, values showed considerable variation from both predicted and measured prism strengths from Table 4.2. In particular, the apparent difference in strength between walls F1 and F2 should be noted. The high strength for wall F2 must be viewed with some reserve, since the measured depth of the compression zone was small for this wall, and comparatively small errors in measurement of c will have large effects on computed $f'_{m\,w}$ values. It will be shown later that wall moment capacities predicted on the basis of inferred wall compression strengths agree much better with measured capacities than do those based on prism strengths.

Table 5.1 Material Properties (Ksi)

	F 1	F 2	F 3	F 4
f'_{mw}	2.35	3.51	2.81	3.14
f_t	0.32	0.30	0.20	0.26
E_m	2170	2440	1850	2270

Masonry Tensile Strength

When the walls were loaded with the flange in tension, the loads at which various flange cracks developed were rather precisely defined by the audible result of the release, as cracking occurred, of the considerable amount of strain energy stored in the wide flanges. The continuous records of load-deflection hysteresis loops also clearly identified the instant of cracking by a substantial drop in load without change in displacement. By computing the moment at the level where cracking occurred, it was a simple matter to back-calculate to find the corresponding tensile stress at the instant of cracking.

Table 5.1 shows The average values of f_t from 4 or 5 cracks developing at different levels of the wall, but exclude the base crack, where bond of the grout to the wall base, rather than grout tensile strength, governed behavior, and where the instant of crack formation was not well defined.

The values for tension strength in the wall are surprisingly high. It is clear that tension bond strength between mortar and concrete block must have contributed significantly to strength. It should be noted that the tabulated tension strength are based on the assumption that tension stress prior to cracking was uniform across the width of the wide flanges. In fact measurements indicated significant shear lag effects at early stages of loading. Thus the tabulated strengths are a lower bound on actual tension strength. It will be noted that wall F3, with the 16'- 8" wide flange, and hence the greatest shear lag effect, has the lowest apparent tension strength.

Elastic Modulus

A third material properly can be inferred from the test results. From observations of the wall lateral displacements at the early stages of loading before cracking occurred, the elastic uncracked stiffness, and hence modulus of elasticity can be inferred from the expression

$$E_m = K_i\left[\frac{H^3}{3I_g} + \frac{H}{0.4\,A_g}\right] \qquad (5.7)$$

where H is the wall height, K_i is the initial stiffness(lateral load divided by lateral displacement) and I_g and A_g are the moment of inertia and web area of the gross (uncracked) section respectively. Eqn. 5.7 assumes the shear modules is $0.4E_m$, and that shear lag effects are insignificant. As a result of the latter assumption, it should underestimate E_m, particularly for the extra-width flange F3. Inspection of Table 5.1 will show that F3 does indeed have an apparently low modules of elasticity (about 10% below the average for the other walls) and also that wall F2, which has a high apparent compression strength in the wall also has a high value for E_m. Related to the measured prism strength, a stiffness/strength ratio of $E_m = 1000\ f'_{mp}$ is a good average value. However, related to inferred strength in the wall a value of $E_m = 750\ f'_{mw}$ seems more appropriate.

It is should be noted that the value of modulus of elasticity E_m is essential for calculating the natural period of masonry structures, based on which the seismic load applied on the structures can be predicted. According to ACI code for masonry structures, for masonry with net area compression strength of $f'_m = 2500$ psi, the suggested modulus of elasticity is 2.2 to 2.4 10^6 psi, therefore the average value is $E_m = 920\ f'_m$ which coincides well with the test results as above. According to New Zealand code, for all masonry grades, the modulus of elasticity may be taken as 25 Gpa. Therefore for mid-strength of $f'_m = 20$ Mpa, $Em/f'_m = 1250$ which is much higher than the value from ACI code.

5.4 Discussion of Testing Results

Tables 5.2 and 5.3 summarize results from the experiments and analytical studies, for peak response in the two loading directions. Maximum predicted wall-base moments in the direction of the web in compression, based on two different assumed compression strengths are listed in rows 2 and 4 of Table 5.2. and may be compared with maximum experimental wall-base moments, listed in row 1. Moments M_{tp} in row 2 were based on an assumed ultimate compression strain of $\varepsilon_u = 0.003$, and masonry compression strength based on results of prism tests, as given in Table 4.2. It will be observed from the variations in the ratios of experiment to predicted value in row 3 that the agreement is not particularly good, particularly for wall F3. When masonry compression strength inferred from the strain distributions at the wall base (see Table 5.1) are used, the agreement between theory and experiment, as evidenced by the data of rows 4 and 5 is excellent.

Rows 6-8 of Table 5.2 summarize shear strengths of the walls. It will be seen that the maximum shear force (row 6) corresponding to flexural strength was, as expected, less than the shear strength capacity based on transverse reinforcement alone (that is, ignoring any contribution of masonry shear mechanisms). Although shear cracks of significant width developed in all walls, no distress occurred in shear, despite the high level of shear stress developed. For walls F3 and F4 this was close to 300 psi(2 MPa), and should be compared with maximum allowable shear stress permitted by the Uniform Building Code [1] of 75 psi (0.5 MPa) for wall of these proportions.

In the direction of the flange in compression, the masonry compression strength did not affect wall moment capacity significantly. The moments based on both prism test and inferred masonry compression strength were lower than the experimental results as shown from rows 9 to 13 in Table 5.2. The reason may be the effects of strain hardening of vertical reinforcement due to large deformation in this direction. It is obvious that shear strength can never be a problem in this loading direction as shown from rows 14 to 16.

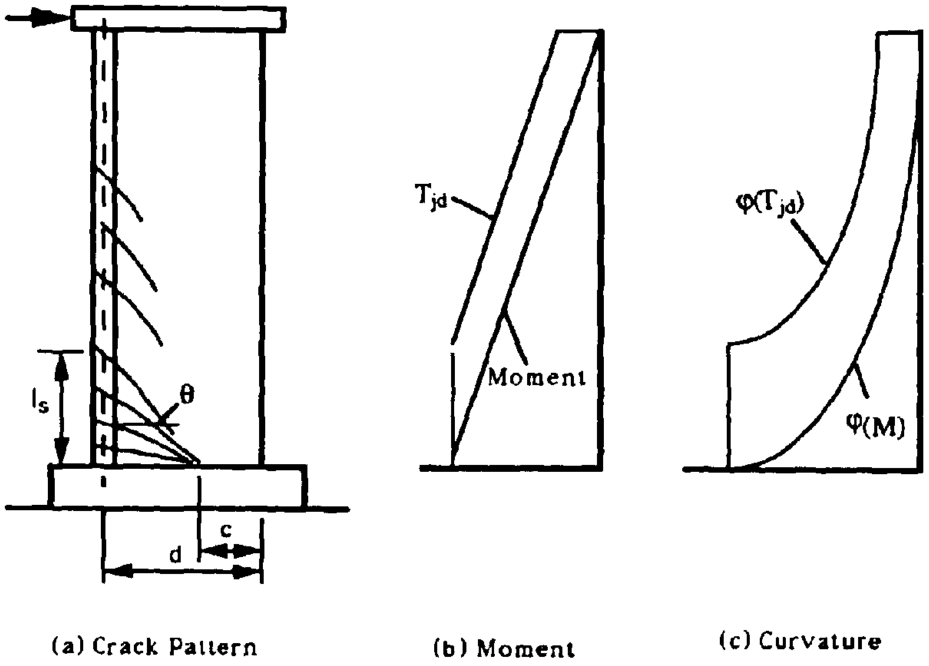

(a) Crack Pattern (b) Moment (c) Curvature

Fig. 5.25 "Tjd" Approach for Predicting Deflection

Table 5.2 Comparisons Between Analytical and Test Strength

	Row	Description	F1	F2	F3	F4
Web in Compression	1	M_{max} (experi.)	9130	7315	10150	10090
	2	M_{tp} (f_m' - prism strength)	9590	6830	7115	9215
	3	M_{max}/M_{tp}	0.95	1.07	1.43	1.10
	4	M_{tw}(f_m' = wall strength)	8930	7070	10080	10040
	5	M_{max}/M_{tw}	1.02	1.03	1.01	1.01
	6	V_{max} (experi.)	63.4	50.8	70.5	70.1
	7	V_{ts} (steel alone)	81.3	81.3	81.3	81.3
	8	v_{ts} -V_{ts}/(td) (Ksi)	0.264	0.212	0.294	0.292
Flange in Compression	9	M_{max} (experi.)	3686	2419	2952	3744
	10	M_{tp} (f_m'- prism strength)	3488	2128	2329	3360
	11	M_{max}/M_{tp}	1.06	1.14	1.27	1.11
	12	M_{tw}(f_m' = wall strength)	3457	2153	2437	3536
	13	M_{max}/M_{tw}	1.07	1.12	1.21	1.06
	14	V_{max} (experi.)	25.6	16.8	20.2	26.0
	15	V_{ts}(steel alone)	81.3	81.3	81.3	81.3
	16	v_{ts} -V_{ts}/(td) (Ksi)	0.107	0.070	0.084	0.108

*: Units: moment --- k-in. shear --- Kips.

Table 5.3 Comparisons Between Analytical and Test Displacement

	Row	Description	F1	F2	F3	F4
Web in Compression	1	Δ_{max} (experi.)	1.62	1.17	1.15	2.44
	2	Δ_f (experi.)	1.01	1.03	1.05	1.54
	3	Δ_v (experi.)	0.61	0.14	0.46	0.90
	4	Δ_{t1} (curvature integration)	0.60	0.61	0.57	0.71
	5	Δ_{t2} (plastic hinge method)	1.06	0.91	1.09	1.93
	6	Δ_{t3f} ("Tjd" approach)	1.11	1.28	1.05	2.28
	7	Δ_{t3v}	0.30	0.23	0.33	0.33
	8	$\Delta_{t3} = \Delta_{t3f} + \Delta_{t3v}$	1.41	1.51	1.38	2.60
	9	Δ_{max}/Δ_{t2}	1.53	1.29	1.39	1.27
	10	Δ_{max}/Δ_{t3}	1.15	0.77	1.09	0.94
*	11	Δ_{max} (experi.)	5.0	6.0	4.0	4.0
	12	Δ_{t2} (plastic hinge method)	5.86	4.75	9.17	5.86

*: Flange in Compression

*2: All units are in inch

Table 5.3 lists experimental and predicted displacements at ultimate conditions. Row 1-3 list the experimental displacement at maximum lateral load (Δ_{max}) and shear (Δ_v) components of Δ_{max} in the direction of the web in compression for the four walls. The flexural deformation Δ_f was found by integrating the measured curvature distribution up the wall, and the shear deformation was defined as $\Delta_v = \Delta_{max} - \Delta_f$, as mentioned earlier in this chapter.

Results from two commonly adopted methods for predicting ultimate displacements are listed in rows 4 and 5. Values in row 4 are obtained by integrating the theoretical curvature distribution up the wall, where the moment-curvature relationship is based on the plane-sections hypothesis. This ignores shear deformations and distortion to strain profiles across horizontal sections resulting from inclined flexure-shear cracking. Comparison of these values with experimental displacements Δ_{max} indicates poor correlation, with experimental deflections at least twice predicted values. If values from row 4, which do not include predicted shear deformation are compared with the flexural component of the experimental displacements (row 2), the agreement is still poor.

An alternative approach, which is often adopted to compensate in some part for the inadequacies of integrating the curvature distribution is to assume an elasto-plastic moment-curvature relationship. For base curvatures φ_b less than that corresponding to yield the displacement at the level of lateral load is based on an assumed linear curvature distribution up the wall. That is

$$\Delta_{t2} = \varphi_b \frac{H^2}{3} \qquad (5.8)$$

For base curvatures greater than the effective yield curvature φ_y, a plastic rotation

$$\theta_p = (\varphi_b - \varphi_y) L_p \qquad (5.9)$$

is calculated, where L_p is an equivalent plastic hinge length. The lateral displacement at the wall top is thus

$$\Delta_{t2} = \varphi_y \frac{H^2}{3} + (\varphi_b - \varphi_y) L_p (H - \frac{L_p}{2}) \qquad (510)$$

Different researchers advocate different effective plastic hinge lengths. The value adopted in this study is

$$L_p = 0.08H + 6d_b \qquad (5.11)$$

where H is the height of the wall and d_b is the diameter of the longitudinal reinforcement in the wall. Eqn. 5.11 was derived from experiments of concrete bridge piers [28] but is supported by analytical studies as being appropriate for shear walls. In equations 5.9 and 5.10, φ_b is based on ultimate compression strains of 0.003 and 0.008 for unconfined and confined masonry respectively. Results of deflections based on this approach, listed in row 5 are still much lower than the experimental maxima, but are in reasonably good agreement with observed flexural deformation.

A third approach is summarized in rows 6-8. In this method, the curvature distribution of method 1 (row 4) is modified to take account of the inclination of flexure shear cracking, as illustrated in Fig. 5.25.

Designers are familiar with the concept that steel stresses at the extreme rebar at some position on the wall (Fig. 5.25 (a)) are related to the moment at the root of the crack (Fig. 5.25 (b)). It follows that steel strains over a length l_s at the base of the wall should be essentially constant, where $l_s = (d - c)\tan\theta$ and d is effective depth to extreme tension rebar, c is depth of compression zone, and θ is the inclination of the flexure shear cracks to horizontal axis. A measure of support for this was provided from the steel strains recorded at different heights of the flanges which showed little reduction with height over the lower region (Figs. 5.12 and 5.13).

Designers account for the shift in steel strain by apportioning steel in accordance with a moment pattern, termed the T_{jd} diagram, that is displaced by an amount l_s, as shown in Fig. 5.25 (b). If this approach is valid, curvatures based on steel strains should also be displaced vertically, by an amount equal to l_s, as shown in Fig. 5.25 (c). Curvature distributions prior to yield based on this approach were used to predict flexural displacements in row 6 of Table 5.3. In addition, plastic rotations for the confined wall F4 were based on the measured maximum compression strain of 0.0144 rather than the conservative design value of 0.008. Since the deflections of row 6 still do not include shear deformation, an estimate for the latter, listed in row 7 was based on the equation.

$$\Delta_{t3v} = \frac{E_m}{\rho_t E_s} \frac{PH}{A_v G_m} \tag{5.12}$$

where P = lateral load, A_v = shear area (=web area), G_m = masonry shear modules = $0.4E_m$, and ρ_t = steel ratio for transverse reinforcement. Eqn. 5.11 effectively modifies the elastic uncracked-section shear deformation on the assumption that the transverse reinforcement provides the resistance to shear deformation after diagonal cracking develops. The total predicted deflection for the four walls are then listed in row 8.

Comparison of the predicted displacements from methods 2 and 3 with the observed displacements, listed as ratios in rows 9 and 10 indicate that the 'traditional' approach underestimates deflection by some 30-50% but the more refined method 3 provides a close estimate of behavior.

The predicted displacements in the direction of the flange in compression, based on the plastic hinge theory are listed in row 12 and the recorded experimental displacements are shown in row 11. Since the tests for all four walls stopped without failure in this loading direction, the comparison between these values is not proper. it seemed that the walls still had the ability to sustain horizontal loading without significant degradation of strength and stiffness, and the final displacements would exceed the predicted values. Theoretically, the behavior with the flange in compression is less sensitive to the width of flange or material properties, and more predictable than with the web in compression. Besides, no wall was found to fail in this direction due to its higher ductility capacity. The comparisons Between SCM and experimental results will be presented in Chapter 7.

5.5 Conclusions

Results from the experiments and analyses enable the following conclusions to be drawn:

1. The flanged masonry walls have unsymmetrical behavior in the two loading directions parallel to the web. In the direction of web in compression, walls had higher strength and stiffness, but much less ductility capacity than the opposite direction. Each wall failed in the direction of loading the web in compression and the failure was sudden and brittle, initiated by a compression failure of the web toe.

2. Hysteretic behavior of the walls was characterized by thin loops, particularly on repetitive loading to a given displacement level. After yielding in the direction of flange in compression, the half-loops in that direction became fatter indicating increased energy dissipation. Quantitative studies on dynamic hysteretic loops and energy dissipation rate to estimate the damping ratio will be presented in chapter 6.

3 Material properties inferred from wall response did not agree well with results of prism tests. Ultimate compression strains measured over the bottom 12 inch of wall greatly exceeded values suggested on the basis of prism tests. It appears that the foundation slab provided strong confinement to the bottom slab, and that the critical section should be considered to exist at the second or third mortar course.

4 Wall moment capacity based on inferred from measured neutral axis position compression strength was in excellent agreement with measured capacity.

5. Displacements due to shear were significant with the web in compression, contributing up to 30% to total deflection at the ultimate state, meanwhile based on gross section, shear displacement would be 17% of the total displacement.

6. Deflection calculations based on a modified elasto-plastic approach which acknowledge the spread of elastic strains caused by diagonal flexure shear cracking, agreed well with experimental values. This approach is simple enough to use as a design approach, and was incorporative in modifying the hysteretic model developed in Chapter 3.

7. The vertical reinforcement ratio affects the response of flanged masonry walls significantly in both directions. With the increase of reinforcement ratio(wall F1 vs. wall F2), the moment capacity and equivalent stiffness increases, but the ductility capacity will decrease, especially in the direction of the web in compression.

8. Flange width has significant effects on the behavior in the direction of the web in compression, i.e. with increasing the flange width, the wall has higher moment capacity and stiffness, but less displacement ductility(wall F3 vs. wall F2). In the direction of flange in compression, the influence of the flange can be ignored.

9. Confining steel plates on mortar beds at the web toe improves the response in the direction of the web in compression substantially. It increases the displacement ductility and improves the falling branch after the maximum response.

6. EXPERIMENTAL STUDIES, PART 2---DYNAMIC TESTS

6.1 Introduction

The second phase of the experimental studies on the seismic behavior of flanged masonry walls, consisted of tests of 5 full scale flanged masonry walls subjected to dynamic loading on a large shake table. The pseudo-static load tests on flanged masonry structural walls presented in the previous chapter confirmed expected performance, including asymmetric force/deformation characteristics, and a brittle failure mode involving compression failure of the web toe.

Although static testing facilitates detailed observation of experimental response during testing, it cannot create a realistic seismic environment to examine the response of structures to earthquake attacks because of the loading rate. As a continuing program, the purpose of these dynamic tests was to investigate the following aspects.

- Examine the behavior of flanged walls under dynamic excitation.

- Check the comparative performance of identical flanged walls subjected to static and dynamic loading.

- Investigate the effects of vertical reinforcement ratio, confining plates on mortar beds at web toe on seismic response of flanged masonry walls.

facilities consist of a single degree of freedom shake table with its control system and a high speed data acquisition system.

The shake table stands about 4 feet (1.22 m) high with a deck of 10 ft. x 16 ft. (3.05 m x 4.88 m) in plan dimensions (see Fig. 6.1). The actuator of the table has a maximum driving force of 100 kips (445 KN) and a total dynamic stroke of 12 inch (305 mm). The control system houses the electronics for the servo-loop control of the test. The system can be operated in displacement control with an external command signal provided from a Compaq Deskpro 286 computer equipped with a Metrabyte DAS-20 I/O analog/digital expansion board. At present, the displacement control histories can be one of the following:

- earthquake records or 'customized records'
- soft-start soft-stop sinusoidal waves
- standard sinusoidal waves

The data acquisition system is composed of an Apple Macintosh II computer equipped with a National Instruments NB-M30-16H-9 12-bit A/D converter board. The system allows the scanning of up to 128 channels at a data sampling rate of 100 KHz.

As with the walls for pseudo-static tests, electric resistance strain gauges (81 in total) were placed on both vertical and horizontal reinforcement to investigate shear lag effects in vertical reinforcement and shear forces carried by transverse reinforcement in the web. Masonry strains in the lower region of the wall were monitored with linear potentiometers attached to steel studs epoxied into holes drilled in the masonry. A further linear potentiometer was orientated in the horizontal position to monitor slippage of the wall on the base. Other instrumentation included measurement of gross top-of-the-wall deformations relative to the base. Three linear potentiometers monitored wall horizontal displacements at the line of 12 feet (center of the top mass), 8 feet and 4 feet above the base respectively. Another 2 gauges monitored vertical movement of the wall. All positions of the instrumentation were the same as for the static tests, and can be found in Figs. 4.2 and 5.1.

In addition to the above, 6 accelerometers were installed to monitor the input and response accelerations. Two of the accelerometers were oriented horizontally, A2 at base level and A1 at the center of the top mass. The remaining 4 accelerometers were installed vertically, with A3 and A4 at the base level (spacing 5 feet) and A5 and A6 at the level of the top mass center (one at each side) to measure the rotation of both base and the top mass during the testing (Fig. 6.1).

Since wall F9 was positioned at a 45 degree skew to the axis of the shake table, three horizontal oriented gauges monitored the displacements only in the web plane. Accelerometers were arranged to measure the horizontal input along the table axis at the base level and horizontal translation response acceleration in the plane of the web at the top; response rotations in the horizontal plane and in the plane of the web at the top respectively. To measure these rotations, four accelerometers were attached to the sides of the top concrete inertia masses at 12 feet (3.66 m) high from the base with two accelerometers on each side.

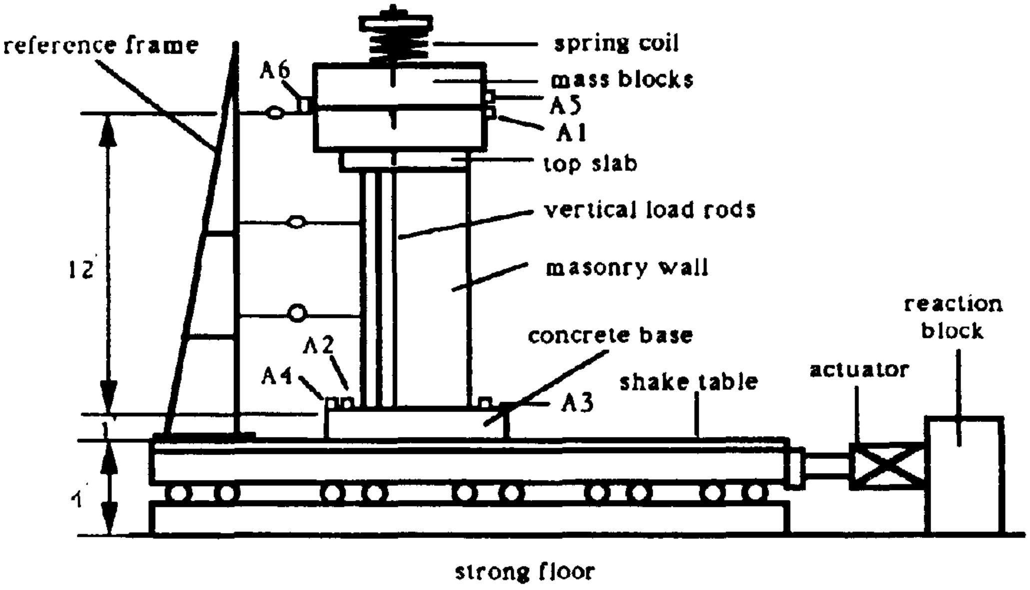

Fig. 6.1 Dynamic Test Facilities and Instrumentation

6.3 Vertical Loading and Test Procedure

6.3.1 Vertical Loading

Since adjustment of vertical load during testing was not feasible, a special system of vertical load application was designed for the dynamic experiments and also adopted for the pseudo-static tests in order to allow comparison of results between the two tests. The load was applied by four 5/8" Dwidag bars anchored at the bottom of the base and stressed against the top slab of the wall, through 4 stiff coil springs (one for each bar). The flexibility of the springs ensured that the axial force maintained the required value as the wall displaced laterally and vertically (refer to section 5.1). Measurements taken during the wall tests showed that the system worked well and the maximum variation of vertical loads was less than 8%. The level of applied axial force was chosen to provide an essentially uniform stress of 100 psi (0.70 Mpa) at the base of the wall. Thus the resultant of the vertical forces coincided with the geometric centroid of the wall sections. Considering the top mass and self-weight of the wall, the applied axial compression force for each bar was 12.35 kips (54.9 KN).

6.3.2 Mass-spring System

To ensure that the specimen would respond adequately to the base excitation, two concrete blocks (each weighing approximately 5 tons) were made to simulate tributary building mass. The blocks were identical with dimensions of 8'-8" x 6' x 1'-4" (2.64 m x 1.83 m x 0.41 m = length x width x height). There were two reasons for casting two blocks instead of one: the capacity of the travelling crane in the lab, and the intent that they may be used separately for subsequent tests. The total concentrated mass at the wall top, including these two blocks and top concrete slab was 23.3 kips, plus one third of wall self weight (2.5 kips), the resulted equivalent mass at the wall top was 25.8 kips.

The blocks were mounted on the top of the wall in such a way that the center of the total top mass was 12 feet (3.66 m) high from the base and coincided with the geometric centroid of the wall sections horizontally to ensure that their mass would produce uniform gravity at cross sections of flanged walls. The test system with a flanged wall on the shake table is shown in Fig. 6.2.

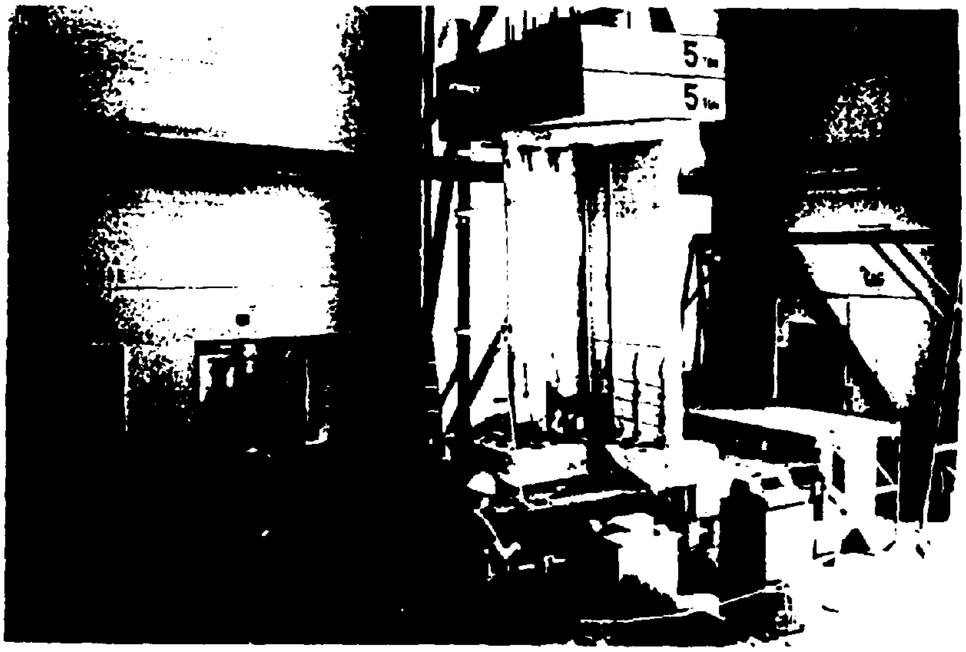

Fig. 6.2 A Flanged Wall on Shake Table During Testing

6.3.3 Test Procedure

The loading sequence for the first three walls (F5, F6 and F7) consisted of the following two phases:

- **Sinusoidal input test:** The excitation was chosen as 5 complete cycles of sinusoidal table displacement with frequency f = 5 Hz.

The first two runs used very small amplitude input to check the natural frequency of the wall before cracking, then the amplitude of the input was gradually increased until the vertical reinforcements in the flange was close to yield in tension.

- **Earthquake record input test:** The earthquake record used was El Centro 1940 N-S. Since the maximum acceleration recorded is about o.3g which is not strong enough to cause damage to the test units, a reduced time factor of 0.25 was applied to increase the intensity of the input. It is well known that theoretically, for a undamped harmonic vibration,

$$v = v_0 \sin (\omega t + \theta_0) \qquad (6.1)$$

the relationship between acceleration and amplitude can be expressed as

$$\ddot{v} = -\omega^2 v_0 \sin (\omega t + \theta_0) = -\omega^2 v \qquad (6.2)$$

where v_0, ω and θ_0 are the amplitude, circular frequency and initial phase of the vibration respectively. Equation (6.2) indicates that the acceleration is proportional to second order of its amplitude. For a earthquake input, the relationship may not be so simple because of the effects of damping and excitation with different frequencies. But using a reduced time factor will certainly increase the frequencies and therefore the intensity of the earthquake input. With a time factor 0.25, the running time for the shake table with El Centro earthquake record during each test was about 8.5 seconds.

Also a displacement (amplitude) factor was used to adjust the intensity of earthquake input for different tests. From equation (6.2), for a undamped vibration, the acceleration is proportion to its amplitude. Again, for earthquake input, the relationship may not be exactly proportional to each other due to effects mentioned above, but should be very close to it. The displacement (amplitude) factor for the first run was chosen in such a way so that it would produce the same level of acceleration at the base as for the last run of sinusoidal input. The displacement factor was gradually increased until the wall reached its maximum response and finally failed.

It should be mentioned that to estimate the difference of natural frequency between on ground and on shake table, wall F5 was tested on strong floor before moving onto the shake table. The method was very simple. First, tieing down the wall base onto the strong floor with Dwidag post-tensioning bars , then connecting the wall top to a fixed strong frame with a steel wire and tensioning the wire to give a small displacement at the wall top (make sure it will not cause any cracking on the wall). Finally, suddenly releasing the wall by cutting off the wire, the wall was in free vibration and natural frequency and damping ratio can be measured. Discussion of the test results will be presented later in this chapter.

Data was recorded at 200 scans/sec. during the entire experiment. The record time was 3 sec. for sinusoidal tests and 10 sec. for earthquake input tests. A typical testing procedure for wall F5 is listed in Table 6.1. For wall F8, only two runs were applied. First, as with the previous walls, a very small amplitude sinusoidal input was used to check the natural frequency and test facilities. Then, a input of El Centro 1940 N-S earthquake record with a time factor = 0.25 and displacement factor = -1.0 which produced the maximum response for wall F5, was applied to investigate the effects of loading history. For wall F9, a similar test procedure to wall F5 was used, but the wall itself was positioned with 45 degree skew to the table axis for a preliminary study on behavior of flanged masonry walls under arbitrary earthquake attacks.

Table 6.1 Test Procedure for Wall F5

	Run No.	Input		Table Run Time(sec.)	Data Acq. Time(sec.)	Comments
		Dm (in)	Am (g)			
Sinusoidal f = 5 Hz	1	0.02	0.051	1.0	3.0	For checking natural freq.
	2	0.02	0.051	1.0	3.0	
	3	0.05	0.128	1.0	3.0	
	4	0.10	0.256	1.0	3.0	
	5	0.10	0.256	1.0	3.0	Visible cracking in FIC
	6	0.20	0.510	1.0	3.0	Yielding in FIC
	7	0.35	0.890	1.0	3.0	Severe cracking in WIC
	8	0.35	0.890	1.0	3.0	Shear cracking in WIC
El Centro 1940 N-S	9	0.25	0.25	8.5	10	
	10	0.25	0.50	8.5	10	
	11	0.25	-0.50	8.5	10	
	12	0.25	-0.75	8.5	10	
	13	0.25	-1.00	8.5	10	Max. response in WIC
	14	0.25	1.00	8.5	10	Wall failed in WIC
	15	0.25	1.00	8.5	10	Wall collapsed in WIC
		f_t (Time factor)	f_d (Disp. factor)			
		Input				

FIC: loading direction of flange in compression
WIC: loading direction of web in compression

6.4 Test Results and Observations

6.4.1 General Behavior Observed

The details observed during tests for all 5 flanged masonry walls are summarized below and following abbreviations are used for the description:

WIC: Direction of loading placing the web in compression

FIC: Direction of loading placing the flange in compression

D: Amplitude of sinusoidal input for the shake table

A: Acceleration of sinusoidal input for the shake table

f_d: displacement factor, i.e. peak displacement ratio of shake table vs. the earthquake record

A_w: Peak response acceleration with WIC

D_w: Peak response displacement with WIC

A_f: Peak response acceleration with FIC

D_f: Peak response displacement with FIC

<u>Wall F5 (#6 Vertical Reinforcement, Identical to F1)</u>

<u>Pretest on Ground</u>

The test method was as mentioned in the previous section, The measured natural frequency was 9 Hz and the damping ratio was 0.02.

<u>Tests with Sinusoidal Input (f = 5 Hz)</u>

The natural frequency 7.2 was measured during the first two runs with D = 0.05 inch and no cracking was found after the tests.

In the direction of the flange in compression (FIC), minor cracking at the web base mortar bed was first noted with D = 0.1 inch (A = 0.26 g), the maximum responses D_f = 0.17 inch and A_f = 0.51 g were measured. With D = 0.2 inch (A = 0.51 g), the crack at the base expanded to the whole cross section of the web and minor cracks at the 2nd, 3rd, 4th and 6th mortar beds in the web formed. The maximum responses D_f = 0.52 inch and A_f = 0.85 g were recorded.

During first run with D = 0.35 inch (A = 0.89 g), the above cracks expanded and a new crack at 8th mortar bed developed. Shear cracking in the web was first noted during second run with D = 0.35 inch, the corresponding responses were D_f = 0.96 inch and A_f = 0.98 g.

In the opposite direction (WIC), a minor crack about 20 inch long formed in the central part of base mortar bed in the flange with D = 0.35 inch. The maximum responses D_w = 0.44 inch and A_w = 1.62 g were recorded.

Tests with El Centro Record (Time Factor 0.25)

During run #9 (f_d = 0.25) through run # 12 (f_d = -0.75), no new cracks were observed. With f_d = -1.0 (run # 13), vertical cracking at the web toe developed and severe shear cracks formed in the web with WIC. The wall reached its maximum ultimate strength in this direction. Then, the strength and stiffness began to degradate during the following runs (#14 and #15, f_d = 1.0), and the wall finally collapsed with WIC resulted from sudden crashing of the bottom three masonry courses at the web toe. The wall inclined in the direction of the web in compression and was held by the safety strips from the top. the recorded maximum responses were D_w = 1.35 inch and A_w = 2.48 g. But in the opposite direction, the wall could sustain the horizontal deformation without significant strength and stiffness degradation. Comparing with static tests, cracking during dynamic tests was less developed, i.e. the number of cracks was less and they expanded slower. The cracking pattern and failure mode after testing are presented in Fig. 6.3 (a) and (b) respectively.

Wall F6 (#4 Vertical Reinforcement, Identical to F2)

Tests with Sinusoidal Input (f = 5 Hz)

The natural frequency measured on the shake table was f = 6.9 Hz during the first two runs with D = 0.05 inch.

Minor cracking at the web base mortar bed was observed with FIC during run #4 (D = 0.1 inch, A = 0.26 g). With D = 0.2 inch (A = 0.51 g), the crack at the base expanded to the whole cross section of the web and a new crack formed at the 2nd mortar bed in the web. The 3rd mortar bed cracked with D = 0.3 inch (A = 0.76 g), the maximum responses D_f = 0.88 inch and A_f = 0.58 g were recorded.

In the direction of the flange in compression (WIC), first crack at base mortar bed in the flange developed during last run of sinusoidal input (D = 0.35 inch). The measured maximum responses D_w = 0.25 inch and A_w = 1.03 g.

Tests with El Centro Record (Time Factor 0.25)

In the direction of the flange in compression (FIC), cracking at 4th mortar bed of the web developed with $f_d = 0.25$. The maximum response $D_f = 0.96$ inch and $A_f = 0.55$ g were recorded. The 7th mortar bed cracked with $f_d = -0.5$, and maximum responses were $D_f = 2.85$ inch and $A_f = 0.70$ g.

In the direction of the web in compression (WIC), the 2nd and 4th mortar beds in the flange cracked with $f_d = -0.25$ and $f_d = -0.375$ respectively. With $f_d = -0.5$, cracking at 7th mortar bed developed and the corresponding responses were $D_w = 0.78$ inch and $A_w = 1.80$ g. During run #12 ($f_d = -0.75$), 6th mortar bed cracked , two shear cracks formed in the web, and vertical cracks at bottom three masonry courses of the web toe also developed. The wall reached its maximum ultimate strength with $D_w = 1.02$ inch and $A_w = 1.90$ g in this direction. Then, the strength and stiffness began to degradate during the last run (#13, $f_d = 0.75$), the bottom three masonry courses at the web toe crashed and the wall collapsed in this direction. But in the opposite direction, the wall could sustain the horizontal deformation without significant strength and stiffness degradation. The cracking pattern and failure mode after the tests are presented in Fig. 6.4 (a) and (b) respectively.

Wall F7 (#6 Vertical Reinforcement, Confined, Identical to F4)

Tests with Sinusoidal Input (f = 5 Hz)

The measured natural frequency of the system during the first two runs was f = 7.0 Hz.

Responses in the direction of the flange in compression (FIC): the base, 3rd and 4th mortar beds in the web cracked with $D = 0.2$ inch ($A = 0.51$ g). Cracks developed at 2nd and 5th mortar beds when $D = 0.35$ inch($A = 0.89$ g), the maximum responses were $D_f = 0.88$ inch and $A_f = 0.94$ g which were very close to the test result of wall F5.

In the opposite direction (WIC), cracking at base mortar bed in the flange formed during the last run of sinusoidal input($D = 0.35$ inch). The maximum responses $D_w = 0.40$ inch and $A_w = 1.58$ g were recorded which were also very close to the test result of wall F5.

Tests with El Centro Record (Time Factor 0.25)

In the direction of the flange in compression (FIC), no new cracks formed during the first several runs. During run # 12 ($f_d = -1.0$), flexural cracks at the 8th, 9th, 10th and 11th mortar beds developed simultaneously.

With WIC, the crack at the base expanded to whole cross section of the flange during the first run with El Centro record ($f_d = 0.25$). When f_d reached 0.5, five minor diagonal cracks formed in the web. During run #11 ($f_d = -0.75$), two major shear cracks in the web developed and vertical cracking at the web toe was found. Also flexural cracks formed at the 2nd, 3rd and 6th mortar beds in the flange.

When f_d reached -1.0, new flexural cracks formed at the 9th and 10th mortar beds in the flange, three major shear cracks formed in the web and two vertical cracks developed at the web toe. The wall reached its maximum ultimate strength in this direction with $D_w = 1.60$ inch and

A_w = 2.75 g. which were slightly larger than the test result of wall F5. Then, the strength and stiffness began to degradate during the next two runs (#13 and #14, f_d = 1.0), and the wall finally collapsed due to sudden crashing of the bottom masonry courses at the web toe. But the wall could still sustain the horizontal deformation without significant strength and stiffness degradation. Fig. 6.5 (a) and (b) show the cracking pattern and failure mode after the tests.

Wall F8 (#6 Vertical Reinforcement, Identical to F5)

Tests with Sinusoidal Input (f = 5 Hz)

The natural frequency measured on the shake table was f = 6.9 Hz and no cracking was found afterwards.

Test with El Centro Record (Time Factor 0.25)

El Centro earthquake record with f_d = -1.0 was applied to the shake table which was the same as the input when wall F5 reached its maximum response in the direction of the web in compression.

During the test, cracks at the bottom 4 mortar beds of the web widely opened in the direction of the flange in compression. In the opposite direction, bottom 4 mortar beds in the flange cracked and vertical cracking at web toe formed. With increasing the deformation, the masonry face shell at web toe began to spall and suddenly the bottom 4 masonry courses crashed, resulting in collapse of the wall in this direction. The maximum responses recorded were D_w = 1.35 inch and A_w = 2.40 g. which were very close to the maximum response of wall F5. Fig.

6.6 (a) and (b) present the cracking pattern in the flange and failure mode after the tests.

Wall F9 (#6 vertical Reinforcement, Identical to F5)

Tests with Sinusoidal Input (f = 5 Hz)

During first run (D = 0.05 inch), rotation of the top concrete blocks was obvious. With D = 0.1 inch, minor cracking at base mortar bed of the web formed. when D reached 0.2 inch, more cracks in the web developed and minor flexural cracking at base mortar bed in the flange toe was observed. Inclined cracks also formed in the web. The maximum responses were D_w = 0.31 in. , A_w =1.0 g and D_f = 044 in., A_f = 0.69 g.

During run #4 (D = 0.4 inch, A = 1.02 g), flexural cracks at mid-height of the web developed. The maximum responses D_w = 0.43 in. , A_w =1.34g and D_f = 0.75 inch, A_f = 0.85 g were recorded.

Tests with El Centro Record (Time Factor 0.25)

During first run with earthquake record (f_d = -0.5), more shear cracks in the web were observed and more flexural and shear cracks in the flange also developed. The maximum responses at this stage were D_w = 0.88 inch , A_w =1.79g and D_f = 1.64 inch, A_f = 0.94 g. When f_d reached -0.75, vertical cracks at the web toe formed with maximum responses D_w = 1.51 inch , A_w =1.92g and D_f = 2.42 inch, A_f = 0.96 g.

During run #7 (f_d = -1.0), severe vertical cracks formed at the web toe and masonry face shell began to spall. It is obvious that the wall would collapse in the direction of the web in compression. Then, the test stopped due to the safety consideration. The crack patterns in the web and flange are presented in Fig. 6.7 (a) and (b) respectively.

(a) Cracking Pattern, before Failure

(b) Toe Crushing, at End of Test

Fig. 6.3 Condition at Different Stages of Testing, Wall F5

(a) Cracking Pattern, before Failure

(b) Toe Crushing, at End of Test

Fig. 6.4 Condition at Different Stages of Testing, Wall F6

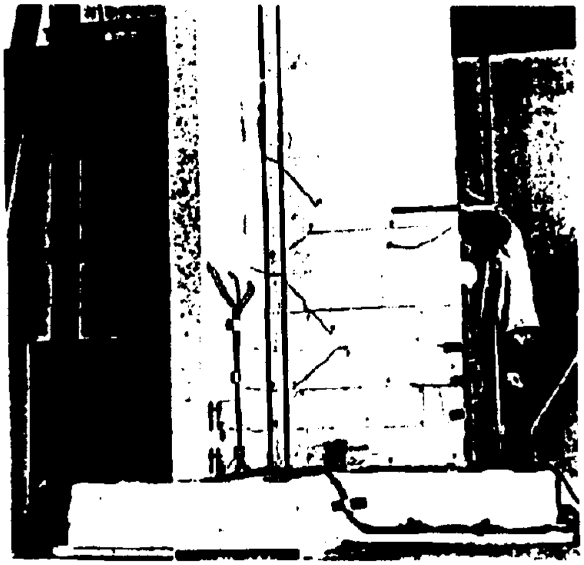

(a) Cracking Pattern, before Failure

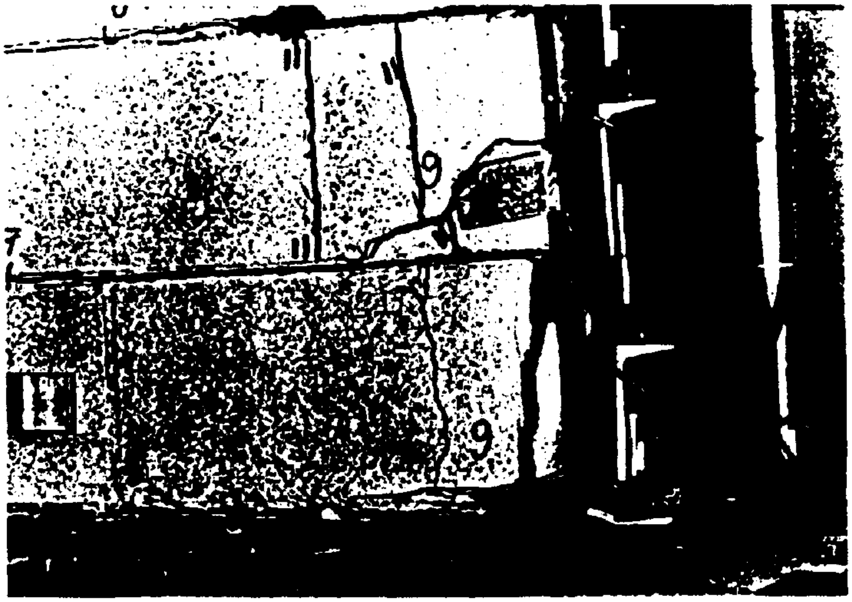

(b) Toe Crushing, Immediately before Failure

Fig. 6.5 Condition at Different Stages of Testing, Wall F7

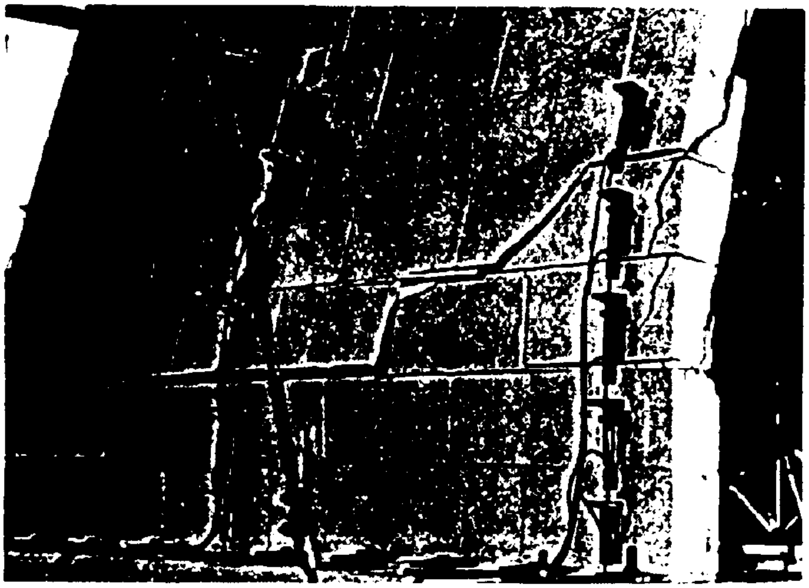

(a) Cracking Pattern in the Flange

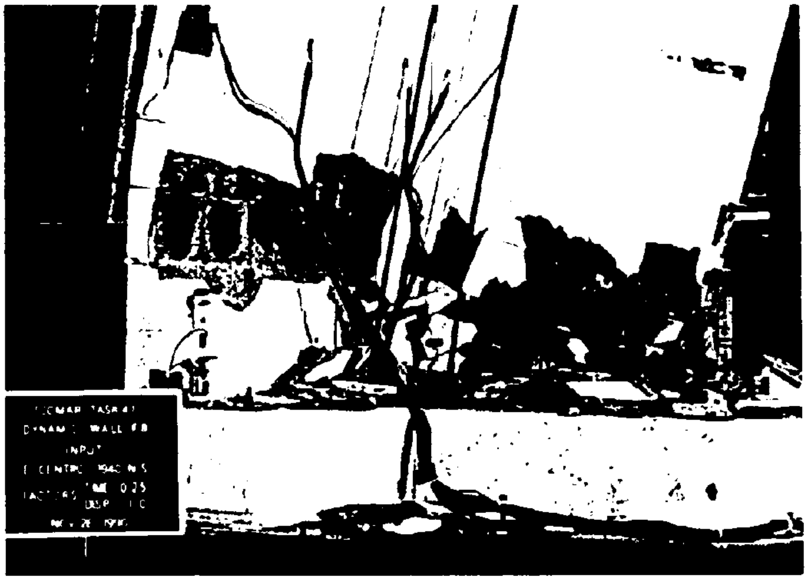

(b) Toe Crushing, at End of Test

Fig. 6.6 Wall F8 after Testing

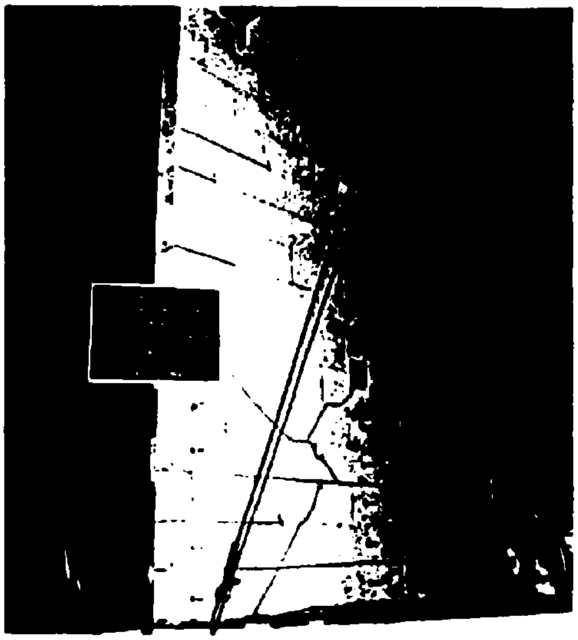

(a) Cracking Pattern in the Flange

(b) Cracking Pattern in the Web

Fig. 6.7 Wall F9 after Testing

6.4.2 Natural Frequency and Damping

The natural frequencies of the flanged masonry walls, predicted and measured during the tests, are listed in Table 6.2. The predicted value was based on a cantilever model with a uniform stiffness along the height (12 feet) and a lumped mass at the center of the top concrete blocks. As a single DOF system, the natural frequency can be calculated with the equation as

$$f = \frac{1}{2\pi}\sqrt{\frac{K}{M}} \qquad (6.3)$$

in which f is the frequency, K and M present the stiffness and mass of the system respectively. The mass included the weight of top concrete slab and blocks and 1/3 of the self-weight of the wall, the total equivalent mass was 25.8 kips. The stiffness was based on the gross cross section of the flanged wall (ignoring the effects of reinforcement) and estimated elastic modulus of masonry 2000 Ksi. Shear modulus was assumed as 40% of the elastic modulus.

Table 6.2 Frequencies of Flanged Masonry Walls (Hz)

Wall No	Predicted Value		Measurd on Ground	Measured on Table
	(1)	(2)		
F5	9.7	8.8	9.0 ($\xi = 0.02$)	7.2
F6	9.7	8.8		6.9
F7	9.7	8.8		7.0
F8	9.7	8.8		6.9

(1) only flexural deformation considered

(2) both flexural and shear deformation considered

It can be seen from the table that the measured result from testing on ground (only wall F5 was tested in this way) coincides well with the predicted value. The test results on the shake table were about 20% lower than the former. This is expected because the flexibility of the shake table and its supporting system (actuator, pumps, etc.) acted as an elastic foundation instead of an absolute solid one. This reduces the stiffness, and therefore the natural frequency of the structural system.

The measured frequency and damping ratio were derived from the first 3 cycles of free vibration of the underdamped system after the excitation at the shake table was stoped, as shown in Fig. 6.8. The frequency can be calculated with equation as

$$f = n / (t_1 - t_0) \tag{6.4}$$

where n is the number of the cycles selected, t0 and t1 are beginning and ending time corresponding to the time period. Assuming the equation of underdamped free vibration have a form of

$$v = v_0 e^{-\xi\omega(t-t_0)} \cos \omega(t-t_0) \tag{6.5}$$

in which $\omega = 2\pi f$ is the circular frequency, ξ is the damping ratio and v_0 is the initial amplitude of the vibration. From t_0 to t_1, the amplitude decreased from v_0 to v_1 due to damping, and the ratio of v_1 vs. v_0 can be calculated from equation (6.5) as

$$\frac{v_1}{v_0} = e^{-\xi\omega(t_1 - t_0)} \tag{6.6}$$

finally the damping ratio is expressed as

$$\xi = \frac{1}{2n\pi} \ln \frac{v_0}{v_1} \tag{6.7}$$

in which v_0 and v_1 can be easily measured from displacement response curve and n is the number of cycles considered.

Figs. 6.9 to 6.11 show the variations of natural frequency and damping ratio with increment of displacement for walls F5, F6 and F7 respectively. It is obvious from these figures that natural frequencies of the walls decreased with increasing the amplitude in both directions due to masonry cracking and steel yielding. Also, the walls were stiffer in the direction of the web in compression than in the opposite direction. On the contrary, the damping ratio of the structures became larger when displacement increased, and it is higher in the direction of the flange in compression than in the direction of the web in compression.

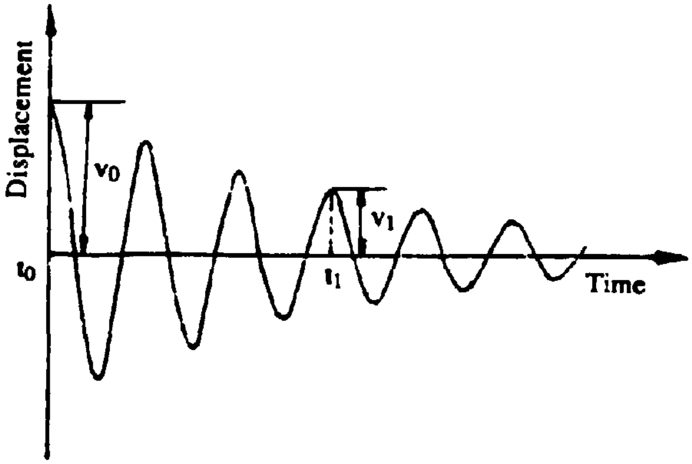

Fig. 6.8 Underdamped Free Vibration

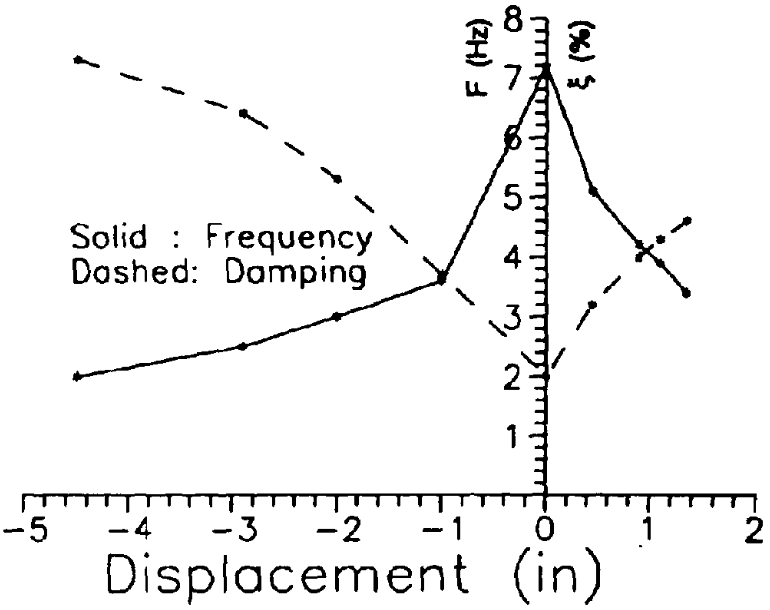

Fig. 6.9 Frequency and Damping, Wall F5

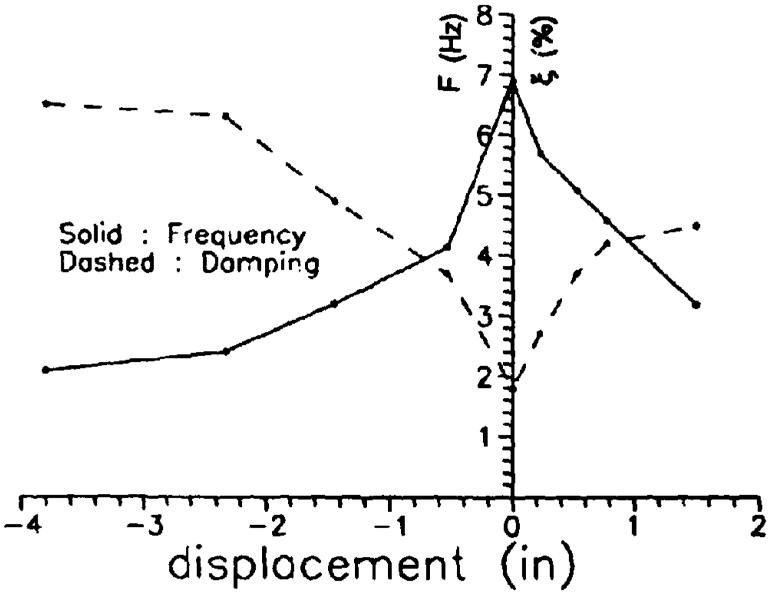

Fig. 6.10 Frequency and Damping, Wall F6

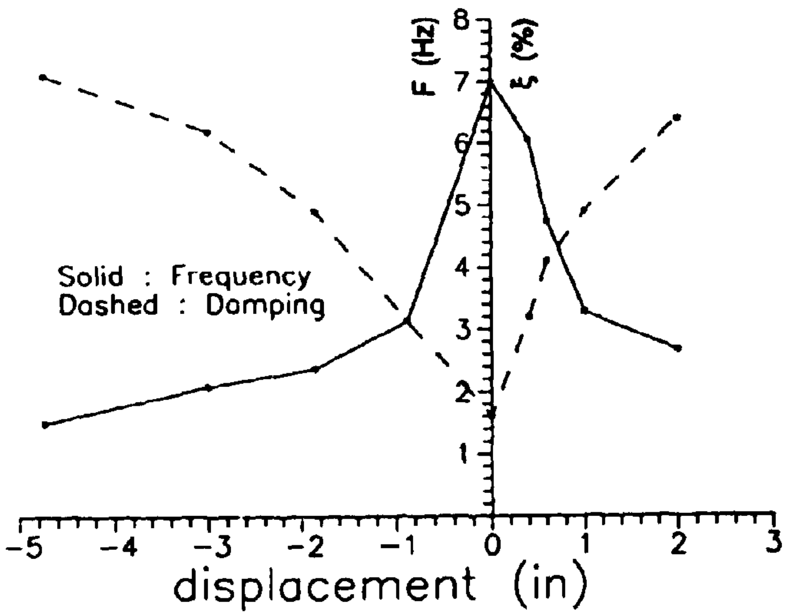

Fig. 6.11 Frequency and Damping, Wall F7

6.4.3 Displacement and Acceleration Response

Figures 6.12 and 6.13 show the typical response displacement and acceleration at the center of top mass during run #7 (Sinusoidal input, f = 5 Hz, D = 0.35 inch and A = 0.89 g) and #13 (El Centro record, time factor = 0.25 and displacement factor = -1) for wall F5. From the plots, it is obvious that the responses of the wall to base excitation are asymmetric in the two directions parallel to the web. With the flange in tension, the response displacement was less and response acceleration was larger than when the flange is in compression, i.e., it is much stiffer when flange is in tension than in the opposite direction. During run #13, the wall reached its maximum response in the direction of the web in compression and strength and stiffness began to degradate. Fig. 6.14 shows the performance of the wall in the last run (run #15, El Centro record, displacement factor = 1) during which the wall finally collapsed in the direction of web in compression.

The same trends can also be seen from the test results of the other walls as shown in Fig. 6.15 through Fig. 6.21. Fig. 6.15 shows the response of wall F6 to sinusoidal input (run #6, f = 5 Hz, D = 0.3 inch, A =0.77 g), Figs. 6.16 and 6.17 present the responses of F6 to run #12 (El Centro record, time factor = 0.25, displacement factor = -0.75) and run #13 (El Centro record, time factor = 0.25, displacement factor = 0.75). During run #12, wall F6 reached its maximum response in the direction of the web in compression and finally collapsed during run #13.

The performances of wall F7 in runs #7, #12 and #14 are shown in Fig. 6.18 to Fig. 6.20 which are corresponding to runs #7, #13 and #15 for wall F5. Unfortunately, the top displacement was not recorded due to instrument problem, the displacements presented in the figures were the displacement at 8' from the base with gauge 2 for run #7 and #12 and displacement at 4' from the base with gauge 3 for run #14 after gauge 2 was disconnected. During run #12, wall F7 reached its maximum response in the direction of the web in compression and collapsed in that direction during run #14. For wall F8, only one run is presented (El Centro record, time factor = 0.25, displacement factor = -1) and the wall reached its maximum response and collapsed in the direction of the web in compression as shown in Fig. 6.21.

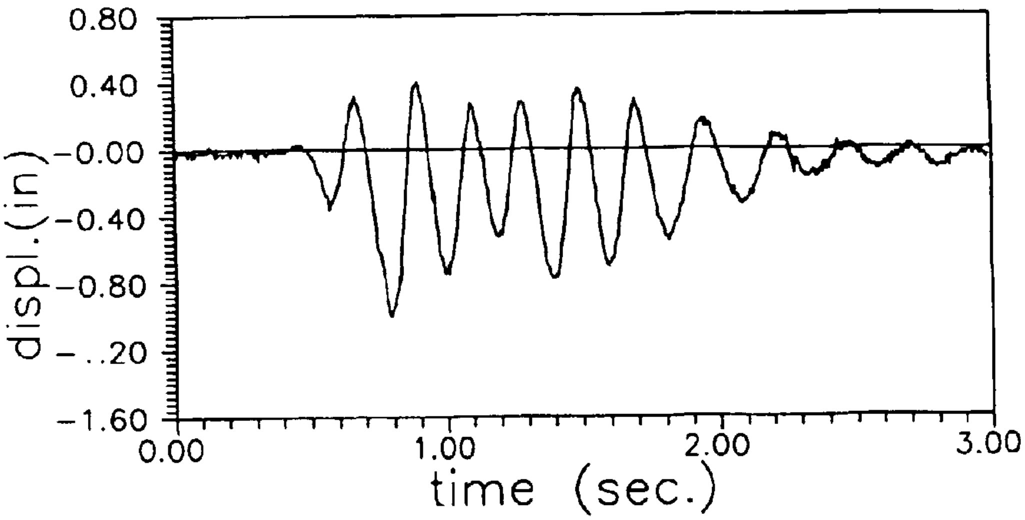

(a) Displacement

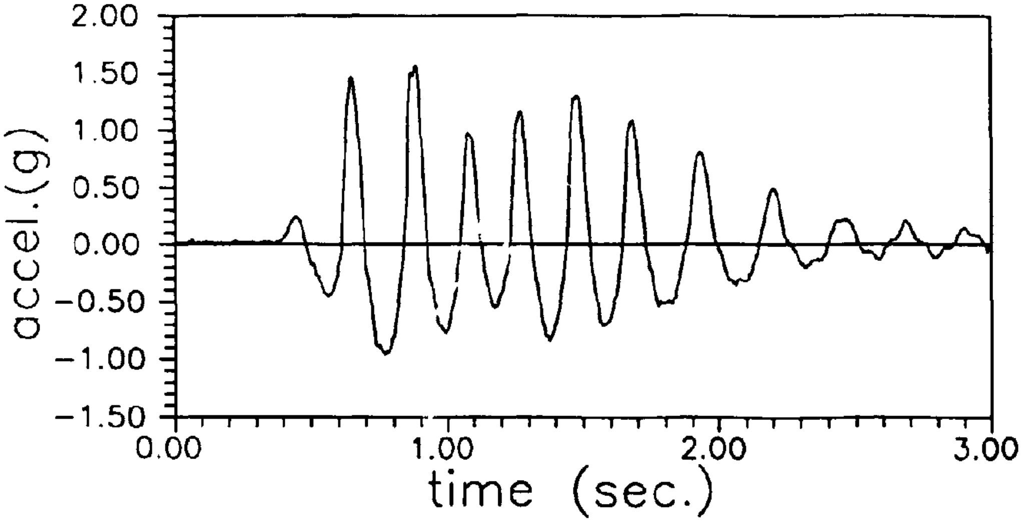

Fig. 6.12 Dynamic Response, Run #7, F5

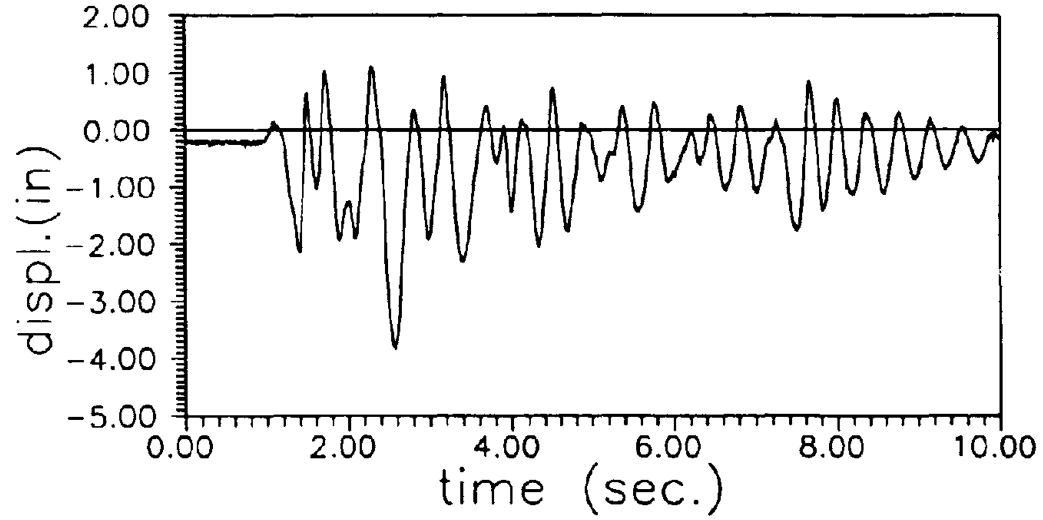

(a) Displacement

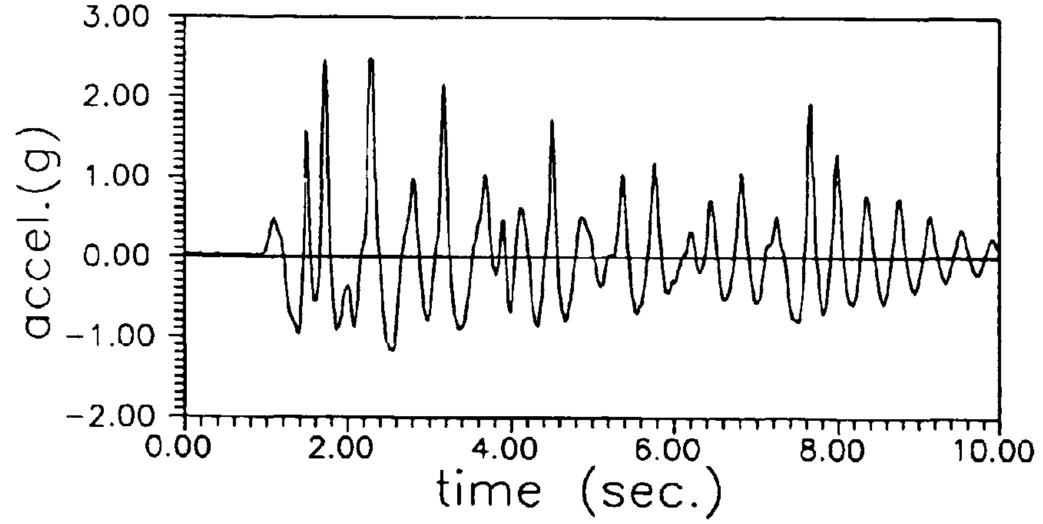

(b) Acceleration

Fig. 6.13 Dynamic Response, Run #13, F5

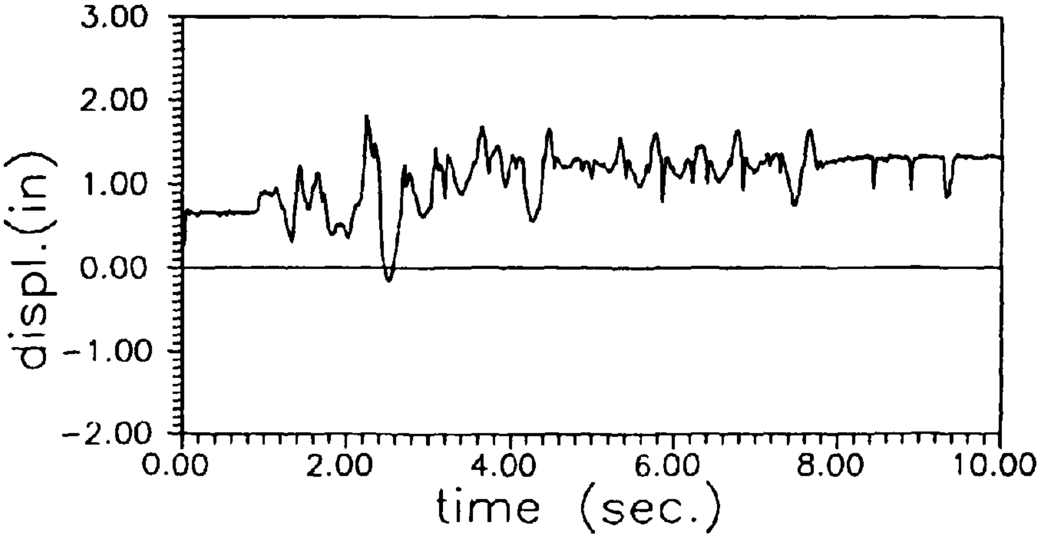

(a) Displacement

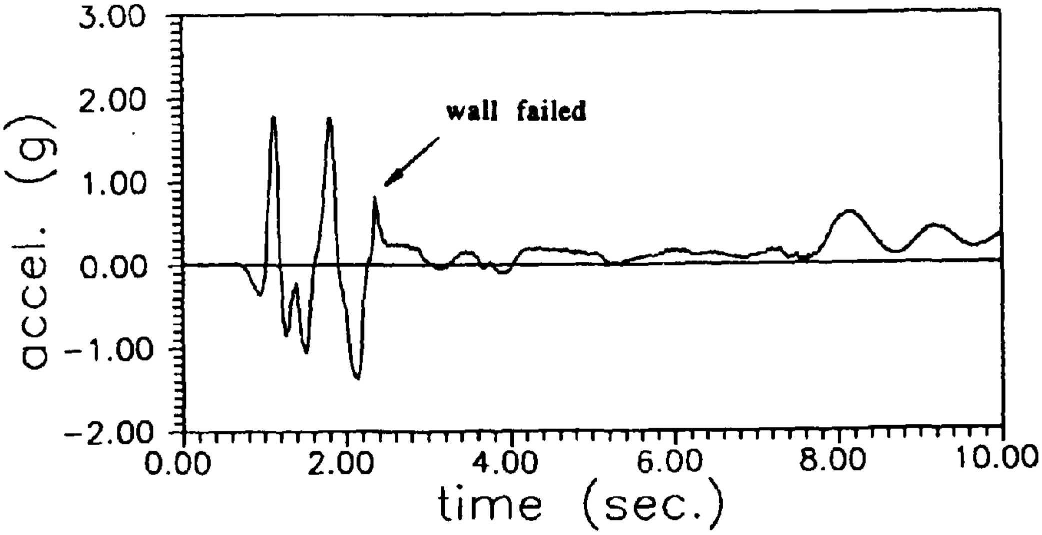

(b) Acceleration

Fig. 6.14 Dynamic Response, Run #15 F5

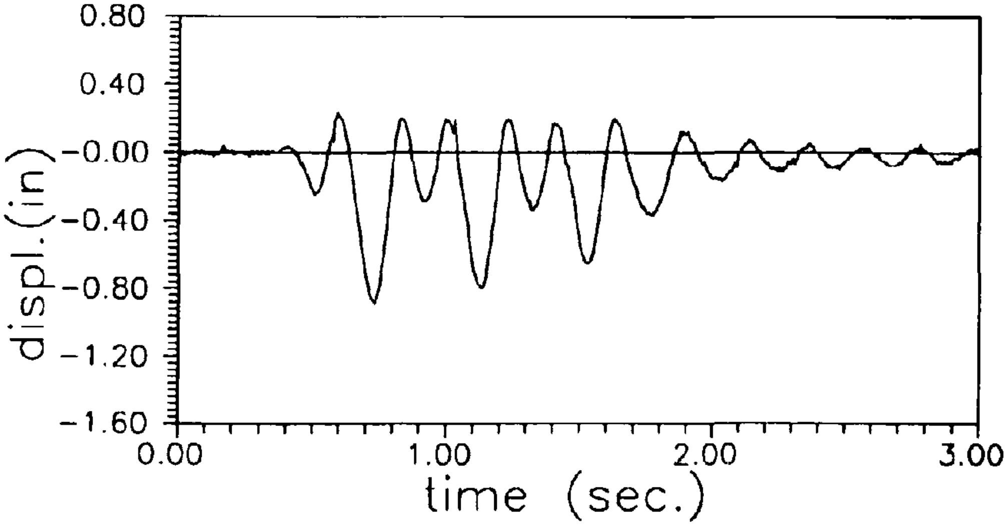

(a) Displacement

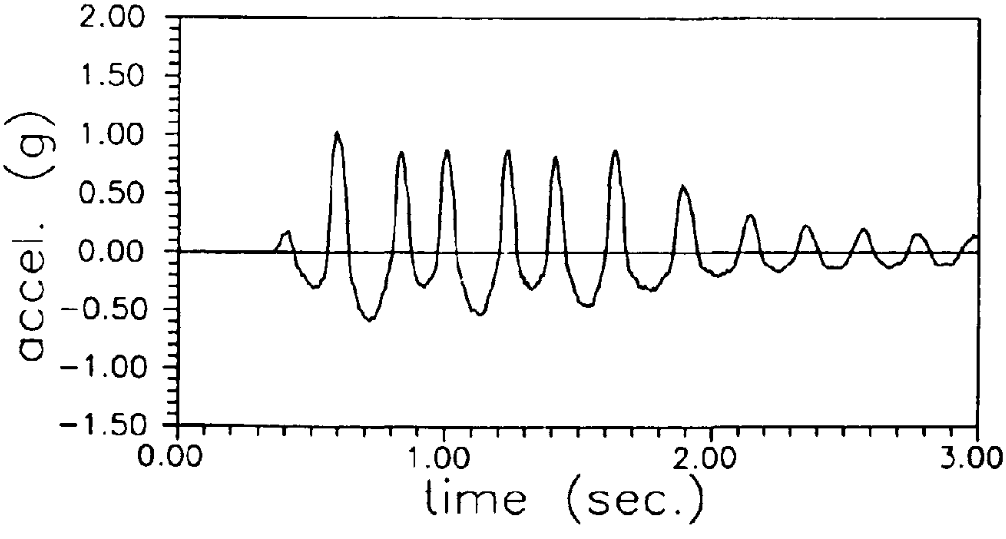

(b) Acceleration

Fig. 6.15 Dynamic Response, Run #6, F6

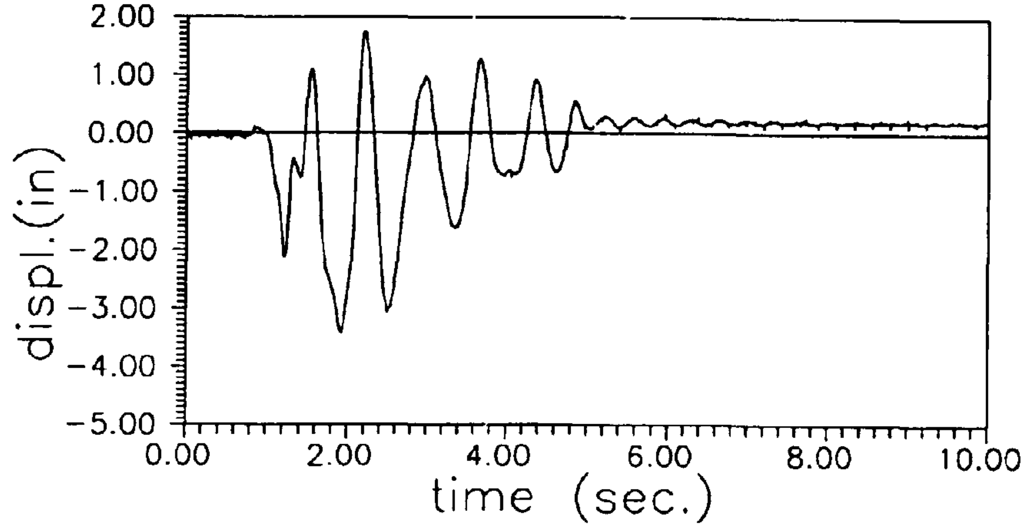

(a) Displacement

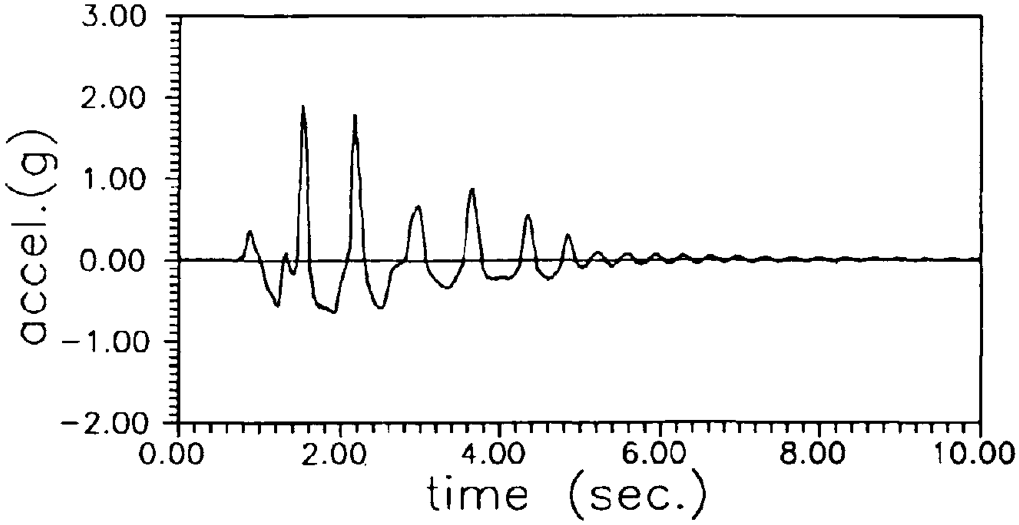

(b) Acceleration

Fig. 6.16 Dynamic Response, Run #12, F6

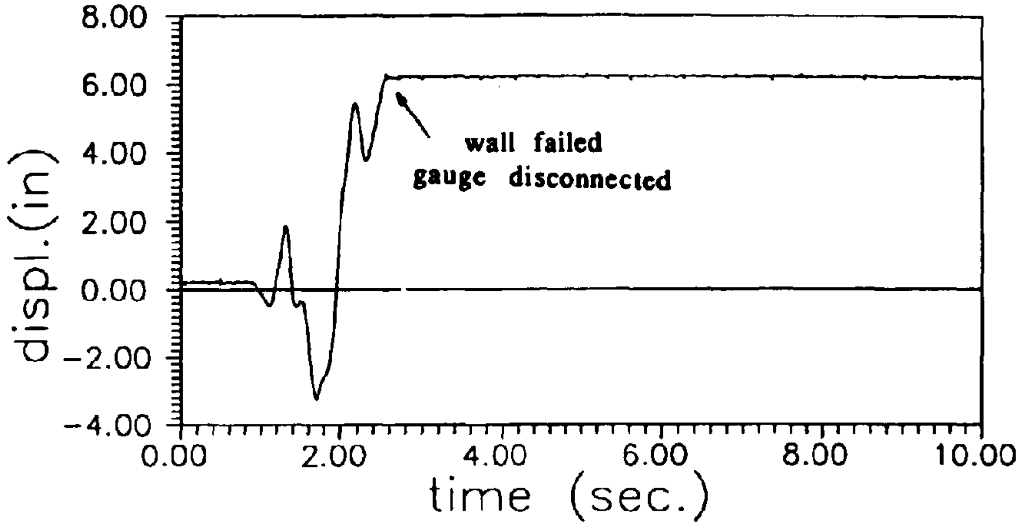

wall failed
gauge disconnected

(a) Displacement

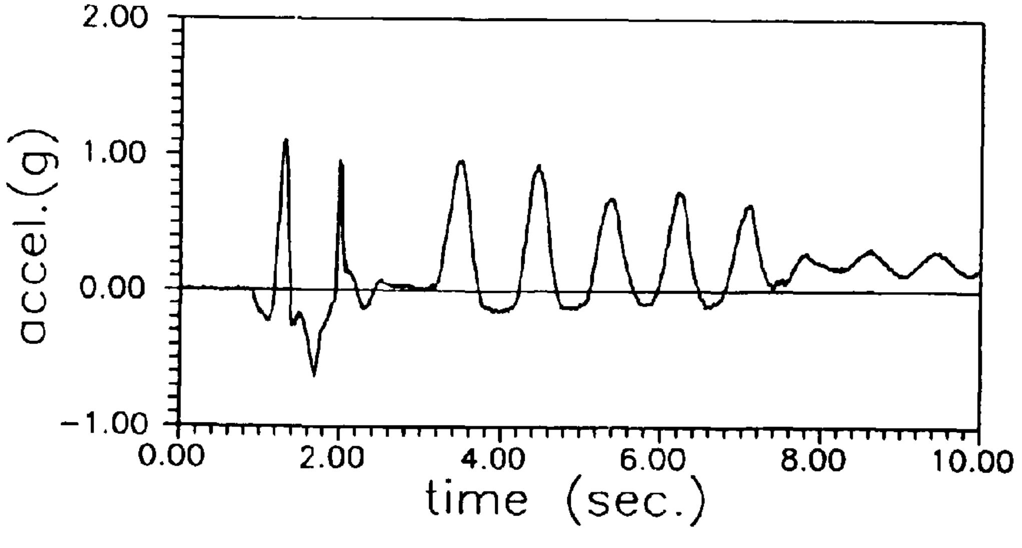

(b) Acceleration

Fig. 6.17 Dynamic Response, Run #13, F6

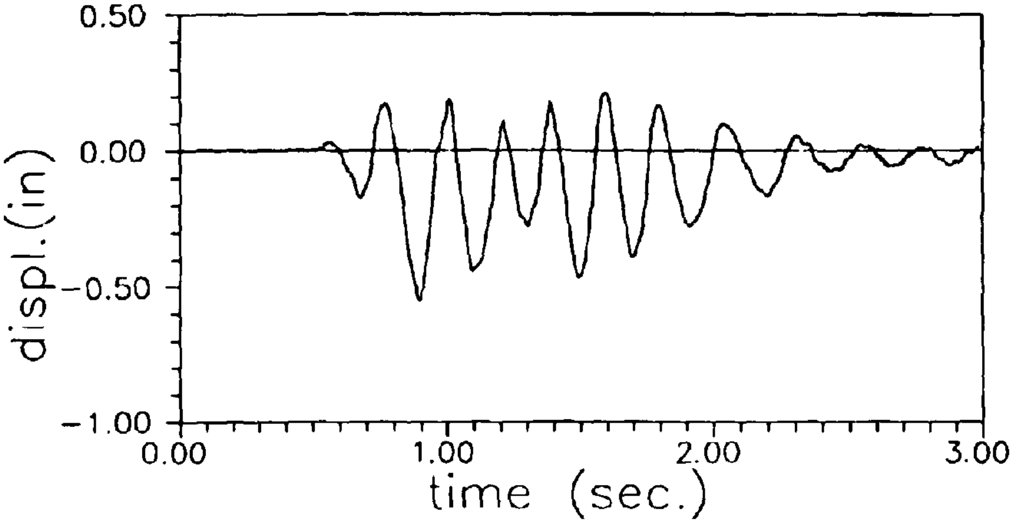

(a) Displacement

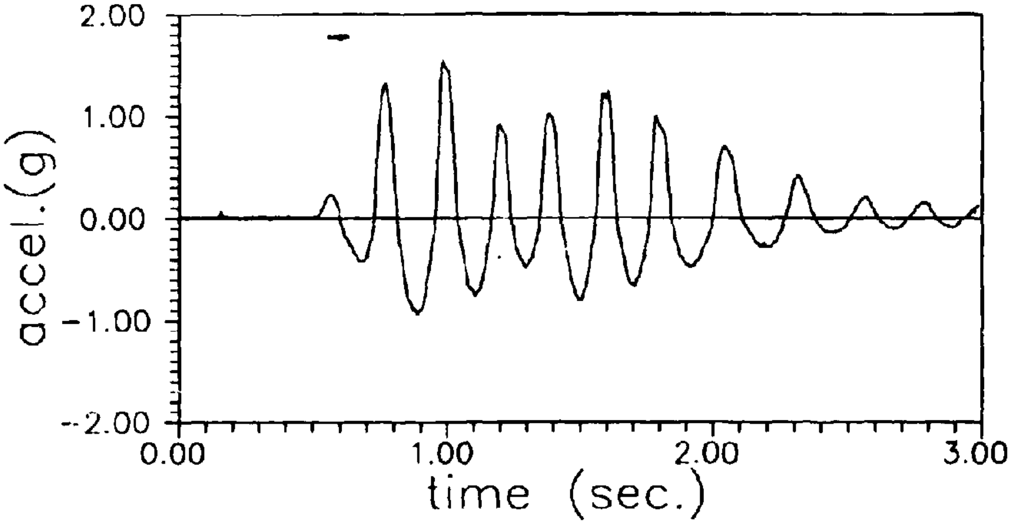

(b) Acceleration

Fig. 6.18 Dynamic Response, Run #7, F7

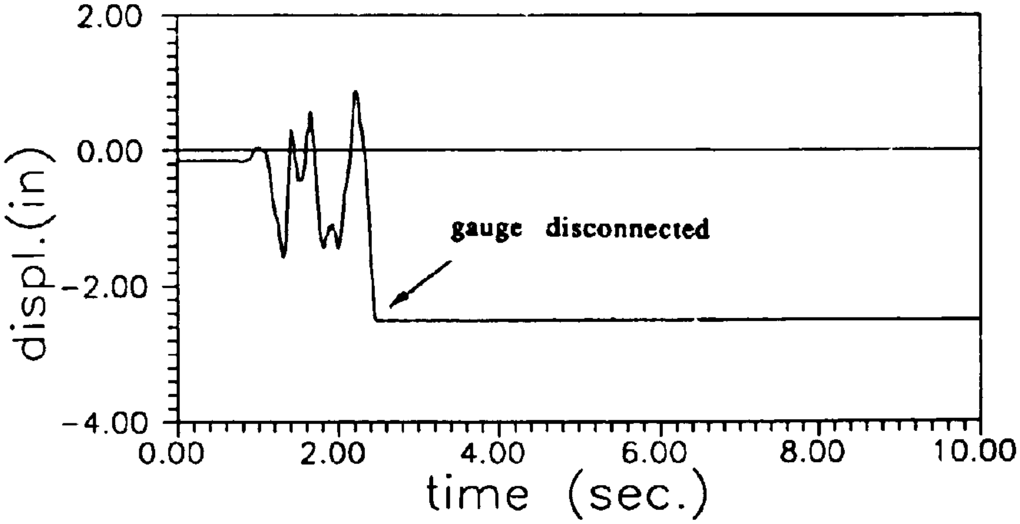

(a) Displacement

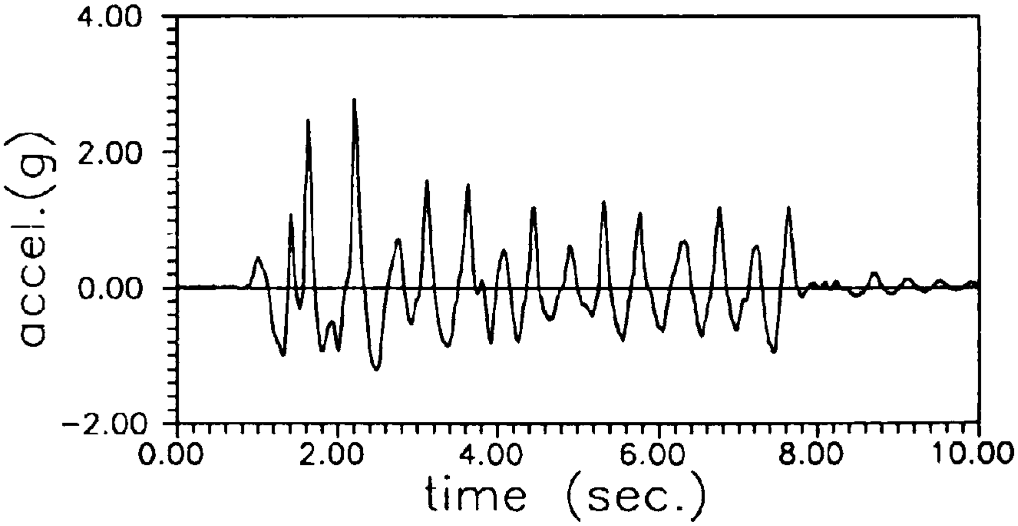

(b) Acceleration

Fig. 6.19 Dynamic Response, Run #12, F7

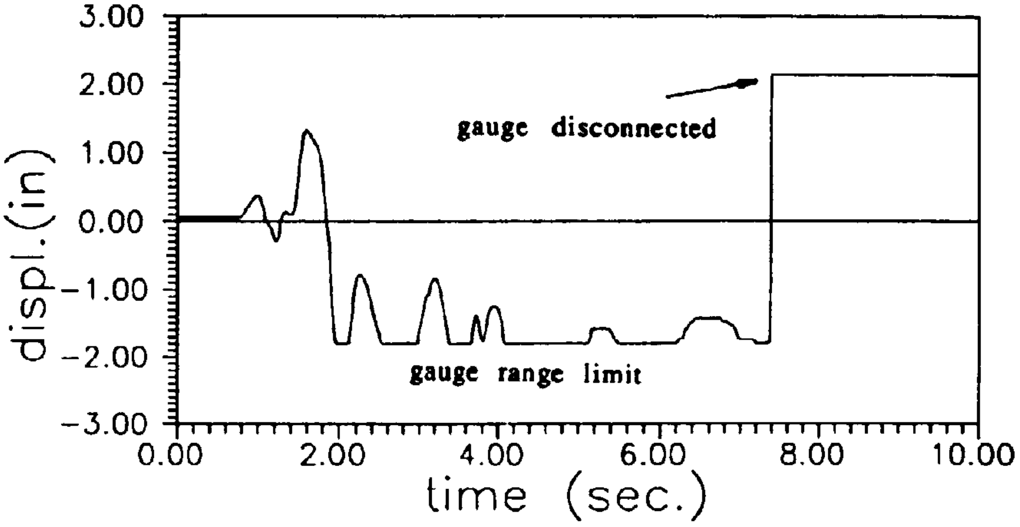

(a) Displacement

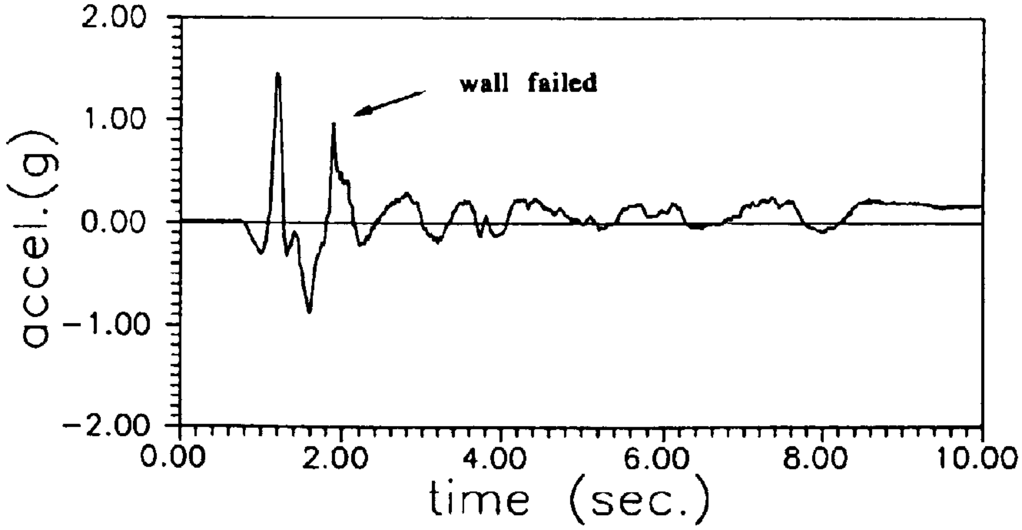

(b) Acceleration

Fig. 6.20 Dynamic Response, Run #14, F7

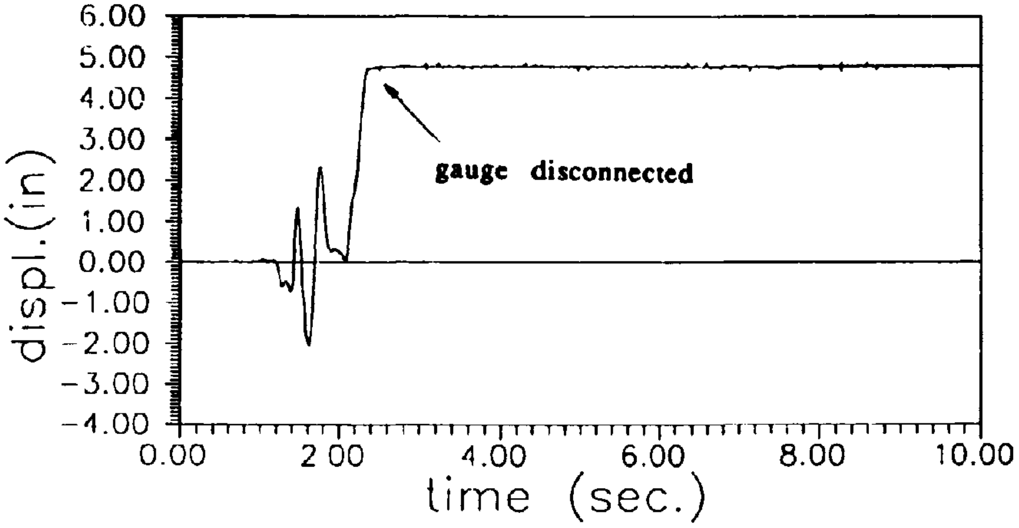

(a) Displacement

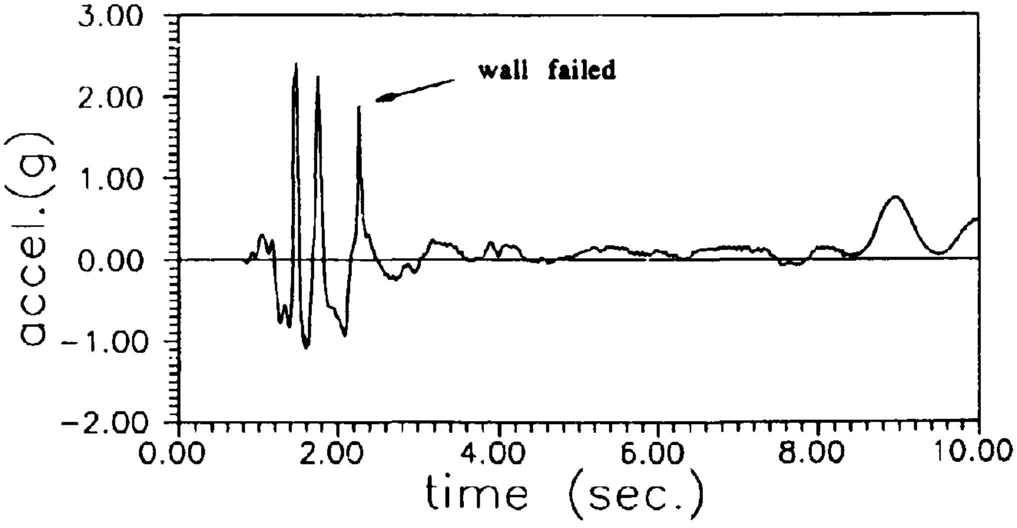

(b) Acceleration

Fig. 6.21 Dynamic Response, Run #2, F8

6.4.4 Hysteresis Loops Under Dynamic Loading

Acceleration-displacement loops measured during runs #4, #7, #10 and #13 of wall F5 are shown in Fig. 6.22 (a), (b), (c) and (d) respectively. The loops show clearly the following trends:

- Before cracking, response is symmetric and linear in both directions. This can be seen from #4, although the noise is significant in the case of low load level.

- Asymmetric characteristics in the two opposite directions after cracking i.e., the stiffness, strength, ductility and the damping.

- The stiffness decreases with the increasing displacement in both directions, but it is more dramatic in the direction of flange in compression.

- The damping ratio becomes larger when the amplitude increases due to loop expansion, especially for the largest loop during which time the wall reached its maximum response. A typical hysteresis loop and corresponding energy dissipation rate can be calculated as shown in Fig. 6.23. The energy dissipation rate can be expressed approximately as area ratio of the Hysteresis loop OABC vs. equivalent elasto-plastic shape in which the slope of AE or BF equals to the initial stiffness OD. The calculated results for #7, #10 and #13 at the peak response of wall F5 are 0.16, 0.19 and 0.23 respectively. For run #4, it was very difficult to calculate because of electric noise recorded during the test. It is obvious that energy dissipation rate increased with increment of displacement and when the flange is in compression, the wall has higher energy dissipation rate than in the opposite direction.

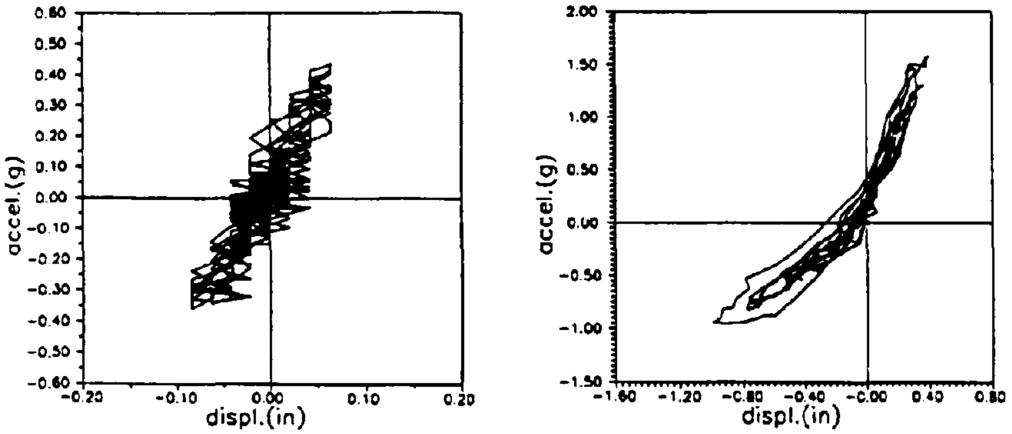

(a) Run #4, Sinusoidal
D = 0.1 in

(b) Run #7, Sinusoidal
D = 0.35 in

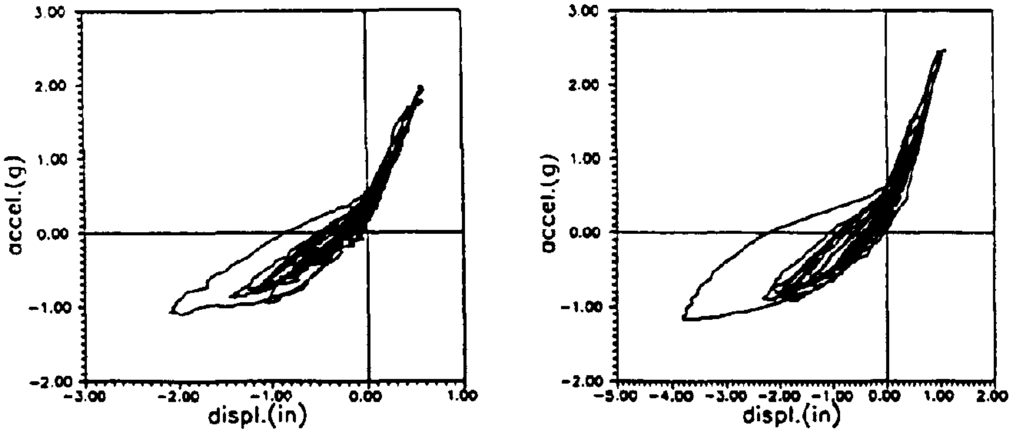

(c) Run #10, El Centro
$f_d = 0.5$

(d) Run #13 El Centro
$f_d = -1.0$

Fig. 6.22 Hysteresis Loops, Wall F5

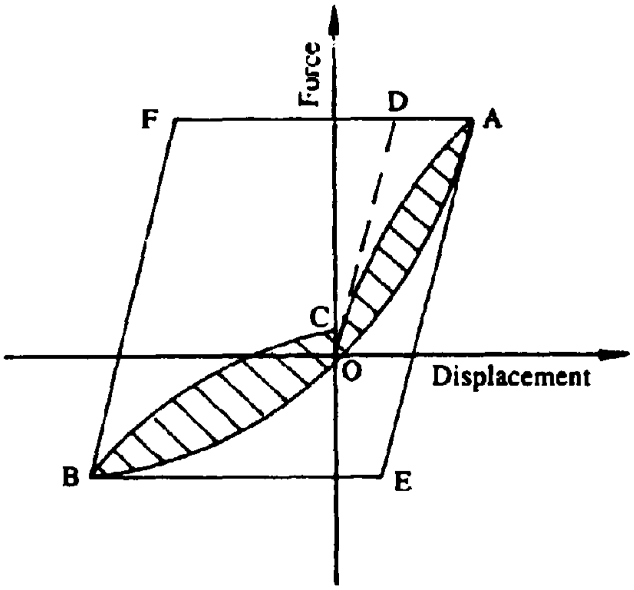

Fig. 6.23 Typical Hysteresis Loop and Energy Dissipation Rate

6.4.5 Ultimate Strength and Ductility

By comparing the test results from wall F5, F6 and F7, the same effects of vertical reinforcement ratio and confining plates on the strength, stiffening and ductility of flanged masonry walls as shown by pseudo-static tests, can be observed. It is obvious that the flexural strength increases with increase of the vertical reinforcement ratio in both directions(wall F6 vs. F5).

Fig. 6.24 shows the comparison of force-displacement envelopes between wall F7 (confined) and F5 (unconfined). The lateral forces were derived by multiplying the maximum response acceleration and total equivalent mass at the wall top (25.8 kips). It can be seen clearly that with the flange in compression, the responses are almost the same (no confining in this direction), but in the opposite direction (flange in tension) the confined wall F7 has higher strength, larger displacement at the peak load , and a flatter falling section than unconfined wall F5. Note that from Fig. 6.24, the displacement ratio of F7 vs. F5 is 1.20 which is much less than the value of 1.5 for wall F4 vs. F1 in pseudo-static tests. Wall F4 and wall F7 failed as a consequence of lateral buckling of the web following a loading sequence where the web reinforcement had been subjected to high residual inelastic tensile strains prior to load reversal placing the web in compression. Before the masonry in the web could support compression stress it was necessary for the web reinforcement to yield in compression, to remove the residual tensile strains and close the cracks. During the process there was no effective lateral support to the web vertical reinforcement, which exhibited lateral instability, placing eccentric loads on the web and causing failure. Therefore, the tested ultimate displacement for Confined walls was much less than expected.

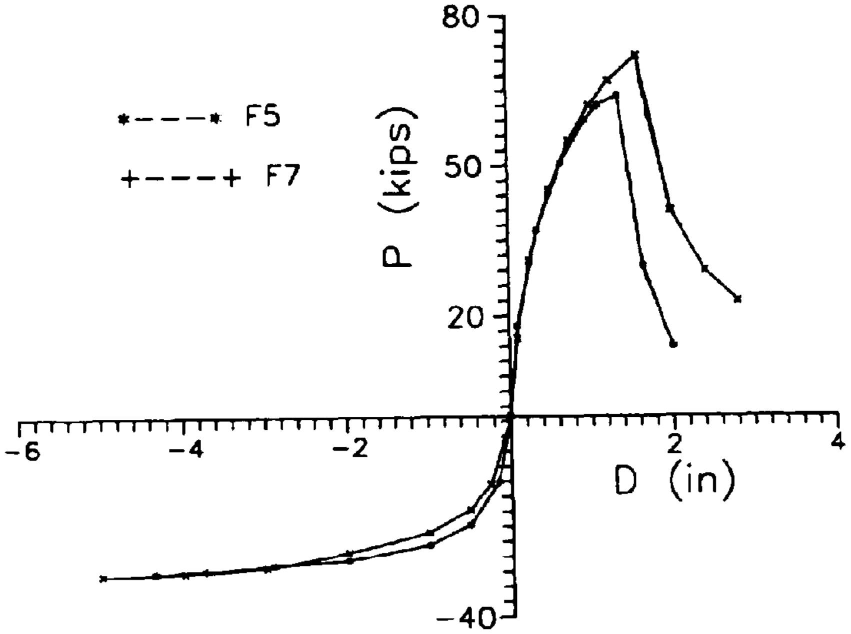

Fig. 6.24 Load-displacement Envelopes, F7 vs. F5

6.4.6 Effects of Loading history

Fig. 6.21 presents the displacement and acceleration response of wall F8 under El Centro 1940 N-S earthquake record (time factor=0.25, displacement factor=-1.0). It can be seen from the figure that the wall reached its maximum response in the direction of the web in compression (A_w =2.40 g) and the corresponding displacement was 1.35 inch, which was equivalent to the maximum response of wall F5 (A_w =2.45 g, D_w = 1.35 inch) during run #13 (Fig. 6.13). The maximum responses in the opposite direction were A_f = 1.10 g and D_f = 2.10 inch. Comparison with run #13 of wall F5 (with the same earthquake input factors), as shown in Fig. 6.13, the responses are quite different because of previous cracks in wall F5, but the maximum responses (flexural strength and displacement) are nearly the same.

6.4.7 Response to Skew Earthquake Input

As a preliminary study on response of T-section masonry walls to skew earthquake attacks, wall F9 was tested with both sinusoidal excitation and earthquake record at 45 degree to the web. After run #7 (El Centro 1940 N-S record, time factor = 0.25, displacement factor = -1.0), the test stopped without structural failure of the wall because of safety consideration. At this stage severe vertical cracking developed at the web toe. Fig. 6.25 shows the positions of accelerometers which were used to monitor the horizontal input and response accelerations during the tests for wall F9. Among them, A2 was attached at the base level to record the input, meanwhile A1, A3, A4 and LVDT were mounted 12 feet high from the base to measure the responses at the top. Fig. 6.26 presents the recorded response acceleration of A3 and A4. Fig. 6.27 presents the response displacement and acceleration parallel to the web for run #4 (sinusoidal input, f = 5 Hz, amplitude = 0.4 in) and separated translation acceleration parallel to the flange (0.5(A3 - A4)) and torque component (0.5(A3 + A4)) are shown in Fig. 6.28. From the comparison, it can be seen that a skew excitation will cause responses in the two orthogonal directions, i.e. parallel to the web and the flange and the maximum response accelerations were 1.35 g and 1.75 g respectively. Therefor the direction of resultant inertial force will differ from the direction of excitation (52 degree vs. 45 degree to the web in this case) due to different stiffness and responses in the two directions. Also the skew excitation causes response in rotation due to the eccentricity between mass and stiffness centers of T-sections. The response inertial torque and maximum shear stress can be estimated as follows:

$$m = M \ddot{\omega} \tag{6.8}$$

where: m is inertial torque, M is inertial modulus of mass, and $\ddot{\omega}$ is angle acceleration. For rectangular section of the mass blocks,

$$M = P(a^2 + b^2)/3g \tag{6.9}$$

$$\ddot{\omega} = A/b \tag{6.10}$$

where: P is the weight, g is gravity acceleration, a and b are half axes of the rectangular section respectively and A is the translation acceleration at the corresponding point. Substituting the values of P = 25.8 Kips, a = 4.33 ft, b = 3 ft, A = 0.5 g into the above equations, m = 19.9 Kft can be obtained.

To estimate the maximum shear stress caused by the inertial torque, use the formula $w = \frac{1}{3}\Sigma ht^2$ for resistance of thin rectangular sections, where: h is the length and t is the thickness of each section. Substituting the dimensions of T-section wall into above expression, then the maximum shear $\tau_m = \frac{m}{w} = 0.16$ Ksi. From the calculation result, the estimated maximum shear caused by inertial torque is significant, therefore the inertial torque in T-section walls caused by skew earthquakes is not negligible.

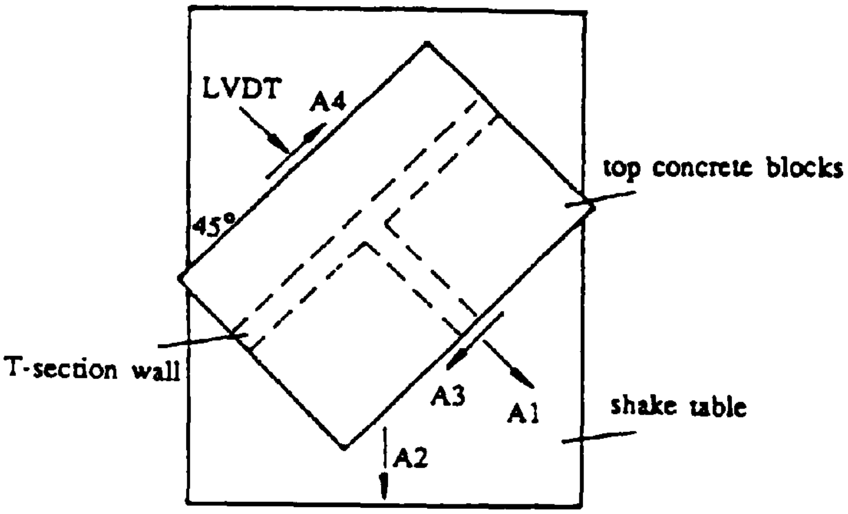

(plane)

Fig. 6.25 Location of Accelerometers for Wall F9

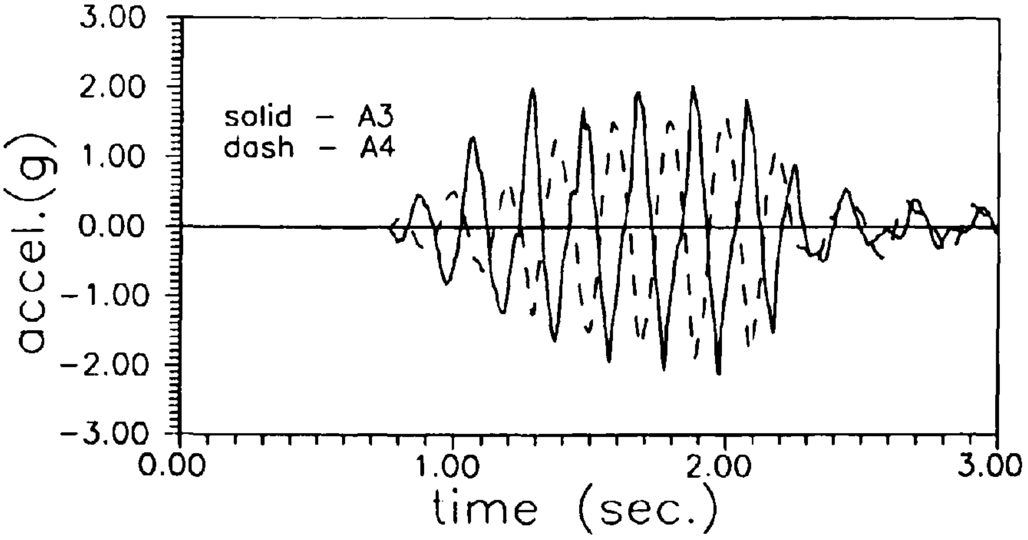

Fig. 6.26 Response Acceleration, A3 and A4, Run #4, F9

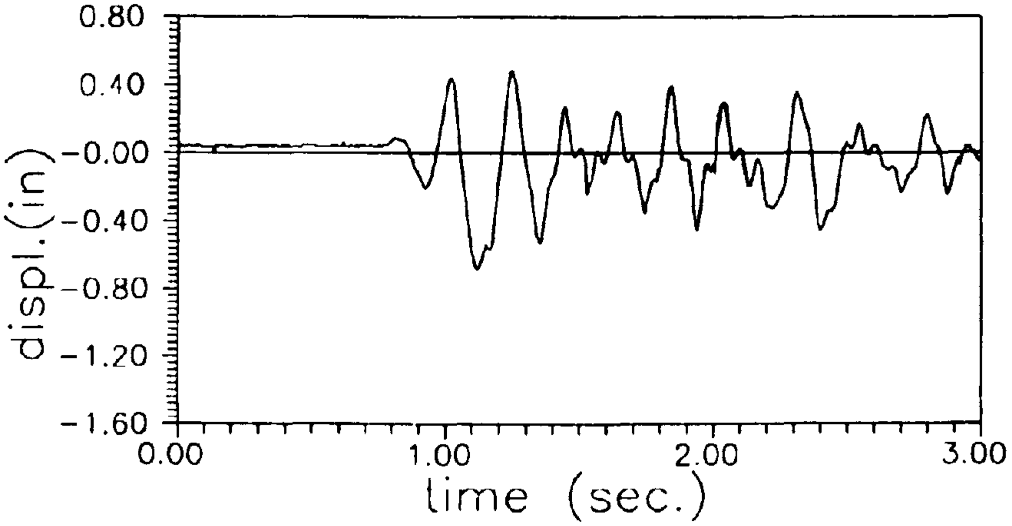

(a) Displacement

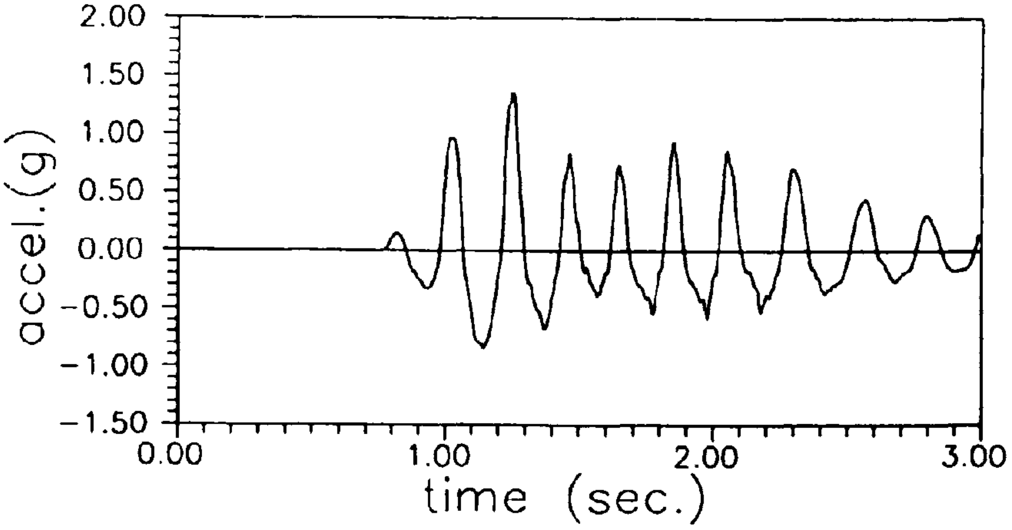

(b) Acceleration

Fig. 6.27 Response // the Web, Run #4, Wall F9

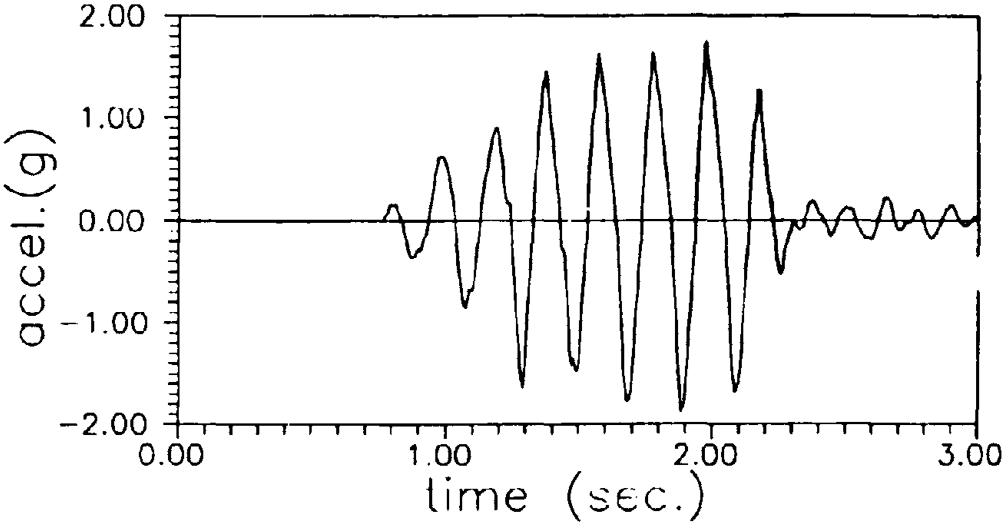

(a) Acceleration Parallel to the Flange

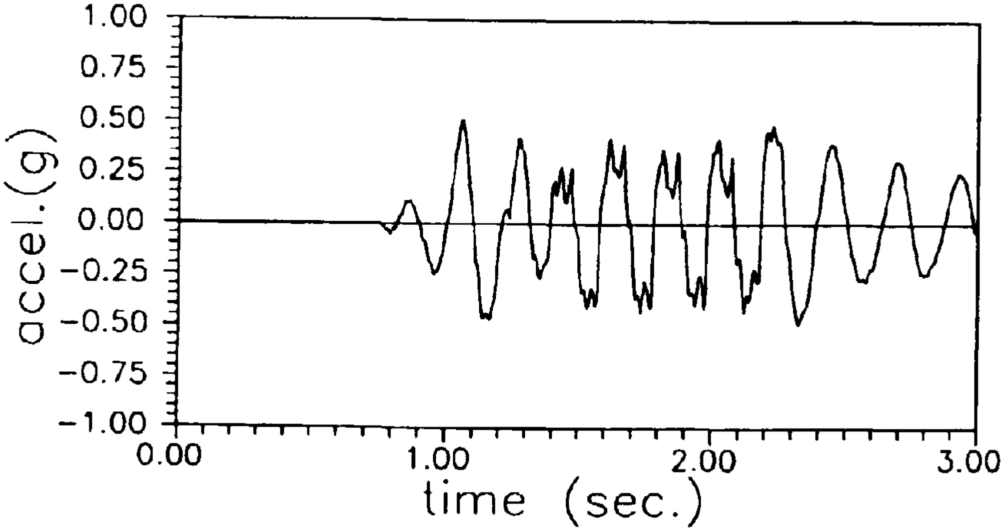

(b) Torque Component at Radius = 3 ft

Fig. 6.28 Response Acceleration, // Flange and Torque, Run #4, F9

Fig. 6.29 (a) shows the location of linear potentiometers at the base level and (b) presents the vertical deformation pattern of masonry surface measured during the test. By checking the vertical displacements at the 4 locations, it is obvious that the assumption of 'plane-section' during the deformation is not valid. Fig. 6.30 (a) and (b) present the input acceleration at base and response acceleration parallel to the web at top for run #7 (El Centro record, time factor = 0.25, displacement factor = -1) of wall F9. The separated response acceleration parallel to the flange and corresponding torque component are shown in Fig. 6.31 (a) and (b) respectively. For a skew earthquake input, like the case of sinusoidal excitation, there were responses in the two orthogonal directions and response of rotation. The maximum response acceleration parallel to web was 1.80 g, meanwhile about 3 g in the direction parallel to the flange, therefor the resultant response did not coincide with the direction of input.

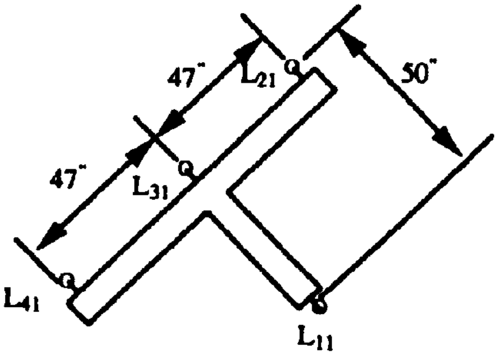

(a) Location of potentiometers

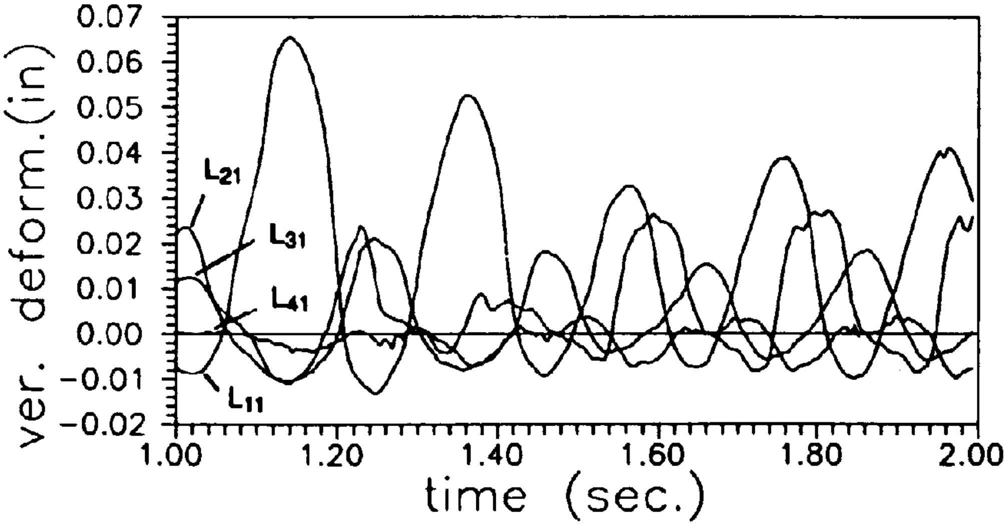

(b) Deformation measured by potentiometers

Fig. 6.29 Vertical deformation at Base, Run #4, F9

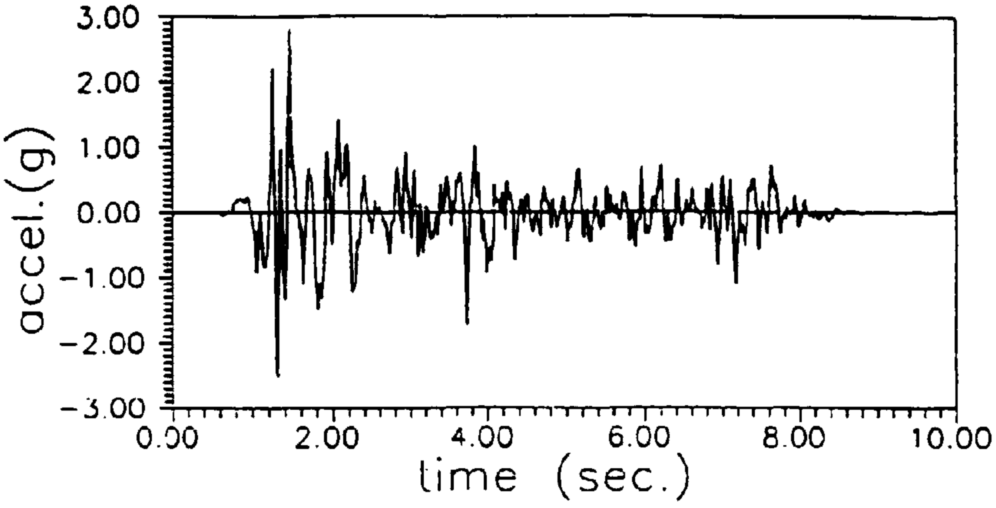

(a) Input Acceleration

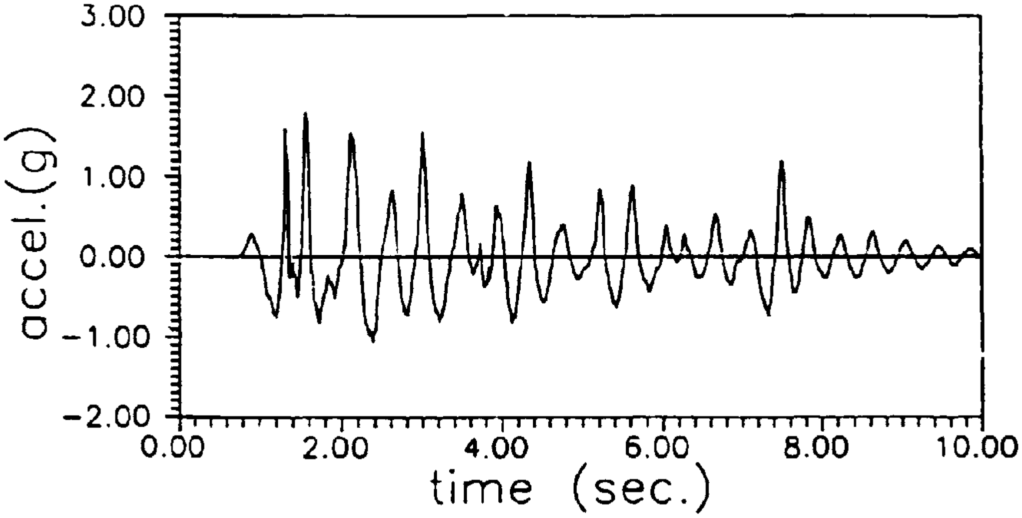

(b) Response acceleration

Fig. 6.30 Input and Response Accelerations, Run #7, F9

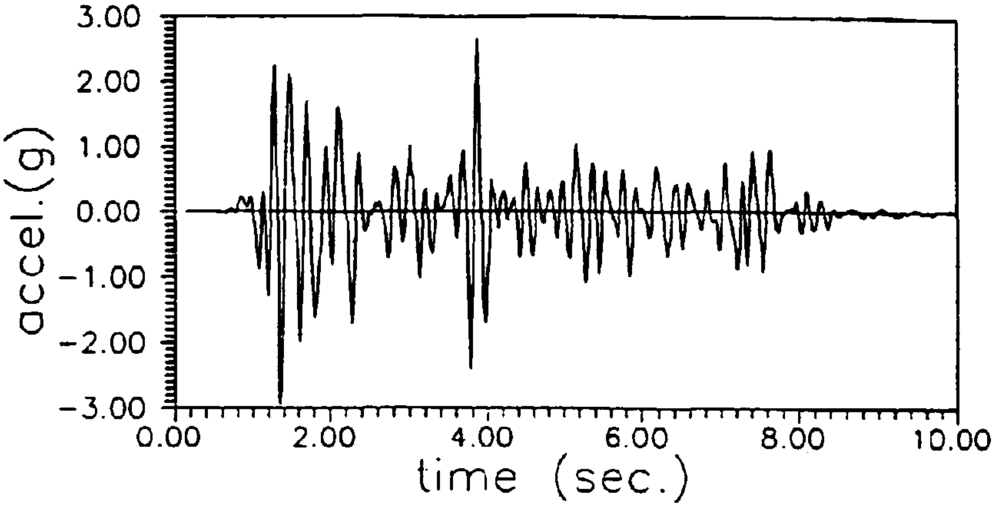

(a) Response Acceleration // Flange

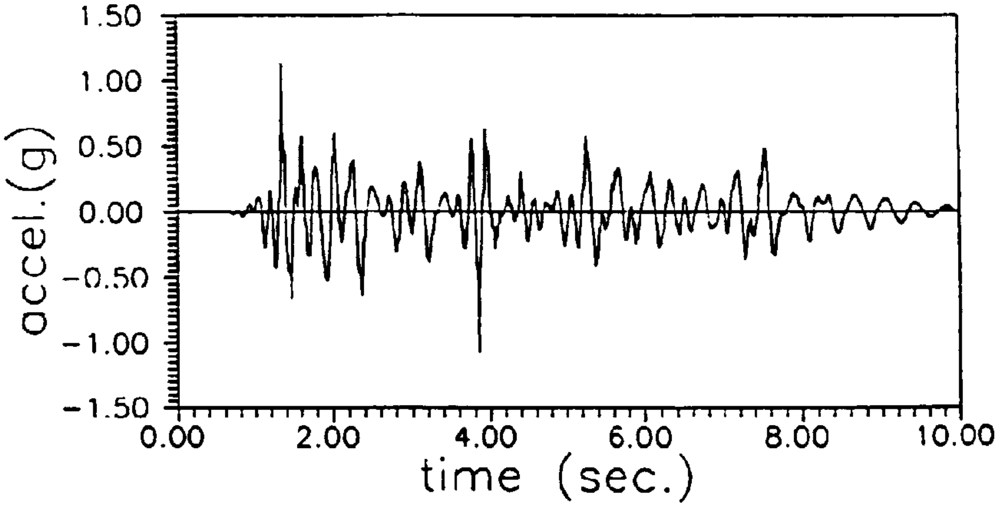

(b) Response Torque component at Radius = 3 ft

Fig. 6.31 Response accelerations // Flange, Run #7, F9

6.5 Comparisons Between Dynamic and Static Responses

Comparisons of load-displacement envelopes between pseudo-static tests and dynamic tests for walls F1/F5, F2/F6 and F4/F7 are shown in Figures 6.32, 6.33 and 6.34 respectively. It can be seen from the curves that the dynamic response has the same feature as the pseudo-static test. But for the identical walls, dynamic tests resulted in less displacement at the peak load than the pseudo-static tests in the direction of the web in compression, with nearly the same ultimate strength. The reason might be in that the all walls for both dynamic and static tests failed due to brittle crushing of masonry followed by buckling of the extreme vertical reinforcement. In the opposite direction, when the response of the wall was governed by tension deformation of the vertical reinforcement, dynamic tests resulted in higher strength and stiffness due to the effects of loading rate. Note that from Fig. 6.33, the dynamic strength of wall F6 is a little lower than the static strength of Wall F2. This is because that the vertical reinforcement for F2 had a much higher yield strength (75.9 Ksi) than the value of wall F6 (62.5 Ksi). (see Table 4.3)

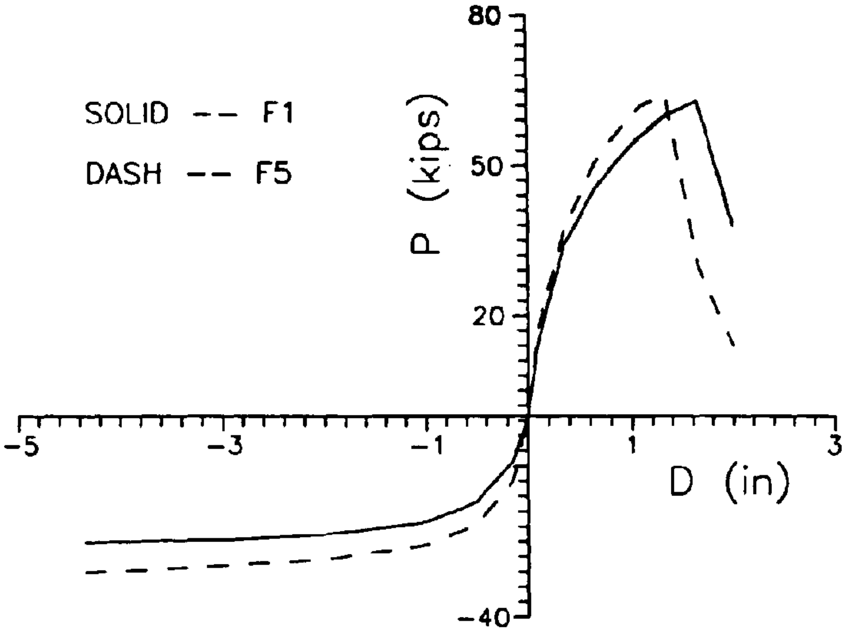

Fig. 6.32 Load-displacement Envelopes, F5 vs. F1

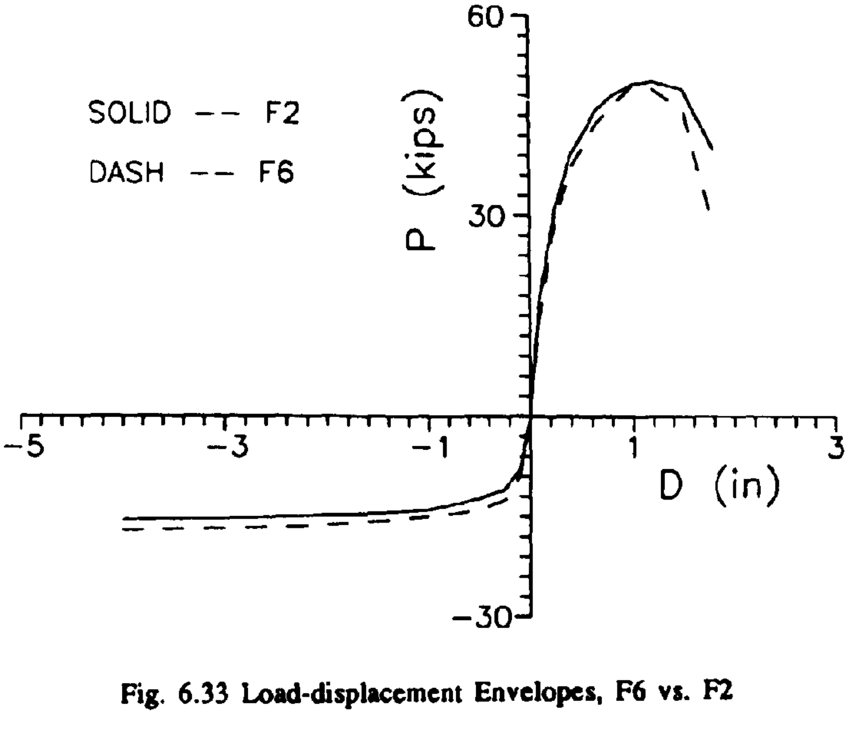

Fig. 6.33 Load-displacement Envelopes, F6 vs. F2

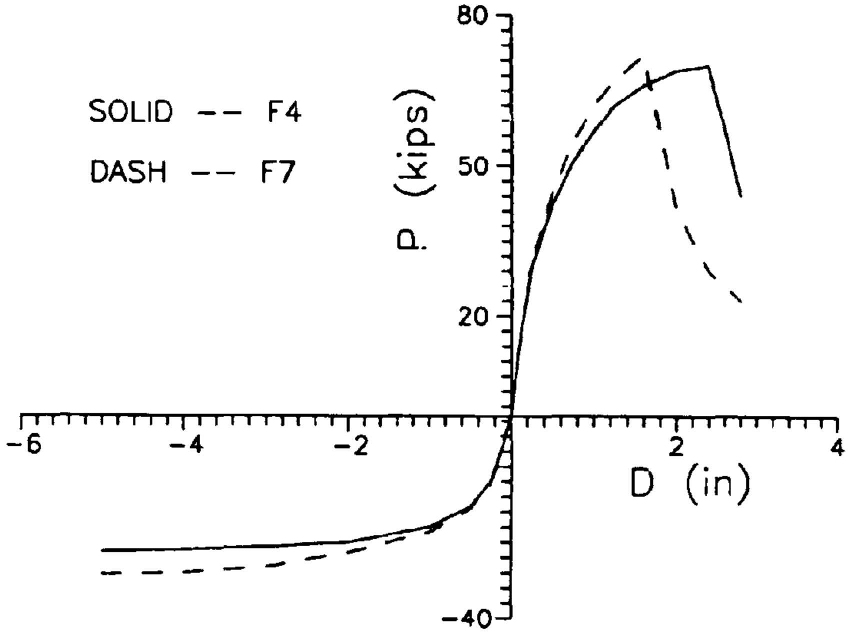

Fig. 6.34 Load-displacement Envelopes, F7 vs. F4

Table 6.3 summarizes the ultimate flexural strength and displacement for both pseudo-static and dynamic tests. Checking the failure mode and position of the walls, it can be found that the failure mode for dynamic tests is the same as for pseudo-static tests.

Table 6.3 Ultimate Strength of Flanged Masonry Walls (Kips)

	Pseudo-static				Dynamic			
Wall No.	F1	F2	F3	F4	F5	F6	F7	F8
Predicted	62.0	49.1	70.0	69.7	63.6	46.4	71.8	63.6
Test Result	63.4	50.8	70.5	70.1	64.0	49.0	71.0	62.0

6.6 Conclusions

The following conclusions can be drawn from the results of the dynamic experiments:

(1) Under dynamic loading, the flanged masonry structural walls have the same asymmetric characteristics in the two directions parallel to the web, and the same failure mechanism, as observed from pseudo-static tests.

(2) The flanged masonry walls have less displacement (ductility) and higher stiffness when subjected to dynamic loading than static loading, with nearly the same ultimate strength in the direction of the web in compression.

(3) The natural frequency of the flanged wall decreases with increasing amplitude. It has different values in the two opposite directions after masonry cracking.

(4) The damping ratio of the wall increases with increasing amplitude. It also has different values in the two directions because of different energy dissipation rate.

(5) The vertical reinforcement ratio and confining plates have the same effects on strength, stiffness and ductility of the structures, as concluded for pseudo-static tests.

(6) Pre-existing cracks can alter the natural frequency and seismic responses of the walls, but the maximum response (ultimate strength) will

remain almost the same provided that the pre-loading does not exceed the ultimate strength of the structure.

(7) Skew earthquakes cause seismic responses in the two orthogonal directions of T-section walls. The resultant inertial force will differ from the direction of excitation due to different stiffness and responses in these two orthogonal directions. Also the skew excitation will result in significant inertial torque because of eccentricity between the mass and stiffness centers in the cross section.

7. TIME - HISTORY RESPONSE ANALYSES

7.1 Introduction

To evaluate the inelastic structural component model developed for flanged masonry walls in Chapter 3 , time-history response analyses for the dynamically tested walls were carried out with the model and special hysteresis loops proposed in that chapter. The hysteresis loops suggested were based on the pseudo-static load test results of flanged masonry walls summarized in Chapters 5. Two kinds of numerical examples are analyzed and presented in this chapter:

- As the first step, load-displacement envelopes for the statically tested walls were computed. The analyses used monotonic increasing load in the two opposite directions and displacement control after maximum loading. Wall F1 and F4 (confined) were analyzed in this way and compared with the experimental results.

- After the static analyses, dynamic time-history response analyses of T-section walls were performed. The walls analyzed were F5 (#6 vertical reenforcement, identical to F1), F6 (#4 vertical reinforcement, identical to F2) and F7 (#6 vertical reinforcement, confined, identical to F4) in order to compare with the static case as well as dynamic test results.

A special time-history computer program was written in FORTRAN 77, capable of carrying out the above analyses. For static analyses, the flanged masonry wall was simplified as a 4-node rectangular element with two nodes at the bottom fixed and two at the top free, as shown in

Fig. 3.3 (b). The load was applied at the top horizontally, and both horizontal and vertical displacements were computed and compared with the test results.

For time-history response analyses, the wall was further simplified to a two node cantilever column (Fig. 3.3 (c), in local coordinate system) in order to reduce computer time. Both sinusoidal excitation and earthquake record input were introduced at the bottom, corresponding to different stages of the test program, and the response horizontal acceleration and displacement at the top of the wall were computed and compared with the test results.

7.2 Load-displacement Envelope

7.2.1 Analysis Procedure

The T-section wall was simplified as a rectangular plane element dimensions equal to that of the web, as shown in Fig. 3.3. As described in Chapter 3, in the global coordinate system, the element has 8 degree of freedom and in the local coordinate system, a plane shear-flexural element has only 3 degree of freedom. The analyses used an incremental approach and for each step, a 3 by 3 element stiffness matrix was first formed in local coordinates, then transformed to a 8 by 8 stiffness matrix in the global coordinates where the boundary conditions were introduced and the degrees of freedom were reduced to four. Then, the horizontal load was applied and structural analysis was performed to calculate the incremental displacements of the two top nodes. After the new response node displacements had been obtained, they were added to the total displacements and transformed to node displacements in local coordinates to calculate new material properties, then the stiffness matrix was updated and transformed back into the global coordinates again. Finally, a new increment of load (or displacement) was applied.

7.2.2 The Moment-curvature Curve

To check the effects of moment-curvature curve shape between the origin and first yielding on the load-displacement responses (section after first yielding remains the same), four different curves were assumed and evaluated as follows:

(1) Bilinear, as the initially proposed skeleton which passes through three points: the origin, first cracking and first yielding.

(2) A parabola which passes through three points (the origin, first cracking and first yielding) and has the following form:

$$\varphi = c_1 M + c_2 M^2 \tag{7.1}$$

in which c_1 and c_2 can be determined by values of curvatures and moments at the points of first cracking and yielding.

(3) A parabola which passes two points (the origin and first yielding) and has the initial stiffness of masonry, the equation has the following form:

$$\varphi = \frac{1}{EI_0} M + c_3 M^2 \tag{7.2}$$

where c_3 can be determined by (φ_y, M_y).

(4) A quartic polynomial which passes through the origin and first yielding point and has the form of

$$\varphi = \frac{1}{EI_0}M + c_4M^4 \qquad (7.3)$$

where c_4 can be calculated in the same way as (3)

The computed lateral force-displacement envelope with quartic moment-curvature curve (4) gave the best prediction, but the differences were not significant between the four curves. The comparisons between computed envelope (curve 4) and tested hysteresis loops will be presented in the following section. For time-history response analyses, tri-linear curve was used to reduce computer time. The shear load-deformation relationship applied for the computation was bilinear curve symmetric in the two opposite directions, as described in Chapter 3.

7.2.3 Comparisons Between Computed and Test Results

Walls F1 and F4 were analyzed with the above structural component model and the quartic moment-curvature curve (Eq. 7.3). The computed load-displacement envelopes and the comparisons with the pseudo-static test hysteresis loops are presented in Figs. 7.1 and 7.2 respectively. It can be seen that for wall F1, the predicted envelope coincides well with the test load-displacement loops. For wall F4, in the direction of flange in compression, the predicted envelope is very close to the test result, but in the direction of web in compression, both computed ultimate strength and displacement are higher than the test results (especially the latter). The reason is as mentioned in Chapter 5 that for confined masonry, the ultimate strain is assumed to be 0.008 for the analysis. During the test, the masonry at the web toe exhibited wide cracks and the extreme vertical reinforcement suffered extensive inelastic tension strains in the direction of loading the flange in compression. When under reverse loading, before the masonry in the web toe could support compression stress, it was necessary for the web reinforcement to yield in compression to remove the residual strain and close the cracks. During the process, there was no effective lateral support to the web vertical reinforcement, which exhibited lateral instability, placing eccentric loads on the masonry and causing failure long before the masonry reached its ultimate compression strain.

Table 7.1 lists both the analytical and experimental horizontal and vertical displacements at the maximum responses for wall F1. It can be seen from the table that the theoretical results coincide well with the measured values for horizontal displacement, including the displacement due to shear. The vertical displacements of top section at each edge of the web monitored at maximum response are listed in row 1 of the Table. Also presented in row 2 of the table are computational results for the same situation with the position of the one-dimensional element in local coordinates coinciding with the neutral axis of the cross section of the flanged wall before cracking. It is obvious that the computed displacement at the free end of web is larger than the measured value, while, at the opposite end, the predicted value is smaller than the test result.

The explanation for the above differences is that the vertical displacement at each end of the web is caused by the rotation of wall cross sections. As a consequence of variation in the neutral axis position resulting from cracking, the flexural response of a T-section wall may result in axial deformation relative to the initial uncracked neutral axis, as shown in Fig. 7.3, which will decrease the displacement at the free end of the web and increase displacement at the opposite end.

To consider the overall effects of variation of neutral axis of cross sections along the wall height, a second analysis was made taking the neutral axis in the SCM modal equal to the mean value of compression depths before cracking and at ultimate state. The computational results with this average neutral axis are also presented in row 3 which are very close to the test results.

From the comparison between the analytical results with SCM modal and experimental results, the following respects can be concluded:

(1) The structural component modal can give reasonable lateral load-displacement prediction for flanged masonry walls in the direction parallel to the web.

(2) The computed response envelope depends on the moment-curvature relationship applied. The quartic curve assumed between first cracking and yielding results in better response envelope for this section than the trilinear curve, but does not affect the response after yielding significantly.

(3) The structural component modal can also predict the vertical displacement well, provided the position of equivalent neutral axis after cracking is assumed properly. The mean value of uncracked cross section and value at ultimate state is a reasonable approximation.

Table 7.1 Displacement at Maximum Loading, Wall F1

	Load (kips)	Horizontal Displ. (in)		Vertical Displ. (in)	
		Total	By shear	Joint end	Free end
Experiment	63.4	1.63	0.62	0.206	-0.275
Analysis 1	66.0	1.56	0.56	0.106	-0.393
Analysis 2	66.0	1.56	0.56	0.236	-0.263

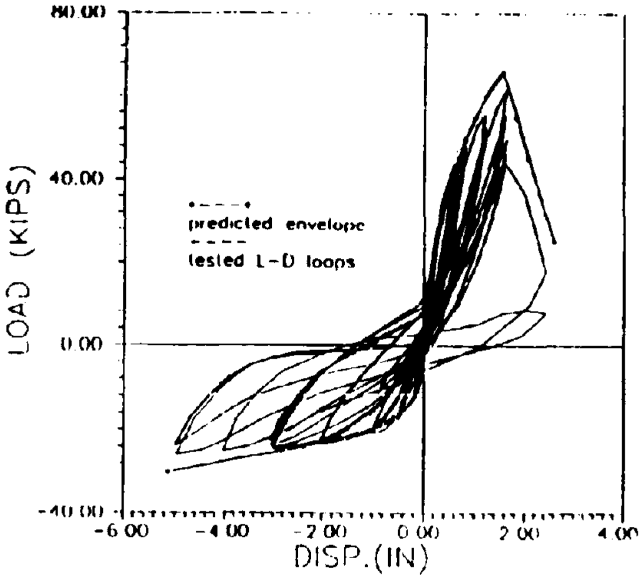

Fig. 7.1 Horizontal Load Displacement, Wall F1

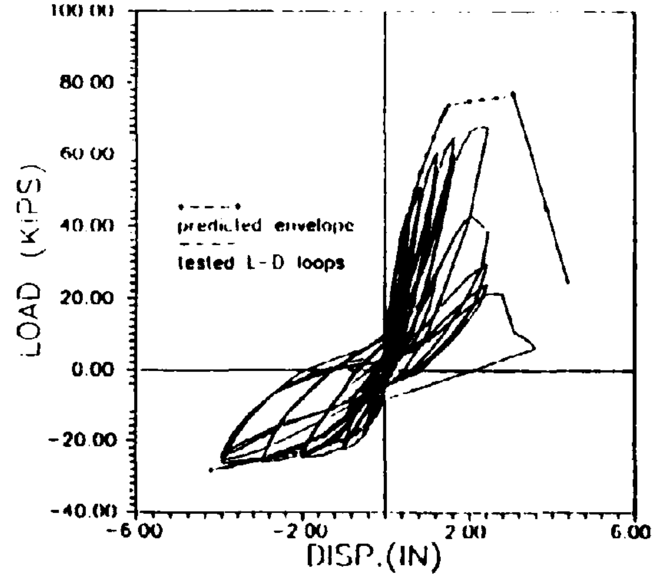

Fig. 7.2 Horizontal Load Displacement, Wall F4

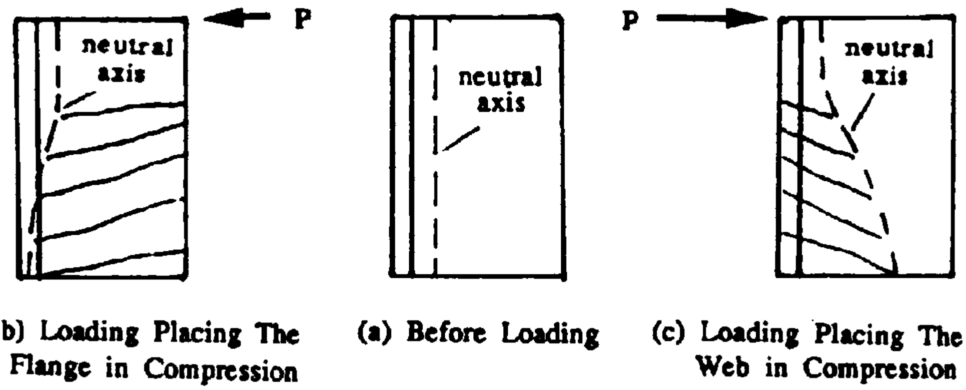

(b) Loading Placing The Flange in Compression

(a) Before Loading

(c) Loading Placing The Web in Compression

Fig. 7.3 Variation of Neutral Axis Position for Flexural Deformation

7.3 Time-history Response Analyses

7.3.1 General Description

The numerical examples presented here are responses of wall F5, F6 and F7. Two critical runs were analyzed for each wall and compared with the experimental results. The parameters and details of the tests are as follows.

Wall F5:

(1) Run #7: input with sinusoidal excitation F = 5 Hz, amplitude A = 0.35 inch (8.89 mm, maximum acceleration 0.89 g), shake table run

time t = 1 second and data acquisition for 3 seconds. This is the last run for sinusoidal tests during which the extreme vertical reinforcement at the web free end was close to yield state.

(2) Run #13: input with earthquake record of El Centro 1940 N-S, time factor 0.25 and displacement factor -1.0. Shake table run time was about 8.5 seconds with 10 seconds of data acquisition. The wall reached its maximum response during this test.

Wall F6:

1) Run #6: input with sinusoidal excitation F = 5 Hz, amplitude A = 0.30 inch (7.62 mm, maximum acceleration 0.76 g), shake table run time t = 1 second and data acquisition for 3 seconds. The extreme vertical reinforcement at the web free end yielded during this test.

(2) Run #12: input with earthquake record of El Centro 1940 N-S, time factor 0.25 and displacement factor -0.75. Shake table run time was about 8.5 seconds with 10 seconds of data acquisition. The wall reached its maximum response during this test.

Wall F7:

The two runs analyzed for confined wall F7 were similar to those for F5. The first case was also run #7 of wall F7 which had the same shake table input and data acquisition requirement as wall F5. The second example was run #12, for which the shake table input and data acquisition were identical to run #13 of wall F5 and the wall reached its maximum response in the direction of the web in compression.

7.3.2 Equations for Dynamic Response Analysis

A structure subjected to excitations at its base is shown in Fig. 7.4, where V_g represents the ground movement and U is the displacement vector of a multi-DOF system relative to the base. In our case, the structure is simplified as a single DOF, but the all following equation are applicable. At any given time t, and using a time increment Δt, the incremental differential equation of equilibrium can be obtained as follows:

$$[M]\{\Delta\ddot{U}\}+[C(t)]\{\Delta\dot{U}\}+[K(t)]\{\Delta U\}=-[M]\{1\}\Delta\ddot{V}_g(t) \qquad (7.4)$$

where $[M]$, $[C(t)]$ and $[K(t)]$ are mass, damping and stiffness matrices of the structure respectively. A Step-by-step integration approach with the Wilson-θ method[24] was employed to solve the incremental equation of equilibrium in the computer program. In our case, since time interval was chosen to be very small comparing the natural period T of the wall (Δt = 0.005 second, T = 0.11 second), the linear acceleration approximation was used (i.e. $\theta = 1$). Since it is proved from the test result that the effect of rotation of the inertia mass is not significant, only one degree of freedom (horizontal displacement) was computed to reduce computation. The damping was assumed to be constant during the computation.

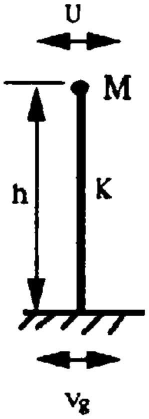

Fig. 7.4 Model for Dynamic Analysis

With linear acceleration integration approach, for each time interval Δt, equation (6.4) was conducted to solve the following equation:

$$\tilde{K}(t)\,\Delta U(t) = \Delta\tilde{P}(t) \tag{7.5}$$

where

$$\tilde{K}(t) = K(t) + \frac{6}{\Delta t^2} M + \frac{3}{\Delta t} C \tag{7.6}$$

and

$$\Delta\tilde{P}(t) = \Delta P(t) + M\left[\frac{6}{\Delta t}\dot{U}(t) + 3\,\ddot{U}(t)\right] + C\left[3\,\dot{U}(t) + \frac{\Delta t}{2}\ddot{U}(t)\right] \tag{7.7}$$

are called equivalent stiffness and load increment matrices respectively in which

$$\Delta P(t) = -M\{1\}(\ddot{V}_g(t + \Delta t) - \ddot{V}_g(t)) \tag{7.8}$$

is the contribution from base excitation. Solving equation (7.5) for $\Delta U(t)$, the incremental velocity and acceleration can then be obtained by the following:

$$\Delta \dot{U}(t) = \frac{3}{\Delta t} \Delta U(t) - 3\dot{U}(t) - \frac{\Delta t}{2} \ddot{U}(t) \tag{7.9}$$

$$\Delta \ddot{U}(t) = \frac{6}{\Delta t^2} \Delta U(t) - \frac{6}{\Delta t} \dot{U}(t) - 3\ddot{U}(t) \tag{7.10}$$

After the incremental values are calculated, the total displacement, velocity and acceleration at the end of time increment can be updated and a new step can start. A computer program was written in FORTRAN 77 to carry out the analysis and is listed in Appendix c for reference.

7.3.3 Analytical Results and Comparisons

Both experimental and analytical response displacements and accelerations at the top mass center for runs #7 and #13 of wall F5, runs #6 and #12 of F6 and runs #7 and #12 of F7 are presented in Fig. 7.5 through Fig. 7.14 respectively. Unfortunately, the top displacement for wall F7 was not recorded due to instrument problem, the comparisons for this wall are only for accelerations in Figs. 7.13 and 7.14. From the comparisons, the following aspects can be noted:

- **Response to Sinusoidal Excitation:** The analytical results have a excellent agreement with the experimental results for both displacement and acceleration, especially for walls F5 and F7. During the forced vibration cycles (about 0.5 sec. to 1.5 sec., because the data recorder started earlier than the shake table in order not to lose data), the analytical curves coincide well with the experimental curves. After the shake table stopped (about 1.5 sec.), the natural period of the vibration with analytical model is a little longer than the test results for the all walls.

- **Response to the Earthquake Record:** The responses during sinusoidal input were mainly within elastic range of material response, although the walls were cracked. To evaluate the structural component model in the inelastic range, responses to earthquake record for these three walls during which each wall reached its maximum response were analyzed and compared with experimental results. From the figures, it can be seen that the analytical responses coincide well with the experimental curves up to the maximum response and agreement decreased after that. Also the agreement is a little better for acceleration than for displacement.

- **Hysteresis Loops:** Figs. 7.15 and 7.16 compare the acceleration (lateral force)-displacement hysteresis loops for runs #7 and #13 of wall F5 between analytical and experimental results respectively. Considering the complicated nature of the hysteresis phenomenon in the inelastic range, the prediction with the analytical model is quite good and acceptable.

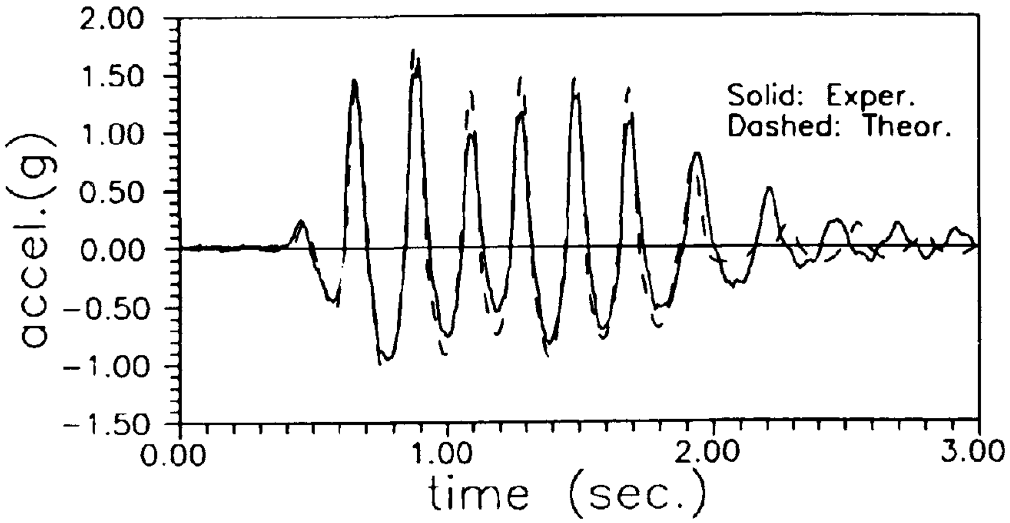

Fig. 7.5 Response Acceleration, Run #7, Wall F5

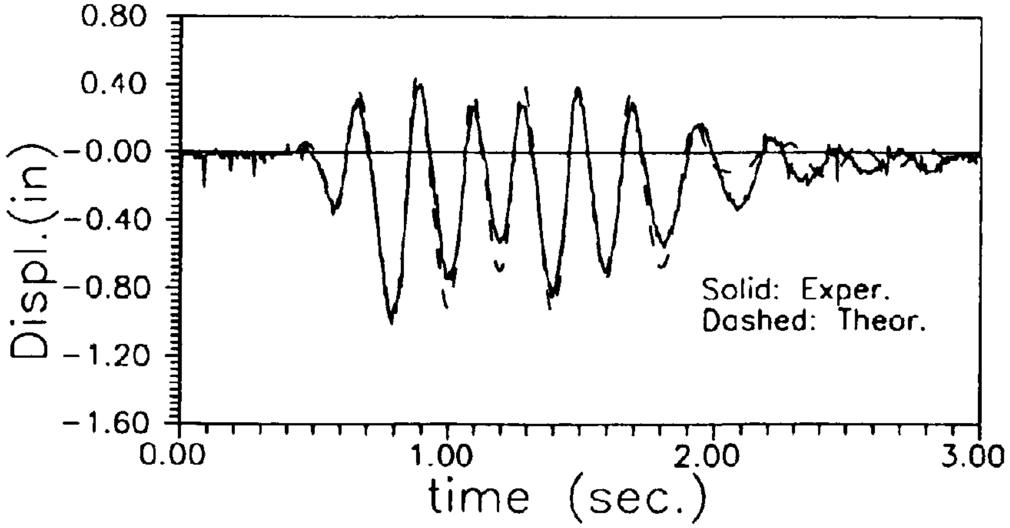

Fig. 7.6 Response Displacement, Run #7, Wall F5

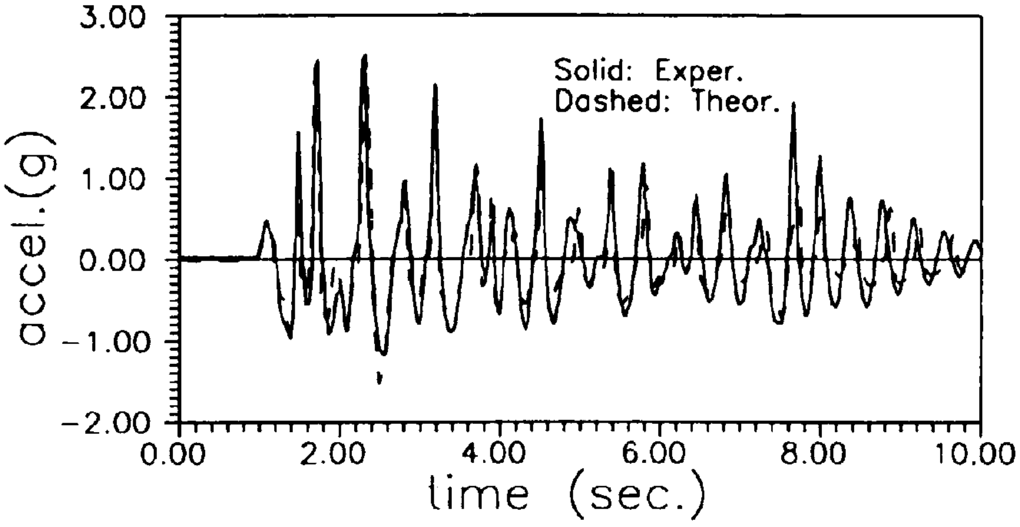

Fig. 7.7 Response Acceleration, Run #13, Wall F5

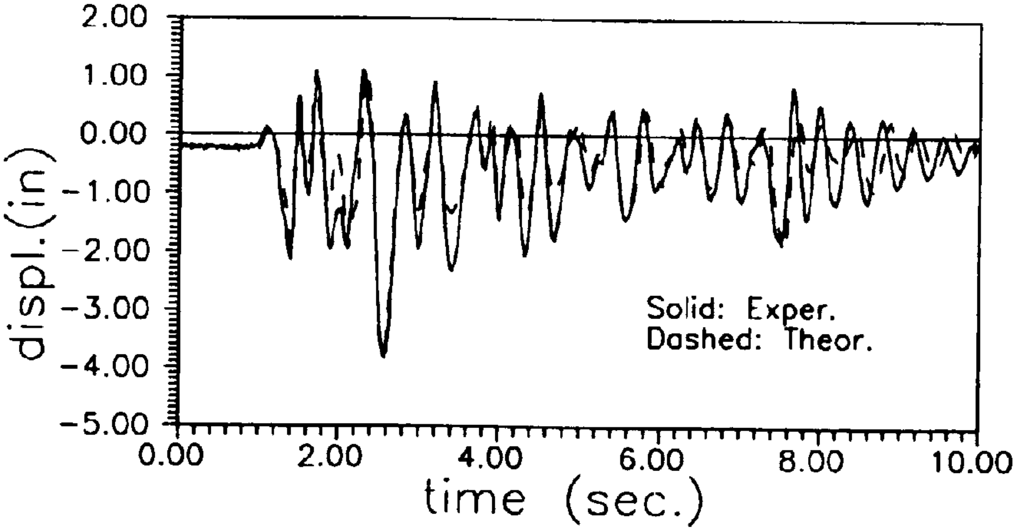

Fig. 7.8 Response Displacement, Run #13, Wall F5

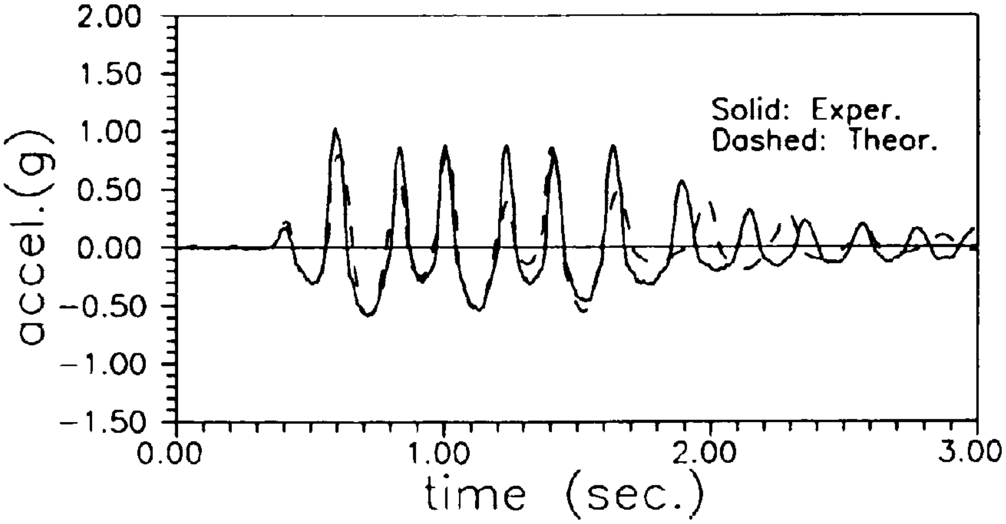

Fig. 7.9 Response Acceleration, Run #6, Wall F6

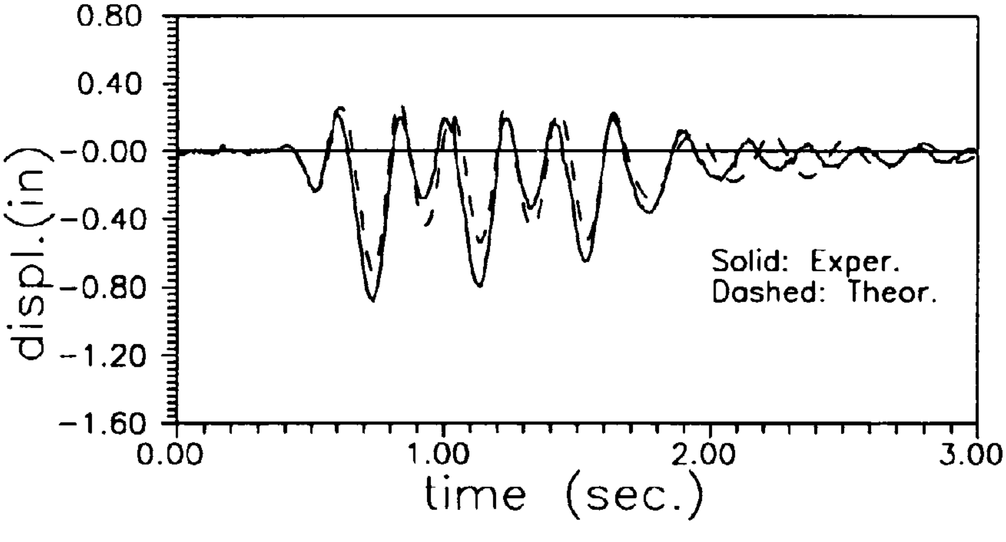

Fig. 7.10 Response Displacement, Run #6, Wall F6

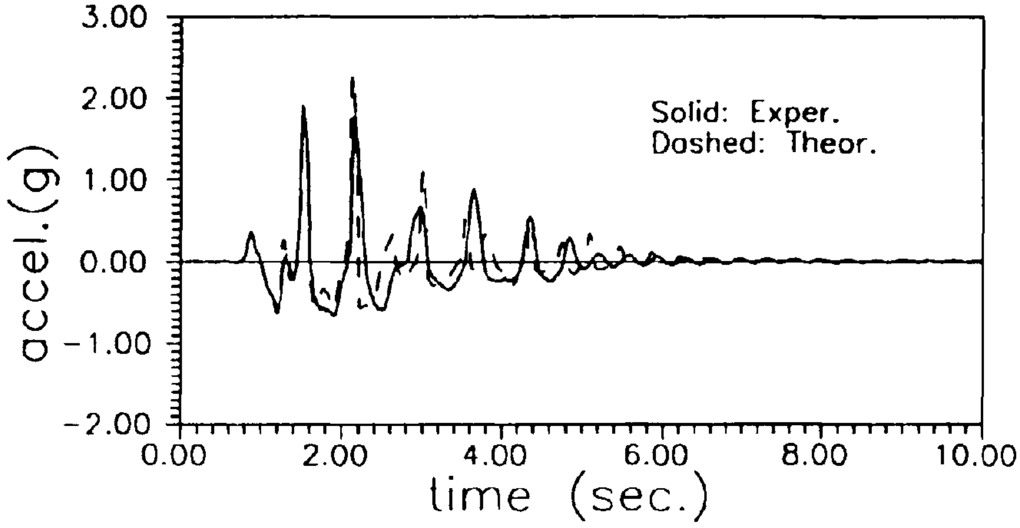

Fig. 7.11 Response Acceleration, Run #12, Wall F6

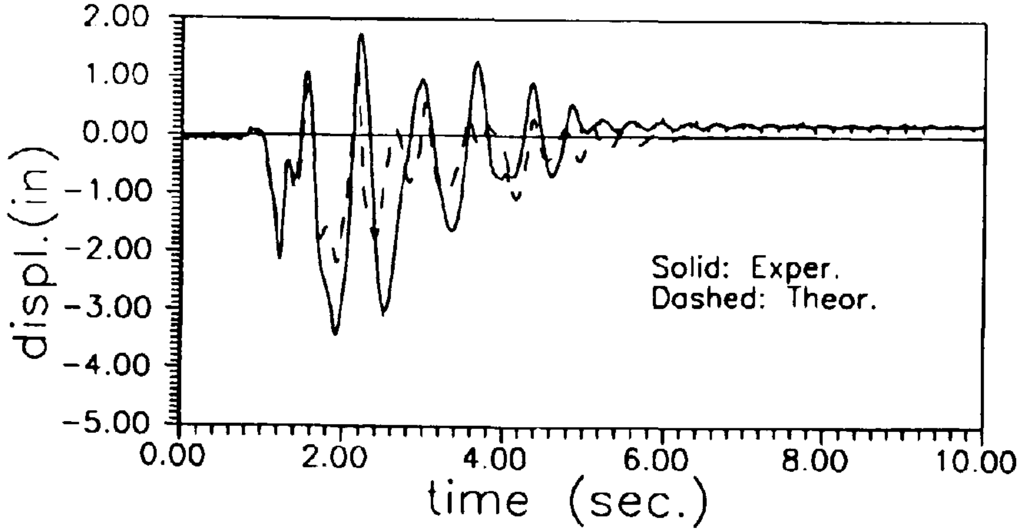

Fig. 7.12 Response Displacement, Run #12, Wall F6

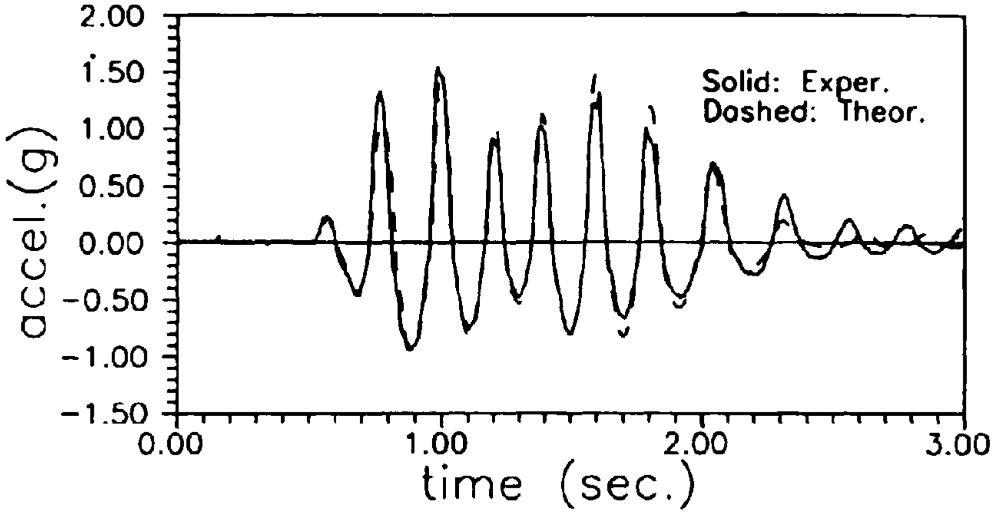

Fig. 7.13 Response Acceleration, Run #7, Wall F7

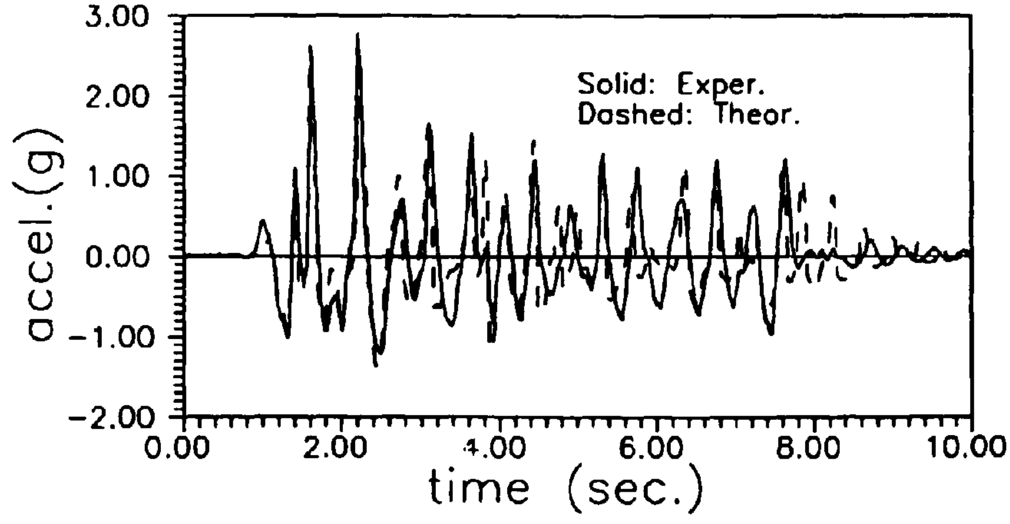

Fig. 7.14 Response Acceleration, Run #12, Wall F7

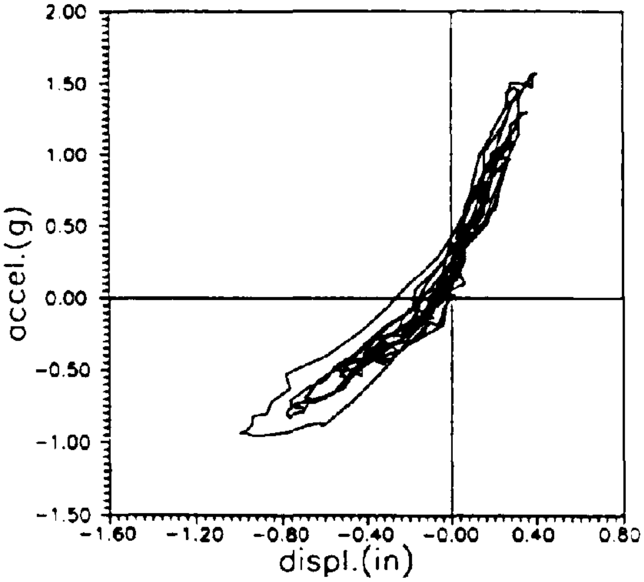

(a) Experimental

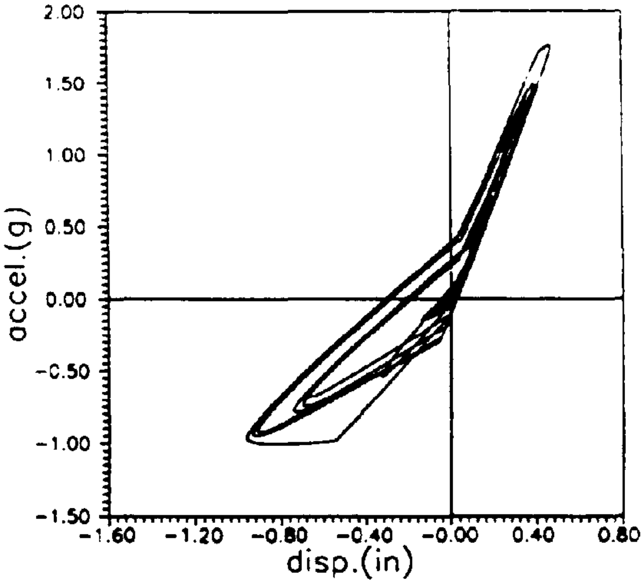

(b) Analytical

Fig. 7.15 Acceleration-displacement Loops, Run #7, Wall F5

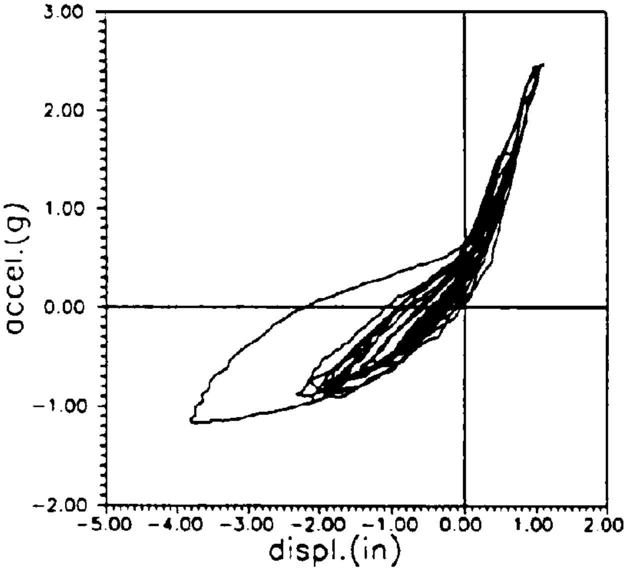

(a) Experimental

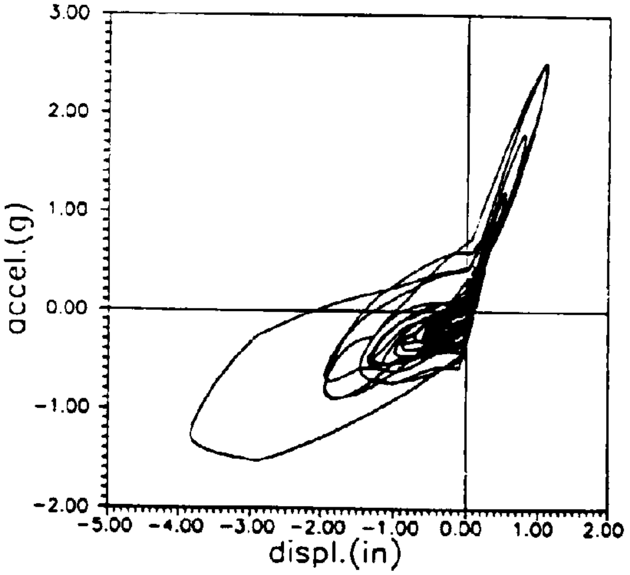

(b) Analytical

Fig. 7.16 Acceleration-displacement Loops, Run #13, Wall F5

7.4 Discussions and Conclusions

The numerical examples for inelastic analysis of flanged masonry walls proved clearly the application of the structural component model and inelastic hysteresis loops proposed in Chapter 3. The computation showed that the response is very sensitive to the assumed damping ratio ξ of the structures and the shape of the hysteresis loops, especially the yield point on the envelope and the stiffness degradation factor λ.

For run #7 of wall F5, $\xi = 0$, 0.02, 0.025, and 0.03 (keeping $\lambda = 0$) and $\xi = 0.02$, $\lambda = 0.2$ have been tried. The computation results show that with $\xi = 0.02$ and $\lambda = 0$, the best result was obtained. This is a little unexpected because that from Fig. 5.8, the damping ratio measured during the test is 0.032 for the direction of web in compression and 0.037 for the flange in compression, respectively. For run #13, $\xi = 0.04$ and $\lambda = 0.2$ resulted in the response closest to the test data, much less than the measured values of $\xi = 0.045$ for web in compression and $\xi = 0.07$ for the flange in compression.

The skeleton of moment-curvature hysteresis loops decides the envelope of the response and the yield point on the line is critical to the response, meanwhile the first cracking point does not change the response significantly. The analytical results of flanged masonry walls and the comparisons with experimental results enable to draw the following conclusions:

(1) The inelastic structural component model developed for flanged masonry walls can simulate the overall nonlinear behavior of the structure and the formation of the plastic hinges at the wall ends.

(2) The proposed asymmetric hysteresis loops worked well for the time-history response analysis on flanged masonry walls, and the damping ratio ξ and stiffness degradation factor λ are critical to the analytical results, and should thus be carefully chosen.

(3) The additional longitudinal deformation of initial neutral line of wall section due to cracking will affect the vertical displacement distribution of top section. Taking the average value of neutral lines corresponding to the compression zones before cracking and at the ultimate state of wall section as the computation neutral line seems to be a reasonable approximation

(4) Further improvement on inelastic analysis of flanged masonry walls can be achieved through using the varying damping ratio and stiffness degradation factor in the two opposite loading directions instead of fixed values and more sophisticated hysteresis loops for shear deformation

(5) More numerical examples, especially the masonry assemblages which have T-section components, are needed to evaluate and calibrate the analytical model developed in this report.

8. EFFECTIVE FLANGE WIDTH OF T-SECTION MASONRY WALLS

8.1 Introduction

Flanged masonry walls have different strength, stiffness and ductility in the two opposite directions parallel to the web when subjected to horizontal in-plane loads. In the direction of flange in compression, the width of flange does not affect the behavior of the wall significantly. On the contrary, when the flange is in tension, the extent to which the flange reinforcement contributes to the flexural strength will be subjected to shear-lag effects.

Because of shear-lag effects, the flange may not participate fully in the action with the web , and an effective flange width is needed for predicting actual strength and stiffness of the structures. Although the New Zealand design code[3] provides some guidance on this effect, its provisions are based on the application of ACI design rules[2] for effective width of T-beam floor, and have not been verified experimentally.

In this chapter, both theoretical and experimental studies on shear-lag effects are introduced. The experimental results are from pseudo-static tests and dynamic tests of full scale flanged masonry walls, including one with very wide flange , as described in chapters 5, and 6 in order to provide a data base for the theoretical studies. The theoretical efforts include using elastic theory to solve a simplified plane-stress problem to simulate the strain and vertical deformation distribution along the flange and allow to extrapolate the experimental results to a more useful range. Based on the results of above studies, formulas for determining the effective flange width are proposed in this chapter.

8.2 Experimental Results

The detail of pseudo-static and dynamic tests on full scale flanged masonry walls can be found in chapters 5, and 6 respectively. The arrangement of straingauges on vertical reinforcement and linear potentiometers at lower part of the wall, which were used to monitor the distribution of vertical strain and deformation along the flange during the tests is shown in Figs. 4.1 and 4.2.

Figures 8.1, 8.2 and 8.3 present the measurement of flange strains and deformations for wall F1 at three different loading levels: before cracking, about yield point and at maximum response respectively. The strains of vertical reinforcement and deformation of masonry face at base level for wall F3 (the wall with the wider flange) are shown in Fig. 8.4. Unfortunately, some of the straingauges were damaged during the grouting or afterwards.

It can be seen from the figures that for wall F1(l/h = 0.722), at lower load level (p = 15 kips, prior to cracking) there is a slight drop for both vertical reinforcement strains and wall vertical deformation from the flange center towards its ends. After cracking, hardly any decrease of vertical strain or deformation is apparent along the flange, especially at the base level. For the wide flange wall F3 (l/h = 1.389), with the increases of width/height ratio, the shear-lag effects are more obvious than that for wall F5 and the ratio of vertical deformation and strain at ends to the center of the flange decreases.

Table 6.3 lists the comparison of ultimate horizontal loads between predicted values and test results for walls F1 to F8. The predicted values were based on the plane cross section assumption, i.e. the whole flange will fully participate in action with the web, including the wide flange wall F3. The comparisons show that the predicted ultimate loads coincide well with the experimental results (for wall F2 and F3, the test results are even a little higher than the predicted ones) which indicates that the whole flange did participate fully in action with the web in each case.

Table 6.2 summarizes the natural frequencies for wall F5 (identical to wall F1). The predicted value was based on the gross section of the wall and elastic modules of masonry $E_m = 2000$ ksi, shear modules $G_m = 0.4 E_m$. The coincidence of predicted frequency with the test result on ground shows that the flange participated fully in the action with the web, therefore it is much stiffer than the case of only rectangular section is considered (5.9 Hz). It is very important to note that the vertical strains in the flange decrease from the web/flange intersection to is two ends and the shape of the distribution curve looks very similar to the solution for a beam on elastic foundation. In the following section, a simulated analysis based on the analogy between the two phenomena is carried out to extrapolate the experimental results to more useful range.

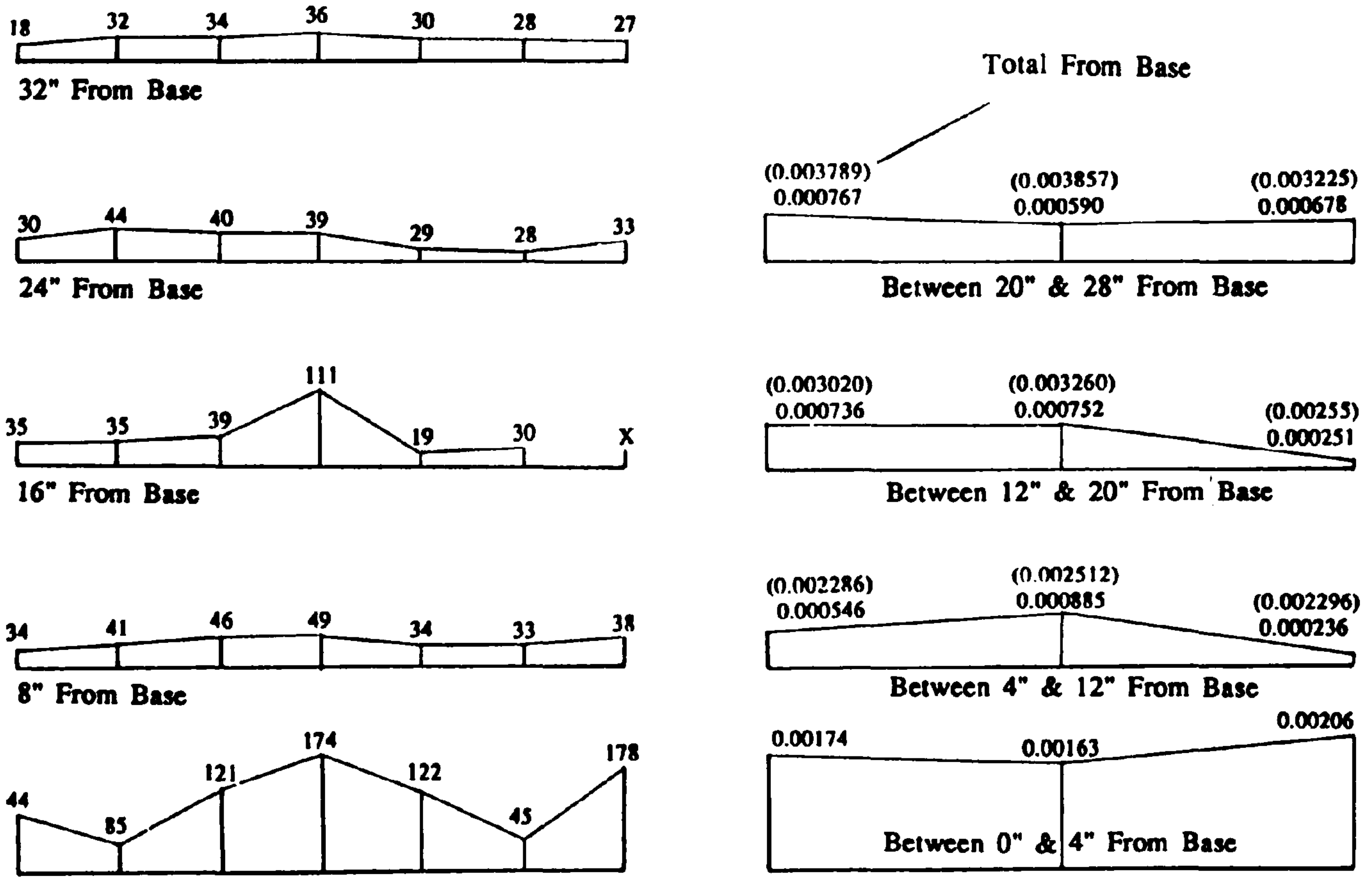

(a) Strain Distribution (mε)

(b) Vertical Deformation (in)

Fig. 8.1 Before Cracking, Wall F1, P_w = 15 Kips

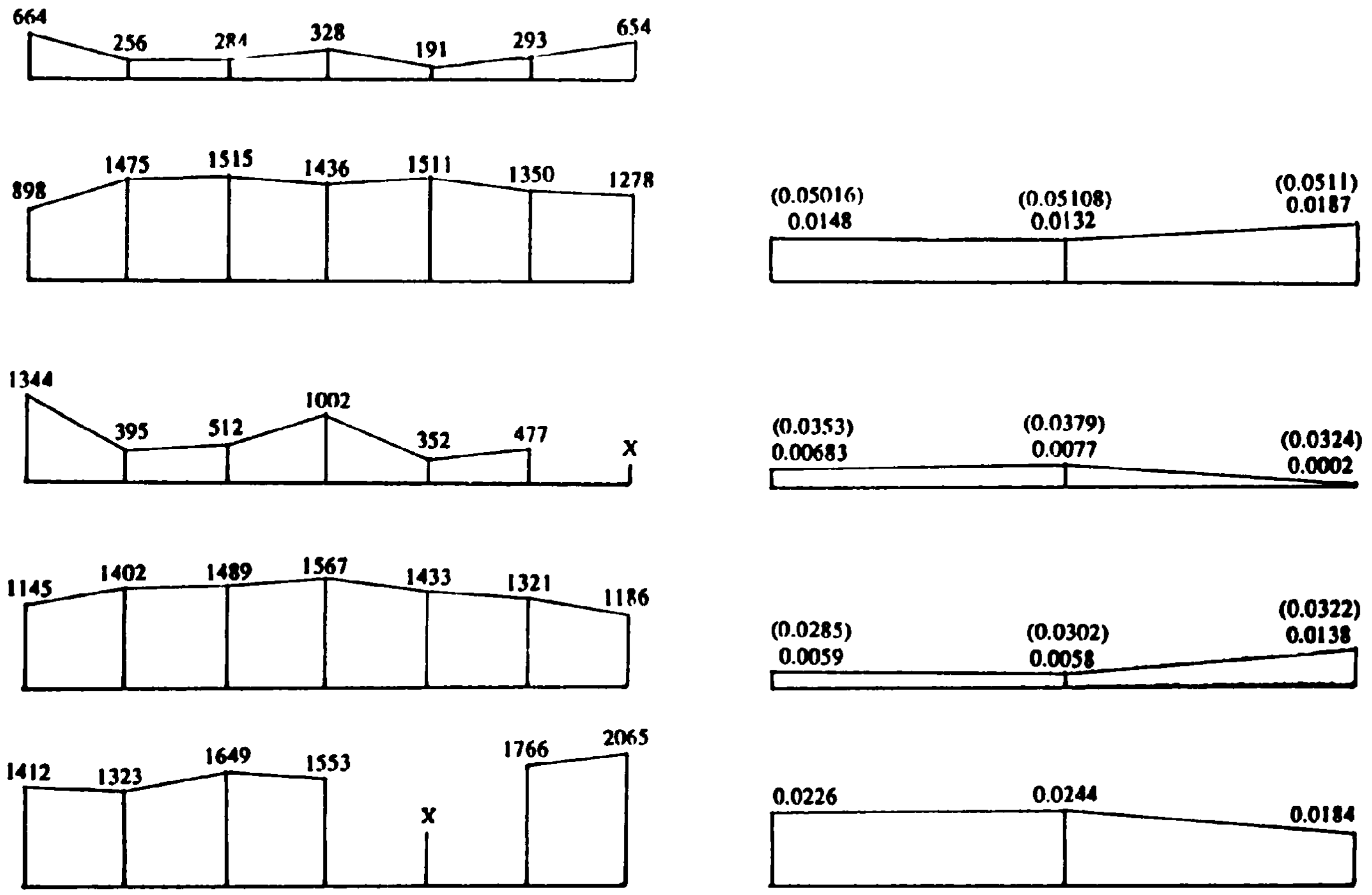

(a) Strain Distribution (mε)

(b) Vertical Deformation (in)

Fig. 8.2 Before Yielding, Wall F1, $P_w = 49$ Kips

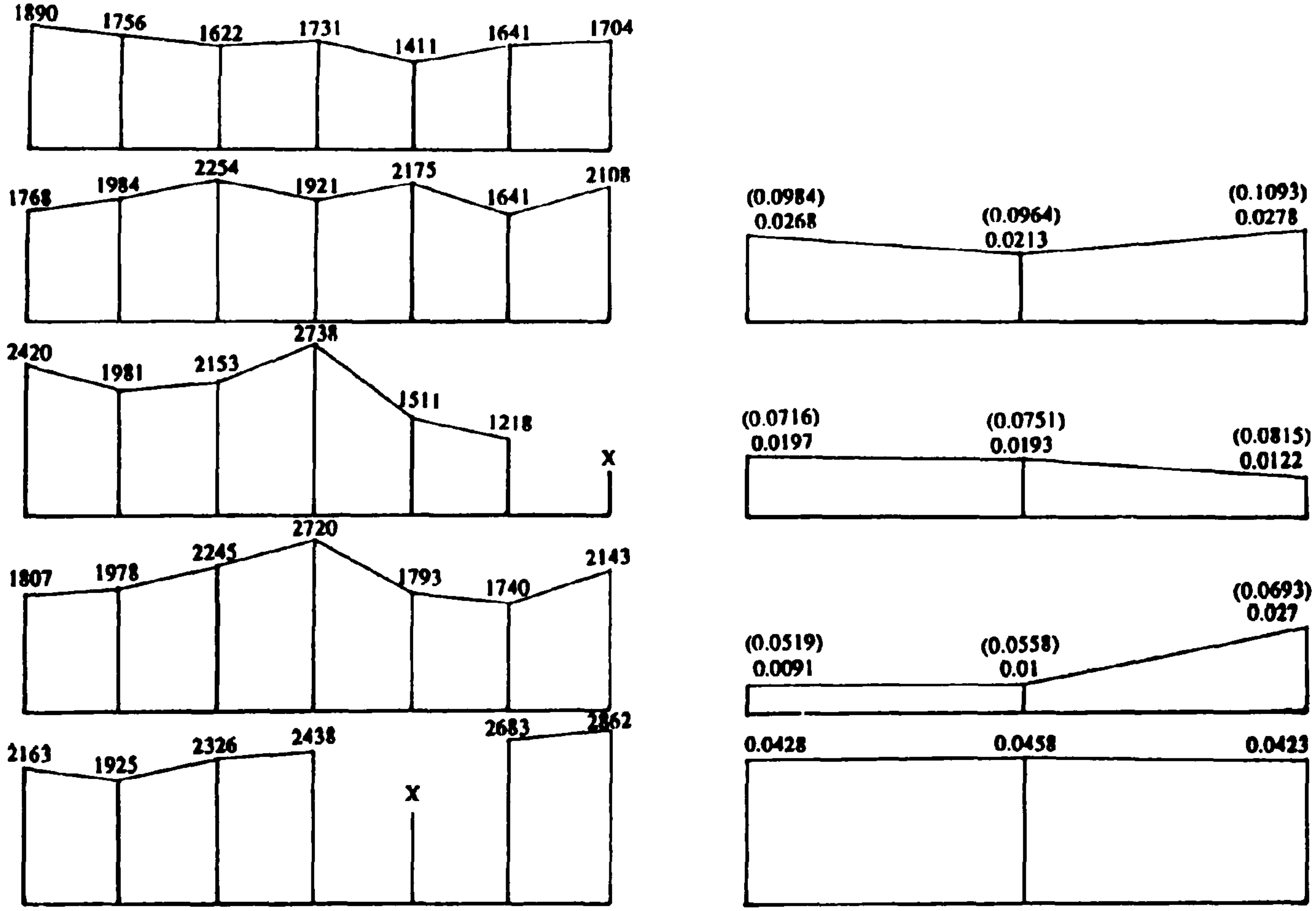

(a) Strain Distribution (με)

(b) Vertical Deformation (in)

Fig. 8.3 At Maximum Response, Wall F1, $P_w = 63.4$ Kips

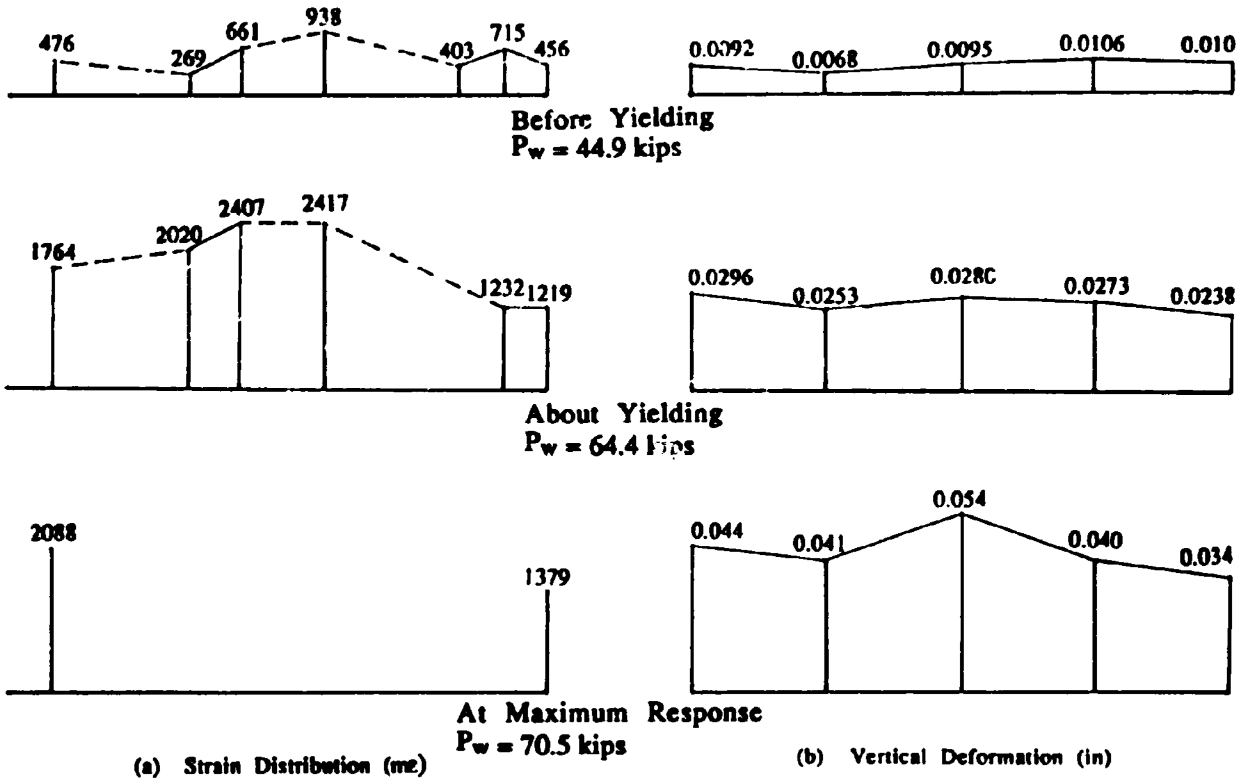

Before Yielding
$P_w = 44.9$ kips

About Yielding
$P_w = 64.4$ kips

At Maximum Response
$P_w = 70.5$ kips

(a) Strain Distribution (me)

(b) Vertical Deformation (in)

Fig. 8.4 Vertical Strain and Deformation At Base, Wall F3

8.3 Analytical Simulation

A typical flanged masonry wall subjected to horizontal loading parallel to the web is shown in Fig. 8.5 (a). When the wall is subjected to bending, there will be a shear flow along the intersection of the web and flange to ensure compatible deformation of the web and flange. To investigate the shear-lag effects in the flange, a separated 2-dimension model is shown in Fig. 8.5 (b). This can be further simplified by simulation as a beam with finite length on an elastic foundation (Fig. 8.5 (c)).

Assuming a Winkler foundation, the differential equation of equilibrium can be derived as

$$E\,I\frac{d^4 w}{dx^4} + K\,w = 0 \tag{8.1}$$

where w represents the vertical displacement function, k is stiffness of the foundation, E and I are elastic modulus and moment of inertia of the flange. The solution of above equation can be expressed as

$$w = e^{\beta x}(c_1\cos\beta x + c_2\sin\beta x) + e^{-\beta x}(c_3\cos\beta x + c_4\sin\beta x) \tag{8.2}$$

in which

$$\beta = \left[\frac{K}{4\,EI}\right]^{1/4} \tag{8.3}$$

and c_1, c_2, c_3 and c_4 are constants which can be determined by the following boundary conditions:

$$
\begin{aligned}
x = 0: &\quad \frac{dw}{dx} = 0, \quad EI\frac{d^3w}{dx^3} = -\frac{P}{2} \\
x = \frac{l}{2}: &\quad EI\frac{d^2w}{dx^2} = 0, \quad EI\frac{d^3w}{dx^3} = 0
\end{aligned}
\tag{8.4}
$$

The expression of w(x) is lengthy and complicated, but the general trend of the deflection curve is to decrease from the center towards the ends, as shown in Fig. 8.2 (a) and the ratio of end deflection to center deflection has the form of

$$
\frac{w_{l/2}}{w_0} = \frac{4\cosh(\frac{\beta l}{2})\cos(\frac{\beta l}{2})}{2 + \cosh(\beta l) + \cos(\beta l)} \tag{8.5}
$$

and the plot is shown in Fig. 8.6 (b).

To simplify expression (8.3), assume that at ultimate state, the wall cracked at the base and is supported on distributed vertical reinforcement. The foundation stiffness k can be approximately expressed as

$$
K = \frac{nA_sE_s}{h_p l} = \frac{\rho E_s t}{h_p} \tag{8.6}
$$

In which n, A_s, E_s and ρ are number, cross section area, elastic modulus and reinforcement ratio of vertical bars respectively and h_p is the height of the vertical reinforcement in the plastic hinge zone. For the rectangular section, the moment of inertia is

$$
I = t\,h^3 / 12 \tag{8.7}
$$

If shear deformation is considered, the equivalent stiffness of the wall can be modified as

$$
I^* = \frac{I}{1 + F} \tag{8.8}
$$

in which F can use the expression in Chapter 2 as following

$$F = \frac{9I}{Al^2} = 0.75\left(\frac{h}{l}\right)^2 \tag{8.9}$$

Substitute I^* and K into expression (8.3), the corresponding value of βl can be calculated.

From Fig. 8.6 (b), when βl = 1.5, the ratio of $w_{l/2}$ to w_0 is close to 1, which indicates that the whole flange can participate in the action entirely. Assuming E_s/E = 10, $h_p = 0.08\,h + 6\,d_b$, where d_b is the diameter of the vertical reinforcement, then l/h = 1.55 can be derived. Similarly, when $\rho l = \pi$, l/h = 3.43 can be obtained.

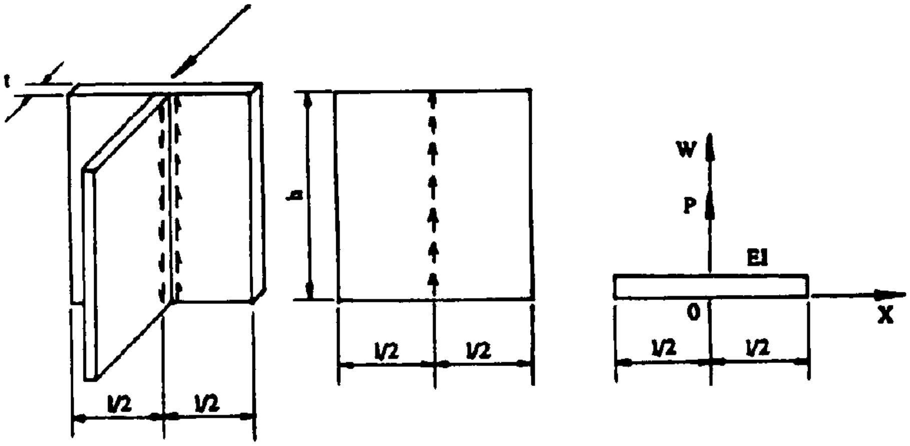

(a) Flanged Wall (b) Two-dimension Model (c) Beam on Elastic Foundation

Fig. 8.5 Interaction Between Flange and Web and Its Modelling

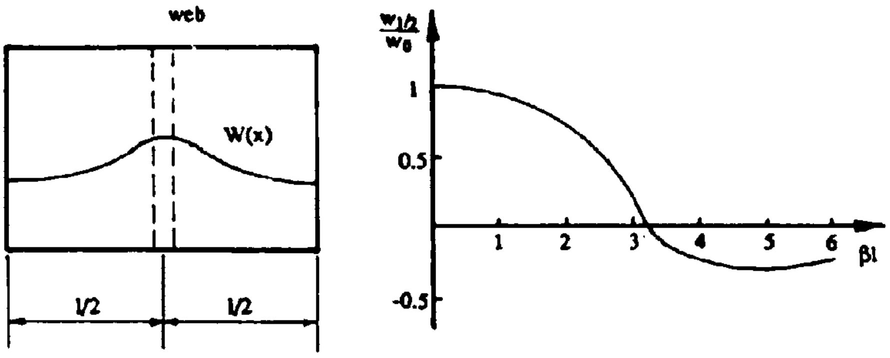

(a) Vertical Displacement Distribution

(b) Variation of $\frac{w_{l/2}}{w_0}$ With βl

Fig. 8.6 Vertical Displacement Distribution

8.4 Inelastic Finite Element Analysis

A computer program using a special inelastic finite element model for masonry assemblages developed by Seible and Kingsley[43] based on an earlier work by Seible and LaRovere[25] was employed to analyze flanged wall F1 to investigate the vertical strain and displacement distribution along the flange, and compare with experimental results and values predicted by the elastic shear lag model described in Section 8.3. Since both the structure and loads are symmetric, only half of the system was analyzed. The element discretion is shown in Fig. 8.7. Analysis simulated the pseudo-static tests with monotonically increasing displacement applied at the loading point. Measured material properties were used in the analysis, with a value of 300 psi being adopted for the average masonry tension strength, as found from analysis of flange cracking, reported in Section 5.3.5.

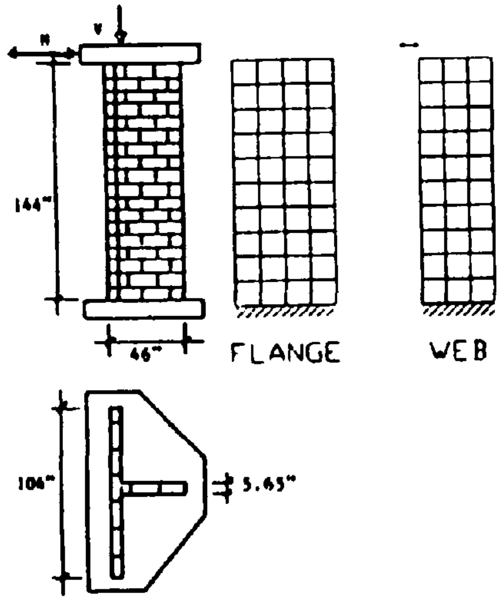

Fig. 8.7 Element Discretion for Flanged Wall F1

The calculated vertical strain and displacement distribution along the flange at different height levels for three loading stages and comparisons with the corresponding test results are presented in Figs. 8.8 to 8.10 respectively. The vertical strains were taken at the Gauss points of each four-node element and the distances from the base are 3, 17.4 and 31.8 inch respectively. The element nodes chosen for vertical displacement were located at the central and end of flange and the distances from the base are 0, 14.4, and 28.8 inch respectively. Three loading stages were selected to check the shear-lag effects: before cracking(P = 17.9 Kips), before first yield(P = 43.1 Kips) and at maximum response(P = 62.7 Kips).

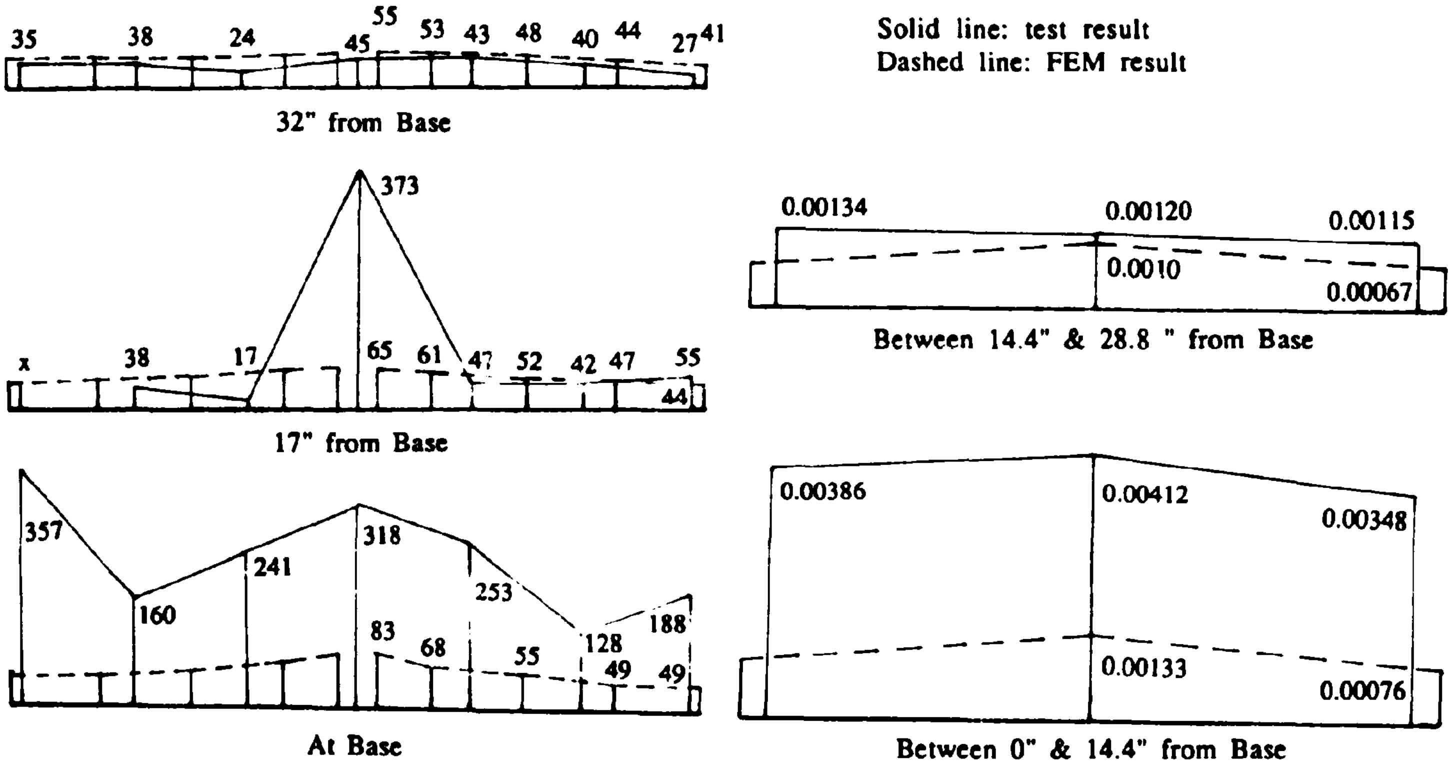

(a) Vertical Strains (με)

(b) Vertical displacement (inch)

Fig. 8.8 Distribution of Vertical Strains and Displacement, F1, P = 17.9 kips

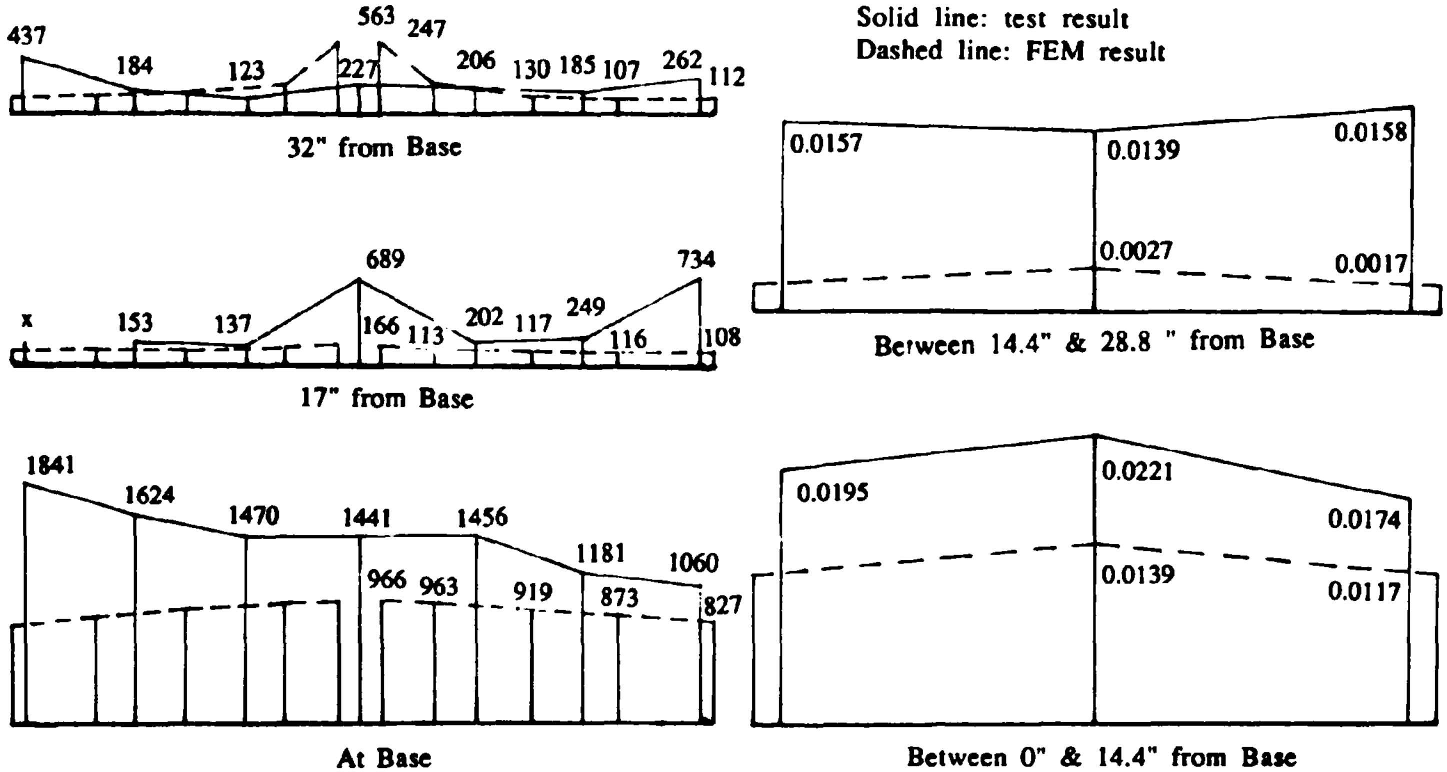

(a) Vertical Strains (με)

(b) Vertical displacement (inch)

Fig. 8.9 Distribution of Vertical Strains and Displacement, F1, P = 43.1 kips

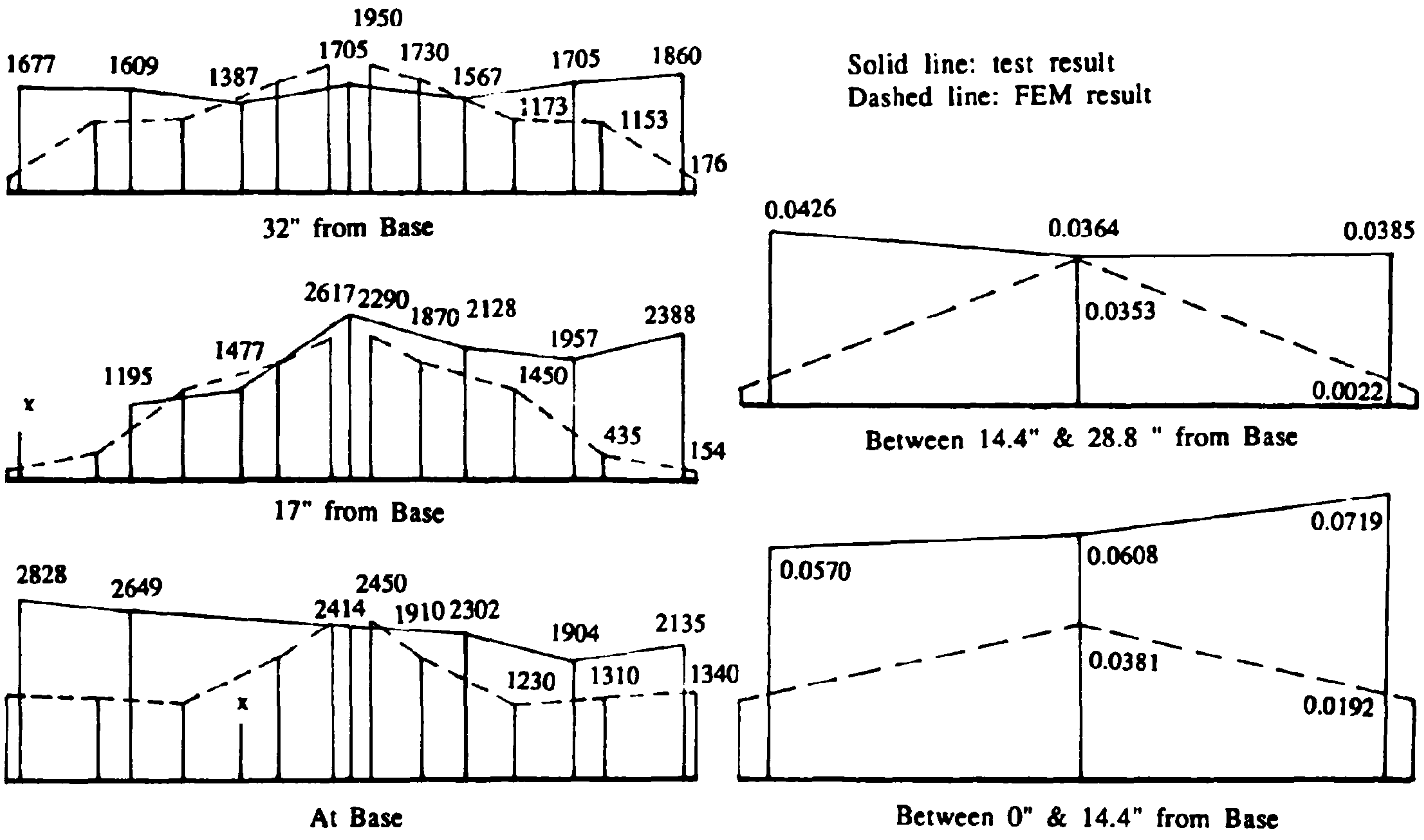

32" from Base

17" from Base

At Base

(a) Vertical Strains (με)

Between 14.4" & 28.8 " from Base

Between 0" & 14.4" from Base

(b) Vertical displacement (inch)

Fig. 8.10 Distribution of Vertical Strains and Displacement, F1, P = 62.7 kips

It can be seen from the figures that the analytical results with this finite element model show the same trends for vertical strain and deformation distribution as that of elastic analysis and test results. At lower load level, the vertical strain and deformation decreases from the center of the flange towards its end along the flange which indicates the shear-lag effects. After cracking, the distribution of vertical strain and deformation becomes even and thus the shear-lag effects is less significant and the effective flange width would be larger after cracking than for uncracked walls.

Before cracking, the vertical strains have reasonable good agreement between the analytical and experimental results which can be seen clearly from the top two cases in Fig. 8.8 (a). The maximum vertical strain at the ultimate state of loading also coincides well with the test result. For other cases, the analytical results have rather poor agreement with the measured values . First, the onset of masonry cracking does not coincide with the test result. In the bottom profile and center section of the middle profile of Fig. 8.8 (a), the analysis indicated that the masonry strains did not exceed the cracking value, where the measured strains on vertical reinforcement clearly indicated that the masonry had already cracked. Fig. 8.10 (a) indicates that all the vertical rebars yielded at the base, but the analysis did not develop yielding over the whole flange section. The predicted vertical displacements are much less than the experimental results for all cases, except before masonry cracking.

From the above comparisons, it can be concluded that although this inelastic finite element model has been shown to predict the global performance of masonry walls and subassemblages very well[25],[43], it needs further improvement to describe detailed behavior of masonry structures after cracking. In this model, masonry and steel reinforcement are treated as overlaid elements in which both materials are subjected to identical strain field. This assumes that masonry and steel are perfectly bonded during deformation. So bond failure and slip between steel and surrounding masonry are not modelled. From experimental observations, it was evident that slip between steel and surrounding masonry at cracked sections was significant, especially at the base level.

The characteristics of the masonry tension model is critical to the prediction of the vertical strains and displacement distributions along the flange. The model adopted by the program uses a linear relationship between tension stress and strain up to tensile strength f_t, then immediately drops the residual tensile capacity to 5 percent of the initial strength. The model assumes masonry to be a homogeneous material and ignore the natural weakness section at mortar beds. As a consequence, strength and stiffness of masonry in the direction normal to the mortar beds will be overestimated. It should be noted that the tension strength of base bed joint was found to be less than at other heights of the wall, since this was a construction joint. This was not modelled in the analytical process and will have contribution to experiment/theory discrepancies.

To determine the cracked conditions, the model uses the principal stress axes resulting in crack formation in a diagonal direction rather than horizontal cracking at bottom half part of the flange which was the real case observed during the tests. After the masonry cracked, the stress-strain relationship in the original plane (horizontal-vertical) was obtained by

$$\begin{Bmatrix} \sigma_x \\ \sigma_y \\ \tau_{xy} \end{Bmatrix} = \begin{bmatrix} E_1c^2+E_2s^2 & 0 & \frac{1}{2}(E_1-E_2)sc \\ & E_1s^2+E_2c^2 & \frac{1}{2}(E_1-E_2)sc \\ \text{sym.} & & \frac{1}{4}(E_1+E_2) \end{bmatrix} \begin{Bmatrix} \varepsilon_x \\ \varepsilon_y \\ \gamma_{xy} \end{Bmatrix} \tag{8.10}$$

where $c = \cos\theta$, $s = \sin\theta$ and θ is the angle between the principal and original coordinate system. Eqn. 8.10 implies that the vertical stiffness of cracked masonry has a significant contribution from the uncracked direction which overestimates the stiffness of cracked masonry and may partly explain why the analytical displacements are much less than the test results.

Nonlinear analyses are normally carried out using either incremental or iterative (successive approximation) methods. It is known that the incremental procedure will increase the stiffness of the system and introduce accumulative errors. On the other hand, the iteration approach may lead the numerical result to converge to a non-real solution.

It can be seen from the above discussion that a more sophisticated inelastic model is needed to predict the detailed behavior of masonry structures due to the complicated nature of the material properties and construction procedure. Unevenness of the material and minor defects in the masonry and grouting may cause earlier cracking which will affect the strain distribution significantly. Therefore, we should not expect any analytical model to predict those random behavior from local effects.

8.5 Conclusion

From the studies above, it is clear that there is shear-lag effect in the flange when the T-section wall is subjected to horizontal forces parallel to the web. When the flange is in compression, the effects of flange width, therefore the shear-lag effects are not significant. On the contrary, in the direction of flange in tension, the shear-lag effects are rather significant for uncracked walls and become less severe after cracking. For the purpose of determining effective flange width, T-section walls can be divided into three groups as follows:

1. **Short flange:** From Fig. 8.6 (b), it is clear that when $\beta l \leq 1.5$, $\frac{w_{l/2}}{w_0}$ is very close to 1. Therefore, the whole flange width will be the effective width. In this group, l/h = 1.5 can be set as the upper limit for this group. (the calculated value is 1.55)

2. **Intermediate flange:** When $\beta l = \pi$, $\frac{w_{l/2}}{w_0} = 0$, the effective flange width can be determined by an equivalent rectangular block with height w_0 and the same area as curved displacement envelope. In this case, l/h = 3.5 can be set up as upper limit (the calculated value is 3.43) and the corresponding effective flange width can approximately estimated as 2.5h. For the T-section walls with its βl value between 1.5 and π, the effective flange width can be determined by interpolating between the above two cases.

3. **Wide flange:** When $\beta l \geq \pi$, the increase of flange width will not cause significant change in vertical displacement distribution,

therefore the effective flange width in this group equals the value at $\beta l = \pi$.

Based on above analyses and the test results, following formulas are proposed for determining the effective flange width to predict the strength and stiffness of T-section walls when subjected to horizontal forces in the direction of flange in tension.

$$l_e = \begin{cases} l & (\, l/h \leq 1.5 \,) \\ 0.75h + 0.5l & (\, 1.5 \leq l/h \leq 3.5 \,) \\ 2.50\,h & (\, l/h \geq 3.5 \,) \end{cases} \tag{8.11}$$

where l_e : effective flange width

l : width of the flange

h : height of the wall

9. SUMMARY AND CONCLUSSIONS

9.1 Conclusions

This is the first systematic research on seismic behavior of flanged masonry walls and the theoretical and experimental studies carried out in this project enables to draw the following conclusions:

(1) General Behavior

The flanged masonry walls have strong unsymmetrical seismic response in the two opposite directions parallel to the web. When the flange is in compression, the wall has lower flexural strength and stiffness, but larger displacement and ductility capacity. Meanwhile, in the direction of flange in tension, they have higher flexural strength and stiffness, but much less ultimate displacement and ductility capacity.

(2) Failure Mechanism

When flanged masonry walls are subjected to earthquake attacks parallel to the web, they will fail in the direction of web in compression due to crushing of masonry , followed by buckling of vertical reinforcement at the free end of web foot. But in the direction of flange in compression, the walls can still sustain the earthquake attacks and undergo deformation.

(3) Flexural Strength and Displacement

The ultimate flexural strength of flanged masonry walls depends mainly on the ratio of vertical reinforcement, axial load level and the width ratio of flange vs. web etc. and can be rationally predicted with cross section analysis which uses the assumption of "plane cross-section" and equivalent compression stress block for masonry. The displacement at top of cantilever flanged masonry walls at yield can be calculated with a equivalent stiffness which is based on a linear curvature distribution along the wall height from zero at the top to the yielding value at the base. The ultimate displacement can be better predicted by assuming that the compression strain at the second mortar bed from the bottom reaches the ultimate value due to the confinement at the bottom masonry bed provided by the strong concrete base.

(4) Shear Strength and Displacement

Transverse reinforcement is needed to maintain the shear strength of the wall after shear cracking. Since shear failure is sudden and brittle, it must not be permitted to happen in structures. According to the capacity design requirements, the shear strength should be greater than the maximum feasible flexural strength to ensure there will be no shear failure occur. The displacement due to shear deformation is small before shear cracking and becomes unsymmetrical in the two opposite directions after shear cracking because of different shear level. In the direction of web in compression, the displacement due to shear at the ultimate state can make up to more than 30% of the total displacement. To predict the shear displacement, bi-linear equivalent stiffness proposed in Chapter 3 can be used and the result is reasonable good.

(5) Confined Walls

The confinement on mortar beds at free end of web toe provided by steel plates increases the ultimate compression strain of masonry in the confined area, therefore improves the ductility capacity and strength of flanged masonry walls in the direction of web in compression. In our case, the test results show that for confined walls, the ultimate displacement increased by 50% for static tests and 25% for dynamic tests. These values are smaller than expected because of early buckling of extreme vertical reinforcement at free end of web foot as discussed in Chapter 4 and Chapter 5.

(6) Dynamic Response

The experimental results proved that when subjected to earthquake attacks, in the direction of flange in tension, both unconfined and confined flanged masonry walls will have less ductility than when subjected to static loading, with nearly the same strength. Under dynamic loading, the ultimate displacement may drop to 70% to 80% of the values in static case. This is very important for designing masonry structures in the seismic zone. The failure mechanism, however, remains the same. There is not any significant difference in the responses of T-section masonry walls under static and dynamic loading in the direction of flange in compression.

(7) Natural Frequency and damping

The natural frequency (fundamental) of flanged masonry walls before cracking can be predicted with the gross cross section and elastic modulus of $E_m = 1000 f'_m$. The damping ratio is about 0.02 for uncracked masonry. After cracking, the frequency decreases and damping ratio increases unsymmetrically in the two opposite directions with higher frequency and lower damping ratio in the direction of web in compression. The average frequency drops to 30-40% of the initial value and the damping ratio will increases to 5 - 6 % of critical dumping on average at yielding state in the direction of web in compression.

(8) Effect of Loading History

The experimental results indicated that a previous loading history does not affect the ultimate strength and ductility capacity significantly, as long as the pre-existing condition never exceeds the ultimate strength. Under earthquake attacks, the performance of T-section walls may differ from each other due to their loading history and pre-existing conditions, but the same structures will have nearly the same maximum response.

(9) Response to Arbitrary Earthquake Attacks

The test of wall F9 subjected to earthquake input at 45 degree skew to the web showed that under arbitrary earthquake attacks, T-section walls will have responses in the two orthogonal directions. Both the resultant inertial force and displacement will not coincide with the initial earthquake input direction and shear stresses caused by additional inertial torque due to the difference between the mass center and rigid center may be significant because of the characteristics of T-section.

(10) Effective Width of Flange

When the flange is in tension, it usually can not participate in the action with the web completely due to the shear-lag effects, therefore a effective flange width is needed for predicting the strength and stiffness of T-section walls. Formulas proposed in Chapter 7, which was based on the theoretical and experimental results, can be used to determine the effective flange width for T-section masonry walls.

(11) Structural Component Model

Inelastic structural component model developed in Chapter 3 can simulate the overall nonlinear material properties inside the flanged masonry walls and formation of plastic hinges at the wall ends.

The numerical examples for static analyses in Chapter 6 show that the model is applicable of load-displacement envelope for both horizontal and vertical displacement predictions. The time history response analyses show the excellent agreement with the experimental results which indicates that the model works well in the case of dynamic and seismic response analyses.

(12) Constitutive Modelling

The unsymmetrical hysteresis loops for flanged masonry walls proposed in chapter 3 utilizes a tri-linear envelope and permits the stiffness degradation and pinching can be used for time history response analyses of flanges masonry walls. The numerical examples in Chapter 6 show that the loops together with the structural component model worked well and can give very good predictions of seismic behavior of T-section masonry walls

9.2 Recommendations for Further Studies

The theoretical and experimental researches in this report mainly deal with seismic behavior of T-section masonry walls in the directions parallel to the web. Dynamic testing of a flanged masonry wall on shake table with earthquake input 45 degree skew to the web was also carried out as a preliminary study on seismic response of T-section walls subjected to arbitrary earthquake attacks. Further studies are recommended to complement this research project and the possible research interests could be the following aspects:

(1) Effects of Openings

The structure investigated in this report was T-section masonry walls without openings. T-section walls in masonry buildings may include openings such as doors and windows. Therefore the behavior of these walls will depend on the size and positions of the openings which affect the continuity of reinforcement as well as the structure itself, even change the load-resistant mechanism from wall structure to a frame system, if the openings are large enough. The behavior of T-section walls with openings is more complicated, an further studies are necessary to investigate their characteristic.

(2) Buckling of Slender Walls

For slender walls, a potential problem is buckling of the wall under combined axial load and lateral disturbance such as earthquakes and winds etc.. The critical lateral load will depend on the ratio of slenderness, axial load level and constrains at the boundaries etc.. For T-section walls, since the web can provide distributed lateral support to the flange in its own plane and vice versa, theoretical and experimental studies are needed to investigate the effects of this interact between flange and web on buckling of slender T-section masonry walls.

(3) Integrity of Masonry Buildings

One of the serious problems for masonry buildings during earthquake attacks is its integrity. It has been found from investigating seismic damage to masonry structures that the most common damage modes for masonry buildings are shear failure in wall plane and wall collapse in out-of-plane direction due to inadequate support from horizontal diaphragm (roof and floor etc.) and walls perpendicular to it. The lost of support was caused by connection failure along the intersection between web and flange or wall and floor. For masonry structures, there is a natural weakness along the intersections. The effectiveness of connection depends on the block type, amount of transverse and vertical reinforcement crossing the intersection and type of connection detail adopted etc.. During both static and dynamic tests, serious cracking between web and flange alone the wall height was formed. This did not cause the flange to collapse in direction of out-of-plane because relatively heavy transverse reinforcement was provided, linking the web and flange, and strong constraints existed from top and base concrete slabs. More experimental studies on different connection detail between web and flange and wall and floor are needed to check the effectiveness of alternative connections. The effects of lateral diaphragm stiffness on seismic performance of masonry buildings should also be investigated.

(4) Response to Arbitrary Earthquake Attacks

As a preliminary study on response of T-section masonry walls to arbitrary earthquake attacks, only one wall was tested in this project. The experiment indicated that both response resultant displacement and inertial force were off the initial input direction, inertial torque due to the difference between mass center and rigid center of the cross section was resulted. The assumption of "plane cross-section" appeared not to be applicable. Since real earthquake attacks are likely to happen in any direction to the structures, seismic response of T-section to skew excitation is more important and need further studies to understand the real performance of the structures under these attacks and develop feasible analytical method to predict the response of T-section masonry walls.

Appendix A

Computer Program for Design Tables of flanged Masonry Walls

```
c     ***** PROGRAM FOR FLANGED MASONRY WALL ANALYSES *****
c
c     ***** MAIN PROGRAM *****
      dimension vp(11),va(9)
      character*14 ma(6)
      character*21 mb(6)
      common e2,bt,p,g,pl,ep,gi
      common /c1/ r1,r2,zm
      common /c2/ e1,fk,ak,an,en
      common /c3/ vr(6,100)
      common /c4/ ar,cu,cv(2,0:1),cv1(10,0:1),qv1(10,0:1)
      common /c5/ qv(2,0:1),cq(3,0:1),dt(10,0:1)
      print *,'rk,tk,zk,fm,fy,bt,zs,fh,hc,sh,ar,pd,ad'
      read *,rk,tk,zk,fm,fy,bt,zs,fh,hc,sh,ar,pd,ad
      print *,'rk=',rk,'tk=',tk,'zk=',zk,'fm=',fm,'fy=',fy,
     6 'bt=',bt,'zs=',zs,'fh=',fh,'hc=',hc,'sh=',sh,'ar=',ar,
     6 'pd=',pd,'ad=',ad
      g=1.0-bt
      ak=1.0+rk*tk
      fk=rk*tk/bt
      en=0.5*(1.0+rk*tk*bt)/ak
      ep=fy/2.0e5
      gi=(0.5-en)**2+0.083333*(1.0+rk*tk*bt*bt)+rk*tk*(en-
     6 0.5*bt)**2
      r1=1.0+zs*fh/fm
      zm=0.5/((3.0+0.29*fm)/(145.0*fm-1000.0)-0.002*r1+
     6 0.75*zs*sqrt(hc/sh))
      if(r1.eq.1.0)  then
      r2=0.9375
      e1=0.0015
      e2=0.0025
      else
      r2=r1
      e1=0.002*r1
      e2=0.008
      end if
      ma(1)='  Icr/Igross  '
      ma(2)='Mi/f m.t.lw**2'
      ma(3)='  u.My/ y.Mi  '
      ma(4)=ma(1)
      ma(5)=ma(2)
      ma(6)=ma(3)
      mb(1)=' Web in compression  '
      mb(2)=mb(1)
      mb(3)=mb(1)
      mb(4)='Flange in compression'
      mb(5)=mb(4)
      mb(6)=mb(4)
      if(ar.eq.i.0) then
      p=pd
      pl=p*rk*tk*zk
      an=ad
```

```
       call coft(0.0)
       call coft(1.0)
       goto 25
       end if
       k=0
       p=0.01
  5    k=k+1
       vp(k)=p
       j=0
       i=9*(k-1)
       pl=p*rk*tk*zk
       do 20 an=0.0,0.4,0.05
       j=j+1
       va(j)=an
       print *,'k=',k,'j=',j,'i+j=',i+j
       call relt(0.0,i+j)
       call relt(1.0,i+j)
  20   continue
       if(p.eq.0.01) then
       p=p+0.01
       else
       p=p+0.02
       end if
       if(p.le.0.2) goto 5
  25   open(unit=1,file='limin.relt',form='formatted',status='new')
       if(ar.eq.1.0) goto 50
       write(1,40) (ma(k),mb(k),rk,g,fy,
     6 (va(i),i=1,9),(vp(i),(vr(k,9*(I-1)+j),j=1,9),i=1,11),k=1,6)
  40   format(///////,17x,'Table',4x,a14,2x,a21,/,
     6 25x,'lf/lw=',f4.2,2x,'g=',f4.2,2x,'fy=',f5.1,' Mpa',//,
     6 28x,'Axial Load Ratio Nu/f m.Ag',/,2x,'fy/f m',9f8.4,//,10f
     6 8.4,/,10f8.4,/,10f8.4,/,10f8.4,/,10f8.4,/,10f8.4,/,10f8.4,/,
     6 10f8.4,/,10f8.4,/,10f8.4,/,10f8.4,///////)
       if(ar.eq.0.0) goto 7U
  50   write (1,60) (i,pd,ad,zs,fh,hc,sh,rk,tk,zk,fm,fy,g,(cv(j,i)
     6 ,j=1,2),(qv(j,i),j=1,2),(cq(j,i),j=1,3),(dt(j,i),j=1,10),
     6 (cv1(j,i),j=1,10),(qv1(j,i),j=1,10),i=0,1)
  60   format(///,28x,'R=',i2,4x,'pd=',f5.3,4x,'ad=',f5.3,/,
     6 20x,'zs=',f5.3,4x,'fh=',f5.1,4x,'hc=',f5.1,4x,'sh=',f5.1,
     6 /,12x,'kl=',f4.2,4x,'kt=',f4.2,4x,'kz=',f4.2,4x,'fm=',f4.1,
     6 4x,'fy=',f5.1,4x,'g=',f4.2,//,10x,'CURVATURE',2f20.5,/,
     6 10x,'MOMENT',3x,2f20.5,//,10x,'COEFFICINT',3e15.5,//,
     6 10x,'Di=',/,5f16.5,/,5f16.5,//,10x,'Cv=',/,5f16.5,/,5f16.5,
     6 //,10x,'Qv',/,5f16.5,/,5f16.5)
 70    print *,'The End of Calculation'
       stop
       end
c      ***** Subroutine for Result *****
       subroutine relt(r,ij)
       external spy,spu
       common e2,bt,p,g,pl,ep,gi
       common /c3/ vr(6,100)
       cn=root(spy,r)
       if(cn.eq.1.0) then
       vr(3+3*r,ij)=1.0
       cn=root(spu,r)
       if(cn.ge.1.0) vr(3+3*r,ij)=0.0
```

```
      vr(2+3*r,ij)=squ(cn,r)
      vr(1+3*r,ij)=9.375e-4*vr(2+3*r,ij)*cn/gi/e2
      return
      end if
      vt=sqy(cn,r)*(1.0-cn-0.5*bt)/ep
      vr(1+3*r,ij)=9.375e-4*vt/gi
      cm=root(spu,r)
      vr(2+3*r,ij)=squ(cm,r)
      vr(3+3*r,ij)=e2*vt/cm/vr(2+3*r,ij)
      return
      end
c     ***** Functions for P-D curve *****
      subroutine coft(r)
      external spy,spu
      common e2,bt,p,g,pl,ep,gi
      common /c4/ ar,cu,cv(2,0:1),cvl(10,0:1),qvl(10,0:1)
      common /c5/ qv(2,0:1),cq(3,0:1),dt(10,0:1)
      ar=0.0
      cn=root(spy,r)
      cm=root(spu,r)
      cv(2,r)=e2/cm
      qv(2,r)=squ(cm,r)
      a=9.375e-4/gi
      if(cn.eq.1.0) then
      ar=1.0
      cv(1,r)=0.75*cv(2,r)
      cu=cv(1,r)
      cm=root(spu,r)
      qv(1,r)=squ(cm,r)
      else
      cv(1,r)=ep/(1.0-cn-0.5*bt)
      qv(1,r)=sqy(cn,r)
      end if
      ar=1.0
      do 10 i=1,5
      cvl(i,r)=i*0.2*cv(1,r)
   10 cvl(i+5,r)=cv(1,r)+i*0.2*(cv(2,r)-cv(1,r))
      do 20 i=1,10
      cu=cvl(i,r)
      cm=root(spu,r)
   20 qvl(i,r)=squ(cm,r)
      do 30 i=1,10
      if(i.eq.1) then
      dt(i,r)=0.33333*cvl(i,r)
      else
      t=qvl(i-1,r)/qvl(i,r)
      s=(cvl(i,r)-cvl(i-1,r))/(qvl(i,r)-qvl(i-1,r))
      dt(i,r)=dt(i-1,r)*t*t+0.5*(1.0-t*t)*(cvl(i-1,r)-
     6s*qvl(i-1,r))+0.33333*s*qvl(i,r)*(1.0-t**3)
      end if
   30 continue
      t=0.0
      do 40 i=5,10
      if(dt(i,r).gt.t) then
      t=dt(i,r)
      k=i
      end if
```

```
 40     continue
        cq(2,r)=dt(k,r)-dt(5,r)*qv(2,r)/qv(1,r)
        cq(3,r)=cv1(k,r)-cv(1,r)*qv(2,r)/qv(1,r)
        cq(2,r)=cq(2,r)/cq(3,r)
        cq(3,r)=1.0-sqrt(1.0-2.0*cq(2,r))
        ar=1.0
        return
        end
c       ***** Function for CN *****
        function root(cyu,r)
        x0=0.0001
        y0=cyu(x0,r)
 10     x0=x0+0.09999
        if(y0.eq.1000.0) then
        print *,'NO ROOT'
        root=1.0
        return
        end if
        y1=cyu(x0,r)
        print *,'x0=',x0,'y1=',y1
        if(y1*y0.lt.0.0.or.y1.eq.0.0) goto 20
        y0=y1
        goto 10
 20     x1=x0-0.1
        x2=x0
        y0=cyu(x1,r)
 30     x=0.5*(x1+x2)
        y=cyu(x,r)
        if(y*y0.gt.0.0) x1=x
        if(y*y0.lt.0.0) x2=x
        if(x2-x1.gt.0.001) goto 30
        root=x
        print *,'x=',x
        return
        end
c       ***** function for Axial Forces ******
        function p1(e)
        common /c1/ r1,r2,zm
        p1=533.33*e*e-88888.9*e**3/r1
        return
        end
        function p2(e)
        common /c1/ r1,r2,zm
        common /c2/ e1,fk,ak,an,en
        p2=1.067*r2*((1.0+e1*zm)*(e-e1)-0.5*zm*(e*e-e1*e1))
        return
        end
        function py(cn,r)
        common e2,bt,p,g,pl
        et=1.0-cn-0.5*bt
        ct=cn-0.5*bt
        if(cn.le.0.5) then
        py=0.5*p*ct*ct/g/et+pl*r*ct/et
        else
        py=0.5*p*et/g+p*(2.0*cn-1.0)/g+pl*r
        end if
        return
        end
```

```
function pu(e2,cn,r)
common e0,bt,p,g,pl,ep
cc=cn*ep/e2
ct=cn-0.5*bt
if(cc.le.ct) then
pu=pl*r+p*(ct-0.5*cc)/g
else if(cn.ge.0.5*bt/(1.0+ep/e2)) then
pu=e2*pl*r*ct/cn/ep+0.5*e2*p*ct*ct/g/cn/ep
else
pu=-pl*r-p+p*(1.0-cn-0.5*bt-0.5*cc)/g
end if
return
end
function pt(e2,cn,r)
common e0,bt,p,g,pl,ep
et=1.0-cn-0.5*bt
cc=cn*ep/e2
if(cc.le.et) then
pt=pl*(1.0-r)+p*(et-0.5*cc)/g
else if(cc.le.cn-1.0+0.5*bt) then
pt=p*(cn-0.5*bt-0.5*cc)/g-p-pl*(1.0-r)
else
pt=e2*pl*(1.0-r)*et/cn/ep+0.5*e2*p*et*et/g/cn/ep
end if
return
end
function spy(cn,r)
common e2,bt,p,g,pl,ep
common /c2/ e1,fk,ak,an,en
et=1.0-cn-0.5*bt
re=ep/et
ce=(cn-bt)*re
ct=cn*re
ek=1.0+fk*r
sum=ak*an+pl*(1.0-r)+0.5*p*et/g
t1=p1(cn*re)/re
t2=p2(cn*re)/re
if(ct.le.e1) then
continue
if(cn.ge.bt) then
pm=t1*ek-r*fk*p1(ce)/re
else
pm=t1*ek
end if
continue
else if(ct.le.e2) then
continue
if(ce.ge.e1) then
pm=p1(e1)/re+t2*ek-r*fk*p2(ce)/re
else
pm=(p1(e1)/re+t2)*ek-r*fk*p1(ce)/re
end if
continue
else
spy=1000.0
return
end if
```

```
      spy=sum-pm-py(cn,r)
      return
      end
      function spu(cn,r)
      common e0,bt
      common /c2/ e1,fk,ak,an,en
      common /c4/ ar,cu,cv(2,0:1),cv1(10,0:1),qv1(10,0:1)
      if(ar.eq.0.0) then
      e2=e0
      else
      e2=cn*cu
      end if
      re=e2/cn
      ce=(cn-bt)*re
      if(e2.ge.e1) then
      t=(p1(e1)+p2(e2))/re
      else
      t=p1(e2)/re
      end if
      ek=1.0+fk*r
      cet=(cn-1.0+bt)/cn
      ceo=(cn-1.0)/cn
      if(ce.ge.e1) then
      pm=(p1(e1)+p2(e2)*ek-r*fk*p2(ce))/re
      else if(cn.ge.bt) then
      pm=t*ek-r*fk*p1(ce)/re
      else
      pm=t*ek
      end if
      if(cn.ge.1.0) pm=pm-p1((cn-1.0)*e2/cn)/re
      if(r.eq.0.0.and.cn.ge.1.0-bt) then
      continue
      if(ceo.ge.e1/e2) then
      pm=(p2(e2)+p2(cet*e2)*fk-(1.0+fk)*p2(ceo*e2))/re
      else if(cet.ge.e1/e2) then
      pm=(p2(e2)+p2(cet*e2)*fk+(1.0+fk)*(p1(e1)-p1(ceo*e2)))/re
      else if(cn.ge.1.0) then
      pm=t+(p1(cet*e2)*fk-(1.0+fk)*p1(ceo*e2))/re
      else
      pm=t+p1(cet*e2)*fk/re
      end if
      continue
      end if
      spu=ak*an+pt(e2,cn,r)-pm-pu(e2,cn,r)
      return
      end
c     ***** Function for Moments *****
      function q1(e)
      common /c1/ r1,r2,zm
      q1=355.56*e**3-66666.7*e**4/r1
      return
      end
      function q2(e)
      common /c1/ r1,r2,zm
      common /c2/ e1,fk,ak,an,en
      q2=1.067*r2*(0.5*(1.0+e1*zm)*(e*e-e1*e1)-0.33333*zm*(e**3-
     6 e1**3))
      return
      end
```

```
      function qy(cn,r)
      common e2,bt,p,g,pl
      ct=cn-0.5*bt
      et=1.0-cn-0.5*bt
      if(cn.le.0.5) then
      qy=0.33333*p*ct**3/g/et+pl*r*ct*ct/et
      else
      qy=0.33333*p*et*et/g+p*(cn-0.5)+pl*r*ct
      end if
      return
      end
      function qu(e2,cn,r)
      common e0,bt,p,g,pl,ep
      ct=cn-0.5*bt
      cc=cn*ep/e2
      if(cc.le.ct) then
      qu=pl*r*ct+0.5*p*(ct*ct-0.33333*cc*cc)/g
      else if(cn.ge.0.5*bt/(1.0+ep/e2)) then
      qu=r*e2*pl*ct*ct/cn/ep+0.33333*p*e2*ct**3/g/cn/ep
      else
      qu=pl*r*(0.5*bt-cn)-0.5*P*((1.0-cn-0.5*bt)**2-cc*cc/3.0)/g
     6 +p*(0.5-cn)
      end if
      return
      end
      function qt(e2,cn,r)
      common e0,bt,p,g,pl,ep
      et=1.0-cn-0.5*bt
      cc=cn*ep/e2
      if(cc.le.et) then
      qt=pl*(1.0-r)*et+0.5*p*(et*et-0.33333*cc*cc)/g
      else if(cc.le.cn-1.0+0.5*bt) then
      qt=-0.5*p*((cn-0.5*bt)**2-0.33333*cc**2)/g+p*(cn-0.5)+pl
     6 *(cn-1.0+0.5*bt)*(1.0-r)
      else
      qt=pl*(1.0-r)*et*et*e2/cn/ep+0.33333*p*et**3*e2/g/cn/ep
      end if
      return
      end
      function sqy(cn,r)
      common e2,bt,p,g,pl,ep
      common /c2/ el,fk,ak,an,en
      et=1.0-cn-0.5*bt
      re=ep/et
      ct=cn*re
      ce=(cn-bt)*re
      ek=1.0+fk*r
      sum=ak*an*((1.0-en-cn)*(1.0-r)+(en-cn)*r)+pl*(1.0-r)*et
     6 +0.33333*p*et*et/g
      t1=q1(cn*re)/re/re
      t2=q2(cn*re)/re/re
      if(ct.le.el) then
      continue
      if(cn.ge.bt) then
      qm=t1*ek-r*fk*q1(ce)/re/re
      else
      qm=t1*ek
      end if
```

```
      continue
      else
      continue
      if(ce.ge.el) then
      qm=q1(e1)/re/re+t2*ek-r*fk*q2(ce)/re/re
      else
      qm=(q1(e1)/re/re+t2)*ek-r*fk*q1(ce)/re/re
      end if
      continue
      end if
      sqy=sum+qm+qy(cn,r)
      return
      end
      function squ(cn,r)
      common e0,bt
      common /c2/ e1,fk,ak,an,en
      common /c4/ ar,cu,cv(2,0:1),cv1(10,0:1),qv1(10,0:1)
      if(ar.eq.0.0) then
      e2=e0
      else
      e2=cn*cu
      end if
      re=e2/cn
      ce=(cn-bt)*re
      ek=1.0+fk*r
      ceo=(cn-1.0)/cn
      cet=(cn-1.0+bt)/cn
      if(e2.ge.e1) then
      t=(q1(e1)+q2(e2))/re/re
      else
      t=q1(e2)/re/re
      end if
      if(ce.ge.e1) then
      qm=(q1(e1)+q2(e2)*ek-r*fk*q2(ce))/re/re
      else if(cn.ge.bt) then
      qm=t*ek-r*fk*q1(ce)/re/re
      else
      qm=t*ek
      end if
      if(cn.ge.1.0) qm=qm-q1((cn-1.0)*e2/cn)/re/re
      if(r.eq.0.0.and.cn.ge.1.0-bt) then
      continue
      if(ceo.ge.e1/e2) then
      qm=(q2(e2)+q2(cet*e2)*fk-(1.0+fk)*q2(ceo*e2))/re/re
      else if(cet.ge.e1/e2) then
      qm=(q2(e2)+q2(cet*e2)*fk+(1.0+fk)*(q1(e1)-q1(ceo*e2)))/re/re
      else if(cn.ge.1.0) then
      qm=t+(q1(cet*e2)*fk-(1.0+fk)*q1(ceo*e2))/re/re
      else
      qm=t+q1(cet*e2)*fk/re/re
      end if
      continue
      end if
      squ=ak*an*((1.0-cn-en)*(1.0-r)+(en-cn)*r)+qt(e2,cn,r)
     6+qm+qu(e2,cn,r)
      return
      end

c       ***** The End of Program *****
```

Appendix B

Computer Program for Time-history Analysis of flanged Masonry Walls

```
C       ***** PROGRAM FOR TIME-HISTORY RESPONSE ANALYSIS *****
C
        PROGRAM MAIN
        CHARACTER*10 FILE1,FILE2,FILE3,FILE4,FILE5
        DIMENSION A0(2000),DV(2000),AV(2000),PV(2000),VT(2000),DB(2000)
        COMMON /VS/ DU0,U0,U1,U2,V1,V2,V3,V4,V5,V6,V7,V8,V9,W0,C0,GC
     6  ,DT,MK,MA,B0,S0
        COMMON /VG/ GW0,GW1,GW2,GW3,GF0,GF1,GF2,DWC,DWY,DWU,DFC,DFY,TL
     6  ,P1,P2,DWB,DFB,PWM,PFM,PWY,PFY
        COMMON /VQ/ Q0,Q1,QC,DWS,DFS,P1M,P2M,TM
        COMMON /VC/ H,H1
        WRITE(*,*) 'INPNT - W0,E,VI,H,H1,G,A,CK,MA,N,RP'
        READ(*,*) W0,E,VI,H,H1,G,A,CK,MA,N,RP
        DM=H**3/(3.0*E*VI)
        IF(MA.EQ.1) DM=DM+H/(G*A)
        G0=1.0/DM
        OM=SQRT(G0/W0)
        C0=2.0*CK*OM*W0
        T0=6.28/OM
        WRITE(*,*) 'INPNT - FILE1'
        READ(*,5) FILE1
5       FORMAT(A10)
        WRITE(*,*) 'INPNT - FILE2'
        READ(*,5) FILE2
        WRITE(*,*) 'INPUT - FILE3'
        READ(*,5) FILE3
        WRITE(*,*) 'INPUT - FILE4'
        READ(*,5) FILE4
        WRITE(*,*) 'INPUT - FILE5'
        READ(*,5) FILE5
        OPEN(UNIT=11,FILE=FILE1,STATUS='OLD')
        OPEN(UNIT=22,FILE=FILE2,STATUS='NEW')
        OPEN(UNIT=33,FILE=FILE3,STATUS='NEW')
        OPEN(UNIT=44,FILE=FILE4,STATUS='NEW')
        OPEN(UNIT=55,FILE=FILE5,STATUS='NEW')
        WRITE(22,10) W0,E,VI,H,H1,G,A,CK,MA,N,RP,G0,OM,C0,T0
10      FORMAT(//,20X,'THE DATA FOR CALCULATION',//,5X,'W0=',E12.5,5X,
     6  'E=',E12.5,5X,'VI=',E12.5,5X,'H=',E12.5,/,5X,'H1='E12.5,5X,
     6  'G=',E12.5,5X,'A=',E12.5,5X,'CK=',E12.5,/,5X,'MA=',I12,5X,'N=',
     6  I12,5x,'RP=',E12.5,///,5X,'K=',E13.5,5X,'W=',E13.5,5X,'C=',E13.5
     6  ,5X,'T=',E13.5)
        DO 15 I=1,N
        READ(11,*) A0(I)
15      A0(I)=RP*A0(I)
        WRITE(*,*) 'INPUT-GW0,GW1,GW2,GW3,GF0,GF1,GF2,DWC,DWY,DWU,DWL
     6  ,DFC,DFY,TL,P1,P2,DT,CT,MJ,MK'
        READ(*,*) GW0,GW1,GW2,GW3,GF0,GF1,GF2,DWC,DWY,DWU,DWL
     6  ,DFC,DFY,TL,P1,P2,DT,CT,MJ,MK
        WRITE(22,20) GW0,GW1,GW2,GW3,GF0,GF1,GF2,DWC,DWY,DWU,DWL
     6  ,DFC,DFY,TL,P1,P2,DT,CT,MJ,MK
20      FORMAT(//,5X,'GW0=',E11.5,5X,'GW1=',E11.5,5X,'GW2=',E11.5,5X,
     6  'GW3=',E11.5,/,5X,'GF0=',E11.5,5X,'GF1=',E11.5,5X,'GF2=',E11.5,
     6  5X,'DWC=',E11.5,/,5X,'DWY=',E11.5,5X,'DWU=',E11.5,5X,'DWL=',
```

```
     6 E11.5,5X,'DFC=',E11.5,/,5X,'DFY=',E11.5,5X,'TL=',E12.5,5X,'P1='
     6 ,E12.5,5X,'P2=',E12.5,/,5X,'DT=',E12.5,5X,'CT=',E12.5,5x,
     6 'MJ=',I12,5X,'MK=',I12)
       WRITE(*,*) 'INPUT-Q0,Q1,QC'
       READ(*,*) Q0,Q1,QC
       WRITE(22,22) Q0,Q1,QC
22     FORMAT(//,5X,'Q0=',E12.5,5X,'Q1=',E12.5,5X,'QC=',E12.5)
       IF(DT.GE.1.0) GOTO 24
       TV=CT*DT
       V2=3.0/TV
       V3=2.0*V2
       V1=V3/TV
       V4=0.5*TV
       V5=V1/CT
       V6=-V3/CT
       V7=1.0-3.0/CT
       V8=0.5*DT
       V9=DT*DT/6.0
24     CONTINUE
       WRITE(*,*) 'INPUT-BO,PWM,DWB,DWS,PFM,DFB,DFS'
       READ(*,*) BO,PWM,DWB,DWS,PFM,DFB,DFS
       WRITE(22,25) BO,PWM,DWB,DWS,PFM,DFB,DFS
25     FORMAT(//,5X,'BO=',E12.5,5X,'PWM=',E11.5,5X,'DWB=',E11.5,5X,
     6 'DWS=',E11.5,/,5X,'PFM=',E11.5,5X,'DFB=',E11.5,5X,'DFS=',E11.5)
       TM=TL
       S0=0.0
       U0=B0+S0
       U1=0.0
       U2=0.0
       PI=0.0
       AWM=0.0
       AFM=0.0
       GW0=GW0/H
       GW1=GW1/H
       GW2=GW2/H
       GF0=GF0/H
       GF1=GF1/H
       P1=P1/H
       P2=P2/H
       PWY=GW1
       PFY=GF1
       H2=H*H/3.0
       DWC=DWC*H2
       DWY=DWY*H2
       DWU=DWU*H2
       DWL=DWL*H2
       DFC=DFC*H2
       DFY=DFY*H2
       DWM=0.0
       DFM=0.0
       IF(DWB.LT.DWC) THEN
       PWM=GW0
       DWB=DWC
       END IF
       IF(DFB.GT.DFC) THEN
       PFM=GF0
       DFB=DFC
       END IF
```

```
      GW2=(GW2-GW1)/(DWU-DWY)
      GW1=(GW1-GW0)/(DWY-DWC)
      GW0=GW0/DWC
      GW3=GW3*GW0
      GF1=(GF1-GF0)/(DFY-DFC)
      GF0=GF0/DFC
      GF2=GF2*GF0
      QC=QC/H
      Q0=Q0*G*A/H
      Q1=Q1*G*A/H
      IF(DWB.LT.DWC) DWS=PWM/Q0
      IF(DFB.GT.DFC) DFS=PFM/Q0
      IF(DT.GE.1.0) THEN
      GC=0.0
      ELSE
      GC=ADDV(V1,V2,W0,C0)
      END IF
      WRITE(22,26) GW0,GW1,GW2,GW3,GC,GF0,GF1,GF2,PWY,PFY,P1,P2,
     6 QC,Q0,Q1,DWC,DWY,DWU,DWL,DFC,DFY
26    FORMAT(//,5X,'GW0=',E11.5,5X,'GW1=',E11.5,5X,'GW2=',E11.5,
     6 5X,'GW3=',E11.5,/,5X,'GC=',E12.5,5X,'GF0=',E11.5,5X,'GF1=',
     6 E11.5,5X,'GF2=',E11.5,/,5X,'PWY=',E11.5,5X,'PFY=',E11.5,5X,
     6 'P1=',E12.5,5X,'P2=',E12.5,/,5X,'QC=',E12.5,5X,'Q0=',E12.5,
     6 5X,'Q1=',E12.5,5X,'DWC=',E11.5,/,5X,'DWY=',E11.5,5X,'DWU=',
     6 E11.5,5X,'DWL=',E11.5,5X,'DFC=',E11.5,/,5X,'DFY=',E11.5,//)
      J=1
      DB(1)=B0
      DV(1)=U0
      AV(1)=0.0
      PV(1)=0.0
      VT(1)=0.0
      DO 30 I=1,N
      IF(DT.GE.1.0) W0=-1.0
      IF(I.EQ.1) THEN
      DP=-W0*A0(1)*CT
      ELSE
      DP=-W0*((A0(I)-A0(I-1))*CT+A0(I-1))
      END IF
      CALL STEP(GI,QI,PI,DP)
      WRITE(*,*) 'I',I,'GI',GI,'QI',QI,'PI',PI
      IF(U0.GE.DWL) THEN
      WRITE(*,*) 'THE WALL FAILS AT I=', I, 'U0=', U0,'PI=',PI
      WRITE(22,28) I,U0,U2,A0(I),PI
28    FORMAT(//,20X,'THE WALL FAILS AT',/,I5,4E16.5)
      END IF
      AVI=(U2+A0(I))/386.0
      IF(MJ.EQ.1.OR.I.EQ.1.OR.I.EQ.J*MJ) THEN
      J=J+1
      DB(J)=B0
      DV(J)=U0
      AV(J)=AVI
      PV(J)=PI
      VT(J)=(J-1)*DT
      END IF
      CALL CHO1(DWS,S0,I,IS1)
      CALL CHO2(DFS,S0,I,IS2)
```

```
      CALL CHO1(DWB,BO,I,IB1)
      CALL CHO2(DFB,BO,I,IB2)
      CALL CHO1(DWM,U0,I,ID1)
      CALL CHO1(AWM,AVI,I,IA1)
      CALL CHO1(PWM,PI,I,IP1)
      CALL CHO2(DFM,U0,I,ID2)
      CALL CHO2(AFM,AVI,I,IA2)
      CALL CHO2(PFM,PI,I,IP2)
      P1M=PWM
      P2M=PFM
30    CONTINUE
      WRITE(22,40)
40    FORMAT(///,20X,'THE RESULT OF CALCULATION',///,3X,'TIME',10X,
     6 'DISPLA',10X,'ACCELE',10X,'SHEAR',12X,'DISPB',/)
      WRITE(22,45) (VT(I),DV(I),AV(I),PV(I),DB(I),I=1,J)
45    FORMAT(F7.2,4E17.5)
      WRITE(22,50) DWM,ID1,DWB,IB1,AWM,IA1,PWM,IP1,
     6 DFM,ID2,DFB,IB2,AFM,IA2,PFM,IP2
50    FORMAT(//,20X,'THE ENVELOP OF RESPONSE',//,5X,'+DM=',E12.4,I7,
     6 /,5X,'+DB=',E12.4,I7,/,5X,'+AM=',E12.4,I7,/,5X,'+PM=',E12.4,I7,
     6 /,5X,'-DM=',E12.4,I7,/,5X,'-DB=',E12.4,I7,/,5X,
     6 '-AM=',E12.4,I7,/,5X,'-PM=',E12.4,I7)
      WRITE(33,55) (VT(I),DV(I),I=1,J)
55    FORMAT(F8.3,E16.5)
      WRITE(44,55) (VT(I),-AV(I),I=1,J)
      WRITE(55,60) (DV(I),-AV(I),I=1,J)
60    FORMAT(2E16.5)
      STOP
      END
C
C     ***** FUNCTIONS & SUBROUTINES *****
C
      FUNCTION ADDV(C1,C2,V1,V2)
      ADDV=C1*V1+C2*V2
      RETURN
      END
C     *************************
      SUBROUTINE STEP(GI,QI,PI,DP)
      COMMON /VS/ DU0,U0,U1,U2,V1,V2,V3,V4,V5,V6,V7,V8,V9,W0,C0,GC,
     6 DT,MK,MA,BO,SO
      IF(DT.GE.1.0) THEN
      DU0=DP-PI
      ELSE
      DU0=DP+W0*ADDV(V3,2.0,U1,U2)+C0*ADDV(2.0,V4,U1,U2)-PI
      END IF
      GOTO(10,20,30) MK
10    GI=FORG(BO,PI,DU0)
      GOTO 40
20    GI=FOR2(BO,PI,DU0)
      GOTO 40
30    GI=FOR3(BO,PI,DU0)
40    CONTINUE
      IF(MA.EQ.1) THEN
      QI=FORQ(SO,PI,DU0)
      GH=GI*QI/(GI+QI)
      ELSE
      GH=GI
      END IF
```

```
      GG=GH+GC
      DU0=DU0/GG
      IF(DT.GE.1.0) GOTO 50
      DU2=ADDV(V5,V6,DU0,U1)+V7*U2
      DU1=(DU2+U2)*V8+U1
      DU0=ADDV(1.0,2.0,DU2,U2)*V9+DT*U1
      U1=DU1
      U2=DU2
50    B0=B0+DU0*QI/(GI+QI)
      S0=S0+DU0*GI/(GI+QI)
      PP=DU0*GH
      PI=PI+PP
      U0=U0+DU0
      RETURN
      END
C     ************************
      FUNCTION FORG(DI,PI,DP)
      COMMON /VG/ GW0,GW1,GW2,GW3,GF0,GF1,GF2,DWC,DWY,DWU,DFC,DFY,
     6 TL,P1,P2,DWB,DFB,PWM,PFM,PWY,PFY
      COMMON /VC/ H,H1
      GT(DM,PM)=(PM-PI)/(DM-DI)
      RG(G1,G2)=1.0/G1+3.0*H1/G2/H
      GWY=PWY/DWY
      GFY=PFY/DFY
      IF(DI.GT.0.0.AND.PI.GT.0.0) THEN
      CONTINUE
      IF(DP.LE.0.0) THEN
      CONTINUE
      IF(PI.LE.DI*GWY) THEN
      G=GWY
      ELSE
      G=PI/DI
      END IF
      CONTINUE
      ELSE IF(DI.LT.DWB) THEN
      G=GT(DWB,PWM)
      ELSE IF(DI.LE.DWC) THEN
      G=GW0
      ELSE IF(DI.LE.DWY) THEN
      G=GT(DWY,PWY)
      ELSE IF(DI.LE.DWU) THEN
      H1=H*(1.0-PWY/PI)
      G=RG(GWY,GW2)
      FORG=1.0/G
      RETURN
      ELSE
      G=GW3
      END IF
      CONTINUE
      ELSE IF(DI.LT.0.0.AND.PI.LT.0.0) THEN
      CONTINUE
      IF(DP.GE.0.0) THEN
      CONTINUE
      IF(PI.GE.DI*GFY) THEN
      G=GFY
      ELSE
      G=PI/DI
      END IF
```

```
      CONTINUE
      ELSE IF(DI.GT.DFB) THEN
      G=GT(DFB,PFM)
      ELSE IF(DI.GE.DFC) THEN
      G=GF0
      ELSE IF(DI.GE.DFY) THEN
      G=GT(DFY,PFY)
      ELSE
      H1=H*(1.0-PFY/PI)
      G=RG(GFY,GF2)
      FORG=1.0/G
      RETURN
      END IF
      CONTINUE
      ELSE IF(DI.EQ.0.0.AND.PI.EQ.0.0) THEN
      CONTINUE
      IF(DP.GT.0.0) THEN
      G=GW0
      ELSE
      G=GF0
      END IF
      CONTINUE
      ELSE IF(DI.GE.0.0) THEN
      CONTINUE
      IF(DP.GE.0.0.OR.PI.GE.P2+DI*GWY) THEN
      G=GWY
      ELSE
      G=(PI-P2)/DI
      END IF
      CONTINUE
      ELSE IF(DP.LE.0.0.OR.PI.LE.P1+DI*GFY) THEN
      G=GFY
      ELSE
      G=(PI-P1)/DI
      END IF
      FORG=G
      RETURN
C     ********************
      ENTRY FOR2(DI,PI,DP)
      GWY=PWY/DWY
      GFY=PFY/DFY
      IF(DI.GT.0.0) THEN
      CONTINUE
      IF(DP.LE.0.0) THEN
      R2=PI/DI
      ELSE IF(DI.LT.DWB) THEN
      R2=GT(DWB,PWM)
      ELSE IF(DI.GE.DWU) THEN
      R2=GW3
      ELSE IF(DI.GE.DWY) THEN
      H1=H*(1.0-PWY/PI)
      R2=RG(GWY,GW2)
      FOR2=1.0/R2
      RETURN
```

```
      ELSE IF(DI.GE.DWC) THEN
      R2=GT(DWY,PWY)
      ELSE
      R2=GWO
      END IF
      CONTINUE
      ELSE IF(DI.LT.0.0) THEN
      CONTINUE
      IF(DP.GE.0.0) THEN
      R2=PI/DI
      ELSE IF(DI.GT.DFB) THEN
      R2=GT(DFB,PFM)
      ELSE IF(DI.GE.DFC) THEN
      R2=GFO
      ELSE IF(DI.GE.DFY) THEN
      R2=GT(DFY,PFY)
      ELSE
      H1=H*(1.0-PFY/PI)
      R2=RG(GFY,GF2)
      FOR2=1.0/R2
      RETURN
      END IF
      CONTINUE
      ELSE IF(DP.GE.0.0) THEN
      R2=GWO
      ELSE
      R2=GFO
      END IF
      FOR2=R2
      RETURN
C     ********************
      ENTRY FOR3(DI,PI,DP)
      GWY=PWY/DWY
      GFY=PFY/DFY
      IF(DI.GT.0.0.AND.PI.GT.0.0) THEN
      CONTINUE
      IF(DP.LE.0.0) THEN
      CONTINUE
      IF(PI.GE.DI*GWY) THEN
      R3=PI/DI
      ELSE IF(PI.GE.DI*GW2) THEN
      R3=PI/(DI*(1.0-TL)+TL*DWY)
      ELSE
      R3=(PI-P2)/DI
      END IF
      CONTINUE
      ELSE IF(DI.LT.DWB) THEN
      R3=GT(DWB,PWM)
      ELSE IF(DI.GE.DWU) THEN
      R3=GW3
      ELSE IF(DI.GE.DWY) THEN
      H1=H*(1.0-PWY/PI)
      R3=RG(GWY,GW2)
      FOR3=1.0/R3
      RETURN
```

```
ELSE IF(DI.GE.DWC) THEN
R3=GT(DWY,PWY)
ELSE
R3=GWO
END IF
CONTINUE
ELSE IF(DI.LT.0.0.AND.PI.LT.0.0) THEN
CONTINUE
IF(DP.GE.0.0) THEN
CONTINUE
IF(PI.LE.DI*GFY) THEN
R3=PI/DI
ELSE IF(PI.LE.DI*GF2) THEN
R3=PI/(DI*(1.0-TL)+TL*DFY)
ELSE
R3=(PI-P1)/DI
END IF
CONTINUE
ELSE IF(DI.GT.DFB) THEN
R3=GT(DFB,PFM)
ELSE IF(DI.GE.DFC) THEN
R3=GFO
ELSE IF(DI.GE.DFY) THEN
R3=GT(DFY,PFY)
ELSE
H1=H*(1.0-PFY/PI)
R3=RG(GFY,GF2)
FOR3=1.0/R3
RETURN
END IF
CONTINUE
ELSE IF(DI.EQ.0.0.AND.PI.EQ.0.0) THEN
CONTINUE
IF( DP.GE.0.0) THEN
R3=GWO
ELSE
R3=GFO
END IF
CONTINUE
ELSE IF(DI.GE.0.0) THEN
CONTINUE
IF(DP.GE.0.0.OR.PI.GE.P2+DI*GWY) THEN
R3=GWY
ELSE
R3=(PI-P2)/DI
END IF
CONTINUE
ELSE IF(DP.LE.0.0.OR.PI.LE.P1+DI*GFY) THEN
R3=GFY
ELSE
R3=(PI-P1)/DI
END IF
FOR3=R3
RETURN
END
```

```
C         **************************
          SUBROUTINE CHO1(CM,CI,I,K)
          IF(CI.GT.CM) THEN
          CM=CI
          K=I
          END IF
          RETURN
          END
C         **************************
          SUBROUTINE CHO2(CM,CI,I,K)
          IF(CI.LT.CM) THEN
          CM=CI
          K=I
          END IF
          RETURN
          END
C         ***********************
          FUNCTION FORQ(DI,PI,DP)
          COMMON /VQ/ Q0,Q1,QC,DWS,DFS,PWM,PFM,TL
          COMMON /VC/ H,H1
          GT(DM,PM)=(PM-PI)/(DM-DI)
          IF(DI.GT.0.0) THEN
          CONTINUE
          IF(DP.LT.0.0) THEN
          Q=PI/DI
          ELSE IF(DI.LT.DWS) THEN
          Q=GT(DWS,PWM)
          ELSE IF(DI.GE.QC/Q0) THEN
          Q=Q1
          ELSE
          Q=Q0
          END IF
          CONTINUE
          ELSE IF(DI.LT.0.0) THEN
          CONTINUE
          IF(DP.GT.0.0) THEN
          Q=PI/DI
          ELSE IF(DI.GT.DFS) THEN
          Q=GT(DFS,PFM)
          ELSE IF(DI.LT.-QC/Q0) THEN
          Q=Q1
          ELSE
          Q=Q0
          END IF
          CONTINUE
          ELSE
          Q=Q0
          END IF
          FORQ=Q
          RETURN
          END
C
C         ***** END OF PROGRAM *****
```

REFERENCES

1. "Uniform Building Code", International Conference of Building Officials, 1988.

2. ACI Committee 531, " Building Code Requirements for Concrete Masonry Structures and Commentary", American Concrete Institute, Detroit, 1981.

3. " Code of Practice for Masonry Design", NZS 4203p, Standards Association of New Zealand, Wellington, 1984.

4. Park, R and T. Paulay, " Reinforced Concrete Structures", The Southeast Book Company, John Wiley & Sons, 1975.

5. Paulay, T, M.J.N. Priestley and A.J. Synge, " Ductility of Earthquake Resisting Squat Shear Walls", ACI Journal, Proceedings, Vol. 79, No. 4, July/Aug. 1982.

6. Priestley, M.J.N., "Seismic Resistant of Reinforced Concrete Masonry Shear Walls with High Steel Percentages", Bulletin, New Zealand National Society for Earthquake Engineering, Vol. 10, No. 1, March 1977.

7. Priestley, M.J.N. and D.M. Elder, "Seismic Behavior of Slender Concrete Masonry Shear Walls". Research Report 82-4, Department of Civil Engineering, University of Canterbury, March 1982.

8. Mayes, R.L., Y. Omoto and R.W.Clough, "Cyclic Shear Tests of Masonry Piers", Report EERC 76-8, University of California, Berkeley, May 1976.

9. Priestley, M.J.N. and D.M. Elder, "Cyclic Loading Tests of Slender Concrete Masonry Shear Walls", Bulletin, New Zealand National Society for Earthquake Engineering, Vol. 15, No. 1, March 1982.

10. Shing, P. B. et al, " Strength and Ductility of Reinforced Masonry Shear Walls", Proceedings of 5 NAMC, University of Illinois, Urbana/Champaign, June 1990.

11. Priestley, M.J.N., " Flexural Strength of Rectangular Unconfined Masonry Shear Walls with Distributed Reinforcement", TNS Journal, Vol. 5,No. 2, July/Dec. 1986.

12. Priestley,M.J.N., "Ductility of Unconfined and Confined Concrete Masonry Shear Walls", TMS Journal, Vol. 1, No. 2, July/Dec. 1981.

13. Priestley, M.J.N. and Y.K. Chai, " Seismic Design of Reinforced Concrete Masonry Moment Resisting Frames", TMS Journal, Vol. 5, No. 1, Jan./June 1985.

14. Abrams, D.B. and T.J. Paulson,"Perceptions and Observations of Seismic Response for Reinforced Masonry Building Structures", Proceedings of 5 NAMC, University of Illinois, Urbana/Champaign, June 1990.

15. Seible, F. et al, "Simulated Seismic Testing of Three-storey Full-scale Reinforced Masonry In-plane Subassemblages", Proceedings of 5 NAMC, University of Illinois, Urbana/Champaign, June 1990.

16. Adham, S. et al, " Out-of-plane Dynamic Testing of Concrete Masonry Walls", as above.

17. Hamid, H. et al, "Hysteretic Response and Ductility of Reinforced Concrete Masonry walls under Out-of-plane Loading", as above.

18. Priestley, M.J.N. and D.M. Elder," Stress-strain Curve for Unconfined and Confined Concrete Masonry", ACI Journal, Proceedings, Vol. 80, No. 3, May/June 1983.

19. Hart, G.C. et al," Analytical Stress-strain Curves for Grouted Concrete Masonry", TMS Journal, Jan.-June 1989.

20. Hegemier, G.A. et al," Behavior of Concrete Masonry under Biaxial Stresses", Proceedings of the North American Masonry Conference, Aug 1978.

21. Arya, S.K. and G.A. Hegemier, "On Nonlinear Response Prediction of Concrete Masonry Assemblies", as above.

22. Hamid, A.A. and R.G.Drysdale, " Proposed Failure Criteria for Brick Masonry under Combined Stresses", Proceedings of the Second North American Masonry Conference, Aug. 1982.

23. Motta, F. and E. Damore, " Numerical Modelling of the Structural Behavior of Masonry Buildings", Proceedings of the International Brick Masonry Conference, Aug., 1985.

24. Arturo, Tena-colunga and D.P. Abrams," Estimating Response of Masonry Structures with Linear Finite Elements", Proceedings of 5NAMC, University of Illinois, Urbana/Champaign,June 1990.

25. Seible, F., H.L. LaRovere and G.R. Kingsley, "Nonlinear Analysis of Reinforced Concrete Masonry Subassemblages", as above.

26. Hart, G.C. et al,"SCM Model for University of Colorado Single Flexural Walls", TCCMAR Report Task 2.1, 1989.

27. He, Limin. and M.J.N. Priestley," Seismic Behavior of Flanged Masonry Shear Walls - Preliminary Studies", Report SSRP- 88/01, Department of Applied Mechanics and Engineering Sciences, University of California, San Diego, May 1988.

28. Priestley, M.J.N. and R. Park, " Strength and Ductility of Reinforced Concrete Columns under Seismic Loading", ACT Structural Journal, Vol. 84 No. 1, Jan./Feb., 1984.

29. Priestley, M.J.N. and Y.K. Chai," Prediction of Masonry compression Strength", New Zealand Concrete Construction, Vol. 28, March and April, 1984 (two parts).

30. Noland, J. L., " 1990 Status Report: U.S. Coordinated Program for Masonry Building Research", The Sixth Meeting of the Joint Technical Coordinating Committee on Masonry Research, Oct. 20-22, 1990. Seattle, USA.

31. Clough, R.W. and J. Benzien, " Dynamics of Structures", McGraw-Hill Book Company, 1975.

32. Vecchio, F.J. and M.P. Collins, " The Modified Compression-field Theory for Reinforced Concrete Element Subjected to Shear", ACI Journal, Proceedings Vol. 83, No. 2, March-April, 1986.

33. Okamoto, S., " Overview of Japanese Research Activities for RM Buildings", The Sixth Meeting of the Joint Technical Coordinating Committee on Masonry Research, Oct. 20-22, 1990. Seattle, USA.

34. Teshigawara, M. and T. Nishi, "Correlation Study Between Fundamental Structure Test and Seismic Response of RM walls, Test Planning", The Fourth Meeting of the Joint Technical Coordinating Committee on Masonry Research, Oct. 17-19, 1988. San Diego, USA.

35. Imai, H. and M. Miyamoto," Seismic Behavior of Reinforced Masonry Walls with Small Openings", The Fourth Meeting of the Joint Technical Coordinating Committee on Masonry Research, Oct. 17-19, 1988. San Diego, USA.

36. Matsumura, "Effectiveness of Shear Reinforcement in Fully Grouted Hollow Clay Masonry Walls', The Fourth Meeting of the Joint Technical Coordinating Committee on Masonry Research, Oct. 17-19, 1988. San Diego, USA.

37. Imai, H. ," Seismic Behavior of Reinforced Masonry Walls with Small Openings (B)", The Fifth Meeting of the Joint Technical Coordinating Committee on Masonry Research, Oct. 26-28, 1989. Tsukuba, Japan.

38. Teshigawara, M. and T. Nishi, "Seismic Capacity of Reinforced Masonry Walls under High Axial Force (b)", The Fifth Meeting of the Joint Technical Coordinating Committee on Masonry Research, Oct. 26-28, 1989. Tsukuba, Japan.

39. Arinaga, S. and A. Bara, " Shear Strength and deformation of Reinforced Masonry Panel under Diagonal Compression Load", The Fifth Meeting of the Joint Technical Coordinating Committee on Masonry Research, Oct. 26-28, 1989. Tsukuba, Japan.

40. Nishi, T. and M. Teshigawara, "Correlation Study on Diagonal Crack Strength Between diagonal Compression Test and Bending Shear of RM walls(B)", The Sixth Meeting of the Joint Technical Coordinating Committee on Masonry Research, Oct. 20-22, 1990. Seattle, USA.

41. Kubota and Murakami," Flexural Test of Reinforced Concrete Masonry Walls - Effect of Lap Joint of Reinforcement", The Fourth Meeting of the Joint Technical Coordinating Committee on Masonry Research, Oct. 17-19, 1988. San Diego, USA.

42. Kaminosono, T., " Out -of-plane Behavior of Masonry Wall-Slab and Masonry Wall-Subbeam Subassemblages", The Fifth Meeting of the Joint Technical Coordinating Committee on Masonry Research, Oct. 26-28, 1989. Tsukuba, Japan.

43. Seible, F. and G.R.Kingsley, " Modeling of Concrete and Masonry Structures Subjected to Seismic Loading", Experimental and Numerical Methods in Earthquake Engineering, pp281-318, ECSC, EEC, EAEC, 1991, Brussels and Luxembourg.